

THE NATURE OF THE FERRIC HYDROPEROXIDE
INTERMEDIATE IN HEME OXYGENASE:
A MAGNETIC RESONANCE
INVESTIGATION

By

GRÉGORI ALEXIS ARNAUD CAIGNAN

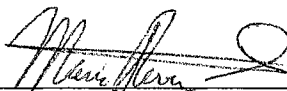
Bachelor of Science
Université des Sciences et Technologies de Lille
Villeneuve d'Ascq, France
1998

Masters of Science
Oklahoma State University
Stillwater, Oklahoma
2000

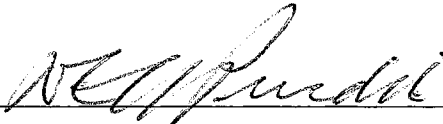
Submitted to the Faculty of the
Graduate College of the
Oklahoma State University
in partial fulfillment of
the requirements for
the Degree of
DOCTOR OF PHILOSOPHY
December, 2003

THE NATURE OF THE FERRIC HYDROPEROXIDE
INTERMEDIATE IN HEME OXYGENASE:A
MAGNETIC RESONANCE
INVESTIGATION

Thesis Approved:



Thesis Advisor



Warren T Ford



Dean of the Graduate College

ACKNOWLEDGEMENTS

I wish to thank my advisor, Dr. Mario Rivera, for his support and guidance. He furnished me with opportunities I never thought to encounter and in so doing opened up a world of dreams.

I am very grateful to all of my committee members for their help and advice. Special mention must be made of Dr. Richard Bunce who not only served as the chair of my committee but with whom we collaborated for most of my work. He has been a great source of advice during my entire stay at OSU and a seemingly never ending source of wit and sarcasm on wednesday nights.

Over the past few years, I have had the opportunity and pleasure to collaborate with Dr. F. Ann Walker and Dr. Angela Wilks. They are great persons whose knowledge, help and advice have been invaluable.

I am indebted to Dr. Margaret Eastman for all her help, collaboration and friendship. Without her I would not have accomplished as much and would likely not be heading in my present direction.

I would also like to recognize all of my friends without whom the rigours of graduate school would no doubt have been much harder to accept.

Finally, I wish to acknowledge my parents for their love and unconditional support. They are the light by which I have found my way.

“What is now proved was once only imagined” – W. Blake

TABLE OF CONTENTS

Chapter	Page
I INTRODUCTION	1
Heme Oxygenase	1
<i>a) Biological function</i>	1
<i>b) Mammalian enzymes</i>	3
<i>c) Bacterial enzymes</i>	4
The First Step in the Catalytic Cycle of Heme Oxygenase	6
<i>a) Regioselectivity</i>	6
<i>b) Formation of the activated oxygen species</i>	7
Research Direction	8
References	10
II NUCLEAR MAGNETIC RESONANCE SPECTROSCOPIC ANALYSIS OF PARAMAGNETIC HEMES AND HEME PROTEINS	12
Heme Proteins	12
Nuclear Magnetic Resonance Spectroscopy of Paramagnetic Hemes and Heme Proteins	17
<i>a) ¹H Shifts, axial ligands and axial ligand geometry</i>	20
<i>b) ¹³C NMR Spectroscopy in the analysis of hemoproteins</i>	26
References	30
III MODELS OF THE LOW-SPIN IRON(III) HYDROPEROXIDE INTERMEDIATE OF HEME OXYGENASE: MAGNETIC RESONANCE EVIDENCE FOR THERMODYNAMIC STABILIZATION OF THE d _{xy} ELECTRONIC STATE AT AMBIENT TEMPERATURES	35
Introduction	35
Experimental Section.....	39

Chapter	Page
a) <i>Reagents</i>	39
b) <i>Synthesis of alkyl peroxide porphyrinate complexes</i>	40
c) <i>Sample preparation for magnetic resonance</i>	43
d) <i>NMR spectroscopic investigations</i>	44
e) <i>EPR spectroscopic investigations</i>	44
Results and Discussion	45
a) <i>Synthesis of alkyl peroxide complexes of Fe^{III}TPP</i>	45
b) <i>Pulsed ENDOR spectroscopy reveals that [TPPFe(OCH₃)(OO^tBu)]⁻ has a d_π electron configuration at 8 K</i>	49
c) <i>¹³C NMR spectroscopy reveals that [TPPFe(OCH₃)(OO^tBu)]⁻ has d_{xy} electron configuration at 193 K, and, by extrapolation, at room temperature</i>	57
d) <i>Variable temperature ¹³C NMR spectroscopy of [meso-TPPFe(OCH₃)(OO^tBu)]⁻ indicates a thermodynamic equilibrium between electron configurations</i>	60
e) <i>Magnetic resonance spectroscopy of [TPPFe(OCH₃)₂]⁻ and [TPPFe(OO^tBu)₂]⁻</i>	69
Relevance to Enzyme Systems and Concluding Remarks.....	72
References	78
IV THE HYDROXIDE COMPLEX OF <i>PSEUDOMONAS AERUGINOSA</i> HEME OXYGENASE AS A MODEL OF THE LOW-SPIN IRON(III) HYDROPEROXIDE INTERMEDIATE IN HEME CATABOLISM: ¹³ C NMR SPECTROSCOPIC STUDIES SUGGEST THE ACTIVE PARTICIPATION OF THE HEME IN MACROCYCLE HYDROXYLATION	83
Introduction	83
Experimental Section	87
a) <i>Protein preparation and reconstitution with ¹³C-labeled heme</i>	87
b) <i>Spectroscopic studies</i>	89
Results and Discussion.....	90
a) <i>Characterization of the hydroxide complex of pa-HO by ¹H NMR and electronic absorption spectroscopy</i>	90
b) <i>¹³C NMR chemical shifts are diagnostic of heme electronic structure</i>	96

Chapter	Page
<ul style="list-style-type: none"> c) <i>¹³C NMR spectroscopy reveals the coexistence of at least three spin states exhibiting different degrees of population of the iron-d_{π} orbitals</i>..... 	99
Relevance to the Mechanism of Heme Hydroxylation Carried out by HO.....	113
References	117
V A NOVEL ELECTRONIC STRUCTURE IN THE AZIDE COMPLEX OF <i>PSEUDOMONAS AERUGINOSA</i> HEME OXYGENASE: MECHANISTIC IMPLICATIONS FOR HEME DEGRADATION.....	121
Introduction.....	121
Experimental Section	125
a) <i>Protein preparation and reconstitution with ¹³C-labeled heme</i>	125
b) <i>Spectroscopic Studies</i>	127
Results and Discussion.....	128
a) <i>Electronic absorption and ¹H NMR spectroscopic characterization of the azide complex of pa-HO</i>	128
b) <i>¹H and ¹³C NMR resonance assignments for pa-HO in complex with azide</i>	134
c) <i>Heme methyl ¹H chemical shifts suggest the heme electronic structure of pa-HO-N₃ is not the common S = 1/2, d_{π}</i>	137
d) <i>¹³C NMR Spectroscopy of the porphyrin methyl carbons suggests a change in the electronic structure of the heme</i>	142
e) <i>¹³C NMR spectroscopy of porphyrin core carbons: an electronic configuration diagnostic tool</i>	146
f) <i>Deformations of the porphyrin ring from planarity allow a previously unobserved spin density delocalization mechanism</i>	152
Mechanistic Implications for Heme Degradation and Concluding Remarks...	157
References	161
VI THE OXIDATION OF HEME TO β - AND δ -BILIVERDIN BY <i>PSEUDOMONAS AERUGINOSA</i> HEME OXYGENASE IS A CONSEQUENCE OF AN UNUSUAL SEATING OF THE HEME.....	165

Chapter	Page
Introduction	165
Experimental	168
<i>a) General methods</i>	168
<i>b) Bacterial strains</i>	168
<i>c) Mutagenesis of pEHmuO</i>	168
<i>d) Expression and purification of wild type and mutant pa-HOs</i>	169
<i>e) Reconstitution of the wild type and pa-HO mutants</i>	170
<i>f) Electronic absorption spectroscopy of the wild type and mutant pa-HOs</i>	170
<i>g) Determination of the extinction coefficient for the heme pa-HO complexes</i>	170
<i>h) Reaction of the heme pa-HO complexes with NADPH cytochrome P450 reductase or ascorbate</i>	171
<i>i) HPLC analysis of heme pa-HO reaction products</i>	171
<i>j) Preparation of HOs reconstituted with ¹³C-labeled heme</i>	172
<i>k) Resonance Raman spectroscopy</i>	174
<i>l) NMR spectroscopy</i>	174
Results	175
<i>a) Expression, purification and structural characterization of the wild type and mutant pa-HOs</i>	175
<i>b) Resonance Raman characterization</i>	176
<i>c) Catalytic turnover of the pa-HO mutants</i>	181
<i>d) Resonance assignments for cyanide-inhibited wild type pa-HO and cd-HO</i>	183
<i>e) Interpretive model for the NMR spectroscopic studies</i>	189
<i>f) The orientation of the histidine plane in pa-HO is different from that of other known mammalian and bacterial heme oxygenases</i>	196
<i>g) A dynamic exchange between two heme seatings in Asn-19 Lys/Phe-117 Tyr pa-HO is responsible for the altered regioselectivity of the double mutant</i>	200
Relevance to the Mechanism of Action of HO and Concluding Remarks	216
References	220

LIST OF TABLES

Table		Page
Chapter V		
1	^1H and ^{13}C chemical shifts for heme substituents of <i>pa</i> -HO-N ₃	136
Chapter VI		
1	Characteristic features of the UV-Visible spectra of wild type and mutant <i>pa</i> -HO complexes	177
2	Regioselectivity of heme oxygenation	182
3	^1H and ^{13}C NMR chemical shifts for the cyanide complexes of <i>pa</i> -HO and <i>cd</i> -HO	194

List of Figures

Figure	Page
Chapter I	
1. Amino acid sequence alignment of <i>Neisseriae meningitidis</i> (nm-HO), <i>Corynebacterium diphtheriae</i> (cd-HO) and <i>Pseudomonas aeruginosa</i> (pa-HO) heme oxygenases	5
Chapter II	
1 Protoheme IX	14
2 Common spin states for the physiologically relevant oxidation states of iron...	15
3 (A) Schematic representation of the Fe(II) heme in deoxymyoglobin. (B) A view of the heme active site of oxy-myoglobin. (C) A view of the active site of mitochondrial cytochrome b_5	16
4 a) Electron density and nodal properties of porphyrin $3e(\pi)$ orbitals, that interact with the d_{xz} and d_{yz} orbitals of low spin Fe(III) respectively. b) Spin density for two angles of the proximal histidine plane, 0° and 45° , with respect to the axis along the nitrogen atoms of pyrrole rings II and IV....	22
5 Right: Right-handed coordinate system and nomenclature used for describing the projection of the His-imidazole plane onto the porphyrin ring. Left: Dependence of observed heme-methyl shifts on the angle ϕ formed between the molecular x axis and the projection of the imidazole plane	24
Chapter III	
1 Representation of the $3a_{2u}(\pi)$ porphyrin orbital	38
2 Schematic cross-sectional representation of the cell used to obtain electronic absorption spectra at low temperatures	42

Figure	Page
3 Electronic absorption spectra of [TPPFe(OCH ₃) ₂] ⁻ (A), [TPPFe(OCH ₃)(OO ^t Bu)] ⁻ (B), and [TPPFe(OO ^t Bu) ₂] ⁻ (C). The corresponding EPR spectra are shown in (D) by traces 1, 2 and 3 respectively	48
4 Mims ENDOR spectra of <i>meso</i> - ¹³ C in [TPPFe(OCH ₃)(OO ^t Bu)] ⁻ (traces 1 and 2) and in [TPPFe(N-Me-Im) ₂] ⁺	50
5 Davies ENDOR spectra of <i>meso</i> - ¹³ C in [TPPFe(^t BuNC) ₂] ⁺	51
6 (A) ¹³ C NMR spectrum of [<i>meso</i> - ¹³ C-TPPFe(OCH ₃)(OO ^t Bu)] ⁻ obtained at 193 K. (B) Electronic absorption spectra of [TPPFe(OCH ₃)(OO ^t Bu)] ⁻ at (a) 195 K, (b) after three hours at 231 K and (c) spectrum obtained from TPPFeCl at 195 K. (C) Electronic absorption spectra of (a) [TPPFe(OCH ₃)(OO ^t Bu)] ⁻ , (b) [TPPFe(OCH ₃) ₂] ⁻ and (c) [TPPFe(OO ^t Bu) ₂] ⁻	59
7 ¹³ C NMR spectra of [<i>meso</i> - ¹³ C-TPPFe(OCH ₃)(OO ^t Bu)] ⁻ obtained at different temperatures	64
8 Temperature dependence of the <i>meso</i> - ¹³ C isotropic shift for several complexes, with fits for (a) a ‘pure’ d _{xy} electron configuration; (b) a ‘pure’ dπ electron configuration; (c) a chemical equilibrium between the two; and a thermally-accessible excited state, either (d) 20 cm ⁻¹ , (e) 50 cm ⁻¹ , (f) 100 cm ⁻¹ , (g) 150 cm ⁻¹ , (h) 200 cm ⁻¹ , (i) 300 cm ⁻¹ , or (j) 520 cm ⁻¹ above the ground state	65
9 Variable temperature <i>meso</i> - ¹³ C NMR spectroscopic data obtained for [TPPFe(OCH ₃) ₂] ⁻ , [TPPFe(OCH ₃)(OO ^t Bu)] ⁻ , and [TPPFe(OO ^t Bu) ₂] ⁻	71

Chapter IV

1 A: Electronic absorption spectra obtained during the titration of ferric HO with sodium hydroxide. B: CD spectra obtained at pH 6.5, pH 8.5 and pH 10.0.	91
2 Dowfield portion of the ¹ H NMR spectra of <i>pa</i> -HO obtained at 25 °C and pH 6.3 (a), 8.3 (b), 9.3 (c) and 10.3 (d)	93
3 ¹ H NMR spectra of (a) Fe ^{III} -OH at pH 10.3, (b) Fe ^{III} -CN at pH 7.4 and (c) Fe ^{III} -CN at pH 10.3 obtained at 25 °C	94
4 Left: Typical porphyrin core carbon chemical shifts for (a) Fe ^{III} -porphyrinates with the S=1/2, dπ electron configuration, (b) Fe ^{III} -porphyrinates with the S=3/2, (d _{xy}) ² (d _{xz} ,d _{yz}) ² (d _z ²) ¹ electron configuration. Right: schematic representation of the 3a _{2u} (π) and 3e(π) porphyrin orbitals.....	97

Figure	Page
5 ^{13}C NMR spectra of <i>pa</i> -HO reconstituted with heme labeled with ^{13}C at the meso and α positions. Spectra were collected at pH values of 6.3 (a), 7.3 (b), 8.3 (c) and 10.3 (d)	100
6 A portion of the ^{13}C NMR spectra obtained at 37 °C from a solution of the Fe^{III} -OH complex of <i>pa</i> -HO (pH 10.3) reconstituted with heme labeled at C_α and C_m carbons (A) and C_α and C_β carbons (B)	101
7 Temperature dependence of the C_α , C_β and C_m chemical shifts for the Fe^{III} -OH complex of <i>pa</i> -HO	104
8 A portion of the ^{13}C NMR spectra obtained at 37 °C from a solution of the Fe^{III} -OH complex of <i>pa</i> -HO (pH 10.3) reconstituted with heme labeled at C_α and C_m (A) and C_α and C_β carbons (B).....	105
9 ^{13}C NMR spectra (37°C) of the Fe^{III} -OH complex of <i>pa</i> -HO (pH 10.3) reconstituted with heme labeled at the C_α and C_m (A) and C_α and C_β carbons (B)	106
10 ^{13}C NMR spectra of <i>pa</i> -HO reconstituted with heme labeled with ^{13}C at the C_m and C_α positions. Spectrum A is that of the hydroxide complex of <i>pa</i> -HO at pH=10.3 and 37 °C and B is the spectrum obtained after the addition of 4 equivalents of sodium cyanide under identical pH and temperature conditions	109
11 ^{13}C NMR spectra of the Fe^{III} -OH complex of <i>pa</i> -HO obtained at different temperatures	110

Chapter V

1 Electronic absorption spectra of <i>Pseudomonas aeruginosa</i> heme oxygenase at pH=7.4 (A) and in complex with cyanide (B) and azide (C). Spectra were recorded at room temperature.....	130
2 High frequency portion of the ^1H NMR spectra of <i>pa</i> -HO obtained at 25 °C and pH 7.4. Spectra after the addition of 0 (a), 0.5 (b), 1 (c) and 1.5 (c) equivalents of sodium azide	132
3 ^1H NMR spectra of (a) (Fe^{III} - N_3) <i>pa</i> -HO at pH 7.4, (b) (Fe^{III} -OH) <i>pa</i> -HO at pH 10.3 and (c) (Fe^{III} -CN) <i>pa</i> -HO at pH 7.4. All spectra were acquired at 25 °C	133
4 High (A) and low (B) frequency portions of the HMQC spectrum of <i>pa</i> -HO- N_3 reconstituted with ^{13}C labeled heme prepared from [1,2- ^{13}C]-ALA	138

Figure	Page
5 NOESY spectrum of <i>pa</i> -HO-N ₃ at 25 °C.....	139
6 Plot of calculated versus observed shifts of heme methyl protons. Panel A: (+) Typical S=1/2, d _π cyanide complexes of heme oxygenase from <i>Pseudomonas aeruginosa</i> , <i>Corynebacterium diphtheriae</i> and sperm whale myoglobin; (●) azide complex of sperm whale metmyoglobin. Panel B: 1Me (● or ○), 3Me (▲ or Δ), 5Me (■ or □) and 8Me (◆ or ◇)	143
7 Schematic representation of the ¹³ C NMR spectra of <i>pa</i> -HO-CN, metmyoglobin cyanide, <i>pa</i> -HO-N ₃ and <i>pa</i> -HO-OH. All spectra were obtained at 25 °C with the exception of the one corresponding to <i>pa</i> -HO-CN which was taken at 10 °C	144
8 Left: Typical porphyrin core carbon chemical shifts for (a) Fe ^{III} -porphyrinates with the S=1/2, d _π electron configuration, (b) Fe ^{III} -porphyrinates with the S=3/2, (d _{xy}) ² (d _{xz} ,d _{yz}) ² (d _z ²) ¹ electron configuration. Right: schematic representation of the 3a _{2u} (π) and 3e(π) porphyrin orbitals.....	148
9 ¹³ C NMR spectra obtained at 35 °C from a solution of ferric azido- <i>pa</i> -HO reconstituted with heme labeled at the C _α and C _m carbons (A) and C _α and C _β carbons (B)	151
10 Temperature dependence of the C _α and C _β chemical shifts for the Fe ^{III} -N ₃ (A) and Fe ^{III} -OH (B) complexes of <i>pa</i> -HO	153
11 Schematic representation of the a _{1u} porphyrin π frontier molecular orbital.....	156

Chapter VI

1 High-frequency region of the RR spectra of ferric heme – protein complexes in wt <i>nm</i> -HO (A), wt <i>pa</i> -HO (B), and N19K/F117Y <i>pa</i> -HO (C).....	179
2 High-frequency region of the RR spectra of ferrous heme – protein complexes in wt <i>nm</i> -HO (A), wt <i>pa</i> -HO (B), and N19K/F117Y <i>pa</i> -HO (C).....	180
3 (A) ¹³ C labeling pattern obtained when protoporphyrin IX is biosynthesized from [1,2- ¹³ C]-ALA. (B) ¹³ C labeling pattern obtained from [5- ¹³ C]-ALA	184
4 Low (A) and high (B) frequency (¹³ C) portions of the HMQC spectrum of wild type <i>pa</i> -HO-CN reconstituted with heme derived from [1,2- ¹³ C]-ALA showing both contour plot and 1-D ¹³ C spectrum	186

Figure	Page
5 Portion of the HMQC spectrum of wild type <i>pa</i> -HO-CN reconstituted with heme derived from [5- ¹³ C]-ALA showing both contour plot and 1-D ¹³ C spectrum	188
6 WEFT-NOESY of <i>pa</i> -HO reconstituted with heme derived from [5- ¹³ C]-ALA	190
7 HMQC spectrum of <i>cd</i> -HO-CN reconstituted with heme derived from [1,2- ¹³ C]-ALA	191
8 Portion of the HMQC spectrum of <i>cd</i> -HO-CN reconstituted with heme derived from [5- ¹³ C]-ALA	192
9 WEFT NOESY of <i>cd</i> -HO-CN reconstituted with heme derived from [5- ¹³ C]-ALA	193
10 Right: Right-handed coordinate system and nomenclature used for describing the projection of the His-imidazole plane onto the porphyrin ring. Left: Dependence of observed heme-methyl shifts on the angle ϕ formed between the molecular <i>x</i> axis and the projection of the imidazole plane	197
11 High frequency portion of the ¹ H NMR spectra of (a) <i>cd</i> -HO-CN and (b) <i>pa</i> -HO-CN reconstituted with heme derived from [1,2- ¹³ C]-ALA	199
12 Variable temperature ¹ H NMR spectra of the Asn-19 Lys/Phe-117 Tyr double mutant of <i>pa</i> -HO-CN. Spectra were acquired at (a) 35, (b) 30, (c) 20, (d) 15 and (e) 10 °C	201
13 HMQC spectrum of the cyanide inhibited Asn-19 Lys/Phe-117 Tyr <i>pa</i> -HO reconstituted with heme derived from [1,2- ¹³ C]-ALA. Only the low frequency (¹³ C) region of the spectrum, which displays the methyl resonances, is shown .	204
14 EXSY spectrum of the double mutant of <i>pa</i> -HO-CN	207
15 Stereoview of the heme binding environment in <i>nm</i> -HO	210
16 Stereoview of the predicted wild type (A) and alternative (B) heme seatings in mutant <i>pa</i> -HO-CN, modeled into the fold of <i>nm</i> -HO	215

Chapter I

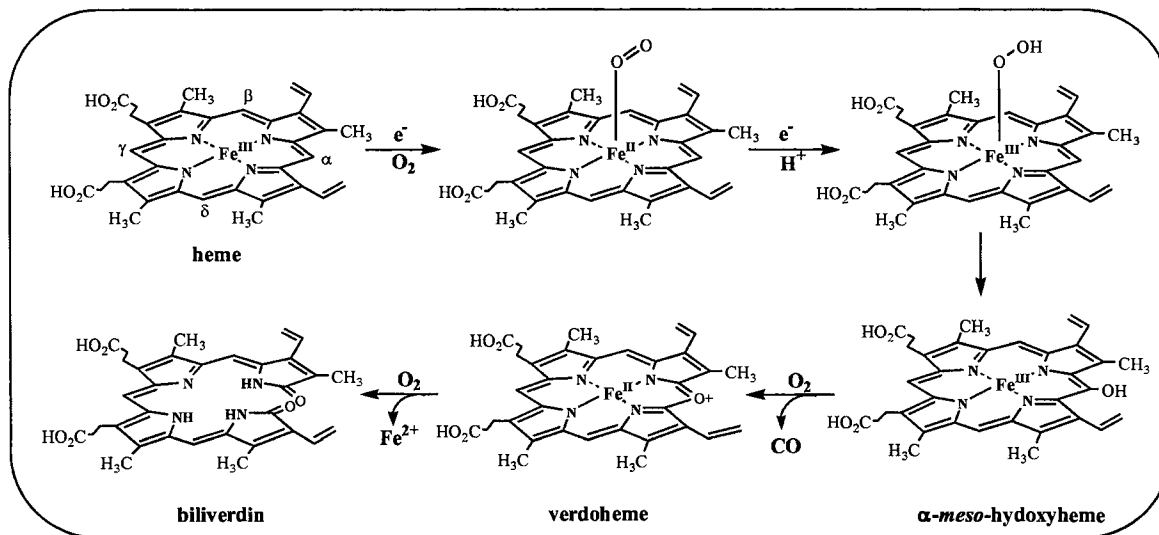
INTRODUCTION

Heme Oxygenase

a) Biological function

Heme oxygenase (HO) is an enzyme responsible for the catalytic degradation of heme to biliverdin, carbon monoxide (CO) and free iron [1]. Present in mammals, plants and bacteria, HO is highly unusual in that it uses heme as both its substrate and its prosthetic group. The catalytic cycle of HO, shown in scheme I, starts with the oxidation of heme to α -*meso*-hydroxyheme, a reaction which requires a molecule of oxygen and 2 reducing equivalents [2]. This is followed by the conversion of α -*meso*-hydroxyheme to verdoheme, which consumes a second molecule of oxygen and 1 electron. Finally, verdoheme reacts with a third oxygen molecule and additional reducing equivalents to produce α -biliverdin while releasing a molecule of CO. The electrons required for this catalytic process are provided, by NADPH-cytochrome P450 reductase in mammals and by ferredoxin in plants [3].

HO in mammals is responsible for the physiological catabolism of heme. The heme oxygenation process removes free heme released from hemoglobin present in tissue when blood vessels rupture. Free heme is a nefarious oxidant but HO activity will convert it to biliverdin that will in turn yield bilirubin, a potent antioxidant that may play an important role in minimizing intracellular oxidative damage. Heme catabolism is also



Scheme I: Heme oxygenase catalytic cycle

of critical importance as it satisfies most of the iron requirements of the body where our daily diets furnish only 1-3% of the iron utilized in the synthesis of red blood cells. Another product of HO catalytic activity is carbon monoxide [4]. The role of CO, long considered a poisonous product of heme oxygenation, has now become a subject of increasing interest as a growing body of evidence suggests it may act as a neural messenger. The roles recently being attributed to CO include its function as a neural messenger in learning and memory, as a factor in neuroendocrine regulation, as an endogenous modulator of vascular tone, and as a protective agent in hypoxia and endotoxic shock [5-7].

In plants, HOs play a significant role in the synthesis of the tetrapyrrole-containing chromophores of photosynthetic organisms while in bacteria they seem to play a vital role in the acquisition of iron, an element essential for the organism's survival and pathogenicity [5].

b) Mammalian enzymes

Two heme oxygenase isoforms are known to exist in mammals, HO-1 and HO-2, and a third form (HO-3) has been reported. HO-1, found in a variety of tissues, is the form that has been primarily examined because it is induced by a variety of agents. HO-2 on the other hand, primarily localized in the brain and testes, is resistant to induction by exogenous factors. The molecular masses of human HO-1 and HO-2 are 33 and 36 kDa, respectively [3]. The protein sequences of these 2 isoforms have 43% identity and show regions of high sequence conservation, most notably in the regions corresponding to the proximal and distal sides of the heme binding pocket. These two enzymes have

hydrophobic sequences at their C-terminal ends that are involved in binding to microsomal membranes [3]. Consequently, in order to facilitate the structural studies of the enzymes, truncated forms, where the membrane binding domains have been removed, were constructed and introduced into bacterial systems allowing the over-expression of soluble forms of the proteins [8-10].

c) Bacterial enzymes

In contrast to mammalian HOs, bacterial enzymes are not membrane bound and quite soluble with molecular masses that are on average significantly smaller. The heme oxygenase isolated from the gram-positive pathogen *Corynebacterium diphtheriae* (*cd*-HO) has a mass of approximately 24 kDa while the HOs from the gram-negative organisms *Neisseriae meningitidis* (*nm*-HO) and *Pseudomonas aeruginosa* (*pa*-HO) are roughly 23.5 and 22 kDa respectively [11-14].

The *cd*-HO, *nm*-HO and *pa*-HO enzymes have 35, 21 and 22% identity to HO-1 and contain a highly conserved histidine residue that serves as the proximal ligand to the heme in all heme oxygenases characterized thus far (See Figure 1) [11, 14, 15]. In spite of the low percentage of identical amino acids, the crystal structures of *nm*-HO and *cd*-HO have revealed that these proteins have very similar folds [15]. Recent characterization of the *Corynebacterium diphtheriae* and *Neisseriae meningitidis* bacterial HOs revealed that like all the previously characterized enzymes, they hydroxylate the heme exclusively at the α -*meso*-position by a mechanism similar to their mammalian counterparts [12, 14]. In contrast, the heme oxygenase from *Pseudomonas aeruginosa*, hydroxylates heme predominantly at the δ -*meso*-position [11].

```

cd-HO      -----MTTATAGLAVELKQSTAQAHEKAEHSTFMSDLLKGR LGVAEFTR
nm-HO      ----MSETENQALTF AKRLKADTTAVHDSVDN----LVMSVQPFVSKENYIK
pa-HO      MDTLAPESTRQNLRSQRLNLLTNEPHQRLES----LVKSKEPFASRDNFAR
              20                               40

cd-HO      LQEQAWLFYVALEQAVDAVRAS-GFAESLLDPALNRAEVLARDLDKLN GS
nm-HO      FLKLQSVFHKAVDHIYKDAELNKA IPELEYMARYDAVTQDLKDLGE----
pa-HO      FVAAQYLFQHDLEPLYRNEALARLFPGLASRARDDAARADLADLGH----
              60                               80

cd-HO      RWRSRITASPAVIDYVNRLESIRDNDG PALVAHHYVRYLGDLSGGQVIA
nm-HO      ----EPYKFDKELPYEAG--NKAIG-----WLYCAEGSNLGA AFLF
pa-HO      ----PVPEGDQSVREADLSLAEALG-----WLFVSEGSKLGA AFLF
              120

cd-HO      RMMQRHYGVDP--EALGFYHFEGIAK LKVKDEYREKLN SLELSDEQREH
nm-HO      KHAQKLDYNGEHG----ARHLAPHPDGRG KHWR AFVEHLNALNLTP EAEA
pa-HO      KKAAALELDENFG----ARHLAEPEGGRA QGWKSFVA ILDGIELNEE EER
              140                               160

cd-HO      LLKEATDAFVFNHQVFADLGKGLZ
nm-HO      EAIQGAREAFAYKVVLRETFGLAADAE APEGMMPHRH
pa-HO      LAAKGASDAFNRF GDLLERTFA
              180

```

Figure 1. Amino acid sequence alignment of the *Neisseriae meningitidis* (nm-HO), *Corynebacterium diphtheriae* (cd-HO) and *Pseudomonas aeruginosa* (pa-HO) heme oxygenases. Residues in blue correspond to conserved residues. The conserved proximal histidine is indicated in red. The alignment was performed using the ClustalW 1.8 program on the Baylor College of Medicine Search Launcher.

The First Step in the Catalytic Cycle of Heme Oxygenase

a) Regioselectivity

The heme oxygenase catalytic cycle begins with the exclusive hydroxylation of the porphyrin ring at the α -*meso* position. This regioselectivity is not a property inherent to the heme group as the coupled oxidation of porphyrin in solution clearly shows the formation of all four regioisomers [4]. Coupled oxidation of the prosthetic heme groups of myoglobin and hemoglobin, which yield low amounts of biliverdin isomers, has been used as a model of the heme oxygenase reaction. The coupled oxidation of sperm whale myoglobin produces exclusively α -biliverdin but human hemoglobin gives both α - and β -biliverdin isomers. These regiospecificities were postulated to be a consequence of steric interactions of the iron-bound dioxygen molecule with active site residues. However, further studies conducted with heme-containing bulky substituents at varying meso positions showed that myoglobin does not discriminate between the different meso-substitutions. In this context, it is interesting to consider the results obtained when hemes substituted with methyl groups at the β -, γ - and δ -*meso*-positions were subjected to oxidation by HO. The heme was oxidized at the single *meso*-substituted position or a combination of two positions while the β -*meso*-methylheme did not react well. By placing methyl groups at the meso-positions the regiospecificity of heme oxygenation was shifted away from the α -*meso*-position [4]. The steric effect of the methyl groups was not expected to be significant and therefore suggested that other factors were at play. It was then suggested that electronic effects might play a role in the regioselectivity of heme oxygenation. To test this hypothesis, heme was synthesized with formyl groups at different meso carbons. If the electron donating effect of a methyl group attached to a

meso carbon seemed to direct oxidation to that position, it was thought that an electron withdrawing substituent should produce the opposite effect. As expected, the oxidation of α -*meso*-formyl heme occurred at a position other than the formyl-substituted α -meso-carbon. These results strongly argue for a key role of electronic effects in the observed regioselectivity of heme oxygenase [5].

b) Formation of the activated oxygen species

The first step in the catalytic cycle of HO requires one molecule of oxygen and 2 reducing equivalents, which suggests that the same results might be obtained by direct reaction with H₂O₂. This was indeed found to be the case and indicated that a ferric peroxo complex might be an intermediate in the catalytic turnover of HO. Proof that the heme is hydroxylated by a hydroperoxy group axially coordinated to the heme iron was recently obtained by finding that radiolytic reduction of the Fe^{II}-O₂ complex at 77 K produces the Fe^{III}-OOH complex, as judged from the similarity between the EPR and ENDOR properties of the HO-1 complex and those of corresponding hemoglobin β -chain complexes. Annealing this Fe^{III}-OOH complex at 200 K converts it into Fe(III) α -*meso*-hydroxyheme thereby confirming that the ferric hydroperoxide is an obligatory intermediate in the first step of the HO catalytic cycle [16, 17].

Although the reactivity of the ferric hydroperoxide remains undefined, knowing that heme oxygenation takes place via an obligatory iron bound hydroperoxide has important consequences. In this context it becomes particularly important to consider a recent publication by Avila and co-workers. The studies conducted on axial mutants of mitochondrial cytochrome *b*₅ revealed that although meso-hydroxyheme is formed during

the degradation of heme by the enzyme heme oxygenase or by the process known as coupled oxidation of model hemes and hemoproteins not involved in heme catabolism, the corresponding mechanisms by which *meso*-hydroxyheme is generated are different. The authors concluded that in the coupled oxidation process, O₂ is reduced to non-coordinated H₂O₂, which reacts with Fe^{II}-heme to form *meso*-hydroxyheme [18]. This sheds considerable doubt over the validity and usefulness of the conclusions drawn from the coupled oxidation studies conducted on model systems and reaffirms the need to elucidate the reactivity and regioselectivity of heme oxygenation.

Research Direction

The key role played by heme oxygenases in mammals, bacteria and plants has been described above. HOs possess a variety of functions: they participate in iron homeostasis and protect against oxidative damage in mammals while allowing bacteria to mine their hosts for the iron they need in order to drive their energy processes. In plants, heme oxygenases produce precursors to the photosynthetic pigments that allow the energy from light to be harvested. These functions, all critical to the well being of these different organisms depend on HO activity thereby underscoring the need for a thorough understanding of the heme oxygenase catalytic cycle.

We have chosen to focus our attention on the first step in the catabolism of heme. Although, it has recently been corroborated that heme is hydroxylated by a hydroperoxy group axially coordinated to the ferric heme iron, almost nothing is known regarding the electronic nature of the crucial Fe^{III}-OOH intermediate. Furthermore, as mentioned above, the origin of α -regioselectivity in heme oxygenation is still undefined.

As the following chapters will show, we have demonstrated the pivotal role the electronic structure of the Fe^{III}-OOH heme oxygenase complex may play in dictating both the reactivity of and regioselectivity observed in the first step of the catalytic cycle of heme oxygenation. By virtue of the distal ligand field modulating effects conveyed by the network of hydrogen bonded water molecules present in the active site of heme oxygenases, the ferric hydroperoxy intermediate is capable of adopting novel electronic configurations which contribute to make the heme an active participant in its own hydroxylation. These novel electronic configurations prime the heme for oxidation by not only placing significant amounts of spin density at the meso positions but also by inducing deformations of the porphyrin ring from planarity. These deformations would place the terminal oxygen of the peroxy moiety closer to certain meso carbons thereby facilitating hydroxylation. Furthermore, by taking advantage of the unprecedented δ regioselectivity of HO from the *Pseudomonas aeruginosa* bacterium, we were able to identify the mechanism responsible for this novel regiospecificity.

The studies conducted indicate that the reactivity and regioselectivity of the first step in the catalytic cycle of heme oxygenation are likely due to both the electronic structure of the heme in the Fe^{III}-OOH intermediate and the presence of heme orienting steric interactions in the active site of the heme oxygenase enzyme.

References

1. Tenhunen, R., Marver, H.S., and Schmid, R.; *J. Biol. Chem.*, (1969). **244**: 6388-6394.
2. Wilks, A., Torpey, J., and Ortiz de Montellano, P.R.; *J. Biol. Chem.*, (1994). **269**: 29553-29556.
3. Yoshida, T. and Migita, C.T.; *J. Inorg. Biochem*, (2000). 33-41.
4. Ortiz de Montellano, P.R. and Wilks, A., in *Advances in Inorganic Chemistry*. 2000. p. 359-407.
5. Ortiz de Montellano, P.R. and Auclair, K., in *The Porphyrin Handbook*, K.M. Kadish, K.M. Smith, and R. Guilard, Editors. 2003, Elsevier Science (USA).
6. Otterbein, L.E. and Choi, A.M.K.; *Am. J. Physiol. Lung Cell Mol. Physiol.*, (2000). **279**: L1029-L1037.
7. Baranano, D.E., Dore, S., Ferris, C.D., and Sololomon, H.S.; *Clinical Neuroscience Research*, (2001). **1**: 46-52.
8. Mansfield Matera, K., Zhou, H., Migita, C.T., Hobert, S.E., Ishikawa, K., and Katakura, K.; *Biochemistry*, (1997). **36**: 4909-4915.
9. Takahashi, S., Wang, J., Rousseau, D., Ishikawa, K., Yoshida, T., Host, J.R., and Ikeda-Saito, M.; *J. Biol. Chem.*, (1994). **269**: 1010-1014.
10. Ishikawa, K., Mansfield Matera, K., Zhou, H., Fuji, H., and Sato, M.; *J. Biol. Chem.*, (1998). **273**: 4317-4322.
11. Ratliff, M., Zhu, W., Deshmukh, R., Wilks, A., and Stojilovic, I.; *J. Bacteriol.*, (2001). **183**: 6394-6403.
12. Zhu, W., Wilks, A., and Stojilovic, I.; *J. Bacteriol.*, (2000). **182**: 6783-6790.

13. Chu, G.C., Katakura, K., Zhang, X., Yoshida, T., and Ikeda-Saito, M.; *J. Biol. Chem.*, (1999). **274**: 21319-21325.
14. Wilks, A. and Schmitt, M.P.; *J. Biol. Chem.*, (1998). **273**: 837-841.
15. Schuller, D.J., Zhu, W., Stojilovic, I., Wilks, A., and Poulos, T.; *Biochemistry*, (2001). **40**.
16. Davydov, R.M., Yoshida, T., Ikeda-Saito, M., and Hoffman, B.; *J. Am. Chem. Soc.*, (1999). **121**: 10656-10657.
17. Davydov, R., Kofman, V., Fuji, H., Yoshida, T., Ikeda-Saito, M., and Hoffman, B.; *J. Am. Chem. Soc.*, (2002). **124**: 1798-1808.
18. Avila, L., Huang, H.-w., Damaso, C.O., Lu, S., Moenne-Loccoz, P., and Rivera, M.; *J. Am. Chem. Soc.*, (2003). **125**: 4103-4110.

Chapter II

NUCLEAR MAGNETIC RESONANCE SPECTROSCOPIC ANALYSIS OF PARAMAGNETIC HEMES AND HEME PROTEINS.

Heme Proteins

Heme containing proteins and enzymes are vital components of most living organisms [1]. A common feature among hemoproteins is the heme prosthetic group (protoheme IX) Figure 1, which upon interacting with the protein polypeptide, is capable of tuning its reactivity and performing a large variety of chemical functions. Hence, hemoproteins participate in electron transfer reactions (cytochromes) [2], oxygen activation and insertion reactions (monooxygenases) [3], oxygen transport and storage (hemoglobin and myoglobin) [4], oxygen sensing in nitrogen-fixing bacteria (FixL) [5], heme metabolism (heme oxygenase) [6, 7], and regulatory functions based on nitric oxide (guanylyl cyclase, nitrophorins) [8, 9], to name a few. It is therefore important to elucidate how nature tunes the redox properties and reactivity of the ubiquitous heme within a protein so that the resultant activity is that of oxygen binding, oxygen activation, oxygen sensing, or electron transport at different redox potentials. In this context, the heme active site is a chromophore that is amenable to be studied by a variety of spectroscopic techniques, such as nuclear magnetic resonance (NMR), electron paramagnetic resonance (EPR), resonance Raman, electronic absorption, and magnetic circular dichroic (MCD) spectroscopies.

The oxidation state of the heme-iron is an important modulator of the physical, chemical and biochemical properties of hemoproteins. For instance, myoglobin and hemoglobin form an oxyferrous complex, whereas the ferric oxidation state of these two hemoproteins is non-functional. Electron transfer proteins (cytochrome *b₅*, cytochrome *c*) have evolved to rapidly shuttle between the ferric and ferrous oxidation states, and oxygen activating hemoproteins (cytochrome P450, peroxidases) exhibit changes in the oxidation state of the heme iron (Fe^{II} , Fe^{III} , Fe^{IV}) as the reaction progresses through the catalytic cycle. It is therefore desirable to probe the heme active site in the different oxidation states.

The electronic structure of the heme changes with the oxidation and coordination state of the iron. Hemoproteins can adopt different spin states as the relative energies of the metal orbitals are disrupted by endogenous (protein donated) and exogenous ligands of varying field strengths (Figure 2). For example, the heme iron in the deoxy form of hemoglobin and myoglobin is pentacoordinated; four equatorial positions are occupied by the pyrrole nitrogens in the heme, and one of the axial positions is occupied by a proximal histidine ligand, as shown schematically in Figure 3-A. The pentacoordinated Fe(II) in deoxy-myoglobin adopts a high-spin, $S = 2$ state. However, if an additional strong-field ligand, like O_2 or CO , coordinates opposite the proximal histidine (the distal side), the resulting hexacoordinated ferrous iron adopts a low-spin, $S = 0$ configuration. This is illustrated by a view of the active site of oxy-myoglobin in Figure 3-B. In a similar manner, ferric heme oxygenase, which is coordinated by an endogenous histidine and a weak-field water ligand on the distal side [10, 11] is found in the high-spin, $S = 5/2$ state.

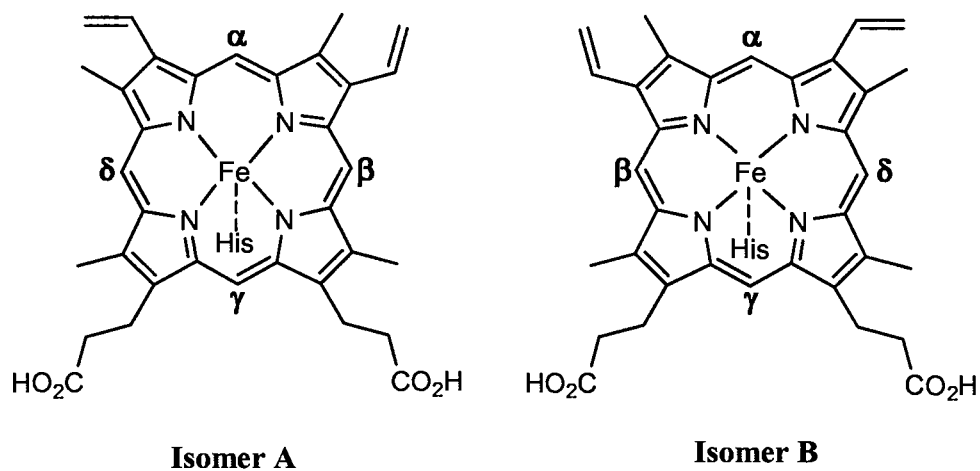


Figure 1. Protoheme IX. The numbering scheme follows the Fisher nomenclature more commonly used in the magnetic resonance literature [12, 13]. Using this nomenclature the heme substituents are identified by their common names and a number indicating their position on the heme macrocycle, e.g. 1 methyl, 2 vinyl, 6 propionate. The substituents with more than one carbon are further characterized by the use of greek letters to designate the number of bonds separating their carbons from the pyrrole ring, e.g. 2 vinyl- α , 6 propionate- β . In the asymmetric polypeptide fold, two heme isomeric forms (A and B) result from a 180° rotation of the heme about the α - γ meso axis.

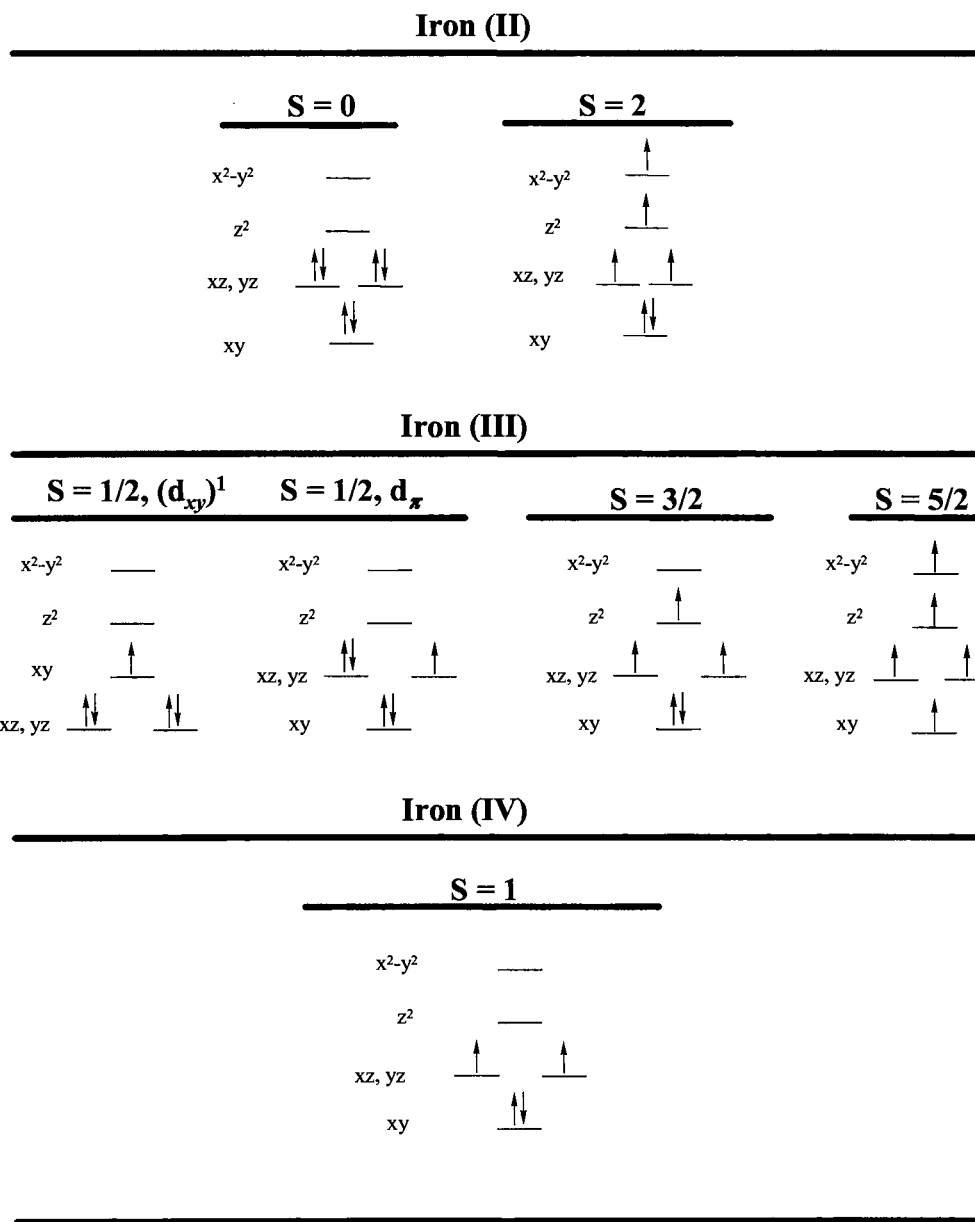


Figure 2. Common spin states for the physiologically relevant oxidation states of iron.

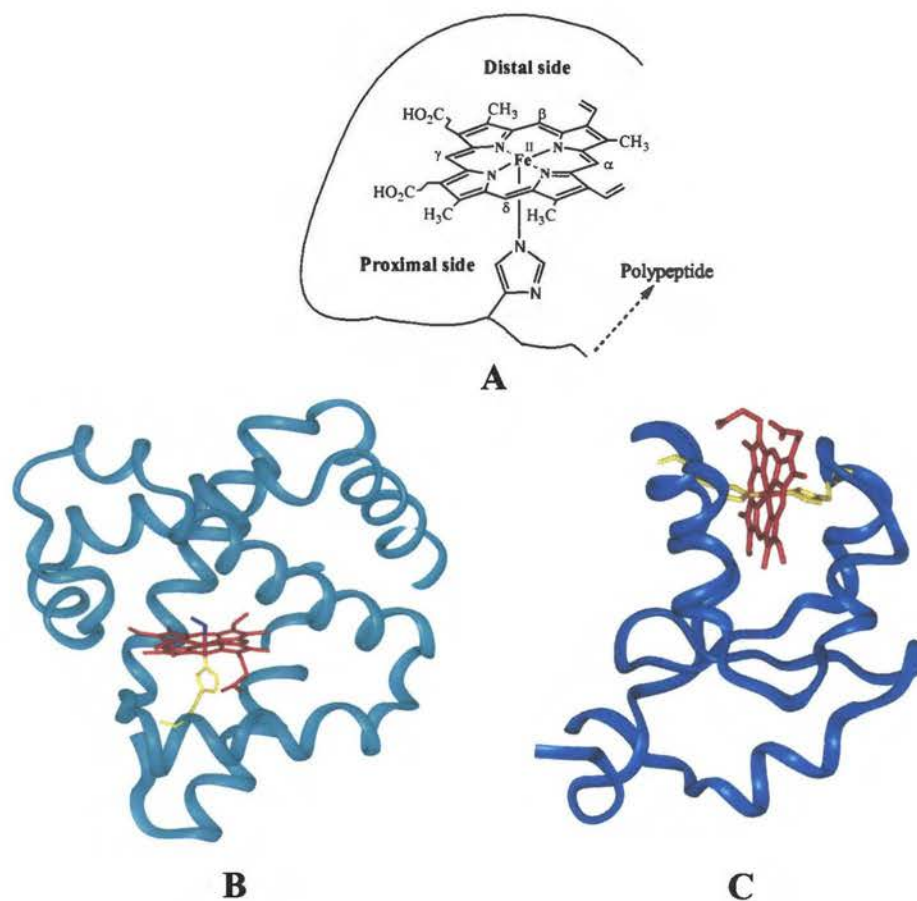


Figure 3. (A) Schematic representation of the Fe(II) heme in deoxy-myoglobin. (B) A view of the heme active site of oxy-myoglobin, where the proximal histidine ligand is yellow, the heme is red, and the distal O₂ ligand is blue (PDB access code 1AJ6). A view of the active site of mitochondrial cytochrome *b*₅, where the heme (red) is coordinated by two axial histidine ligands shown in yellow (PDB access code is 1B5M).

Replacement of the water molecule by a strong field ligand like cyanide produces a low-spin, $S = 1/2$ state. By comparison, hemoproteins that function in electron transfer are typically hexacoordinated in the ferric ($S = 1/2$) as well as in the ferrous ($S = 0$) oxidation states. The active site structure of the electron transfer protein cytochrome b_5 , where the heme is coordinated by two axial histidine ligands, is shown in the view of Figure 3-C. The coordination state of the heme iron often dictates the spin state, making the latter a useful tool to probe the ligation state of the metal center. More importantly, these coordination/spin state changes contribute to the mechanism of activity of all hemoproteins, thus underscoring the importance of their investigation by spectroscopic means.

Nuclear Magnetic Resonance Spectroscopy of Paramagnetic Hemes and Heme Proteins

Heme complexes and hemoproteins fall into the category of paramagnetic molecules, as all of the common iron electronic configurations, with the exception of Fe(II) low-spin, $S = 0$, possess one or more unpaired electrons (Figure 2). These unpaired electrons have a profound effect on the observed NMR chemical shifts as a consequence of the strong electron-nuclear hyperfine interaction. This interaction, which gives rise to the paramagnetic shift (δ_{para}) is composed of a scalar or contact contribution (δ_{con}), that arises from unpaired spin delocalization onto nuclei on the ligands, and a dipolar or through-space contribution, δ_{dip} (equation 1) [14]. The typically large chemical shifts observed for paramagnetically affected resonances (δ_{obs}) can be segmented into diamagnetic and paramagnetic contributions (equation 2).

$$\delta_{\text{para}} = \delta_{\text{con}} + \delta_{\text{dip}} \quad (1)$$

$$\delta_{\text{obs}} = \delta_{\text{dia}} + \delta_{\text{para}} \quad (2)$$

Thus, in order to isolate and analyze the paramagnetic (δ_{para}), also called isotropic (δ_{iso}) or hyperfine (δ_{hyp}) shifts, the corresponding chemical shifts of an isostructural diamagnetic molecule (δ_{dia}) should be subtracted from the observed shifts (equation 3) [15].

$$\delta_{\text{para}} = \delta_{\text{obs}} - \delta_{\text{dia}} \quad (3)$$

It is important to understand the nature of the contact and dipolar shift contributions in order to appreciate and interpret the information that can be obtained from paramagnetic shifts. The contact contribution to the paramagnetic shift is brought about by scalar coupling between electron spins and individual nuclei. When a single spin level with an isotropic g tensor is populated, and to the extent that Curie law is valid (usually approximately applicable for ferrihemes), the contact shift can be expressed by equation 4, where S is the total spin quantum number, g is the isotropic (average) g value, γ is the magnetogyric ratio of the nucleus in question, T is the absolute temperature, β is the Bohr magneton, k is the Boltzmann constant, h is the Planck constant and A is the hyperfine (scalar) coupling constant for coupling the spin of the electron to the spin of the nucleus of interest [13, 16-19].

$$\delta_{\text{con}} = \frac{Ag\beta S(S+1)}{3\gamma_N h k T} \quad (4)$$

Interpretation of the contact contribution to the ^1H paramagnetic shift in terms of metal ligand covalency is done in the context of the McConnell equation [20] (equation 5), which relates the hyperfine coupling for each individual proton in an aromatic

fragment (A^H) to the unpaired spin density at the carbon to which the proton is attached (ρ_C). Q_H is an empirical parameter (- 63 MHz). In the case of an aromatic carbon atom

$$A^H = Q_H \rho_C \quad (5)$$

the hyperfine coupling constant A^C can be related to the spin density centered on its π orbital (ρ_C^π) and to the spin density centered on the π orbitals of the three atoms x_i bonded to it ($\rho_{x_i}^\pi$) (equation 6) [21]. S^C accounts for spin polarization of the 1s orbital by unpaired spin density located on the p_z (π) orbital of the same carbon atom, Q_{Cx_i} accounts for spin polarization of the 2s orbitals on neighboring carbons by unpaired π spin density on the observed carbon atom, and Q_{x_iC} for spin polarization of the 2s electrons on the observed carbon atom by π spin density on the neighboring carbons [19, 22-25].

$$A^C = (S^C + \sum_{i=1}^3 Q_{Cx_i}^C) \rho_C^\pi + \sum_{i=1}^3 Q_{x_iC}^C \rho_{x_i}^\pi \quad (6)$$

For a methyl carbon atom bound to the pyrrole- β carbon of heme, one obtains equation 7, where C' denotes the aromatic carbon to which the methyl group is bound ($Q_{C'C}^C \sim -39$ MHz) [17, 22, 26]. It is therefore clear that the δ_{con} contribution to the observed shift for a heme methyl carbon depends only on the unpaired electron density on the pyrrole- β carbon to which the methyl carbon is bound. This point will play a key role in the discussion of Chapter V.

$$A^C = Q_{C'C}^C \rho_C^\pi \quad (7)$$

The dipolar contribution to the isotropic shift results from through-space interactions (dipole coupling) of the nuclear and electron magnetic moments. For heteronuclei (^{13}C) the δ_{dip} contribution to the isotropic shift consists of two terms, a metal centered ($\delta_{\text{dip}}^{\text{M}}$) and a ligand centered ($\delta_{\text{dip}}^{\text{L}}$) contribution. The term $\delta_{\text{dip}}^{\text{M}}$ results from

coupling between the nucleus under observation and the unpaired spin density on the metal, and the term $\delta_{\text{dip}}^{\text{L}}$ results from coupling between the nucleus under observation and unpaired spin density on the p_z orbitals of the ligand. The $\delta_{\text{dip}}^{\text{L}}$ term is known to be small in low-spin ferrihemes [27] and in the case of heme substituents such as heme methyls, which do not participate directly in the delocalized π orbitals, $\delta_{\text{dip}}^{\text{L}}$ is negligible [26, 28]. A general expression for the predominant $\delta_{\text{dip}}^{\text{M}}$ contribution is given by equation 8, where r is the metal nucleus distance vector, N is Avogadro's number, χ_{ji} are

$$\delta_{\text{dip}}^{\text{M}} = \frac{1}{12\pi\mu_0 N} \left\{ \left[\chi_{zz} - \frac{1}{2}(\chi_{xx} + \chi_{yy}) \right] \left(\frac{3\cos^2\theta - 1}{r^3} \right) + \frac{3}{2}(\chi_{xx} - \chi_{yy}) \left(\frac{\sin^2\theta \cos^2 2\Omega}{r^3} \right) \right\} \quad (8)$$

the principal components of the magnetic susceptibility tensor, θ is the angle between the proton-metal vector and the z molecular axis, Ω is the angle between the projection of the r vector on the xy plane and the x axis, and μ_0 is the vacuum permeability [12, 13, 29].

a) ^1H Shifts, axial ligands and axial ligand geometry

The electron configuration of the ferric iron in heme, d^5 , typically requires two strong field ligands to stabilize the low-spin ($S = 1/2$) state. Thus, ferric heme proteins exhibiting a low-spin state typically employ the histidine-imidazole, the methionine thioether, or the cysteine thiolate as the axial ligands. Many of the cytochromes c and cytochrome b_{562} from *E. coli* exhibit a histidine and a methionine as axial ligands [30], whereas cytochromes b_5 , microsomal [31] or mitochondrial [32], and the four hemes of cytochrome c_3 [33] possess a bis-histidine coordinated heme. By comparison, the globins, including the inactive, Fe^{III} (met) forms of hemoglobin, myoglobin [4], and monomeric hemoglobins [34], as well as heme oxygenase [10, 11], the NO carrying

nitrophorins [35], and the peroxidases [12] have only one histidine axial ligand. Most of the molecules in the latter group exhibit a water molecule (weak field ligand) coordinated at the sixth position, thus they are in the $S = 5/2$ high-spin state. NMR spectroscopic studies of the paramagnetic active site of these high-spin proteins are typically conducted in the presence of an exogenous strong-field ligand, that binds (or replaces the aqua ligand) at the sixth position, therefore converting the hemoprotein to its low-spin state. The $S = 1/2$, d_{π} spin state is most commonly attained and the discussion below pertains only to this electronic configuration. The exogenous strong-field ligands are typically cyanide, imidazoles, pyridines, or azide, although cyanide is sometimes preferred because its cylindrical symmetry does not introduce a perturbation of the symmetry of the porphyrin π molecular orbitals.

Early work conducted with met-myoglobin-cyanide revealed that the heme methyl groups exhibit significant C_2 symmetry in that the methyl group resonances appear to be grouped pairwise in the proton NMR spectrum [36]; two methyl resonances exhibit large hyperfine shifts (~ 20 ppm) and the other two display significantly smaller shifts, resonating ca. 8 ppm. It is now days clear that the orientation of planar axial ligands exerts a large influence on the spread of the methyl resonances originating from low-spin ferric heme proteins, as well as in low-spin porphyrinates [18, 37, 38]. The fundamental property that brings about this spread in the chemical shift of heme substituents is the interaction of the proximal histidine ligand with the iron-centered e -symmetry d orbitals, which in turn, individually interact with porphyrin $3e(\pi)$ orbitals. These interactions, which have been presented in pictorial form [13, 37, 39], can be

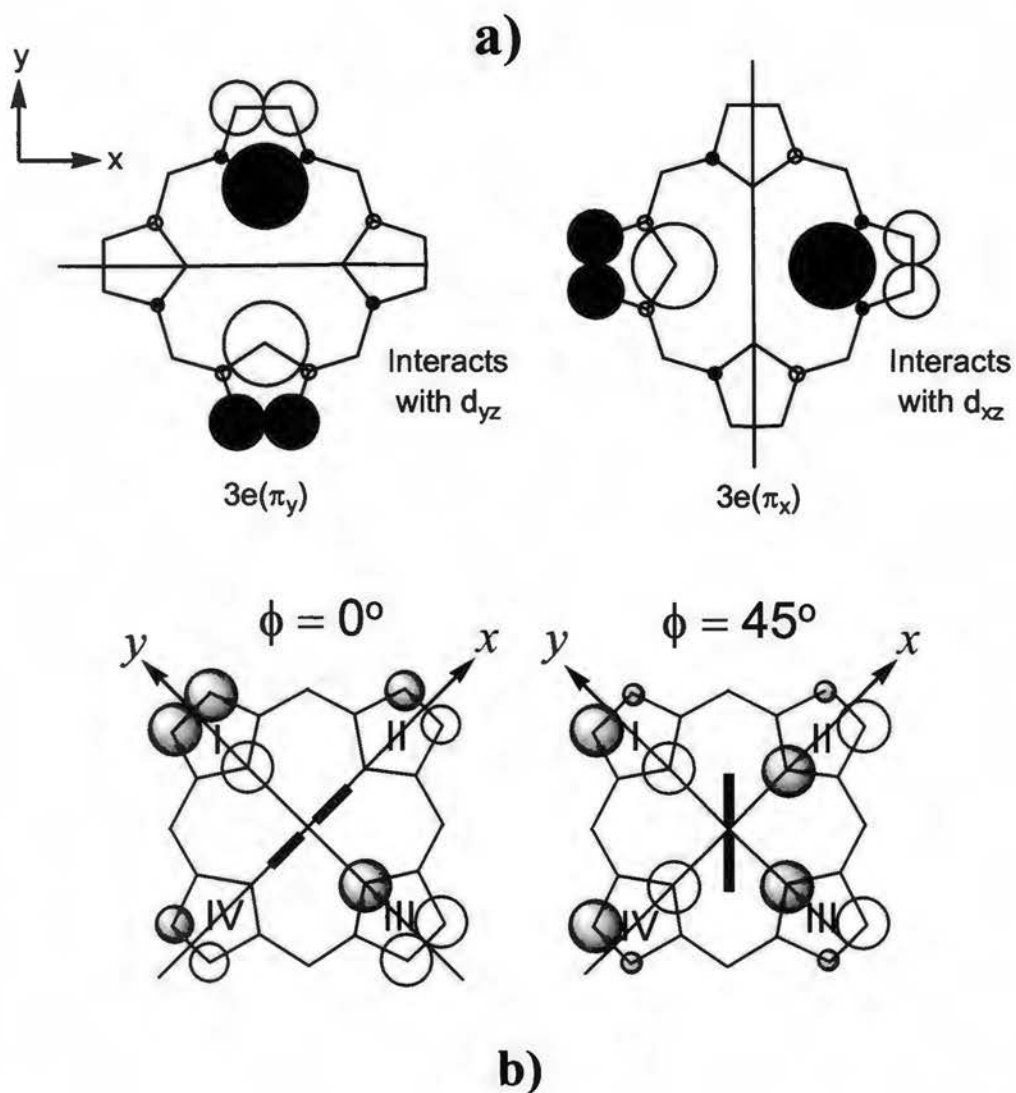


Figure 4. a) Electron density and nodal properties of porphyrin $3e(\pi)$ orbitals [36], which interact with the d_{xz} and d_{yz} orbitals of low spin Fe(III), respectively. b) Spin density for two angles of the proximal histidine plane (represented by a thick black line), 0° and 45° , with respect to the axis along the nitrogen atoms of pyrrole rings II and IV. The size of the circles is proportional to the electron density at each position. Adapted from references 13 and 37.

readily understood by considering the degenerate pair of porphine $3e(\pi)$ molecular orbitals (Figure 4-a), which interact with the d_{xz} and d_{yz} orbitals of low-spin Fe(III). The histidine-imidazole π orbitals lie perpendicular to the plane of the imidazole ring, thus these orbitals interact with the iron d_{xz} and d_{yz} orbitals and the porphyrin $3e(\pi)$ orbitals. This interaction, which can be thought of as being modulated by the angle the imidazole plane makes with the axis along the nitrogen atoms of pyrrole rings II and IV, lifts the degeneracy of the $3e(\pi)$ orbitals, modulates their relative energy difference, and largely determines the degree of uneven distribution of electron spin density among the four pyrrole rings in the porphyrin macrocycle (see Figure 4-b) [37, 40].

The effect of axial ligand nodal plane orientation on the contact and dipolar ^1H shifts of low-spin ferrihemes has been calculated as a function of the angle of the axial ligand plane with respect to the axis along the nitrogen atoms on pyrrole rings II and IV [41]. Estimates of the δ_{con} contribution to the isotropic shift were obtained from Hückel methods. Calculations of g -anisotropy, assuming counter rotation of the g tensor [42] were used to estimate the contribution of δ_{dip} . It was found that for systems having one axial ligand, or two axial ligands in parallel planes, the δ_{con} and δ_{dip} contributions to the isotropic shift are comparable at the meso-hydrogen position, whereas the contact contribution dominates the isotropic shifts of heme methyl groups. The predicted isotropic shifts were plotted as a function of axial ligand nodal plane orientation for b and c type hemes (Figure 5) [41]. These plots, which represent a straightforward visual aid to estimate the orientation of the axial ligands, show very good agreement in the order of the predicted shifts, and reasonable agreement in the magnitude of the shifts. This approach

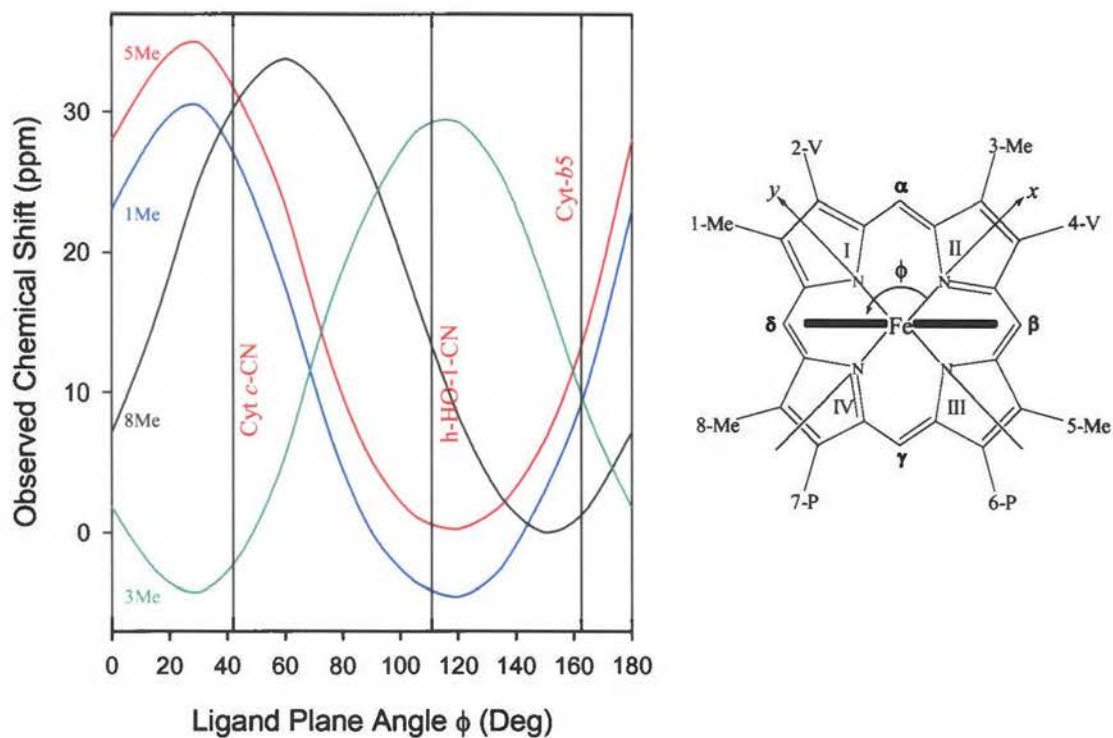


Figure 5. Right: Right-handed coordinate system and nomenclature used for describing the projection of the His-imidazole plane onto the porphyrin ring. The x axis is aligned along the nitrogen atoms of pyrrole rings II and IV of the heme, the y axis is along the nitrogen atoms of pyrrole rings I and III, and the z axis is normal to the heme. Left: Dependence of observed heme-methyl shifts on the angle ϕ formed between the molecular x axis and the projection of the imidazole plane. Examples are given for the bis-histidine coordinated cytochrome b_5 and the histidine-cyanide coordinated human HO-1 and cytochrome c . Adapted from reference 41.

has been made more quantitative with the finding of equations that describe the relationship between axial ligand geometry and ^1H shifts for *c* and *b* hemes [43].

The plot shown in Figure 5 summarizes calculations in the case of *b* hemes axially coordinated by proximal histidine and distal cyanide ligands, or by two histidine ligands parallel to one another [41]. The plot permits the straightforward correlation of the observed shifts for the four heme methyl groups (1Me, 3Me, 5Me, and 8Me) as a function of the angle ϕ formed between the axial ligand plane and the molecular *x* axis. Using the information in this plot and the NMR resonance assignments obtained for the heme methyl groups [44, 45], it was possible to correctly predict an angle ϕ of 125° for the proximal histidine imidazole plane of human heme oxygenase [41] before the X-ray crystal structure was obtained [10]. Thus, the calculations summarized in the plot of Figure 5 provide a straightforward predictive framework to study heme containing proteins and enzymes even if their structure is not available. More recently a study has been published that correlates the order of heme methyl resonances in the high-spin form of several ferriheme proteins [46]. There is an apparent 90° shift in the nodal plane of the orbital involved in spin delocalization compared to the histidine-imidazole plane. This 90° rotation has been explained in terms of almost complete use of only one of the d_π (d_{xz} or d_{yz}) metal orbitals to delocalize electron density into one of the two $4e(\pi^*)$ porphyrin orbitals [46].

As will be shown in Chapter V, the dependency of heme methyl ^1H chemical shifts on the endogenous axial histidine plane orientation, is a powerful concept. Its use enabled us to elucidate the nature of the different heme seatings present in a mutant of the

pa-HO protein thereby explaining the mechanism underlying the previously unobserved δ -*meso*-regioselectivity of the wild type enzyme.

b) ^{13}C NMR spectroscopy in the analysis of hemoproteins

The high sensitivity of the proton has led to an overwhelming emphasis on the utilization of ^1H NMR spectroscopy to study paramagnetic hemoproteins [14, 15, 47, 48]. For these molecules ^1H NMR spectroscopy is capable of providing unique structural and electronic information for the heme active site and residues near the active site because of the large hyperfine shifts that result from unpaired electron density [12, 14, 18, 49-51]. Nevertheless, ^1H NMR spectroscopy of paramagnetic proteins has some fundamental limitations: (a) Asymmetric delocalization of unpaired electron density results in large isotropic shifts for some of the heme substituents but small to negligible isotropic shifts for others. This means that some of the resonances originating from the heme are resolved from the diamagnetic envelope of resonances and thus are relatively easy to observe, whereas other heme resonances are not resolved from the diamagnetic envelope and consequently their observation and assignment are difficult. (b) Heme substituents in the reduced (usually diamagnetic) state lack isotropic shifts and are therefore difficult to examine by ^1H NMR spectroscopy. (c) Efficient spin-spin relaxation often makes through-bond proton-proton correlations in COSY and TOCSY experiments unobservable. The development of cross peak coherence in these experiments ($\pi Jt = \pi/2$) requires that $t = 1/(2J)$. Hence, 70 ms and 35 ms, respectively, are required to develop cross peak coherences for vicinal ($J = 7$ Hz) and geminal ($J = 14$ Hz) ^1H - ^1H couplings. Since cross peak coherence must develop completely during the detection period, La Mar

has pointed out that in the case of paramagnetic systems, where the condition $T_2^{-1} > {}^3J_{HH}$ applies, the COSY cross peaks from signals with short T_2 values will be weak and some times undetectable [14, 52]. In fact, it has been proposed that the COSY cross peaks observed in paramagnetic systems originate from dipolar coupling and Curie spin-nuclear spin relaxation [52, 53]. By comparison, the larger heteronuclear coupling ${}^1J_{CH} \sim 140$ Hz requires only ~ 4 ms for the development of cross peak coherence, thus making heteronuclear correlation experiments immensely attractive when one is interested in studying paramagnetic heme centers by NMR spectroscopy. In diamagnetic molecules, connectivities are detected across portions of molecules without the use of small ${}^3J_{HH}$, using heteronuclear correlation experiments based on scalar ${}^{13}\text{C}$ - ${}^{13}\text{C}$ and ${}^{13}\text{C}$ - ${}^{15}\text{N}$ correlations. The relatively large value of the ${}^1J_{CC}$ coupling constant (~ 50 Hz) is much larger than typical ${}^3J_{HH}$, hence, similar experiments should be directly applicable to the observation and assignment of paramagnetically-affected resonances.

Despite the potential utility of ${}^{13}\text{C}$ NMR spectroscopy in the study of paramagnetic proteins, the inherent lower sensitivity of ${}^{13}\text{C}$ has largely limited the effective use of natural abundance ${}^{13}\text{C}$ NMR spectroscopy to observe resonances originating from the paramagnetic heme cofactor. In the 1970s and 1980s the most common application of ${}^{13}\text{C}$ NMR spectroscopy to the analysis of heme proteins involved the characterization of resonances originating from the distal carbonmonoxide (CO) ligand of hemoproteins coordinated by a ${}^{13}\text{C}$ -enriched CO molecule [54, 55]. An early attempt to overcome the problems imposed by the low natural abundance of ${}^{13}\text{C}$ nuclei was to develop synthetic methods to introduce ${}^{13}\text{C}$ labels into the vinyl groups of the

heme macrocycle [48, 56]. These pioneering experiments, which permitted the observation of ^{13}C resonances from heme vinyl groups in high- and low-spin myoglobin derivatives [48], demonstrated the practicality and importance of applying ^{13}C NMR spectroscopy to the analysis of paramagnetic hemoproteins. More recently, the ^1H - ^{13}C COSY spectra of natural abundance ferricytochrome *c* [57] and that of sperm whale myoglobin [58], were utilized to assign the ^{13}C resonances originating from the heme methyl groups. Subsequently, the proton-detected heteronuclear multiple quantum coherence (HMQC) experiment [59] was utilized to identify several heme carbons and their corresponding proton resonances in the paramagnetic active site of cytochrome *c*₅₅₀ [60], which culminated in the assignment of most proton and carbon resonances for tuna ferricytochrome *c* [61]. This experiment has found widespread use in the identification of ^1H and ^{13}C resonances originating from protonated carbon atoms in paramagnetic heme centers [62-64]. However, resonances not resolved from the paramagnetic envelope are often times difficult to assign, even with the aid of the HMQC experiment [65, 66].

As will be shown in the following chapters, by taking advantage of biosynthetic methods that allow us to obtain ^{13}C labeled hemes, the limitations of ^{13}C NMR mentioned above can be largely attenuated while giving us access to information not readily obtained by ^1H NMR alone. For example, the observation and assignment of core porphyrin quaternary carbons is a challenging task as their closer proximity to the heme-iron makes these carbons more strongly affected by the unpaired electron. However, there is a relatively straightforward correlation between the chemical shifts of these core

carbons and the coordination state and electronic structure of the heme. As will be shown in Chapters III, IV and V the efforts needed to observe and assign the resonances originating from the porphyrin core carbons is completely justified as it greatly facilitates the assessment of heme electronic structure.

References

1. Turano, P. and Lu, Y., in *Handbook on Metalloproteins*, H. Sigel, Editor. 2001, Marcel Dekker, Inc: New York. p. 269-356.
2. Scott, R.A. and Mauk, A.G., eds. 1996, University Science Books: Sausalito, CA.
3. Sono, M., Roach, M.P., Coulter, E.D., and Dawson, J.H.; *Chem. Rev.*, (1996). **96**: 2841-2847.
4. Springer, B.A., Sligar, S.G., Olson, J.S., and Phillips, J.G.N.; *Chem. Rev.*, (1994). **94**: 699-714.
5. Agron, P.G., Ditta, G.S., and Helinski, D.R.; *Proc. Natl. Acad. Sci.*, (1993). **90**: 3506.
6. Ortiz de Montellano, P.R.; *Curr. Opin. Chem. Biol.*, (2000). **4**: 221-227.
7. Ortiz de Montellano, P.R. and Wilks, A., in *Advances in Inorganic Chemistry*. 2000. p. 359-407.
8. Ribeiro, J.M.C., Hazzard, J.M., Nussenzweig, R.H., Champagne, D.E., and Walker, F.A.; *Science*, (1993). **260**: 543.
9. Bellamy, T.C. and Garthwaite, J.; *Mol. Cell. Biochem.*, (2002). **230**: 165-176.
10. Schuller, D.J., Zhu, W., Stojilovic, I., Wilks, A., and Poulos, T.; *Biochemistry*, (2001). **40**.
11. Schuller, D.J., Wilks, A., Ortiz de Montellano, P.R., and Poulos, T.; *Nature Struct. Biol.*, (1999). **6**: 860-867.
12. La Mar, G.N., Satterlee, J.D., and De Ropp, J.S., in *The Porphyrin Handbook*, R. Guilard, Editor. 2000, Academic Press. p. 185-297.
13. Walker, F.A., in *The Porphyrin Handbook*, R. Guilard, Editor. 2000.

14. La Mar, G.N. and De Ropp, J.S., in *Biological Magnetic Resonance*, J. Reuben, Editor. 1993, Plenum Press: New York. p. 1-111.
15. Satterlee, J.D., Alam, S., Yi, Q., Erman, J.E., Constantinidis, I., Russel, D.J., and Moench, S.J., in *Biological Magnetic Resonance*, J. Reuben, Editor. 1993, Plenum: New York. p. 275-297.
16. Kurland, R.J. and McGarvey, B.R.; *J. Magn. Reson.*, (1970). **2**: 286.
17. Wuthrich, K. and Baumann, R.; *Helv. Chim. Acta.*, (1973). **56**: 585-596.
18. Satterlee, J.D.; *Annu. Rep. Nucl. Magn. Reson. Spectrosc.*, (1986). **17**: 70-178.
19. Bertini, I. and Luchinat, C.; *Coord. Chem. Rev.*, (1996). **150**: 1-296.
20. McConnell, H.M.; *J. Chem. Phys.*, (1956). **35**: 1312-1323.
21. Karplus, M. and Fraenkel, G.K.; *J. Chem. Phys.*, (1961). **35**: 1312-1323.
22. Wuthrich, K. and Baumann, R.; *Helv. Chim. Acta.*, (1974). **57**: 336-350.
23. Mispelter, J., Momenteau, M., and Lhoste, J.M., in *Biological Magnetic Resonance*, J. Reuben, Editor. 1993, Plenum Press: New York. p. 299-355.
24. Goff, H.M.; *J. Am. Chem. Soc.*, (1981). **103**: 3714-3722.
25. Wuthrich, K., Billeter, M., and Braun, W.; *J. Mol. Biol.*, (1983). **180**: 715-740.
26. Turner, D.L.; *Eur. J. Biochem.*, (1993). **211**: 563-568.
27. Banci, L., Bertini, I., Pieratelli, R., and Villa, A.J.; *Inorg. Chem.*, (1994). **33**: 4338-4343.
28. Louro, R.O., Medina, M., Aguiar, A.P., Hervas, M., De la Rosa, M., Gomez-Moreno, C., Turner, D.L., and Xavier, A.V.; *J. Biol. Inorg. Chem.*, (1998). **3**: 68-73.

29. Bertini, I., Turano, P., and Xavier, A.V., *The Hyperfine Coupling in Nuclear Magnetic Resonance of Paramagnetic Molecules*, ed. G.N. La Mar. 1995, London: Kluwer Academic Publishers. 29-54.
30. Mathews, F.S., Bethge, P.H., and Czerwinski, W.; *J. Biol. Chem.*, (1979). **254**: 1699-1706.
31. Durley, R.C.E. and Mathews, F.S.; *Acta Cryst.*, (1996). **D52**: 65-76.
32. Rodriguez-Maranon, M.J., Feng, Q., Stark, R.E., White, S.P., Zhang, X., Foundling, S.I., Rodriguez, V., Schilling III, C.L., Bunce, R.A., and Rivera, M.; *Biochemistry*, (1996). **35**: 16378-16390.
33. Turner, D.L., Costa, H.S., Coutinho, I.B., LeGall, J., and Xavier, A.V.; *Eur. J. Biochem.*, (1997). **243**: 474-481.
34. Volkman, B.F., Alam, S.L., Satterlee, J.D., and Markley, J.L.; *Biochemistry*, (1998). **37**: 10906-10919.
35. Weichsel, A., Andersen, J.F., Champagne, D.E., Walker, F.A., and Montfort, W.R.; *Nat. Struct. Biol.*, (1998). **5**: 304-309.
36. Shulman, R.G. and Glarum, S.H.; *J. Mol. Biol.*, (1971). **57**: 93-115.
37. Walker, F.A.; *J. Am. Chem. Soc.*, (1980). **105**: 6923-6929.
38. Goff, H.; *J. Am. Chem. Soc.*, (1980). **102**: 3252-3254.
39. Walker, F.A.; *Coord. Chem. Rev.*, (1999). **185-186**: 471-534.
40. Walker, F.A., Buehler, J., West, J.T., and Hinds, J.L.; *J. Am. Chem. Soc.*, (1983). **105**: 6923-6929.
41. Shokhirev, N.V. and Walker, F.A.; *JBIC*, (1998). **3**: 581-594.
42. Shokhirev, N.V. and Walker, F.A.; *J. Am. Chem. Soc.*, (1998). **120**: 981-990.

43. Bertini, I., Luchinat, C., Parigi, G., and Walker, F.A.; *JBIC*, (1999). **4**: 515-519.
44. Gorst, C.M., Wilks, A., Yeh, D.C., Ortiz de Montellano, P.R., and La Mar, G.N.; *J. Am. Chem. Soc.*, (1998). **120**: 8875-8884.
45. Gorst, C.M., Wilks, A., Paolesse, R., Smith, K.M., Ortiz de Montellano, P.R., and La Mar, G.N.; *Biochemistry*, (1994). **33**: 6631-6641.
46. Shokireva, T.K., Shokirev, N.V., and Walker, F.A.; *Biochemistry*, (2003). **42**: 679-693.
47. Banci, L., in *Biological Magnetic Resonance*, J. Reuben, Editor. 1993, Plenum: New York. p. 79-112.
48. Sankar, S.S., La Mar, G.N., Smith, K.M., and Fujinari, E.M.; *Biochim. Biophys. Acta*, (1987). **912**: 220-229.
49. Walker, F.A. and Simonis, U., in *Biological Magnetic Resonance*, J. Reuben, Editor. 1993, Plenum: New York. p. 275-297.
50. Banci, L., Piccioli, M., and Scozzafava, A.; *Coord. Chem. Rev.*, (1992). **120**: 1-28.
51. Bertini, I. and Luchinat, C.; *Curr. Opin. Chem. Biol.*, (1999). **3**: 145-151.
52. Bertini, I., Luchinat, C., and Tarchi, D.; *Chem. Phys. Lett.*, (1993). **203**: 445-449.
53. Bertini, I., Luchinat, C., Piccioli, M., and Tarchi, D.; *Concepts in Magn. Reson.*, (1994). **6**: 307-335.
54. Moon, R.B., Dill, K., and Richards, J.H.; *Biochemistry*, (1977). **16**: 221-228.
55. Behere, D.V., Gonzalez-Vergara, E., and Goff, H.M.; *Biochim. Biophys. Acta*, (1985). **131**: 607-613.
56. Nelson, M.J. and Huestis, W.H.; *Biochim. Biophys. Acta*, (1980). **623**: 467-470.

57. Santos, H. and Turner, D.L.; *FEBS Letters*, (1985). **184**: 240-244.
58. Yamamoto, Y.; *FEBS Letters*, (1987). **222**: 115-119.
59. Summers, M.F., Marzilli, L.G., and Bax, A.; *J. Am. Chem. Soc.*, (1986). **108**: 4285-4294.
60. Timkovich, R.; *Inorg. Chem.*, (1990). **30**: 37-42.
61. Sukits, S.F. and Satterlee, J.D.; *Biophys J.*, (1996). **71**: 2848-2856.
62. Santos, H. and Turner, D.L.; *FEBS Letters*, (1986). **194**: 73-77.
63. Costa, H.S., Santos, H., and Turner, D.L.; *Eur. Biophys. J.*, (1996). **25**: 19-24.
64. Wei, X., Ming, L.-J., Cannons, A.C., and Solomonson, L.P.; *Biochim. Biophys. Acta*, (1998). **1382**: 129-136.
65. Louro, R.O., Waal, E.C., Ubbink, M., and Turner, D.L.; *FEBS Letters*, (2002). **510**: 185-188.
66. Hernandez, G., Wilks, A., Paolesse, R., Smith, K.M., Montellano, O.d., and La Mar, G.N.; *Biochemistry*, (1994). **33**: 6631-6641.

Chapter III

MODELS OF THE LOW-SPIN IRON(III) HYDROPEROXIDE INTERMEDIATE OF HEME OXYGENASE: MAGNETIC RESONANCE EVIDENCE FOR THERMODYNAMIC STABILIZATION OF THE d_{xy} ELECTRONIC STATE AT AMBIENT TEMPERATURES

Introduction

The degradation of heme in mammalian cells is catalyzed by the enzyme heme oxygenase (HO) [1-,3]. In a molecular oxygen- and electron-dependent set of reactions HO cleaves the α -*meso* bridge to produce CO, biliverdin and free iron. Not long ago, the HO system was regarded only in the context of the maintenance of cellular heme homeostasis as a catabolic enzyme, and the products of HO activity were considered toxic waste material. More recently this view has changed drastically after the discovery that all products of HO enzymatic action possess important biological activity. CO functions to regulate vasomotor tone and neurotransmission in a manner akin to NO,[4,5] iron released from HO-1 activity upregulates ferritin expression,[6] and bilirubin, formed when biliverdin is reduced by biliverdin reductase, is a potent antioxidant [7]. Since the regulation of HO activity has ramifications for a variety of physiological functions, it is important to attain a detailed understanding of the mechanism by which heme is converted to CO, Fe and biliverdin.

Although several important aspects of the mechanism of action of HO have not yet been elucidated, the evidence gathered so far demonstrates that HO acts via a

mechanism different from that currently accepted for other oxygen activating hemoproteins such as cytochromes P450, peroxidases, and catalases, (recently reviewed) [1-3,8] as well as the mitochondrial enzyme complex and cytochrome *c* oxidase (recently reviewed) [9]. Nevertheless, the reactions catalyzed by HO display some of the characteristic fundamental aspects shared by the catalytic mechanism of action of all oxygen-activating heme proteins. The ferric enzyme is initially reduced to its ferrous state [10], followed by formation of an oxyferrous complex ($\text{Fe}^{\text{II}}\text{-O}_2$), which accepts a second electron from NADPH cytochrome P450 reductase, and thereby is transformed into a ferric hydroperoxy ($\text{Fe}^{\text{III}}\text{-OOH}$) species [10]. Based on the reactivity of HO toward hydrogen peroxide and alkyl hydroperoxides, it was proposed that the nature of the species that oxidizes the HO-bound heme to *α -meso* hydroxyheme is a ferric hydroperoxide ($\text{Fe}^{\text{III}}\text{-OOH}$) [3,10]. Strong evidence supporting this conclusion was recently produced by cryoreduction of the ferrous dioxygen complex of HO ($\text{Fe}^{\text{II}}\text{-O}_2$) in order to produce an intermediate that was identified by EPR spectroscopy as corresponding to the $\text{Fe}^{\text{III}}\text{-OOH}$ complex [11]. Upon warming, this intermediate was converted into the corresponding *α -meso* hydroxyheme complex, thus confirming a ferric hydroperoxide intermediate as a precursor of *α -meso* hydroxyheme.

The EPR spectrum corresponding to the $\text{Fe}^{\text{III}}\text{-OOH}$ complex of HO displays *g*-values of 2.37 (or 2.38, depending on treatment), 2.19, and 1.93 at 77 K [11]. The sum of the squares of the principal *g*-values (Σg^2) for the hydroperoxy complex of HO is about 14.1. It is interesting to consider this value in the context of recently reported studies of low-spin Fe(III) porphyrinates [1215 These reports demonstrated the presence of a novel electronic configuration, $(d_{xz}, d_{yz})^4(d_{xy})^1$, where the unpaired electron resides in the d_{xy}

orbital. Interestingly, all model hemes known to possess the $(d_{xz}, d_{yz})^4(d_{xy})^1$ electron configuration (hereafter abbreviated as d_{xy}) displayed EPR spectra with $\Sigma g^2 < 14$. By comparison, low-spin Fe(III) hemes possessing the more common $(d_{xy})^2(d_{xz}, d_{yz})^3$ electron configuration (hereafter abbreviated as d_π), display EPR spectra with the typical $g_{xx}^2 + g_{yy}^2 + g_{zz}^2 \approx 16$ [14,16].

On the basis of these arguments, it was possible to speculate that the electronic configuration of the Fe^{III}-OOH complex of HO might have an unpaired electron residing in the d_{xy} orbital. What is noteworthy about a d_{xy} electronic configuration is that it places a large amount of π -spin density on the porphyrin *meso* carbons [12-16]. To delocalize spin density from the d_{xy} orbital into the porphyrin π system, the macrocycle has to ruffle significantly, so that the components (projections) of the p_z orbitals of the macrocycle in the xy plane have the proper symmetry to interact with the d_{xy} orbital [12]. The porphyrin orbital that has the proper symmetry to interact with the d_{xy} orbital in this ruffled macrocycle conformation is the $3a_{2u}(\pi)$ orbital [12] shown in Figure 1. It is evident from the relative sizes of the circles in the schematic representation of the $3a_{2u}(\pi)$ orbital that the *meso* carbons possess large electron density. Large electron and spin density at the *meso* positions, in turn, may explain the attack of the Fe^{III}-OOH intermediate on a heme *meso* carbon, as discussed in more detail later in this work. Consequently, the main object of the investigations reported herein is to determine the electron configuration of hydroperoxide or alkyl peroxide complexes of Fe^{III} porphyrinates.

Some years ago Tajima and coworkers showed that synthetic hemes in the presence of alkyl peroxides and a variety of sixth ligands, including methoxide,[17-19] imidazolate [20], or a second alkyl peroxide,19 as well as heme proteins with histidine

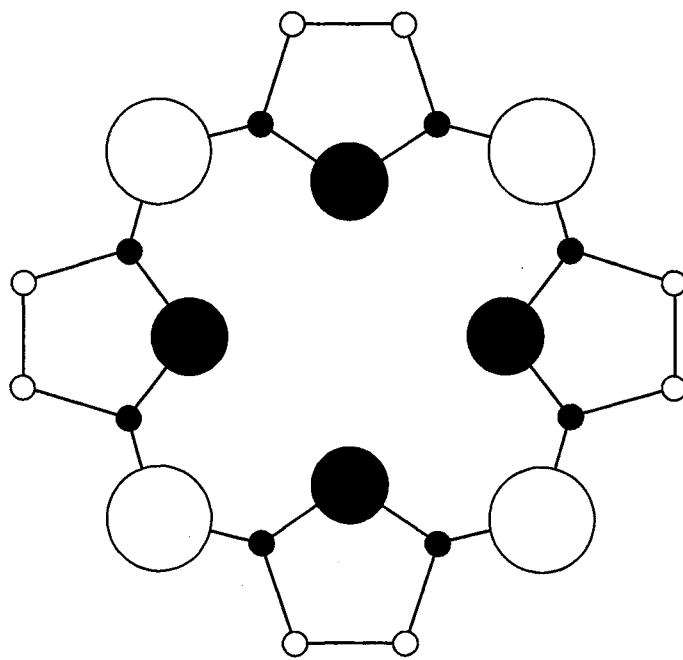


Figure 1. Representation of the $3a_{2u}(\pi)$ porphyrin orbital. The sizes of the circles are proportional to the electron density.

[21,22] or cysteinate [23] sixth ligands, yield very similar EPR spectra with compressed g anisotropy ($\Sigma g^2 \sim 14$). These spectra are very similar to those obtained for the Fe^{III} -OOH complexes of various heme protein enzymes, which were prepared by cryoreduction and then annealing of the corresponding Fe^{II} - O_2 complexes [11,24]. The g -values of the complexes of Tajima and coworkers (2.32, 2.16, 1.95, methoxide, *t*-butylperoxide [21]; 2.25, 2.15, 1.96, bis-*t*-butyl-peroxide [21]; 2.32, 2.19, 1.94, imidazolate, hydroperoxide [20]) are very similar to those of annealed hemoglobin-hydroperoxide (2.31, 2.18, 1.94) [11], heme oxygenase-hydroperoxide (2.37, 2.19, 1.93) [11], and cytochrome P450-hydroperoxide (2.29, 2.16, 1.96) [24]. We thus reasoned that magnetic resonance investigation of the Tajima model complexes could provide important information concerning the orbital of the unpaired electron, and hence the likely conformation of the porphyrinate ring of these model complexes, which could thus yield insights into the electronic and molecular structure of the catalytically active hydroperoxide complex of heme oxygenase. As will be shown below, we find that at 8 K the unpaired electron of $[\text{TPPFe}(\text{OCH}_3)(\text{OO}^t\text{Bu})]^-$, $[\text{TPPFe}(\text{OO}^t\text{Bu})_2]^-$, and $[\text{TPPFe}(\text{OCH}_3)_2]^-$ resides in one of the d_π orbitals, while at physiological temperatures the unpaired electron of those complexes that are stable enough to investigate is indeed in the d_{xy} orbital.

Experimental Section

a) Reagents.

Tetramethylammonium hydroxide (TMAOH) 25% (w/w) in methanol and 70% (w/w) aqueous *tert*-butylhydroperoxide ($^t\text{BuOOH}$) were purchased from Alfa Aesar.

TMAOH was used as received, whereas ^tBuOOH was extracted into methylene chloride by swirling 2.5 mL of the aqueous peroxide solution with 6 mL of dichloromethane in a separatory funnel. The organic phase was separated and then dried over anhydrous MgSO₄ before being filtered into a brown glass container. Dichloromethane solutions of ^tBuOOH were prepared before each experiment. Chloroiron(III) tetraphenylporphyrin (TPPFeCl) and *meso*-¹³C-TPPFe^{III}Cl were purchased from Porphyrin Products and used without further purification. ¹³C labeled perchlorato-iron(III) tetraphenylporphyrin (*meso*-¹³C-TPPClO₄) was prepared from *meso*-TPPFeCl according to a published procedure [25].

b) Synthesis of alkyl peroxide porphyrinate complexes.

Alkyl peroxide complexes of TPPFe were synthesized by a modification of the synthetic procedures reported by Tajima and coworkers [17-23]. These investigators reported the synthesis and characterization (EPR and electronic absorption spectra) of [TPP(OCH₃)₂]⁻, [TPPFe(OCH₃)(OO^tBu)]⁻, and [TPPFe(OO^tBu)₂]⁻ in frozen glasses at 77 K. An important aim of the investigation reported here is the study of these complexes by ¹³C NMR spectroscopy in solution. Consequently, modifications were necessary to synthesize and characterize the complexes at temperatures above the melting point of CH₂Cl₂. As a first step toward this goal, conditions were explored that allowed us to reproduce the electronic absorption spectra, previously obtained from frozen glasses at 77 K [17-19], in solutions thermostatted at 195 K. In order to facilitate these experiments, the cell shown in Figure 2 was constructed out of glass. To assemble the cell, the “dip probe” (a) is inserted through the cap (b) and secured with O-ring (c) and teflon® washer

(d). The cap is then threaded onto the main body of the cell (e), where it will push upon the washer, causing the O-ring to expand, thereby making the assembly gas-tight. Two side-ports were built into the glass cell: the first (f) serves as an inlet for argon, needed to establish a water-free atmosphere; the second (g) is fitted with a rubber septum, which can be removed for the addition of reactants. Reagents are introduced into the cell with the aid of polyethylene capillary tubing (0.8 mm I.D., 1.8 mm O.D.) and a peristaltic pump. The dip probe (Ocean Optics) enables ultraviolet and visible light from the excitation source to be directed into the sample solution through a fiber optic (i). The light passes through the solution in the probe cavity (h) and is reflected by a mirror back to a second fiber optic (i'), to be sent to a detector where the signal is processed. The probe can be equipped with sampling cavities of varying path lengths. For the purposes of these studies a sampling cavity with a 0.2 cm path length was used.

A typical procedure for synthesizing the alkyl peroxide complexes is described in what follows. A dichloromethane solution of TPPFeCl (6 mL, 0.2 mM), previously dried over MgSO_4 , was added into the cell through the reagent port (g). The cell was then thermostated at $-78\text{ }^\circ\text{C}$ with the aid of an acetone-dry ice bath. It is important to maintain a constant stream of argon to avoid the condensation of atmospheric water inside the cell. A solution of TMAOH in methanol (104 μL , 2.4 M) was added to the solution containing TPPFeCl , thus generating $[\text{TPPFe}(\text{OCH}_3)_2]^-$. The resultant solution was frozen by immersing the cell in liquid nitrogen, followed by the addition of a solution of ${}^t\text{BuOOH}$ in CH_2Cl_2 (125 μL , 1 M). The latter freezes almost instantaneously on the surface of the frozen solution of $[\text{TPPFe}(\text{OCH}_3)_2]^-$. The cell is then transferred back to an acetone-dry ice bath, where the solid solution is allowed to thaw at $-78\text{ }^\circ\text{C}$ with continuous stirring.

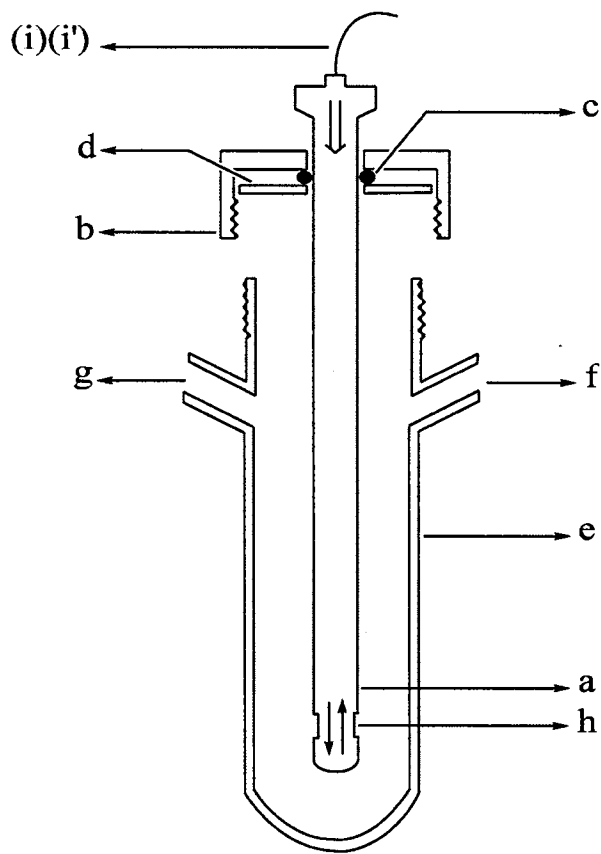


Figure 2. Schematic cross-sectional representation of the cell used to obtain electronic absorption spectra at low temperatures: (a) dip probe, (b) threaded cell-cap, (c) O-ring; when the cap is threaded into position the teflon® washer (d) forces the o-ring to expand, thus producing an air tight seal. The cell body is outfitted with a port for argon inlet (f) and a port for reagent delivery and argon outlet (g). The latter can be sealed with a rubber septum. The sampling cavity (h) utilized in the experiments has a path length of 0.2 cm and the dip probe is connected to the excitation source and diode array detector via optical fibers (i and i').

The color of the solutions changes to a cherry red. The electronic absorption spectrum recorded at $-78\text{ }^{\circ}\text{C}$ in this “dip probe” cell is very similar to that reported for $[\text{TPPFe}(\text{OCH}_3)(\text{OO}^t\text{Bu})]^-$ at 77 K [19]. Similar experiments allowed us to determine that the molar proportions needed to obtain electronic absorption spectra characteristic of the different alkyl peroxide complexes at $-78\text{ }^{\circ}\text{C}$ are 1 TPPFeCl (0.2 mM): 200 OH^- : 100 $^t\text{BuOOH}$ for $[\text{TPPFe}(\text{OCH}_3)(\text{OO}^t\text{Bu})]^-$, and 1 TPPFeCl (0.2 mM): 200 OH^- : 600 $^t\text{BuOOH}$ for $[\text{TPPFe}(\text{OO}^t\text{Bu})_2]^-$. These proportions were subsequently utilized to synthesize the complexes for magnetic resonance spectroscopic studies.

c) Sample preparation for magnetic resonance spectroscopic studies.

The alkyl peroxide complexes were synthesized at $-78\text{ }^{\circ}\text{C}$ in an EPR or NMR tube. A typical synthesis was carried out as follows: The NMR/EPR tube was flushed with argon through a polyethylene capillary tube. A solution of *meso*- ^{13}C -TPPFeCl (500 μL , 3 mM) in CD_2Cl_2 was added into an NMR/EPR tube with the aid of a polyethylene capillary tube and a peristaltic pump. TMAOH (125 μL , 2.4 M) was then introduced into the NMR/EPR tube in a similar fashion, thus resulting in the formation of $[\textit{meso}\text{-}^{13}\text{C}\text{-TPPFe}(\text{OCH}_3)_2]^-$. Mixing of the solutions was performed with the help of a thin ($\sim 1\text{ mm}$ diameter) ceramic rod. The ceramic rod was left in the solution and the NMR tube immersed in liquid nitrogen, while constantly flushing with a stream of argon. To synthesize $[\textit{meso}\text{-}^{13}\text{C}\text{-TPPFe}(\text{OCH}_3)\text{-}(\text{OO}^t\text{Bu})]^-$, a solution of $^t\text{BuOOH}$ (50 μL , 3 M) was then carefully added with the aid of a clean polyethylene capillary tube and a peristaltic pump. The solution of $^t\text{BuOOH}$ froze almost instantaneously on top of the frozen solution of $[\textit{meso}\text{-}^{13}\text{C}\text{-TPPFe}(\text{OCH}_3)_2]^-$. The NMR/EPR tube was then transferred to an

acetone-dry ice bath and the solutions allowed to melt while mixing with the ceramic rod. The solution containing the alkyl peroxide complex was frozen in liquid nitrogen and transferred into a previously thermostatted NMR probe or EPR cavity.

d) NMR spectroscopic investigations.

^{13}C NMR spectra of [*meso*- ^{13}C -TPPFe(OCH₃)(OO^tBu)]⁻ was obtained on a Varian Unity Inova spectrometer operating at a ^{13}C frequency of 100.576 MHz. The spectra were acquired over 16 k data points, with a spectral width of 8.6 kHz, 90 ms acquisition time, 40 ms relaxation delay and 40,000 scans. The baseline was flattened with a spline fitting of predefined baseline regions. The temperature of the sample was set and regulated through the use of a standard variable temperature unit furnished by Varian Instruments, which functions by controlling a heating element which is exposed to the stream of cooled gas. The variable temperature unit was calibrated by using the Wilmad temperature calibration sample, which utilizes the temperature-dependent difference in resonance frequency of the two peaks of methanol.

e) EPR spectroscopic investigations.

Continuous wave EPR spectra were recorded on a Bruker ESP-300E spectrometer, at 77 K using an immersion dewar. The pulsed ENDOR experiments were carried out on a home-built X/P-band pulsed EPR spectrometer equipped with a pulsed ENDOR accessory [26,27]. In these experiments, the Mims [28] and Davies [29] pulsed ENDOR techniques were employed. To minimize the Mims ENDOR spectrum distortions due to the blind spots [30,31], the spectra were detected at several time

intervals τ between the first and second microwave (mw) pulses of the three-pulse sequence, and then summed up. The measurement temperature, chosen to optimize the electron spin relaxation times for the pulsed EPR experiments, was about 8 K.

Results and discussion

a) Synthesis of alkyl peroxide complexes of Fe^{III}TPP.

Tajima and coworkers have described the synthesis of alkyl peroxide complexes of Fe^{III}-tetraphenylporphyrin, such as [TPPFe(OCH₃)₂]⁻, [TPPFe(OCH₃)(OO^tBu)]⁻, and [TPPFe(OO^tBu)₂]⁻ in several reports [17-23]. Three important aspects prompted us to reinvestigate the synthesis of alkyl peroxide complexes previously reported by Tajima et al.: **(a)** The stoichiometric proportions needed to prepare the alkyl peroxide complexes are significantly different from one report to another. In our hands, the stoichiometric proportions previously reported do not lead to the synthesis of the desired alkyl peroxide complexes. **(b)** The alkyl peroxide (^tBuOOH), utilized in the previous reports was distilled under reduced pressure, a step that is potentially hazardous, and at best could lead to significant decomposition of the peroxide. We have thus used aqueous ^tBuOOH extracted into CH₂Cl₂, followed by drying with MgSO₄. **(c)** The alkyl peroxide complexes prepared by Tajima have been studied only in frozen glasses at 77 K [17-23]. Because it was our intention to conduct ¹³C NMR spectroscopic studies of the alkyl peroxide complexes in solution, it was important to search for appropriate conditions for the preparation of the complexes at temperatures above the melting point of CH₂Cl₂. Consequently, the alkyl peroxide complexes were prepared at -78 °C (195 K) and the formation of products was monitored with the aid of electronic absorption spectroscopy.

The appropriate stoichiometric proportions needed to prepare $[\text{TPPFe}(\text{OCH}_3)(\text{OO}'\text{Bu})]^-$ were determined by comparing the electronic absorption spectrum obtained in solution at 195 K with those reported by Tajima in frozen glasses at 77 K [17-19]. To ensure that the conditions found by electronic absorption spectroscopy could be more readily translated into the concentrations needed for the NMR and EPR spectroscopic experiments, the “dip probe” (see Methods) was outfitted with a 2.0 mm-path cavity and only the visible region (450-800 nm) of the spectrum was monitored. This allowed us to increase the concentration of porphyrin several-fold relative to what is possible if one utilizes an optical path of 1 cm and observes the Soret band. In fact, the concentration used to prepare the alkyl peroxide complexes for the NMR experiments is only four fold higher than that used with the electronic absorption spectroscopy studies. This increased concentration should maintain the thermodynamic stability of the complex, even in the face of increased temperature (178-218 K), by overcoming the expected decrease in K_{eq} for complex formation as the temperature is raised. Experiments conducted in this fashion allowed us to establish that addition of a 200-fold molar excess of tetramethylammonium hydroxide in methanol to a solution containing TPPFeCl in CH_2Cl_2 results in the formation of a complex that displays the electronic spectrum shown in Figure 3-A. This spectrum, obtained at 195 K, is similar to that reported for $[\text{TPPFe}(\text{OCH}_3)_2]^-$ in a frozen glass at 77 K [18], and is typical of low-spin Fe(III) porphyrinates having either the d_{xy} or the d_{π} electron configuration [32]. When the complex is prepared in an EPR tube (see Methods) and the resultant solution is frozen at 77 K for spectroscopic analysis, an EPR spectrum (Figure 3-D, trace 1) identical to that reported by Tajima [18,19] for $[\text{TPPFe}(\text{OCH}_3)_2]^-$ is obtained. Addition of 100-fold

excess of ^tBuOOH, with respect to TPPFeCl, to [TPPFe(OCH₃)₂]⁻ results in the formation of [TPPFe(OCH₃)(OO^tBu)]⁻. The electronic absorption spectrum of this complex at 195 K (Figure 3-B) and EPR spectrum at 77 K (Figure 3-D, trace 2) are characteristic of a low-spin iron(III) porphyrinate and very similar to those reported for [TPPFe(OCH₃)(OO^tBu)]⁻ at 77 K [18,19]. Addition of more ^tBuOOH to a solution of [TPPFe(OCH₃)(OO^tBu)]⁻, 600-fold excess with respect to TPPFeCl, results in the formation of [TPPFe(OO^tBu)₂]⁻. The EPR spectrum of this complex at 77 K (Figure 3-D, trace 3) is identical to that reported by Tajima and coworkers [18,19] for [TPPFe(OO^tBu)₂]⁻. It can also be seen from Figure 3-C that the electronic spectrum of [TPPFe(OO^tBu)₂]⁻ at 178 K is characteristic of a low-spin porphyrinate, and clearly distinct from the electronic spectrum exhibited by [TPPFe(OCH₃)(OO^tBu)]⁻. The electronic spectrum of [TPPFe(OO^tBu)₂]⁻ had not been reported previously.

The results summarized above clearly indicate that the stoichiometric proportions of reactants utilized to synthesize the different alkyl peroxide complexes at 195 K produce solutions with optical signatures very similar to those obtained by Tajima at 77 K [18-20]. In addition, EPR spectra of the low-spin complexes synthesized with these stoichiometric proportions are not only identical to those reported previously [18-20], but also do not contain the high-spin Fe(III) EPR signals, present in some of the previous reports [17,18,20,21]. Consequently, it can be concluded that the alkyl peroxide complexes, previously characterized only at 77 K [17-21], are also stable at 195 K.

A second point of practical importance in the synthesis of these alkyl peroxide complexes is that it is not necessary to distill the alkyl hydroperoxide. It is sufficient to

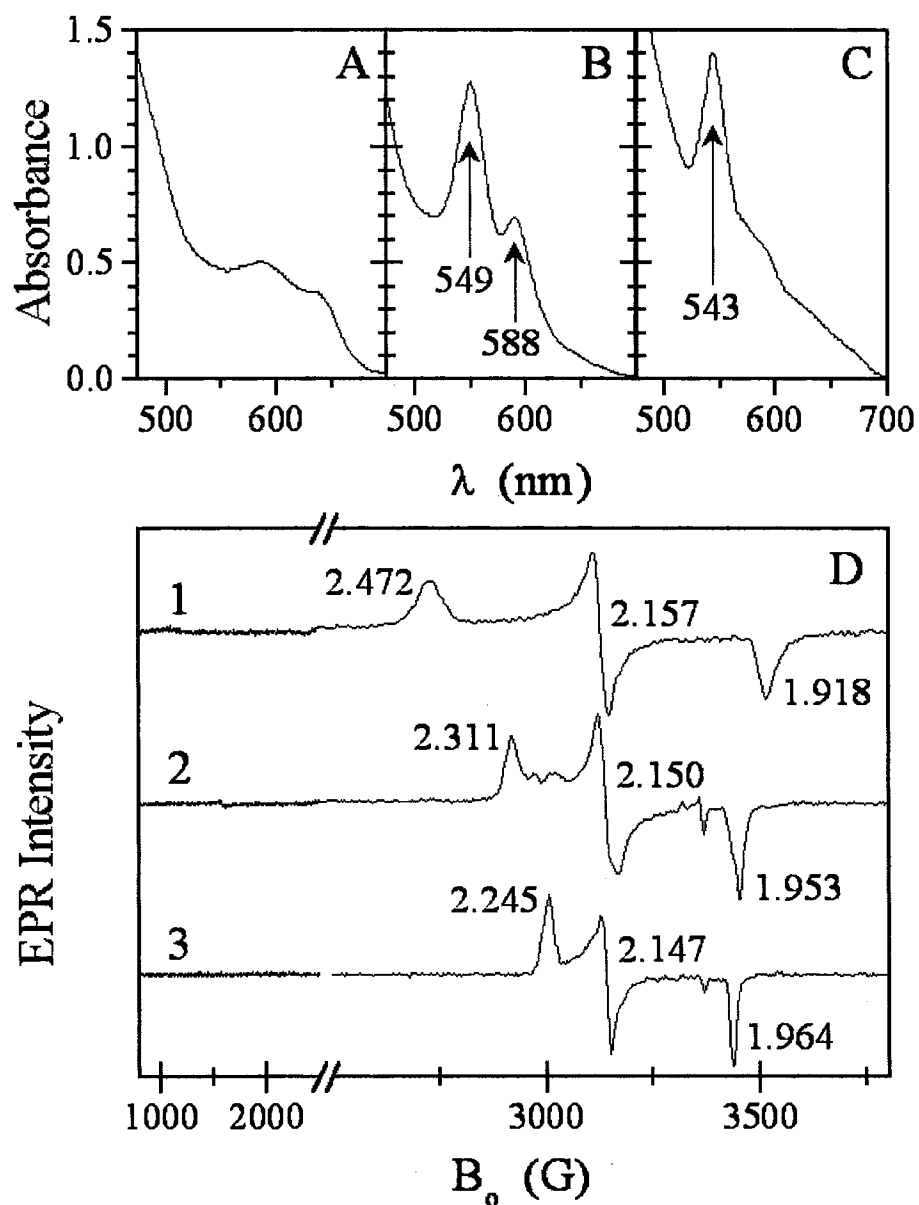


Figure 3. Electronic absorption spectra of $[\text{TPPFe}(\text{OCH}_3)_2]^-$ (A), $[\text{TPPFe}(\text{OCH}_3)(\text{OO}^t\text{Bu})]^-$ (B), and $[\text{TPPFe}(\text{OO}^t\text{Bu})_2]^-$ (C). The corresponding EPR spectra are shown in (D) by traces 1, 2 and 3, respectively. The small peaks at $g = 2$ in traces 2 and 3 are due to $^t\text{BuOO}\bullet$.

extract t BuOOH from its aqueous commercial solution into CH_2Cl_2 , followed by drying the organic phase with MgSO_4 . The CH_2Cl_2 solution of t BuOOH obtained in this manner permits the successful synthesis of the alkyl peroxide complexes at 195 K if care is taken to exclude atmospheric water from the system.

b) Pulsed ENDOR spectroscopy reveals that $[\text{TPPFe}(\text{OCH}_3)(\text{OO}^t\text{Bu})]^-$ has a d_π electron configuration at 8 K.

It is evident from the EPR spectra summarized in Figure 3 that $\Sigma g^2 \leq 14$ for all three complexes. This raised the possibility that these complexes might possess a d_{xy} electron configuration. This possibility was investigated by pulsed ENDOR at 8 K and by ^{13}C NMR spectroscopy at higher temperatures (see below). The Mims ENDOR [27] spectra of $[\text{meso-}^{13}\text{C-TPPFe}(\text{OCH}_3)(\text{OO}^t\text{Bu})]^-$, recorded at the low-field (g_{LF}) and high-field (g_{HF}) extrema of the EPR spectrum, are shown in Figure 4, traces 1 and 2. Traces 3 and 4 in the same figure show the spectra of $[\text{meso-}^{13}\text{C-TPPFe}(\text{N-MeIm})_2]^+$, an example of a “pure” d_π electron configuration [13-16]. The hyperfine splittings in all spectra do not exceed 1.7 MHz. In the ENDOR spectra recorded at the intermediate positions of the EPR spectra the splittings are similar (not shown). Figure 5 shows for comparison the pulsed ENDOR spectra of $[\text{meso-}^{13}\text{C-TPPFe}(^t\text{BuNC})_2]^+$, an example of a “pure” d_{xy} electron configuration [14,16], recorded at $g_{\text{LF}} = g_x = g_y$ (trace 1), $g_{\text{HF}} = g_z$ (trace 5), and at intermediate g -values that correspond to different angles θ_{BZ} between the external magnetic field \mathbf{B}_0 and the normal \mathbf{Z} to the heme plane (at g_{LF} $\theta_{\text{BZ}} = 90^\circ$, and at g_{HF} $\theta_{\text{BZ}} = 0^\circ$, as indicated in Figure 5). The spectra in Figures 4 and 5 are considerably different both in appearance and in the frequencies of the ^{13}C transitions, and can be used

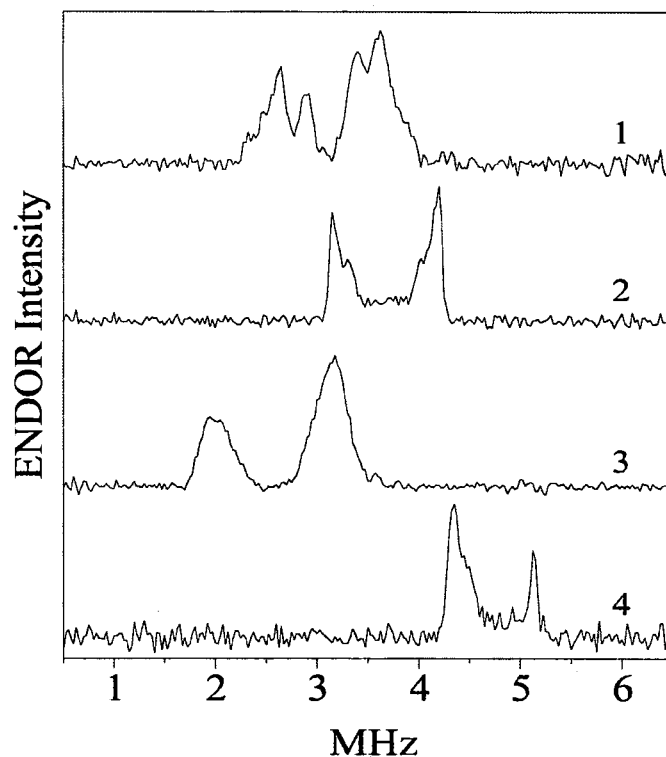


Figure 4. Mims ENDOR spectra of *meso*- ^{13}C in $[\text{TPPFe}(\text{OCH}_3)(\text{OO}^t\text{Bu})]^-$ (traces 1 and 2) and in $[\text{TPPFe}(\text{N-MeIm})_2]^+$ (traces 3 and 4). The spectra were obtained as differences between those of the samples enriched with ^{13}C and the samples with a natural abundance of isotopes ($\sim 1\%$ of ^{13}C). Traces 1 and 2 are detected at $B_o = 2920 \text{ G}$ ($g_{\text{LF}} = g_z$) and $B_o = 3430 \text{ G}$ ($g_{\text{HF}} = g_x$), respectively. They represent a result of summation of spectra recorded at the time intervals τ between the first and second microwave (mw) pulses of 300, 400, 500 and 600 ns. Traces 3 and 4 are detected at $B_o = 2385 \text{ G}$ ($g_{\text{LF}} = g_z$) and $B_o = 4425 \text{ G}$ ($g_{\text{HF}} = g_x$), respectively. Trace 3 represents a result of summation of the spectra obtained at $\tau = 250, 350, 450$ and 550 ns, while trace 4 is a result of summation of the spectra at $\tau = 250$ and 350 ns. Experimental conditions: temperature, $\sim 8 \text{ K}$; mw frequency, 9.445 GHz ; time interval T between the second and third mw pulses, $60 \mu\text{s}$; radiofrequency pulse duration, $T_{\text{RF}} = 30 \mu\text{s}$ (about 180° for weakly-coupled ^{13}C).

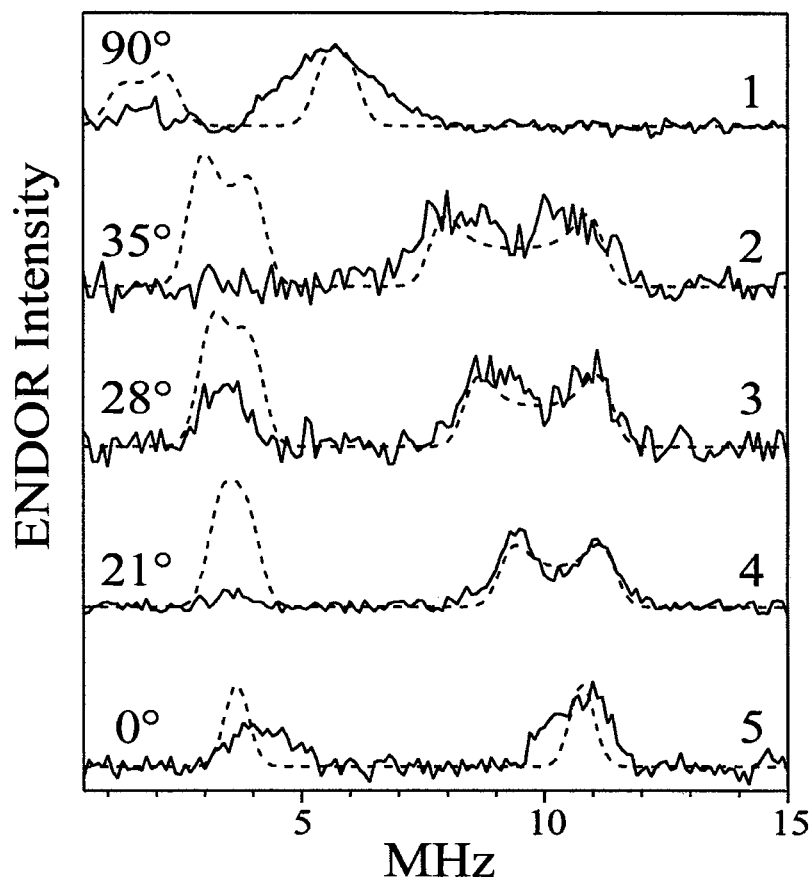


Figure 5. Davies ENDOR spectra of *meso*- ^{13}C in $[\text{TPPFe}(\text{tBuNC})_2]^+$. The spectra were obtained as differences between those of the samples enriched with ^{13}C and the samples with a natural abundance of isotopes ($\sim 1\%$ of ^{13}C). Traces 1 through 5 are detected at $B_0 = 3035\text{ G}$ ($g_{\text{LF}} = g_{\text{L}} = g_{\text{X}} = g_{\text{Y}}$), 3325 G , 3375 G , 3425 G and 3495 G ($g_{\text{HF}} = g_{\text{I}} = g_{\text{Z}}$), respectively. The angles θ_{BZ} between B_0 and Z corresponding to these B_0 are shown at the left side of the Figure. Experimental conditions: temperature, about 8 K ; mw frequency, 9.445 GHz ; mw pulse durations, 100 ns (180°), 50 ns (180°) and 100 ns (180°); time interval T between the first and second mw pulses, $60\text{ }\mu\text{s}$; $\tau = 700\text{ ns}$; radiofrequency pulse duration, $T_{\text{RF}} = 30\text{ }\mu\text{s}$. Dashed traces are simulated with $\rho_{\text{C}} = 0.079$, $\rho_{\text{Fe}} = 1-4\rho_{\text{C}} = 0.68$, $\theta_{\text{pZ}} = 21^\circ$.

“as is” to distinguish one type of the electronic configuration from the other. Thus, we can already make a conclusion that the ENDOR spectra clearly indicate that at 8 K the electron configuration of [TPPFe(OCH₃)(OO^tBu)] is d_{π} , and that the unusually small value of Σg^2 observed for this complex probably arises from orbital quenching in this relatively weak-field anionic ligand system.

In order to understand the origin of the difference between the ENDOR spectra originating from Fe^{III}-porphyrinates with d_{π} and d_{xy} electron configurations, we must consider in some detail the relation between the hyperfine interaction (hfi) parameters of *meso*-¹³C and the spin density distributions in the porphyrin π -systems. In the case of the d_{xy} electronic configuration the main contributions to the *meso*-¹³C hfi come from two sources. First, there is a dipole interaction between the electronic spin density ρ_{Fe} localized in the d_{xy} orbital and the magnetic moment of the *meso*-¹³C nucleus. This interaction can be reasonably accounted for by using the point dipole approximation, and is characterized by the anisotropic hfi coupling constant

$$T_{\text{Fe}} \approx -\rho_{\text{Fe}} g g_n \beta \beta_n / h R_{\text{FeC}}^3 \quad (1)$$

which corresponds to the perpendicular component of the axially symmetric anisotropic hfi tensor. The axis of this tensor is directed along the radius-vector \mathbf{R}_{FeC} connecting the central Fe³⁺ ion with the *meso*-carbon. The parameters entering Equation (1) are as follows: g and g_n are, respectively, the electronic and nuclear g -factors; β and β_n are the Bohr magneton and the nuclear magneton, h is Planck's constant, $R_{\text{FeC}} \approx 3.4 \text{ \AA}$. The value of T_{Fe} corresponding to $\rho_{\text{Fe}} = 1$ is about -0.5 MHz (at $g = 2$).

The other contribution to the hfi is from the π -spin density ρ_C localized on the *meso*-carbon itself. The anisotropic hfi is characterized by the axially symmetric tensor with the perpendicular component $T_C \sim -50\rho_C$ MHz (at $g = 2$) [33,34]. The axis of this tensor is directed along the carbon *p*-orbital, close to the heme normal \mathbf{Z} , and is perpendicular (approximately, if the macrocycle is ruffled) to the axis of the hfi tensor determined by ρ_{Fe} . The isotropic hfi constant a_C resulting from ρ_C is about $100\rho_C$ MHz [33,34].

The contributions of spin densities on other atoms in the porphyrin ring and, possibly, in the ligands, may be neglected because these spin densities are close to zero, as is the case for the pyrrole carbons. In addition, other atoms are at fairly large distances from a given *meso*-carbon, and the spin densities on them are limited ($\rho < 0.1$ [35]). Somewhat stretching the model, the spin densities on pyrrole nitrogens that are located close to the central Fe can be included in the effective value of ρ_{Fe} , which will only lead to a slight nonaxiality of the corresponding anisotropic hfi tensor and to a slightly overestimated value of ρ_{Fe} .

With the model formulated above, the total hfi constant $A_{//}$ corresponding to $\mathbf{B}_0 // \mathbf{Z}$ can be written as:

$$A_{//} = a_C + T_{Fe} - 2T_C \approx 100\rho_C - 0.25g_z\rho_{Fe} + 50g_z\rho_C \quad (2)$$

where all numerical factors are in MHz, and the proportionality of the anisotropic hfi to the electronic *g*-value is factored out. If $\mathbf{B}_0 \perp \mathbf{Z}$, the hfi constant A_{\perp} varies from

$$A_{\perp} = a_C + T_{\text{Fe}} + T_C \approx 100\rho_C - 0.25g_{\perp}\rho_{\text{Fe}} - 25g_{\perp}\rho_C \quad (3)$$

when $\mathbf{B}_0 \perp \mathbf{R}_{\text{FeC}}$, to:

$$A_{\perp} = a_C - 2T_{\text{Fe}} + T_C \approx 100\rho_C + 0.5g_{\perp}\rho_{\text{Fe}} - 25g_{\perp}\rho_C \quad (4)$$

when $\mathbf{B}_0 // \mathbf{R}_{\text{FeC}}$. In Equations (3) and (4) g_{\perp} is $g_{\text{LF}} = g_X = g_Y$.

To first order approximation in hfi, the two ^{13}C ENDOR lines are located at the frequencies of $|v_C \pm A/2|$, where v_C is the ^{13}C Zeeman frequency. Two situations are possible. In the weak coupling limit, when $v_C > A/2$, the doublet of ENDOR lines will be centered at v_C and split by A . In the strong coupling limit, when $v_C < A/2$, the doublet will be centered at $A/2$ and split by $2v_C$. The doublet of ^{13}C lines seen in spectrum 5 of Figure 5 (near g_Z , $B_0 = 3495$ G, $v_C \approx 3.74$ MHz), is centered at the frequency $v_{\text{cnt}} \approx 7.5$ MHz $> v_C$. It then clearly corresponds to the strong coupling case, and we can immediately estimate $A_{//} \approx 2v_{\text{cnt}} \approx 15$ MHz. Since the anisotropic hfi contribution from ρ_{Fe} is very small compared with $A_{//}$ (at $g = g_Z \approx 1.93$, $T_{\text{Fe}} \approx 0.48$ MHz, even at $\rho_{\text{Fe}} = 1$), it can be neglected in Equation (2), and $\rho_C \approx 0.076$ can be readily estimated. If we include in the effective ρ_{Fe} all spin densities but those located on the *meso*-carbons (and for the d_{xy} system that virtually means only the spin densities on the pyrrole nitrogens), we may estimate $\rho_{\text{Fe}} \approx 1 - 4\rho_C \approx 0.7$. Substituting $\rho_C \approx 0.076$ into Equation (3) or (4) where, again, T_{Fe} is neglected, we can easily find $A_{\perp} \approx 3.4$ MHz. Using this value, the position of the high-frequency ^{13}C line, $v_C + A_{\perp}/2$, in the ENDOR spectrum at $g_{\perp} \approx 2$ [23] can be estimated. The estimated frequency is about 4.95 MHz, very close to the maximum of

the high-frequency line observed in the experimental spectrum 1 in Figure 5. Thus, it is seen that the ENDOR spectra recorded at both canonical orientations are successfully explained with this model for the hfi, which shows that it is reasonably accurate.

The ENDOR spectra recorded at B_0 values other than those corresponding to the turning points of the EPR spectrum show ^{13}C transition frequencies intermediate between those observed at the turning points (see traces 2-4 in Figure 5). In addition, the high-frequency line in these spectra exhibits a splitting (we do not intend to discuss the low-frequency line, since it has a much lower intensity in the experimental spectra, and its shape is considerably affected by noise). This feature is interpreted as indicative of the p -orbitals of the *meso*-carbons (and their associated anisotropic hfi tensor axes) being not exactly parallel to \mathbf{Z} . An alternative explanation with significantly inequivalent carbons fails because spectrum 5, recorded at g_z , does not show resolved splittings, which indicates that the spin densities on all four *meso*-carbons are nearly identical.

To estimate the angle θ_{pZ} between \mathbf{Z} and the axis of the *meso*-carbon p -orbital (assuming for simplicity θ_{pZ} to be the same for all four *meso*-carbons), numerical simulations of the ENDOR spectra have been performed with a variation of θ_{pZ} , ρ_C and $\rho_{\text{Fe}} = 1 - 4\rho_C$. A reasonable fit was obtained for $\rho_C \approx 0.079$, $\rho_{\text{Fe}} \approx 0.68$, and $\theta_{pZ} \approx 21^\circ$ (dashed traces in Figure 5). The spin density $\rho_C \approx 0.079$ found in this work for [*meso*- ^{13}C -TPPFe(^tBuNC) $_2$] $^+$ is close to $\rho_C \approx 0.06$ found earlier for another d_{xy} system, [OEPFe(PhNC) $_2$] $^+$, using the ENDOR lines of the *meso*-protons [36].

Now the *meso*- ^{13}C ENDOR spectra of the d_π systems shown in Figure 4 will be considered briefly. The spectra recorded at g_z show better (trace 1) or worse (trace 3) resolved sets of doublets (asymmetric in amplitude, probably, because of the implicit

TRIPLE effect [37,38]) centered at the ^{13}C Zeeman frequency and split by the hfi constants A_Z . Different doublet splittings indicate some inequivalence of the spin density distributions “seen” by different *meso*-carbons.

The main contribution to the *meso*- ^{13}C anisotropic hfi in these systems is made by $\rho_{\text{Fe}} \sim 0.8$ [39]. For example, for [*meso*- ^{13}C -TPPFe(OCH₃)(OO^tBu)]⁻ ($g_Z \sim 2.3$), the corresponding anisotropic coupling constant T_{Fe} (see Equation (1)) is about 0.5 MHz. The spin densities on the *meso*-carbons are very small (≤ 0.003 , according to our Hückel calculations), and may contribute no more than $T_C \sim -0.17$ MHz to the anisotropic hfi and $a_C \sim 0.3$ MHz to the isotropic hfi constant. Another important contribution to the hfi parameters of *meso*- ^{13}C is made by the π -spin density ρ_α on the adjacent pyrrole α -carbons. The contribution from ρ_α to the isotropic hfi of *meso*- ^{13}C may be estimated as $a_\alpha \sim -35 \rho_\alpha$ MHz [40]. With ρ_α reaching 0.015 it may be as large as -0.6 MHz, and with two pyrrole α -carbons neighboring each *meso*- ^{13}C , $a_\alpha \sim -1$ MHz is a reasonable estimate. The anisotropic hfi contribution of $\rho_\alpha \sim 0.015$ may be roughly estimated in the point dipole approximation to give the coupling constant $T_\alpha \sim -0.13$ MHz.

It can be seen that the main contributions to the total hfi constant A_Z of the *meso*- ^{13}C are the isotropic contribution of spin densities ρ_α on adjacent pyrrole α -carbons ($a_\alpha \sim -1$ MHz) and the anisotropic contribution from ρ_{Fe} ($T_{\text{Fe}} \sim -0.5$ MHz at $g = g_Z \sim 2.3$). The sum of these contributions gives $A_Z \sim -1.5$ MHz, which correlates with the maximal splitting of about 1.7 MHz observed in spectrum 1 in Figure 4. In spectrum 3, which corresponds to that at $g_Z \sim 2.83$ of [*meso*- ^{13}C -TPPFe(N-MeIm)₂]⁺, the maximal splitting is very similar, about 1.6 MHz. In spectra 2 and 4 recorded at $g_{\text{HF}} = g_X$ the maximal splittings are, naturally, of similar magnitude, about 1.05 MHz in trace 2 ($g_{\text{HF}} \sim 1.95$) and

about 0.9 MHz in trace 4 ($g_{\text{HF}} \sim 1.53$). The general structure of various *meso*- ^{13}C hfi contributions is thus understood. However, the numerous possible contributions prohibits any detailed analysis of the ENDOR spectra in Figure 4 aimed at extracting the exact spin densities on the *meso*- and pyrrole α -carbons.

An important parameter that will be used below in discussion of the ^{13}C NMR isotropic shifts is the ratio of the isotropic hfi constants a_{meso} of *meso*- ^{13}C in the d_{xy} and d_{π} configurations. With $\rho_{\text{C}} \sim 0.08$ estimated above for the d_{xy} configuration a_{meso} is about 8 MHz. For the d_{π} configuration, as discussed above, a_{meso} is mostly determined by the spin polarization contributions from the pyrrole α -carbons and is close to -1 MHz. The ratio of the hfi constants is thus in the range of -8 to -10.

To conclude the discussion of the *meso*- ^{13}C ENDOR spectra it can be mentioned here that they, indeed, show in a very straightforward way the gross features of spin density distribution over the porphyrin ring related to the particular electronic configuration of the iron-porphyrin complex, and may be used to make the corresponding assignments.

c) ^{13}C NMR spectroscopy reveals that $[\text{TPPFe}(\text{OCH}_3)(\text{OO}'\text{Bu})]^-$ has a d_{xy} electron configuration at 193 K, and, by extrapolation, at room temperature.

The picture that emerges from ^{13}C NMR spectroscopic studies over the temperature range 178-218 K is very different from that discussed above for the ^{13}C pulsed ENDOR measurements carried out at 8 K. The ^{13}C NMR spectrum obtained from a solution of [*meso*- ^{13}C -TPPFe(OCH₃)(OO'Bu)]⁻ at 193 K is shown in Figure 6-A. The observed chemical shift for the *meso*-carbon is 422 ppm. The relevance of this chemical

shift becomes evident if one considers that it has recently been shown that the *meso*-carbon chemical shift of ^{13}C -labeled ferrihemes is an excellent diagnostic tool for differentiating between the d_π and d_{xy} electron configuration [41]. Complexes with the d_π unpaired electron configuration have small chemical shifts (tens of ppm) [42], whereas those with the unpaired electron in the d_{xy} orbital typically exhibit large chemical shifts (hundreds of ppm) [41,43]. For instance, the chemical shift observed for [*meso*- ^{13}C -TPPFe(ImH) $_2$] $^-$ is 12 ppm at 193 K (see below), while that of [*meso*- ^{13}C -TPPFe(t BuNC) $_2$] $^+$ is estimated [44] to be somewhat greater than 1000 ppm at 193 K (see below). The chemical shift observed for [*meso*- ^{13}C -TPPFe(OCH $_3$)(OO t Bu)] $^-$ is somewhat less than the average of the two (516 ppm), suggesting a significant population of the d_{xy} electron configuration at 193 K, and a small energy difference between the d_π and d_{xy} electron configurations [45].

Before the electronic configuration of [*meso*- ^{13}C -TPPFe(OCH $_3$)(OO t Bu)] $^-$ can be assigned with complete certainty at 193 K, it is important to consider alternative explanations of the large ^{13}C chemical shift observed for this complex. For example, it is necessary to exclude the possibility that at 193 K [TPPFe(OCH $_3$)(OO t Bu)] $^-$ is in equilibrium with a high spin species such as five-coordinate TPPFe(OCH $_3$) or TPPFe(OO t Bu). Fe $^{\text{III}}$ porphyrinates coordinated by a single anionic ligand are known to display *meso*-carbon chemical shifts in the range of 300 to 500 ppm at ambient temperatures [46,47]. Consequently, it must be established whether at 193 K [TPPFe(OCH $_3$)(OO t Bu)] $^-$ is indeed a low-spin complex.

Pertinent evidence is provided by the fact that the electronic absorption spectrum of [TPPFe(OCH $_3$)(OO t Bu)] $^-$ at 195 K (Figure 6B-a), with well-resolved α and β bands, is

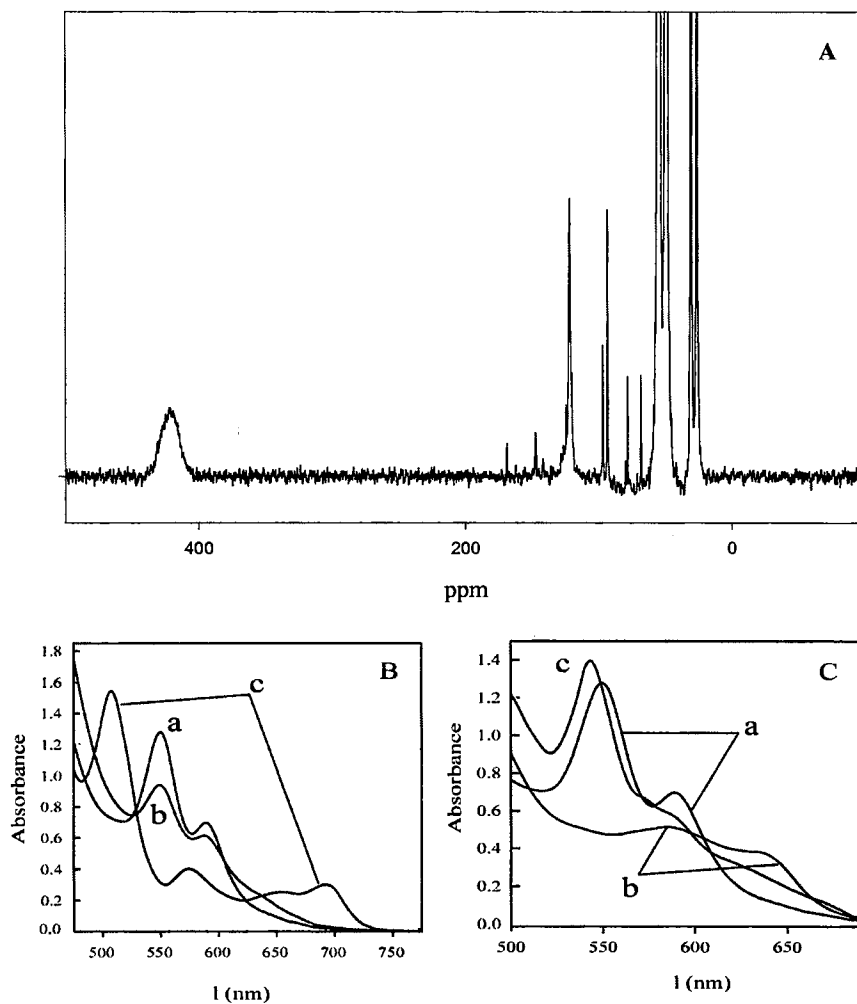


Figure 6. (A) ^{13}C NMR spectrum of $[\textit{meso}\text{-}^{13}\text{C}\text{-TPPFe}(\text{OCH}_3)(\text{OO}'\text{Bu})]^-$ obtained at 193 K. (B) Electronic absorption spectra of $[\text{TPPFe}(\text{OCH}_3)(\text{OO}'\text{Bu})]^-$ at (a) 195 K, (b) after three hours at 231 K and (c) spectrum obtained from TPPFeCl at 195 K. (C) Electronic absorption spectra of (a) $[\text{TPPFe}(\text{OCH}_3)(\text{OO}'\text{Bu})]^-$, (b) $[\text{TPPFe}(\text{OCH}_3)_2]^-$, and (c) $[\text{TPPFe}(\text{OO}'\text{Bu})_2]^-$.

clearly characteristic of a low-spin Fe^{III} porphyrinate [32], and distinct from the electronic spectrum of a high-spin Fe^{III} porphyrinate, such as that corresponding to TPPFeCl (Figure 6B-c). This electronic absorption spectrum is almost identical to that reported by Tajima and coworkers in a frozen glass at 77 K [18,19], while, at the same time, the EPR spectrum detected at 77 K is characteristic of a low-spin iron(III) porphyrinate complex. These observations unambiguously testify that [*meso*-¹³C-TPPFe(OCH₃)(OO^tBu)]⁻ is a low-spin complex at 195 K, as well as at 77 K [17,18]. The low-spin nature of the complex having been established, one can conclude that the chemical shift of the *meso* carbon, 422 ppm at 193 K, clearly indicates that the [TPPFe(OCH₃)(OO^tBu)]⁻ complex at this temperature has at least partial *d*_{xy} electron configuration. The question of the degree of population of the *d*_{xy} electronic state is dealt with in the next section.

d) Variable temperature ¹³C NMR spectroscopy of [*meso*-TPPFe(OCH₃)(OO^tBu)]⁻ indicates a thermodynamic equilibrium between electron configurations.

In order to explore the temperature dependence of the *meso*-carbon resonance in [*meso*-¹³C-TPPFe(OCH₃)(OO^tBu)]⁻ it was necessary to first establish the temperature range over which [TPPFe(OCH₃)(OO^tBu)]⁻ is stable. It was also necessary to determine whether changes in temperature result in equilibria of [TPPFe(OCH₃)(OO^tBu)]⁻ with other species. Examples of such chemical species are the high-spin complexes TPPFe(OCH₃) and TPPFe(OO^tBu) mentioned above, and the low-spin bis-ligand complexes [TPPFe(OCH₃)₂]⁻ and [TPPFe(OO^tBu)₂]⁻. Electronic absorption spectroscopy was again useful in answering these questions. The electronic absorption spectrum of

$[\text{TPPFe}(\text{OCH}_3)(\text{OO}^t\text{Bu})]^-$ at 212 K (CHCl_3 -dry ice bath) is very similar to that obtained at 195 K (Figure 6-B-a), thus providing strong evidence that the system does not undergo an equilibrium involving a change in spin state, and that it does not decompose at this temperature. The solution containing $[\text{TPPFe}(\text{OCH}_3)(\text{OO}^t\text{Bu})]^-$ was warmed to 231 K (CH_3CN -dry ice) for three hours. The resultant electronic absorption spectrum (Figure 6-B-b) is identical in features to those obtained at 212 and 195 K, but is less intense. We interpret these results as indicating that at temperatures above 212 K it is likely that the alkyl peroxide reacts with the porphyrin to produce oxidation products that are much less intensely colored, hence decreasing the absorption intensity. Nevertheless, the spectrum in Figure 6B-b clearly indicates the absence of a high spin species at 212 K. On the basis of these observations it was decided to study $[\text{meso-}^{13}\text{C-TPPFe}(\text{OCH}_3)(\text{OO}^t\text{Bu})]^-$ between 218 and 178 K. The upper limit is imposed by the reactivity of the alkyl peroxide ligand and the lower limit by the freezing point of the solvent.

Electronic absorption spectra obtained at different temperatures also allowed us to conclude that neither the 5-coordinate high-spin $\text{TPPFe}(\text{OCH}_3)$ and $\text{TPPFe}(\text{OO}^t\text{Bu})$, nor the six-coordinate low-spin $[\text{TPPFe}(\text{OO}^t\text{Bu})_2]^-$ and $[\text{TPPFe}(\text{OCH}_3)_2]^-$ complexes exist in detectable concentrations under the conditions used to study $[\text{meso-}^{13}\text{C-TPPFe}(\text{OCH}_3)(\text{OO}^t\text{Bu})]^-$. For example, the data summarized in Figure 6-B allowed us to rule out the presence of high-spin complexes (see above). Evidence supporting the absence of low-spin complexes other than $[\text{TPPFe}(\text{OCH}_3)(\text{OO}^t\text{Bu})]^-$ is shown in Figure 6-C. The electronic absorption spectrum of $[\text{TPPFe}(\text{OCH}_3)(\text{OO}^t\text{Bu})]^-$ (Figure 6-C-a) is clearly distinct from the spectra originating from both $[\text{TPPFe}(\text{OCH}_3)_2]^-$ and $[\text{TPPFe}(\text{OO}^t\text{Bu})_2]^-$, Figures 6-C-b and 6-C-c, respectively. Furthermore, the spectrum characteristic of

[TPPFe(OO^tBu)₂]⁻ can only be observed upon addition of a 600-fold molar excess of ^tBuOOH with respect to TPPFeCl (1 TPPFeCl (0.2 mM): 200 OH⁻: 600 ^tBuOOH). By comparison, [TPPFe(OCH₃)(OO^tBu)]⁻ is prepared by addition of 100-fold molar excess of ^tBuOOH with respect to TPPFeCl (1 TPPFeCl (0.2 mM): 200 OH⁻:100 ^tBuOOH).

When [*meso*-¹³C-TPPFe(OCH₃)(OO^tBu)]⁻ is cooled between 218 and 193 K, the *meso*-carbon shift increases, as is expected for a low-spin ferriheme center possessing the *d_{xy}* electron configuration. However, below 193 K the direction reverses and the *meso*-carbon chemical shift decreases rapidly and becomes increasingly broader (Figure 7). The temperature dependence of the *meso*-carbon chemical shift, shown by • in Figure 8, was fitted to different models. To consider the possibility of a thermally-accessible excited state, the following equation for the contact shift was used [16,45]:

$$\delta_n^{\text{con}} = (F/T)\{W_1C_{n1}^2 + W_2C_{n2}^2e^{-\Delta E/kT}\}/\{W_1 + W_2e^{-\Delta E/kT}\} \quad (5)$$

where δ_n^{con} is the contact shift of the *meso*-carbon, F is the Curie factor that relates the contact shift to the orbital coefficients, T is the absolute temperature, W₁ and W₂ are the weighting factors for the ground and excited state orbitals, respectively (equal in this case because both have spin S = 1/2), C_{n1} and C_{n2} are the orbital coefficients for position n in the ground (1) and excited (2) states, respectively, ΔE is the energy separation between ground and excited states, and k is the Boltzmann constant. For the present case, since the direction of shift is opposite for the *d_{xy}* and *d_π* electronic states of low-spin Fe(III) (Figure 8a and b, respectively), the carbon orbital coefficients are obviously very different—of opposite sign, in fact. Thus, the coefficients C_{n1}² and C_{n2}² in Equation (5)

must include the product of the spin densities at the *meso* position in each state and the sensitivity of the spin density to the various orbital contributions. Based on the ratio of the isotropic hfi constants of *meso*-¹³C in d_{xy} and d_{π} configurations estimated above from ¹³C ENDOR spectra and from spin polarization considerations [42,48], we can take $C_{n2}^2/C_{n1}^2 \sim -10$, with C_{n1}^2 being negative.

Fits of the temperature dependence of the ¹³C isotropic shifts to Equation (5), first of all for the two “pure” complexes, [*meso*-¹³C-TPPFe(^tBuNC)₂]⁺ (d_{xy}) (○ in Figure 8) and [TPPFe(ImH)₂]⁺ (d_{π}) (▼ in Figure 8), show that each has a thermally-accessible excited state of the opposite electron configuration, with the energy between ground and excited state, $\Delta E \sim 97$ and 417 cm^{-1} , respectively. Thus, both of the ¹³C isotropic shift lines of the “pure” complexes in Figure 8 are slightly curved, with that for the d_{xy} electron configuration (**a**) being more curved than that for the d_{π} electron configuration (**b**). The average of the isotropic shifts of the two “pure” electron configurations is shown in Figure 8 by plot (**e**). Plot (**e**) corresponds not only to the simple average of the chemical shifts for the two “pure” electron configurations, but also that calculated from Equation (5) for $\Delta E \sim 50 \text{ cm}^{-1}$. Not only the strict average (**e**) of the two “pure” electron configurations, but also the calculated temperature dependence based upon a variety of ΔE values, including 20 cm^{-1} (**d**), 100 cm^{-1} (**f**), 150 cm^{-1} (**g**), 200 cm^{-1} (**h**), 300 cm^{-1} (**i**), and a very large $\Delta E = 520 \text{ cm}^{-1}$ (**j**) as possible values for the temperature dependence of [*meso*-¹³C-TPPFe(OCH₃)(OO^tBu)]⁻ are shown. All lines (**d**) - (**j**) were calculated from Equation (5) using the ratio $C_{n2}^2/C_{n1}^2 = -10$, as discussed above. The markedly different behavior of the experimental *meso*-carbon chemical shift (● in Figure 8) and those expected for a thermally-accessible excited state clearly demonstrates that the

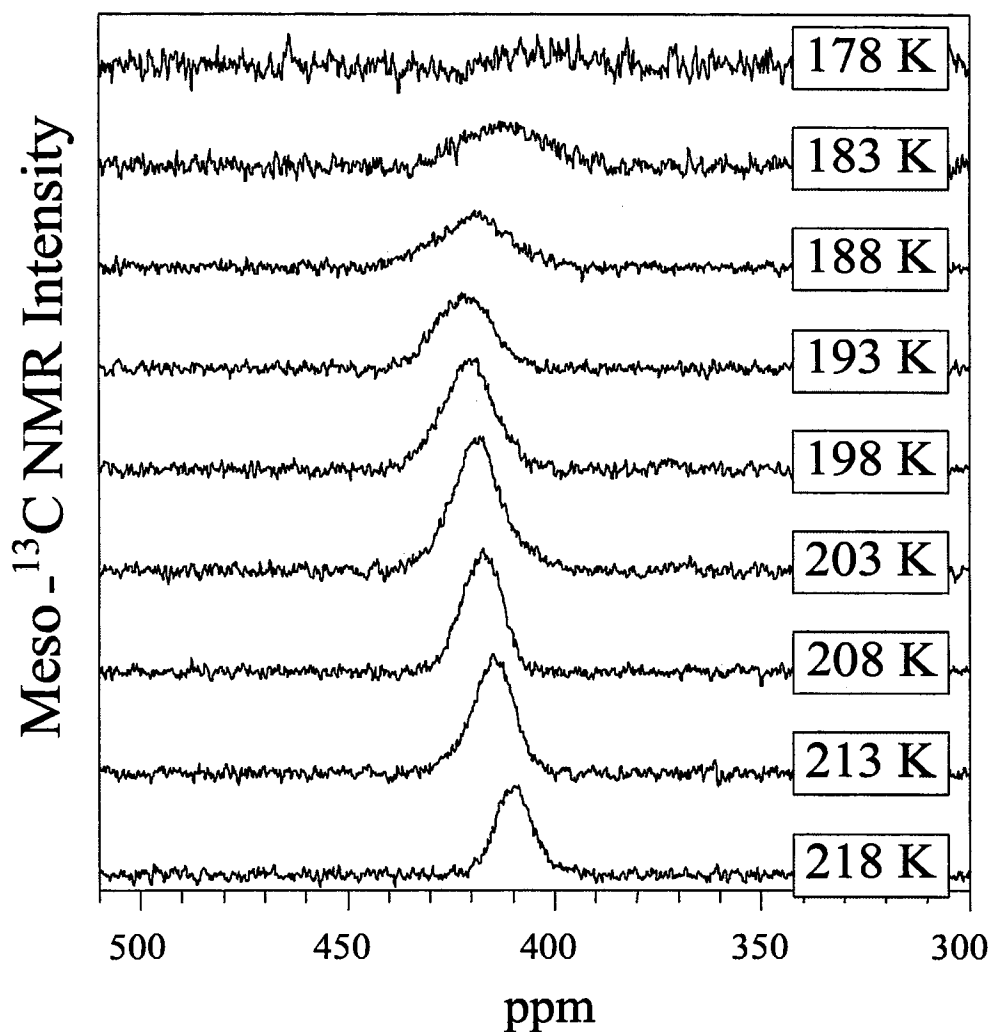


Figure 7. ^{13}C NMR spectra of $[\textit{meso}\text{-}^{13}\text{C}\text{-TPPFe}(\text{OCH}_3)(\text{OO}^t\text{Bu})]^-$, obtained at different temperatures (listed at the right side of the Figure), over 16 k data points, with a spectral width of 8.6 kHz, 90 ms acquisition time, 40 ms relaxation delay and 40,000 scans.

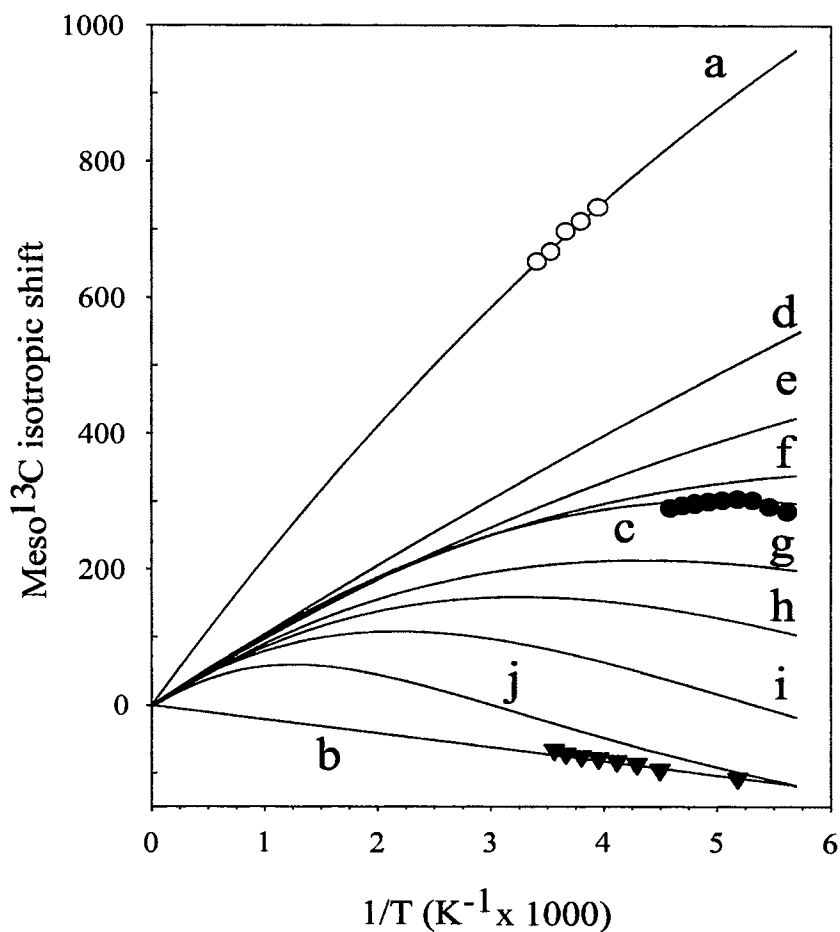


Figure 8. Temperature dependence of the *meso*-¹³C isotropic shift ($\delta_{\text{iso}} = \text{chemical shift} - \delta_{\text{dia}}$ (120 ppm [42])) for several complexes (as indicated in the Figure), with fits for (a) a “pure” d_{xy} electron configuration; (b) a “pure” d_{π} electron configuration; (c) a chemical equilibrium between the two, data points (\bullet) for the $[\text{meso-}^{13}\text{C-TPPFe}(\text{OCH}_3)(\text{OO}^t\text{Bu})]^-$ complex; and a thermally-accessible excited state, either (d) 20 cm^{-1} , (e) $\sim 50 \text{ cm}^{-1}$, (f) 100 cm^{-1} , (g) 150 cm^{-1} , (h) 200 cm^{-1} , (i) 300 cm^{-1} , or (j) 520 cm^{-1} above the ground state. In plots (a)-(j), the diamagnetic chemical shift of the *meso*-¹³C was taken as 120 ppm, as obtained experimentally by Goff for $[\text{TPPCo}(\text{N-MeIm})_2]^+$ [40].

temperature dependence of [*meso*-¹³C-TPPFe(OCH₃)-(OO^tBu)]⁻ is not that expected for a system having a thermally-accessible excited state. In particular, the isotropic shifts reach a maximum at a particular value of inverse temperature, and then decrease. The maximum isotropic shift is reached at a relatively low temperature, 193 K, unlike that for any possible value of ΔE, for which only those cases having ΔE = 150 cm⁻¹ or greater reach a very gentle maximum isotropic shift before decreasing, and the temperatures at which these maxima are reached are all greater than 193 K. However, the approximate similarity of the experimental data points for this complex to the calculated behavior if there were a thermally-accessible excited state with ΔE = ca.100 cm⁻¹ suggests that it is highly likely that these two electron configurations have a very small difference in energy. In fact, it was not possible to fit the experimental temperature dependence of [*meso*-¹³C-TPPFe(OCH₃)(OO^tBu)]⁻ without also considering the existence of a thermodynamic equilibrium that shifts in favor of the *d_{xy}* electron configuration as the temperature is raised. As a first estimation of the equilibrium constants for such a process, the *meso*-¹³C chemical shifts of this complex were compared to those of complexes with “pure” electron configurations, [TPPFe(ImH)₂]⁺ for the *d_π*, and [TPPFe(^tBuNC)₂]⁺ for the *d_{xy}* electron configuration. It can be readily shown that for the ring conformation interconversion,



$$K_{eq} = |(\delta(\text{pure } d_{\pi}) - \delta(\text{peroxo})) / (\delta(\text{pure } d_{xy}) - \delta(\text{peroxo}))| \quad (7)$$

Hence, K_{eq} can be easily calculated, and then a van't Hoff plot ($\log K_{eq}$ vs. $1/T$) constructed to estimate the ΔH and ΔS for this interconversion. Values of $\Delta H \sim +2.53 \pm 0.5$ kJ/mol and $\Delta S \sim +12 \pm 4$ J/mol K are obtained from the best slope and intercept of this plot. These values can then be used in an expression similar to that of Equation (5), but appropriate for a thermodynamic equilibrium, with enthalpy ΔH and entropy ΔS , to calculate the contact shift for the *meso*-carbon of the alkyl peroxide complex as a function of temperature:

$$\delta_n^{\text{con}} = (F/T) \{ C_{n1}^2 + C_{n2}^2 e^{-(\Delta H - T\Delta S)/RT} \} / \{ 1 + e^{-(\Delta H - T\Delta S)/RT} \} \quad (8)$$

Using the same values of C_{n1}^2 and C_{n2}^2 , and the estimated values of $\Delta H \sim +2.53$ kJ/mol and $\Delta S \sim +12$ J/mol K, plot (c) in Figure 8 is obtained. This plot more closely follows the chemical shift dependence of the experimental data points than do the plots obtained from the assumption of a thermally-accessible excited state using any value of ΔE between ground and excited state (Eq. (5), in that the curve reaches a maximum at the point that the experimental data reach a maximum, and then decreases, albeit at a less rapid rate than do the experimental data (see below).

Although both metal- and ligand-centered dipolar shifts are also expected to contribute to the isotropic shifts [42] of the low-spin Fe(III) complexes of this study, their contributions are much smaller than those of the contact shifts, and they likely mirror those of the contact shifts in these complexes in solution where the ligands within each complex ion, as well as the complex ions themselves, are rotating rapidly. Thus, it is felt that within the accuracy of the approximate calculations for lines (c) - (j) of Figure 8, the

dipolar shift contributions will not change the overall picture. Therefore, the results summarized in Figure 8 are consistent with the fact that the temperature dependence of the chemical shift obtained from [*meso*-¹³C-TPPFe(OCH₃)(OO^tBu)]⁻ results from a chemical equilibrium between planar (d_{π}) and ruffled (d_{xy}) conformations, for which the energy of the two electronic configurations is very nearly the same, but there is a thermodynamic equilibrium between the planar and ruffled ring conformations. The small values of both ΔH and ΔS are consistent with such an equilibrium between species that differ in ring conformation.

Both the extreme broadening and the stronger than predicted decrease in chemical shift at the lowest temperatures accessible in the solvent (188 – 178 K, last three points of line (c) in Figure 8) suggest an approach to the intermediate exchange regime. If this is the case, then at considerably lower temperatures, if the solvent did not freeze, the planar and ruffled conformers would be in slow exchange with respect to the NMR time scale, and two *meso*-carbon signals, one from each complex, would be observed. One signal would approach the chemical shift of the planar d_{π} complex and would become more intense, while the other signal would approach the chemical shift of the ruffled d_{xy} complex and become less intense, until it disappeared. Hence, the temperature dependence of the *meso*-carbon chemical shift (● in Figure 8) does not contradict the fact that at 8 K the pulsed ENDOR results (Figure 4) clearly indicate a d_{π} electron configuration. Thus, if the evidence gathered by electronic and magnetic spectroscopy is taken together, it can be concluded that at very low temperatures the electron configuration of [TPPFe(OCH₃)(OO^tBu)]⁻ is indeed d_{π} , but that the d_{xy} configuration becomes highly favored at ambient temperatures *via* a chemical equilibrium. Over the

range of temperatures of the NMR measurements, both electronic states are present and rapidly interconverting, and at physiologically relevant temperatures the d_{xy} electron configuration is expected to be strongly favored ($\Delta G_{310} = -1.19$ kJ/mol, $K_{eq} \sim 6.9$).

e) Magnetic resonance spectroscopy of [TPPFe(OCH₃)₂]⁻ and [TPPFe(OO^tBu)₂]⁻.

The EPR spectra of [TPPFe(OCH₃)₂]⁻ and [TPPFe(OO^tBu)₂]⁻ also display compressed g anisotropy ($\Sigma g^2 \sim 14$), as shown in Figure 3. This observation raised the possibility that the bis-methoxide and bis-alkyl peroxide complexes of TPPFe(III) might have d_{xy} electron configurations. Hence, both complexes were also studied by pulsed ENDOR and ¹³C NMR spectroscopy. The pulsed ENDOR results show that the hyperfine splittings in the spectra obtained from [*meso*-¹³C-TPPFe(OCH₃)₂]⁻ and [*meso*-¹³C-TPPFe(OO^tBu)₂]⁻ are very similar to those of [TPPFe(OCH₃)(OO^tBu)]⁻ and [TPPFe(N-MeIm)₂]⁺ (d_{π}) in Figure 4, and also do not exceed 1.7 MHz. The magnitude of these hyperfine splittings is thus typical of complexes having their unpaired electron residing in a d_{π} orbital, as discussed above for [TPPFe(OCH₃)(OO^tBu)]⁻. It is therefore evident that both [TPPFe(OCH₃)₂]⁻ and [TPPFe(OO^tBu)₂]⁻ have $(d_{xy})^2(d_{xz},d_{yz})^3$ electron configurations at 8 K. ¹³C NMR experiments performed with [*meso*-¹³C-TPPFe(OCH₃)₂]⁻ and [*meso*-¹³C-TPPFe(OO^tBu)₂]⁻ at 193 K, however, indicate that these compounds have a largely d_{xy} electron configuration at this temperature, as shown in Figure 9.

The *meso*-carbon chemical shifts obtained for [*meso*-¹³C-TPPFe(OCH₃)₂]⁻ and [*meso*-¹³C-TPPFe(OO^tBu)₂]⁻ at 193 K are 361 and 444 ppm, respectively (arrows in Figure 9). The magnitude of these chemical shifts is again indicative of low-spin

ferriheme complexes possessing an electron configuration in which the d_{xy} and d_{π} states are essentially isoenergetic. Both complexes were also studied by ^{13}C NMR and electronic absorption spectroscopy as a function of temperature. The electronic absorption spectrum of a solution of $[\text{TPPFe}(\text{OCH}_3)_2]^-$ was found to be temperature independent between 273 and 183 K; temperatures above 273 K were not investigated. In contrast, the electronic absorption spectrum of a solution of $[\text{TPPFe}(\text{OO}^t\text{Bu})_2]^-$ loses intensity relatively rapidly above 195 K. Consequently, ^{13}C NMR spectra for $[\text{meso-}^{13}\text{C-TPPFe}(\text{OO}^t\text{Bu})_2]^-$ were obtained only between 203 and 178 K, whereas $[\text{meso-}^{13}\text{C-TPPFe}(\text{OCH}_3)_2]^-$ was investigated between 273 and 178 K. The results of these experiments, together with those obtained from the variable temperature experiments performed with $[\text{meso-}^{13}\text{C-TPPFe}(\text{OCH}_3)(\text{OO}^t\text{Bu})]^-$, are all shown in Figure 9. It is interesting that the chemical shift of $[\text{meso-}^{13}\text{C-TPPFe}(\text{OCH}_3)_2]^-$ displays a similar trend to that observed for $[\text{meso-}^{13}\text{C-TPPFe}(\text{OCH}_3)(\text{OO}^t\text{Bu})]^-$ as the temperature is changed, except that the temperature at which the direction of the chemical shift reverses and begins to move toward a value expected for a d_{π} electron configuration is higher. The variable temperature behavior of the *meso*-carbon chemical shift of $[\text{meso-}^{13}\text{C-TPPFe}(\text{OCH}_3)_2]^-$ is therefore in agreement with an equilibrium between a d_{xy} (ruffled), and a d_{π} (planar) conformation. Using equation (6), values of $\Delta H = 4.54$ kJ/mol and $\Delta S = 21$ J/mol K were estimated for this complex, yielding $\Delta G_{310} = -1.97$ kJ/mol and $K_{eq} = 24.4$. As the temperature is lowered the equilibrium favors the planar conformer; hence at 8 K pulsed ENDOR clearly shows a d_{π} electron configuration.

The temperature dependence of the *meso*-carbon in $[\text{meso-}^{13}\text{C-TPPFe}(\text{OO}^t\text{Bu})_2]^-$ (■ in Figure 9) indicates that in the temperature range accessible experimentally, the

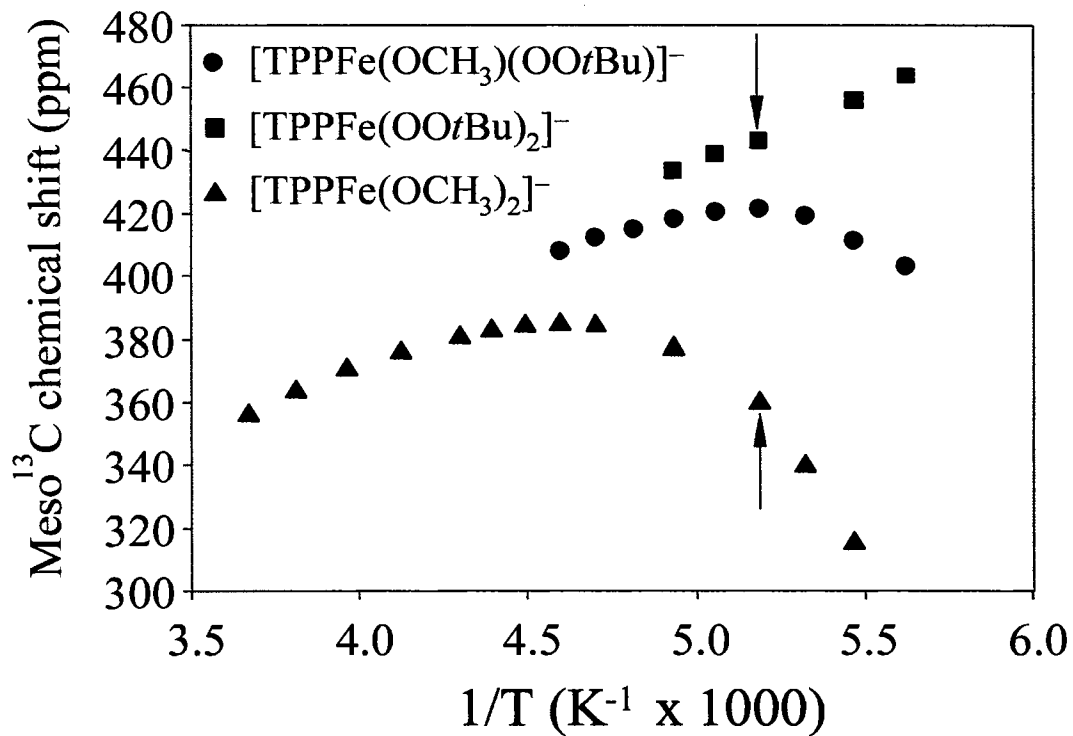


Figure 9. Variable temperature *meso*-¹³C NMR spectroscopic data obtained for [TPPFe(OCH₃)₂]⁻, [TPPFe(OCH₃)(OO^tBu)]⁻, and [TPPFe(OO^tBu)₂]⁻, plotted as experimental chemical shifts. The arrows point to the data points obtained at 193 K (see text).

meso-carbon chemical shift moves to higher frequency as the temperature is decreased. This is what is expected for a low-spin ferriheme complex with a d_{xy} electron configuration. However, since pulsed ENDOR indicates that the electron configuration of this complex at 8 K is d_{π} , it is anticipated that the direction of the *meso*-carbon chemical shift will reverse at a lower (inaccessible) temperature. Hence, the plots in Figure 9 are qualitatively indicative of the relative position of the equilibrium between the d_{xy} (ruffled) and d_{π} (planar) conformations. It is also evident from Figure 9 that as the number of alkyl peroxide axial ligands is increased from zero to two, the relative concentration of the d_{xy} conformer is larger at the lowest temperatures accessible experimentally. This indicates that the alkyl peroxide ligand is more efficient in stabilizing the d_{xy} conformer than is the alkoxide ligand. It is therefore likely that other ferriheme complexes with EPR spectra similar to those shown in Figure 3, including [TPPFe(Im)(OO^tBu)]⁻ [19] and [TPPFe(N-MeIm)(OO^tBu)] [49] will also display variable temperature *meso*-carbon chemical shifts similar to those observed for the alkoxide and alkoxide-alkyl peroxide complexes of TPPFe^{III} reported here, yet different in detail because of different ligand field strength of the unique axial ligand. This possibility is currently under investigation in our laboratories.

Relevance to enzyme systems and concluding remarks.

In addition to the complexes included as part of this study, the EPR spectrum of the Fe^{III}-OOH complex of myoglobin ($\Sigma g^2 = 14.09$) [11,24,50] and that of the Fe^{III}-OOH complex of cytochrome P450_{cam} ($\Sigma g^2 = 13.75$) [23,24] display compressed g anisotropy and very similar g -values to those reported for the corresponding alkyl peroxide complexes. These molecules have in common a hydroperoxide or alkyl peroxide axial

ligand. Thus it seems obvious that the peroxide ligand induces the reduced anisotropy observed in the EPR spectra. Compressed g anisotropy *could* be correlated to a $(d_{xz}, d_{yz})^4(d_{xy})^1$ electronic configuration in those cases, or, as in the model heme systems studied herein, the electron configuration at the very low temperatures utilized to carry out EPR spectroscopic studies is $(d_{xy})^2(d_{xz}, d_{yz})^3$, with the possibility that some or all of these ferriheme centers coordinated by a peroxide ligand have a $(d_{xz}, d_{yz})^4(d_{xy})^1$ electron configuration at ambient temperatures. This has important implications for the mechanism of action of the enzymes heme oxygenase, cytochromes P450 and the peroxidases, since the formation of an obligatory $\text{Fe}^{\text{III}}\text{-OOH}$ intermediate, possessing large electron and spin density at the *meso* positions can be expected to prime a protein or enzyme to oxygenate its heme. Therefore, the ability of a protein to form the important “ $\text{Fe}(\text{V})$ ” and ferryl ($\text{Fe}^{\text{IV}}=\text{O}$) intermediates of cytochromes P450, the peroxidases [8], as well as the α_3 heme of cytochrome oxidase [9], or to oxygenate its own heme, as in heme oxygenase [1-3], would be modulated by the electronic properties of the protein-provided heme ligand, as well as the heme-polypeptide interactions that in the case of cytochromes P450 and the peroxidases presumably retard the attack of the bound hydroperoxide on the *meso*-carbons, and accelerate the decay toward $\text{Fe}^{\text{IV}}=\text{O}$. Having the unpaired electron of low-spin $\text{Fe}(\text{III})$ in the d_{xy} orbital causes the porphyrin ring to ruffle, hence positioning the *meso*-carbons as much as 0.5 to 0.6 Å above or below the porphyrin mean plane [13-16], and also creates large spin density at the *meso*-carbons. The end result is that either the α - and γ -, or the β - and δ -*meso* carbons are placed closer to the terminal OH of the $\text{Fe}^{\text{III}}\text{-OOH}$ moiety at any given moment, thus facilitating their attack by the peroxide ligand. Whether the α - and γ -, or the β - and δ -*meso* carbons are placed closer to the terminal OH of $\text{Fe}^{\text{III}}\text{-OOH}$ at the moment of attack

is likely to be dictated by steric interactions between the porphyrin ring and the polypeptide. Moreover, since heme ruffling positions pairs of *meso*-carbons (e.g. α - and γ -) closer to the reactive Fe^{III}-OOH, if only the α -meso carbon is attacked, as is observed in HO, this implies that the other *meso* carbons must be sterically protected. Hence, the regioselectivity of heme oxygenation may be controlled by electronic, as well as steric effects.

It is interesting that the model complexes used in this study suggest a dynamic equilibrium between a ruffled (d_{xy}) and a planar (d_{π}) conformation. Over the range of temperatures of the NMR measurements, both electronic states are present and rapidly interconverting, and at physiologically relevant temperatures the d_{xy} electron configuration is favored ($\Delta G_{310} = -1.19$ kJ/mol; $K_{eq} = 6.9$). In fact, it may be that this dynamic equilibrium, which in an enzyme may be significantly affected by heme-polypeptide interactions, is an important modulatory mechanism that helps an enzyme channel the Fe^{III}-OOH intermediate toward the formation of a ferryl intermediate in some cases, or toward heme oxygenation in others. In this context, it is interesting to point out that the crystal structures of human [51] and bacterial [52] heme oxygenase strongly suggest that the flexibility of the distal pocket, provided by conserved glycine residues 139 and 143, is an important and conserved motif in these different heme oxygenases. It is therefore tempting to speculate that the flexibility of the distal pocket in heme oxygenase functions to facilitate the dynamic equilibrium between ruffled (d_{xy}) and planar (d_{π}) conformers, thus channeling the reactivity of the Fe^{III}-OOH intermediate toward heme oxygenation, rather than ferryl formation. In fact, when Gly-139 of human HO-1 is mutated for a residue with a bulkier side chain, the resultant enzyme displays

peroxidase-type reactivity [53], and when similar mutations are introduced at position 143, the mutant enzymes lose their oxygen activation activity [54].

Another important modulatory mechanism amongst the enzymes that react through the $\text{Fe}^{\text{III}}\text{-OOH}$ intermediate is that provided by the proximal heme ligand, a histidine in the cases of heme oxygenase, the peroxidases, and cytochrome *c* oxidase, but a cysteinate in the cases of the cytochromes P450 and chloroperoxidase. It is thus possible that in addition to the dynamic equilibrium discussed above, an additional modulatory mechanism amongst the enzymes that react through the $\text{Fe}^{\text{III}}\text{-OOH}$ intermediate is provided by the chemical nature of the proximal ligand, including histidine imidazole protonation state. For example, it is thought that in cytochrome P450, the proximal cysteinate ligand destabilizes the O-O bond through strong electron donation, in conjunction with electron withdrawal from a hydrogen bond network in the distal site of the heme binding domain [55]. In peroxidases, the same “push-pull” mechanism is thought to be operative because the proximal His ligand is ionized or strongly hydrogen bonded [55]. It has been previously proposed that in HO, the lack of effectiveness of the neutral His ligand as an electron donor, may actually lower the rate of O-O cleavage, hence channeling the reaction toward heme oxygenation rather than ferryl complex formation [10,56]. It is therefore important to investigate the effect that the protonation state of the proximal ligand might have on the dynamic equilibrium between planar (d_{π}) and ruffled (d_{xy}) conformers, and such studies are in progress in our laboratories.

If the $\text{Fe}^{\text{III}}\text{-OOH}$ complex in HO indeed has the unpaired electron in the d_{xy} orbital, then large spin density is expected to be present at the *meso*-carbons [13-16]. A limiting resonance structure for such a species may be represented as $\text{Fe}^{\text{II}}(\text{por}^{\cdot-})$, which

raises the possibility of involvement of a radical mechanism for this enzyme. A radical mechanism was considered previously, but discarded because the then proposed radical ($\bullet\text{OH}$) was thought to be too indiscriminate to lead to well-controlled reactivity [10]. However, if the limiting structure $\text{Fe}^{\text{II}}(\text{por}^{\cdot-})$ is considered, then attack of $\bullet\text{OH}$ would produce $\text{Fe}^{\text{II}}(\text{O}^{\cdot-})(\text{por}-(\text{H})(\text{OH}))$, which would rapidly rearrange its Fe-O electron configuration, lose the proton from the attacked *meso* position to re-aromatize the porphyrin ring, and reprotonate the $\text{Fe}^{\text{III}}-\text{O}^{2-}$ to yield the resting Fe^{III} aquo form of the enzyme. It is therefore evident that if the $\text{Fe}^{\text{III}}-\text{OOH}$ intermediate of heme oxygenase does indeed have its unpaired electron residing in the d_{xy} orbital, the electronic structure of the intermediate, which, as we have shown with the model ferriheme complexes, is accessible *via* a dynamic equilibrium that is influenced by the proximal ligand and the surrounding polypeptide, becomes a novel mechanism by which this obligatory intermediate is channeled to favor either heme oxygenation or monooxygenation activity.

It is also noteworthy that bis-pyridine complexes of model *meso*-hydroxyhemes such as OEPO, produced by coupled oxidation of OEPFe(III), [14,16,5759] have more compressed EPR spectra than do their OEPFe(III) counterparts. These observations suggest that that *meso*-hydroxyheme complexes may favor the d_{xy} electron configuration and its limiting $\text{Fe}^{\text{II}}(\text{OEPO})$ radical resonance structure, and thus facilitate the next step in the HO reaction, again by a radical mechanism. Magnetic resonance and chemical reactivity investigations of the alkylperoxide and hydroperoxide complexes of model *meso*-hydroxyhemes and several heme proteins are in progress in our laboratories.

Acknowledgements: The EPR, ENDOR and ^{13}C Chemical shift modeling studies were conducted in collaboration with Dr. Andrei V. Astashkin, Dr. Arnold M Raitsimring, Dr. Tatjana Kh. Shokireva and Dr. F. Ann Walker from the University of Arizona.

References

- [1] Ortiz de Montellano, P. R. *Acc. Chem. Res.* **1998**, *31*, 543-549.
- [2] Ortiz de Montellano, P. R. *Curr. Opin. Chem. Biol.* **2000**, *4*, 221-227.
- [3] Ortiz de Montellano, P. R. and Wilks, A. *Adv. Inorg. Chem.* **2000**, *51*, 359-407.
- [4] Stupfel, M.; Bouley, G. *Ann. N.Y. Acad. Sci.* 1970, *174*, 342.
- [5] Morita, T. and Kourembanas, S. *J. Clin. Invest.* **1995**, *96*, 2676-2682.
- [6] Einstein, R. S.; Garcia-Mayo, D.; Pettingell, W.; Munroe, H. N. *Proc. Natl. Acad. Sci. U.S.A.* **1991**, *88*, 688-692.
- [7] Stocker, R.; Yamamoto, Y.; McDonagh, A. F.; Glazer, A. N.; Ames, B. N. *Science* **1987**, *235*, 1043-1046.
- [8] Loew, G. H. *Chem. Rev.* **2000**, *100*, 407-419.
- [9] Sucheta, A.; Georgiadis, K. E.; Einarsdottir, O. *Biochemistry* **1997**, *36*, 554-565.
- [10] Wilks, A.; Torpey, J.; Ortiz de Montellano, P. R. *J. Biol. Chem.* **1994**, *269*, 29553-29556.
- [11] Davydov, R. M.; Yoshida, T.; Ikeda-Saito, M.; Hoffman, B. M. *J. Am. Chem. Soc.* **1999**, *121*, 10656-10657.
- [12] Safo, M. K.; Walker, F. A.; Raitsimring, A. M.; Walters, W. P.; Dolata, D. P.; Debrunner, P. G.; Scheidt, W. R. *J. Am. Chem. Soc.* **1994**, *116*, 7760-7770.
- [13] Walker, F. A.; Nasri, H.; Torowska-Tyrk, I.; Mohanrao, K.; Watson, C. T.; Shkhirev, N. V.; Debrunner, P. G.; Scheidt, W. R. *J. Am. Chem. Soc.* **1996**, *118*, 12109-12118.
- [14] Walker, F. A. *Coord. Chem. Rev.* **1999**, *185-186*, 471-534.
- [15] Simonneaux, G.; Schünemann, V.; Morice, C.; Carel, L.; Toupet, L.; Winkler, H.; Trautwein, A. X.; Walker, F. A. *J. Am. Chem. Soc.* **2000**, *122*, 4366-4377.

- [16] Walker, F. A. *Proton NMR and EPR Spectroscopy of Paramagnetic Metalloporphyrins*, in *The Porphyrin Handbook*, Kadish, K. M.; Smith, K.M.; Guillard, R., Eds.; Academic Press: San Diego, 2000; pp. 81-183.
- [17] Tajima, K.; Ishizu, K.; Sakurai, H.; Nishiguchi-Ohya, H. *Biochem. Biophys. Res. Commun.* **1986**, *135*, 972-978.
- [18] Tajima, K.; Jinno, J.; Ishizu, K.; Sakurai, H.; Ohya-Nishiguchi, H. *Inorg. Chem.* **1989**, *28*, 709-715.
- [19] Tajima, K.; Tada, K.; Jinno, J.; Edo, T.; Mano, H.; Azuma, N.; Makino, K. *Inorg. Chim. Acta* **1997**, *254*, 29-35.
- [20] Tajima, K.; Oka, S.; Edo, T.; Miyake, S.; Mano, H.; Mukai, K.; Sakurai, H.; Ishizu, K. *J. Chem. Soc., Chem. Commun.* **1995**, 1507-1508.
- [21] Tajima, K. *Inorg. Chim. Acta* **1990**, *169*, 211-219.
- 22 Jinno, J.; Shigematsu, M.; Tajima, K.; Sakurai, H.; Ohya-Nishiguchi, H.; Ishizu, K. *Biochem. Biophys. Res. Commun.* **1991**, *176*, 675-681.
- [23] Tajima, K.; Edo, T.; Ishizu, K.; Imaoka, S.; Funae, Y.; Oka, S.; Sakurai, H. *Biochem. Biophys. Res. Commun.* **1993**, *191*, 157-164.
- [24] Davydov, R.; Macdonald, I. D. G.; Makris, T. M.; Sligar, S. G.; Hoffman, B. M. *J. Am. Chem. Soc.* **1999**, *121*, 10654-10655.
- [25] Nasset, M. J. M.; Cai, S.; Shokhireva, T. Kh.; Shokhirev, N. V.; Jacobson, S. E.; Jayaraj, K.; Gold, A.; Walker, F. A. *Inorg. Chem.* **2000**, *39*, 532-540.
- [26] Borbat, P. P.; Raitsimring, A. M. *Abstracts of 36th Rocky Mountain Conference on Analytical Chemistry*; Denver, CO, July 31 – August 5, 1994; p. 94.
- [27] Astashkin, A. V.; Mader Cosper, M.; Raitsimring, A. M.; Enemark, J. H. *Inorg. Chem.* **2000**, *39*, 4989-4992.

- [28] Mims, W. B. *Proc. Roy. Soc. London* **1965**, 283, 482-457.
- [29] Davies, E. R. *Phys. Lett. A* **1974**, 47, 1-2.
- [30] Grupp, A.; Mehring, M. "Pulsed ENDOR Spectroscopy in Solids," in: *Modern Pulsed and Continuous Wave Electron Spin Resonance*; Kevan, L.; Bowman, M., Eds.; Wiley: New York, 1990, pp.195-229.
- [31] Thomann, H.; Bernardo, M. "Pulsed Electron Nuclear Multiple Resonance Spectroscopic Methods for Metalloproteins and Metalloenzymes," in *Methods in Enzymology*; Riordan, J. F.; Vallee, B. L., Eds.; Academic Press: San Diego, 1993; vol. 227, pp. 118-189.
- [32] Cheesman, M. R.; Walker, F. A. *J. Am. Chem. Soc.* **1996**, 118, 7373-7380.
- [33] Carrington, A.; McLachlan, A.D. *Introduction to Magnetic Resonance with Applications to Chemistry and Chemical Physics*; Harper and Row: New York, 1967.
- [34] Landolt-Börnstein, In *Numerical Data and Functional Relationships in Science and Technology, New Series*; Madelung, O.; Fisher, H., Eds.; Chs. 3, 4; vol. II/17b,c; Springer-Verlag: Berlin, 1987.
- [35] Ghosh, A.; Gonzalez, E.; Vangberg, T. *J. Phys. Chem. B* **1999**, 103, 1363-1367.
- [36] Astashkin, A. V.; Raitsimring, A. M.; Kennedy, A. R.; Shokhireva, T. Kh.; Walker, F. A. *J. Phys. Chem. A* **2001**, 105, 0000-0000.
- [37] Doan, P. E.; Nelson, M. J.; Jin, H.; Hoffman, B. M. *J. Am. Chem. Soc.* **1996**, 118, 7014-7015.
- [38] Astashkin, A. V.; Raitsimring, A. M.; Walker, F. A. *J. Am. Chem. Soc.* **2001**, 123, 1905-1913.
- [39] Scholes, C. P.; Falkowski, K. M.; Chen, S.; Bank, J. *J. Am. Chem. Soc.* **1986**, 108, 1660-1671.

- [40] Zhidomirov, G. I.; Schastnev, P. V.; Chuvylkin, N. D. *Quantum-Chemical Calculations of Magnetic-Resonance Parameters*; Nauka: Novosibirsk, 1978.
- [41] Ikeue, T.; Ohgo, Y.; Takashi, S.; Nakamura, M.; Fujii, H.; Yokoyama, M. *J. Am. Chem. Soc.* **2000**, *122*, 4068-4076.
- [42] Goff, H. M. *J. Am. Chem. Soc.* **1981**, *103*, 3714-3722.
- [43] Ikewue, T.; Ohgo, Y.; Saitoh, T.; Yamaguchi, T.; Nakamura, M. *Inorg. Chem.* **2001**, *40*, 3423-3434.
- [44] The signal broadens and disappears below 258 K, probably because of slowing of the ruffled porphyrinate inversion kinetics.
- [45] Shokhirev, N. V.; Walker, F. A. *J. Phys. Chem.* **1995**, *99*, 17795-17804.
- [46] Mispelter, J.; Momenteau, M.; Lhoste, J. M. *Chem. Comm.* **1979**, 808-810.
- [47] Goff, H. M.; Shimomura, E. T.; Phillippi, M. A. *Inorg. Chem.* **1983**, *22*, 66-71.
- [48] Karplus, M.; Fraenkel, G. K. *J. Chem. Phys.* **1961**, *35*, 1312-1323.
- [49] Rivera, M.; Caignan, G.; Astashkin, A. V.; Raitsimring, A. M.; Shokhireva, T. Kh.; Walker, F. A. Unpublished work.
- [50] Kappl, R.; Höhn Berlage, M.; Hüttermann, J.; Bartlett, N.; Symons, M. C. R. *Biochim. Biophys. Acta* **1985**, *827*, 327-343.
- [51] Schuller, D. J.; Wilks, A.; Ortiz de Montellano, P. R.; Poulos, T. L. *Nature Struct. Biol.* **1999**, *6*, 860-867.
- [52] Schuller, D. J.; Zhu, W.; Stojiljkovic, I.; Wilks, A.; Poulos, T. L. *Biochemistry* **2001**, *40*, 11552-11558.
- [53] Liu, Y.; Koenigs Lightning, L.; Huang, H.; Moënne-Loccoz, P.; Schuller, D. J.; Poulos, T. L.; Loehr, T. M.; Ortiz de Montellano, P. R. *J. Biol. Chem.* **2000**, *275*, 34501-34507.

- [54] Koenigs Lightning, L.; Huang, H.; Moënne-Loccoz, P.; Loehr, T. M.; Schuller, D. J.; Poulos, T. L.; Ortiz de Montellano, P. R. *J. Biol. Chem.* **2001**, *276*, 10612-10619.
- [55] Marnett, L. J.; Kennedy, T. A. In *Cytochrome P450: Structure, Mechanism, and Biochemistry*; Ed. 2; Ortiz de Montellano, P. R., Ed.; Plenum Press: New York, 1995; pp. 49-80.
- [56] Wilks, A.; Ortiz de Montellano, P. R. *J. Biol. Chem.* **1993**, *268*, 22357-22362.
- [57] Balch, A. L.; Latos-Grażyński, L.; Noll, B. C.; Szterenber, L.; Zovinka, E. P. *J. Am. Chem. Soc.* **1993**, *115*, 11846-11854.
- [58] Balch, A. L.; Latos-Grażyński, L.; St. Claire, T. N. *Inorg. Chem.* **1995**, *34*, 1395-1401.
- [59] Balch, A. L.; Koerner, R.; Latos-Grażyński, L.; Noll, B. C. *J. Am. Chem. Soc.* **1996**, *118*, 2760-2761.

Chapter IV

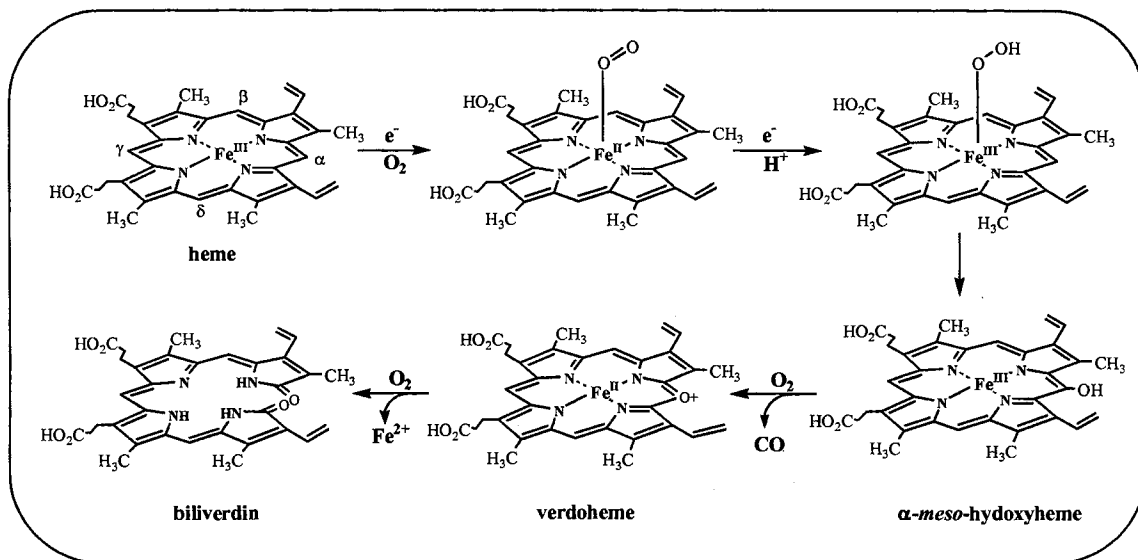
THE HYDROXIDE COMPLEX OF *PSEUDOMONAS AERUGINOSA* HEME OXYGENASE AS A MODEL OF THE LOW-SPIN IRON(III) HYDROPEROXIDE INTERMEDIATE IN HEME CATABOLISM: ¹³C NMR SPECTROSCOPIC STUDIES SUGGEST THE ACTIVE PARTICIPATION OF THE HEME IN MACROCYCLE HYDROXYLATION

Introduction

The enzyme heme oxygenase (HO) is intimately involved in the catabolism of heme. In this process HO catalyzes the electron- and dioxygen-dependent breakdown of heme to biliverdin, iron and carbon monoxide [1]. The catalytic cycle of HO (Scheme 1) starts when the ferric enzyme is reduced by NADPH cytochrome P450 reductase to its ferrous form, followed by the coordination of O₂, which leads to the formation of an oxyferrous complex (Fe^{II}-O₂). The latter accepts a second electron from the reductase and is thereby transformed into the ferric hydroperoxy (Fe^{III}-OOH) oxidizing species [2], which adds a hydroxyl group to the α -meso carbon to form α -mesohydroxyheme (Scheme 1) [3, 4]. Investigations of the reactivity of HO toward peroxides and alkyl peroxides led to the conclusion that heme hydroxylation does not proceed via the formation of a high-valence compound I-like species [3]. Rather, the terminal oxygen of the coordinated peroxide adds to a porphyrin meso carbon, which results in the formation of α -hydroxyheme. In fact, spectroscopic evidence supporting this conclusion was recently obtained by cryoreduction of the oxyferrous complex of HO to produce an

intermediate, identified by EPR spectroscopy to be the $\text{Fe}^{\text{III}}\text{-OOH}$ complex, which upon warming is converted into the α -hydroxyheme complex [5, 6]. The α -mesohydroxyheme complex of HO undergoes a subsequent O_2 -dependent elimination of the hydroxylated α -meso carbon as CO, with the simultaneous formation of verdoheme (Scheme 1). Verdoheme is subsequently oxidized to Fe^{III} -biliverdin, a reaction that is thought to require electrons and molecular oxygen.

It is noteworthy that the formation of an obligatory $\text{Fe}^{\text{III}}\text{-OOH}$ intermediate is shared by the catalytic mechanism of HO and that of monooxygenases (cyt P450) and peroxidases. However, the nature of the structure-function relationships that must be operative to accelerate the meso hydroxylation reaction that commits the enzyme to conduct heme degradation, relative to cleavage of the O-O bond that is typical of monooxygenation reactions, are not yet understood. Evidence gathered from X-ray diffraction and spectroscopic studies conducted with HO revealed a distal heme binding site that exhibits unique chemical properties relative to other heme containing enzymes. For instance: (i) The distal pocket of HO is devoid of a polar side chain that might stabilize a dioxygen ligand [7-9], as is typically the case in the peroxidases and globins. (ii) The distal helix almost grazes the heme and places the backbone atoms of Gly-139 and Gly-143 in human HO-1 in direct contact with the heme [7]. (iii) The distal pocket of heme oxygenase harbors a relatively rigid network of hydrogen bonded water molecules [10], which is believed to ensure adequate proton delivery to the distal O atom of the $\text{Fe}^{\text{II}}\text{-O}_2$ complex, in order to facilitate its reduction to the $\text{Fe}^{\text{III}}\text{-OOH}$ intermediate [6, 11].



Scheme 1: Heme oxygenase catalytic cycle

Magnetic resonance spectroscopic studies conducted with models of the Fe^{III}-OOH complex of HO allowed us to suggest that the heme in this enzyme is likely an active participant in its own hydroxylation [12]. Moreover, the findings from these studies led us to propose that the Fe^{III}-OOH intermediate exists as an equilibrium mixture consisting of a planar heme with a (d_{xy})²(d_{xz},d_{yz})³ electronic configuration (d_π hereafter) and a ruffled heme with a (d_{xz},d_{yz})⁴(d_{xy})¹ electron configuration [12] ((d_{xy})¹ hereafter). At the very low temperatures utilized to carry out the EPR spectroscopic studies the electron configuration is d_π, whereas at the more elevated temperatures used to conduct NMR spectroscopic studies the ruffled heme with the (d_{xy})¹ electronic configuration is favored [12]. These findings prompted us to suggest that ferriheme centers coordinated by a peroxide ligand are likely to have the (d_{xy})¹ electron configuration at ambient temperatures. Significant about the (d_{xy})¹ electronic configuration is the fact that Fe^{III}-porphyrinates possessing an unpaired electron in the d_{xy} orbital are significantly ruffled and place a relatively large amount of spin and electron density on the porphyrin meso carbons [13-16]. Thus, at ambient temperatures, the ruffled porphyrinate ring is expected to aid the attack of the terminal oxygen of the Fe^{III}-OOH intermediate on the meso carbon [12].

The crystal structures of mammalian [7] and bacterial [8] HO enzymes strongly suggest that the flexibility of the distal pocket imparted by conserved glycine residues 139 and 143 is an important and unique structural motif that characterizes these enzymes. Therefore, it is reasonable to hypothesize that upon coordination of a hydroperoxide ligand in the distal site of HO the heme molecule tends to acquire a distorted (i.e. ruffled) conformation, which is accompanied by a corresponding change in heme electronic

structure; the deformation of heme from planarity would be facilitated by the flexible nature of the heme pocket in heme oxygenase. Hence, the conformational flexibility of the heme binding site is also expected to contribute to priming the heme for active participation in its own hydroxylation. These arguments suggest that it is important to test whether the HO fold readily permits macrocycle deformations that bring about changes in electronic structure when a hydroperoxide ligand binds in the distal site. Our studies with models of the $\text{Fe}^{\text{III}}\text{-OOH}$ intermediate (see above) suggest that the equilibrium between planar and distorted porphyrins favor the latter at ambient temperatures; therefore, work aimed at studying the electronic structure of the $\text{Fe}^{\text{III}}\text{-OOH}$ complex of HO should be conducted near ambient temperatures. An obvious problem with this approach is the very high reactivity of this key intermediate at ambient temperatures. In order to circumvent this problem, and as an initial attempt to study the chemical nature of the elusive $\text{Fe}^{\text{III}}\text{-OOH}$ intermediate in HO, we have undertaken a study in which hydroxide was used as a model of the hydroperoxide ligand. As will be shown below, we find that the hydroxide complex of HO ($\text{Fe}^{\text{III}}\text{-OH}$) has properties that are distinct from the planar (d_{π}) hydroxide complexes characteristic of globins and peroxidases in that the heme in $\text{Fe}^{\text{III}}\text{-OH}$ acquires significant unusual electronic structures that strongly suggest nonplanar distortions.

Experimental Section

a) Protein preparation and reconstitution with ^{13}C -labeled heme.

Heme oxygenase from *Pseudomonas aeruginosa* (*pa*-HO) was expressed and purified as described previously [17, 18]. ^{13}C -Labeled δ -aminolevulinic acids (ALA)

were used as biosynthetic precursors for the preparation of protoheme IX (heme) according to previously described methodology [19, 20]. [5-¹³C]- δ -Aminolevulinic acid ([5-¹³C]-ALA) and [4-¹³C]-ALA were synthesized according to methodology described previously [21]. [5-¹³C]-ALA was used to prepare heme labeled at the meso (C_m) and α -pyrrole (C _{α}) carbons shown in Figure 5-A, and [4-¹³C]-ALA was utilized to prepare heme labeled at the C _{α} and β -pyrrole (C _{β}) carbons shown in Figure 5-B. Isotopically labeled heme is initially purified in its complex with rat liver outer membrane (OM) cytochrome b₅ [19, 20]. ¹³C-labeled heme was extracted from OM cytochrome b₅ as follows: While maintaining the temperature at 4 °C, 15 mL of pyridine was added to 2.5 mL of rat OM cytochrome b₅ (1 mM) dissolved in phosphate buffer (μ = 0.1, pH = 7.0). Slow addition of chloroform (10-15 mL) typically resulted in the precipitation of the polypeptide, while maintaining the pyridine hemochrome in the supernatant. The latter is separated from the precipitate by centrifugation, allowed to equilibrate at room temperature, and then dried over anhydrous MgSO₄. The desiccant was separated by filtration and the solution evaporated to dryness with the aid of a rotary evaporator. The solid is redissolved in 3-4 mL of dimethyl sulfoxide and the resultant solution was immediately used to reconstitute HO. To this end, a solution (20 mL) containing approximately 2 μ mol of *pa*-HO was titrated with the solution containing ¹³C-labeled heme until the ratio A₂₈₀/A_{Soret} no longer changed. The resultant solution was incubated at 4 °C overnight and subsequently purified using a Sephadex G-50 column (3 cm x 100 cm), previously equilibrated with phosphate buffer, μ = 0.10 and pH = 7.0.

b) Spectroscopic studies.

^1H and ^{13}C NMR spectra were acquired on a Varian Unity Inova spectrometer operating at frequencies of 598.611 and 150.532 MHz, respectively. ^1H spectra were referenced to the residual water peak at 4.8 ppm, and ^{13}C spectra were referenced to an external solution of dioxane (60% v/v in D_2O) at 66.66 ppm. ^1H spectra from high spin HO were acquired with presaturation of the residual water peak over 137 kHz, with a 125 ms acquisition time, a 25 ms relaxation delay and 2048 scans. Spectra from low spin HO were also acquired with presaturation of the residual water peak, with an acquisition time of 250 ms, and a 25 ms relaxation delay, over a spectral width of 30 kHz. ^{13}C NMR spectra were typically collected from solutions containing approximately 5 mM HO in 50 mM borate buffer at pH 10.3; the pH readings have not been corrected for the deuterium isotope effect. The samples were concentrated to 250 μL in centrifugal concentrators equipped with 10,000 molecular weight cut-off membranes (Centricon-Millipore Co, Bedford, MA) and then transferred to Shigemi NMR tubes (5 mm) with susceptibilities matched to D_2O (Shigemi, Inc., Allison Park, PA). ^{13}C spectra were acquired over 48 K data points, with a spectral width of 300 kHz, an acquisition time of 80 ms, and no relaxation delay; typically 1,000,000 scans were obtained in approximately 24 h.

The conversion of high spin aquo ($\text{Fe}^{\text{III}}\text{-H}_2\text{O}$) to low spin hydroxo ($\text{Fe}^{\text{III}}\text{-OH}$) *pa*-HO was also monitored by electronic absorption spectroscopy, with the aid of a UV-vis S2000 spectrophotometer (Ocean Optics, Dunedin, FL). To this end, a solution of $\text{Fe}^{\text{III}}\text{-H}_2\text{O}$ in water (pH 6.3) was placed in a quartz cuvette (1-cm path length) where it was stirred continuously with the aid of a magnetic bar. This solution was titrated with 0.2 M sodium hydroxide, monitoring the pH and the electronic absorption spectrum after the

addition of each aliquot of base. The data from this titration was fitted to the Henderson-Hasselbach equation in order to obtain the pK_a for the deprotonation of the coordinated water.

Circular dichroism spectra were measured with the aid of a JASCO J-810 spectropolarimeter in the far UV-region (190-250 nm, 0.2 mm resolution, 1.0 mm bandwidth) at 25 °C in 10 mM potassium phosphate buffers at pH 6.0, 8.0 or 10.0 with a protein concentration of 5 μ M. The molar ellipticity ($\text{degree cm}^2 \text{ dmol}^{-1}$) in the far UV region was calculated directly using the JASCO standard software analysis following subtraction of the baseline spectra.

Results and Discussion

a) Characterization of the hydroxide complex of *pa*-HO by ^1H NMR and electronic absorption spectroscopy.

The electronic absorption spectra in Figure 1-A were obtained upon titration of a solution of *pa*-HO from pH 6.3 to pH 10.3. The Soret band shifts from 406 nm at pH 6.3 to 415 nm at pH 10.3, concomitant with the emergence of α and β bands at 540 and 574 nm, respectively. The band at 630 nm, which is typically considered a high spin marker, is clearly present at pH 6.3 but gradually disappears as the pH is increased, until it is no longer detectable at pH 10.3. These pH-dependent changes in the electronic absorption spectra of *pa*-HO exhibit well defined isosbestic points at 482, 524 and 610 nm that are indicative of the equilibrium between the high-spin $\text{Fe}^{\text{III}}\text{-H}_2\text{O}$ and the low-spin $\text{Fe}^{\text{III}}\text{-OH}$ complexes shown in Figure 1; the pK_a for the deprotonation of the coordinated water is

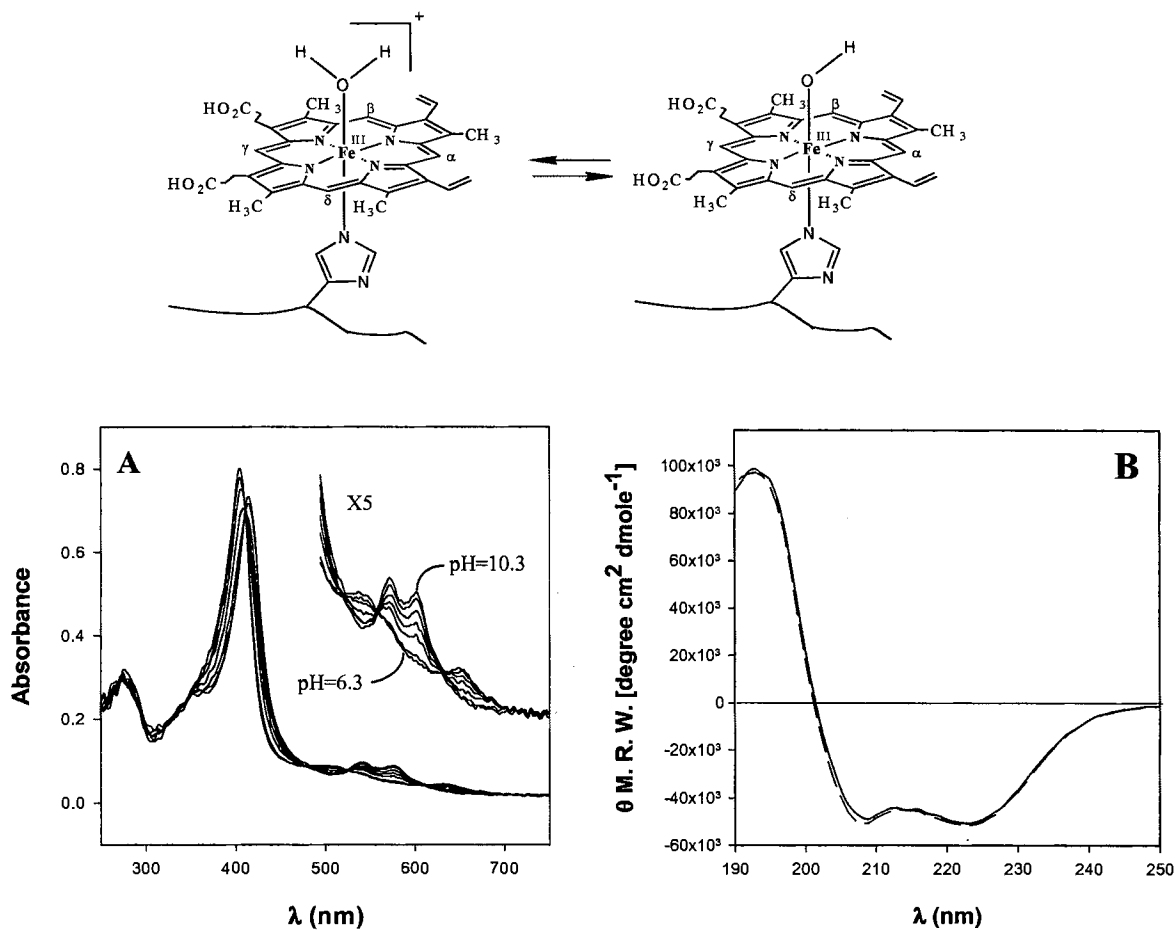


Figure 1. A: Electronic absorption spectra obtained during the titration of ferric HO with sodium hydroxide. B: CD spectra obtained at pH 6.5 (dashed line) and pH 10.0 (solid). The spectrum obtained at pH 8.5 is identical to those shown in the figure but has not been included for clarity.

8.3. The CD spectra obtained at pH 6.0 and 10.0 (Figure 1-B) are essentially superimposable and therefore demonstrate that the fold of *pa*-HO is not affected upon increasing the pH of the solution. On the basis of the above-described observations it is possible to conclude that a stable Fe^{III}-OH complex is formed at pH values above 9.3.

The formation and properties of the hydroxide complex of *pa*-HO have also been studied by ¹H NMR spectroscopy. Thus, the ¹H NMR spectrum obtained at pH 6.3 (Figure 2-a) displays heme-methyl resonances between 60 and 80 ppm, which are typical of high spin heme active sites, where the ferric ion is axially coordinated by a His and H₂O ligands [22] (Fe^{III}-H₂O). As the pH of the solution is increased, the relative intensity of these peaks decreases with the concomitant emergence and growth of heme-methyl peaks near 20 ppm that originate from the low-spin Fe^{III}-OH complex. The fact that at pH values intermediate between 6 and 10 (Figure 2-b and -c) one can observe peaks originating from heme methyl groups in the high-spin Fe^{III}-H₂O, as well as those from the low-spin Fe^{III}-OH complexes in the same spectrum, indicates that these two species are in slow exchange relative to the NMR time scale. Considering the maximum and minimum differences between the high-spin and low-spin heme methyl ¹H signals it is possible to estimate the NMR time scale to be $\sim 7 \times 10^4 \text{ s}^{-1}$. On the other hand, the ¹H NMR spectrum obtained at pH 10.3 (Figure 2-d) does not exhibit heme methyl peaks in the region between 60 and 80 ppm, thus demonstrating the quantitative conversion of the high-spin Fe^{III}-H₂O species to the low-spin Fe^{III}-OH complex.

The high- and low-frequency portions of the ¹H NMR spectrum of the Fe^{III}-OH complex of *pa*-HO (pH 10.3) are shown in Figure 3-a. This spectrum is different from

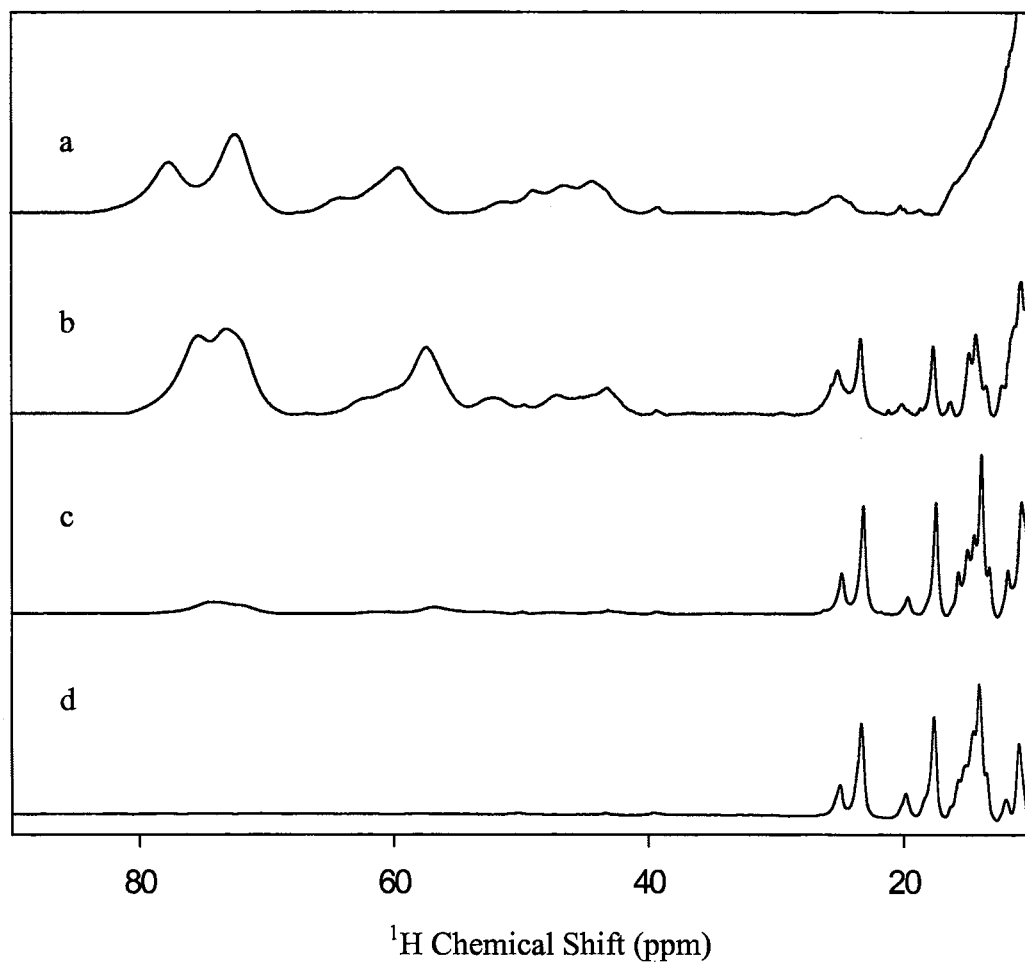


Figure 2. Downfield portion of the ^1H NMR spectra of *pa*-HO obtained at 25 °C and pH 6.3 (a), 8.3 (b), 9.3 (c) and 10.3 (d).

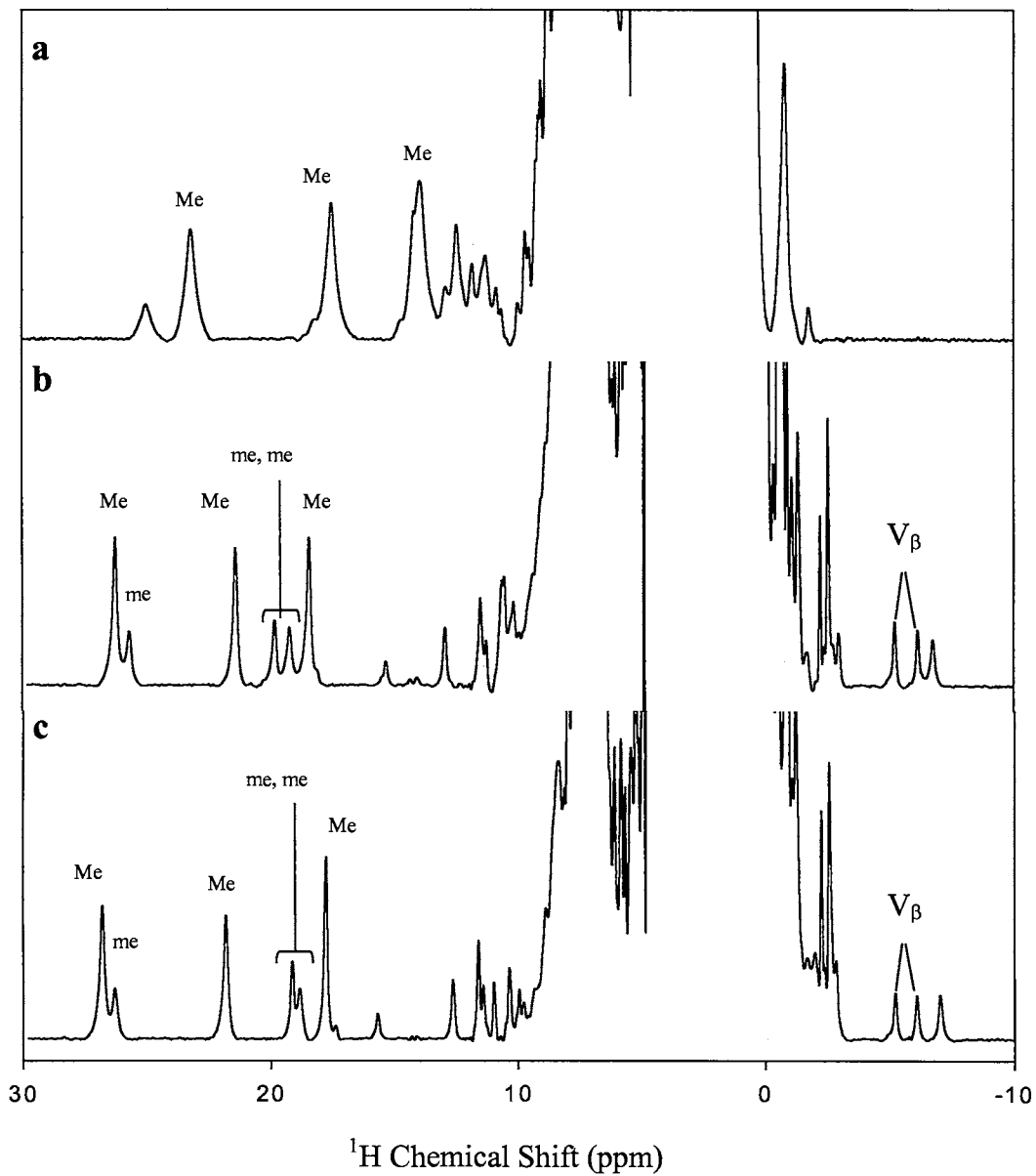


Figure 3. ^1H NMR spectra of (a) $\text{Fe}^{\text{III}}\text{-OH}$ at pH 10, (b) $\text{Fe}^{\text{III}}\text{-CN}$ at pH 7.4 and (c) $\text{Fe}^{\text{III}}\text{-CN}$ at pH 10.3 obtained at 25 °C. Me and me represent heme methyl resonances from major and minor heme orientational isomers, respectively

that obtained from the cyanide complex of *pa*-HO ($\text{Fe}^{\text{III}}\text{-CN}$) at pH 7.4 (Figure 3-b) in that the heme methyl peaks are shifted to lower frequencies (upfield) and the vinyl- β resonances, which in the $\text{Fe}^{\text{III}}\text{-CN}$ complex are near -8 ppm, are shifted to higher frequencies (downfield) and therefore are no longer discernable from the large envelope of protein resonances. The ^1H NMR spectrum of the $\text{Fe}^{\text{III}}\text{-CN}$ complex at pH 7.4 revealed the presence of heme methyl groups from major (Me) and minor (me) heme orientational isomers [18]. The ^1H NMR spectrum of the $\text{Fe}^{\text{III}}\text{-OH}$ complex at pH 10.3 also suggests the presence of major and minor heme orientational isomers. The smaller shifts of the heme methyl and heme vinyl- β protons from the $\text{Fe}^{\text{III}}\text{-OH}$ complex can in principle be interpreted as an indication of a change in the conformation of the proximal His ligand. However, this hypothesis was discarded by studying the ^1H NMR spectrum of the $\text{Fe}^{\text{III}}\text{-CN}$ complex at pH 10.3 (see Figure 3-c), which was obtained after 3 equivalents of NaCN were added to a solution of the $\text{Fe}^{\text{III}}\text{-OH}$ complex at pH 10.3. This spectrum shows that the chemical shifts corresponding to heme methyl and heme vinyl- β protons of the $\text{Fe}^{\text{III}}\text{-CN}$ complex at pH 10.3 are almost identical to the corresponding resonances of the $\text{Fe}^{\text{III}}\text{-CN}$ complex at pH 7.4, therefore strongly suggesting that the conformation of the proximal His ligand and the seating of the heme have not been perturbed at pH 10.3. Furthermore, when these observations are taken together with those made from the electronic absorption and CD spectroscopic studies, it becomes evident that at pH 10.3 the $\text{Fe}^{\text{III}}\text{-OH}$ complex must exhibit a fold nearly identical to that of the $\text{Fe}^{\text{III}}\text{-H}_2\text{O}$ complex. The more compressed shifts of the heme methyl and heme vinyl- β protons in the spectrum of $\text{Fe}^{\text{III}}\text{-OH}$, therefore, are suggestive of an electronic structure different from the typical low-spin d_π configuration. In fact, it will be shown

below that the core carbon resonances of Fe^{III}-OH indicate that this species does not exist in the common low-spin d_{π} electronic structure typical of the hydroxide complex of globins.

b) ¹³C NMR chemical shifts are diagnostic of heme electronic structure.

¹³C NMR spectroscopy is emerging as a powerful experimental tool to study the electronic structure of model hemes. Studies conducted with low-spin ferriheme complexes established that chemical shifts originating from porphyrin core carbons, C_α, C_β, and C_m, permit the relatively straightforward assessment of electronic structure [23-27]. The schematic representations of Figure 4 summarize the relationships between ¹³C chemical shifts and electronic configurations that are relevant to this study: (1) Spin delocalization in ferrihemes with the common S = 1/2, d_{π} electronic structure, which are typically planar, is mainly into the porphyrin 3e(π) orbital shown schematically in Figure 4. It can be seen from the relative sizes of the circles in the schematic representation of the 3e(π) orbital that the C_β carbons possess relatively large electron density, the C_α carbons possess relatively small electron density, and the C_m carbons have zero electron density. As a consequence, low-spin d_{π} ferrihemes exhibit C_β resonances at ~200 ppm, C_α resonances at ~100 ppm and C_m signals near 50 ppm [20, 23] (Figure 4-a). (2) Spin delocalization in ferrihemes with the less common S = 1/2, (d_{xy})¹ electronic configuration is mainly into the 3a_{2u}(π) orbital [28], which exhibits large electron density at the C_m carbons and small electron density at the C_α and C_β carbons (Figure 4). Ferrihemes possessing the (d_{xy})¹ electron configuration (typically ruffled) exhibit large downfield C_m

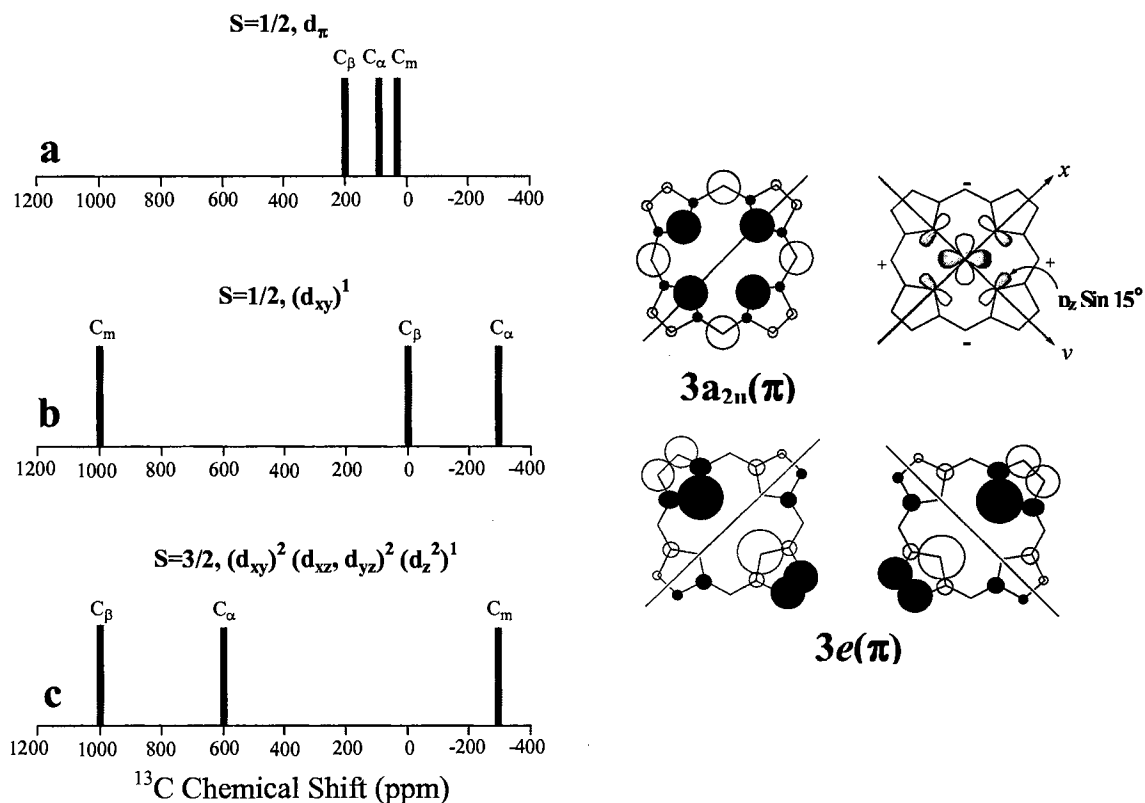


Figure 4. Left: Typical porphyrin core carbon chemical shifts for (a) Fe^{III}-porphyrates with the $S = 1/2, d_{\pi}$ electron configuration, (b) Fe^{III}-porphyrates with the $S = 1/2, (d_{xy})^1$ electron configuration and (c) Fe^{III}-porphyrates with the $S = 3/2, (d_{xy})^2 (d_{xz}, d_{yz})^2 (d_z^2)^1$ electron configuration. Right: schematic representation (adapted from reference [15]) of the $3a_{2u}(\pi)$ and $3e(\pi)$ porphyrin orbitals. The relative size of the circles at each atom are proportional to the calculated electron density. The possible interactions between the d_{xy} orbital and the porphyrin nitrogens of a ruffled porphyrin which allow spin delocalization into the $3a_{2u}(\pi)$ orbital are shown schematically next to this orbital.

shifts (~ 1000 ppm), relatively large upfield C_α (~ -300 ppm) and negligible C_β shifts (~ 20 -70 ppm) [24] (see Figure 4-b). The large downfield C_m shifts are a consequence of delocalization of unpaired electron density from the d_{xy} orbital into the porphyrin $3a_{2u}(\pi)$ orbital of the ruffled porphyrin [13]. Since the $3a_{2u}(\pi)$ orbital has negligible spin density at the C_α position the relatively large upfield C_α shifts are a consequence of spin polarization from the C_m carbons [24]. Unpaired electron density from the d_{xy} orbital can be delocalized into the $3a_{2u}(\pi)$ orbital only if the macrocycle is significantly ruffled, so that the nodal planes of the p_z orbital are no longer in the xy plane and projections of these p_z orbitals have the proper symmetry to interact with the d_{xy} orbital [13] (see Figure 4).

(3) Ferrihemes possessing the $S = 3/2$, $(d_{xy})^2(d_{xz},d_{yz})^2(d_z^2)^1$ spin state are also markedly non-planar and exhibit complicated distortions from nominal D_{4h} symmetry [29, 30], which suggests that these ferriheme complexes might exist in solution as a complex mixture of interconverting conformers with similar energies. Nonplanar hexacoordinated Fe^{III} -porphyrinates possessing the $S = 3/2$ spin state exhibit a unique pattern of ^{13}C NMR shifts [31] with very large downfield C_β shifts (~ 1000 ppm), large downfield C_α shifts (~ 600 ppm) and large upfield C_m shifts (~ -300 ppm) (Figure 4-c). The large downfield shifts of the C_α and C_β carbons are consistent with the presence of unpaired electron density in each of the d_{xz} and d_{yz} orbitals, which are delocalized into the $3e(\pi)$ porphyrin orbital. Since this porphyrin orbital has zero electron density at the meso carbons, the large upfield C_m shift is a consequence of spin polarization from the neighboring C_α carbon [24, 27].

The application of ^{13}C NMR spectroscopy to the study of heme electronic structure in proteins and enzymes is less common because the relatively low sensitivity

and low natural abundance of ^{13}C make the observation of paramagnetically-affected ^{13}C resonances more demanding. This limitation is felt more strongly when one is interested in observing porphyrin C_α and C_β carbons because it is not possible to take advantage of directly attached protons to capitalize on the increased sensitivity of the inverse-detection experiments [32]. To overcome these problems we have developed a biosynthetic method that allows the efficient preparation of ^{13}C -labeled heme from judiciously labeled ALA [21], the first committed precursor in heme biosynthesis, by adequate manipulation of an expression system that overproduces the heme binding protein OM cytochrome b_5 [19, 33]. Heme in OM cytochrome b_5 is not covalently attached to the polypeptide. Therefore, ^{13}C -labeled heme can be extracted and used to reconstitute other proteins of interest. This strategy has been successfully applied to study a complex mixture of heme orientational and heme-rotational isomers present in a solution of *pa*-HO mutants [18]. In the study reported herein we have used heme labeled with ^{13}C at the core carbons to study the electronic structure of the Fe^{III} -OH complex. Observation of the corresponding core carbon resonances revealed the presence of a mixture of Fe^{III} -OH populations which differ in their electronic structure and degree of nonplanar porphyrin distortions. It is noteworthy that this information, which is directly attainable from the ^{13}C NMR shifts, is not easily obtained by other spectroscopic means.

c) ^{13}C NMR spectroscopy reveals the coexistence of at least three spin states exhibiting different degrees of population of the iron- d_π orbitals.

A portion of the ^{13}C NMR spectrum of Fe^{III} -OH reconstituted with heme labeled at the C_m and C_α carbons is depicted in Figure 6-A. If the pH of the solution is decreased

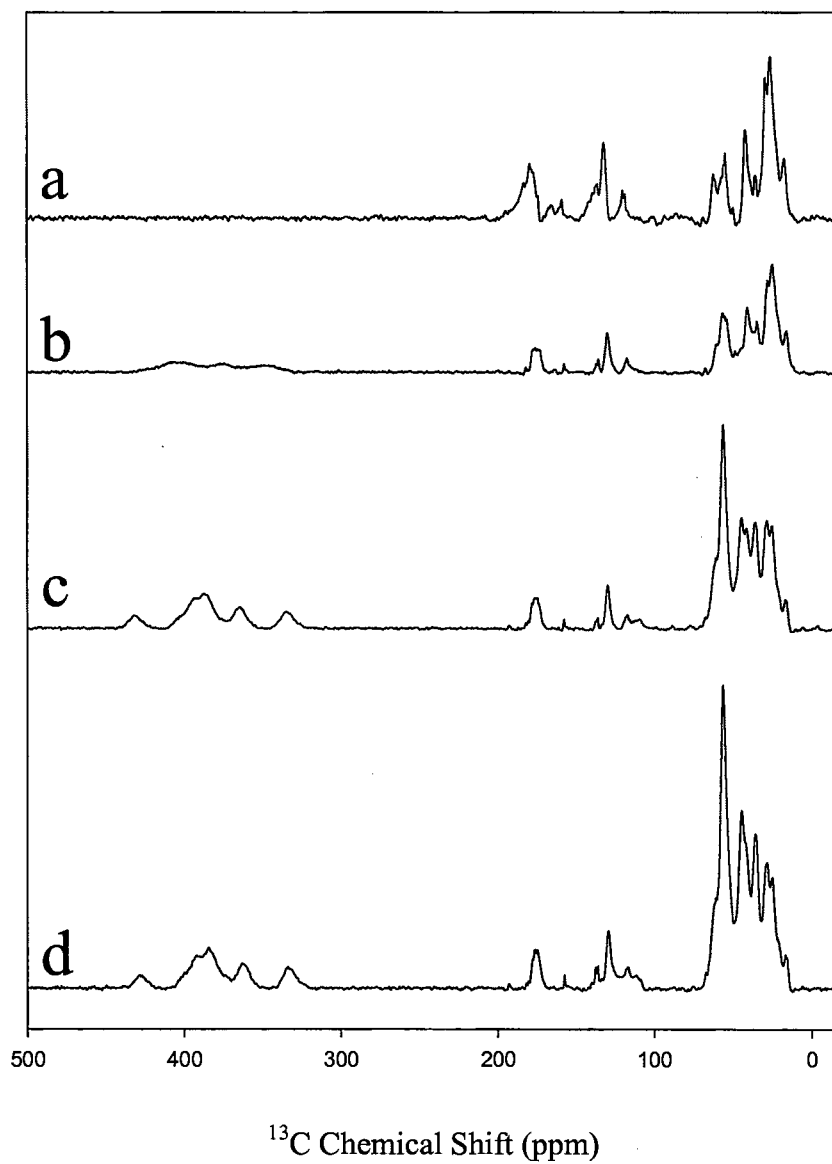


Figure 5: ^{13}C NMR spectra of paHO reconstituted with heme labeled with ^{13}C at the meso and α positions. Spectra were collected at pH values of 6.3 (a), 7.3 (b), 8.3 (c) and 10.3 (d).

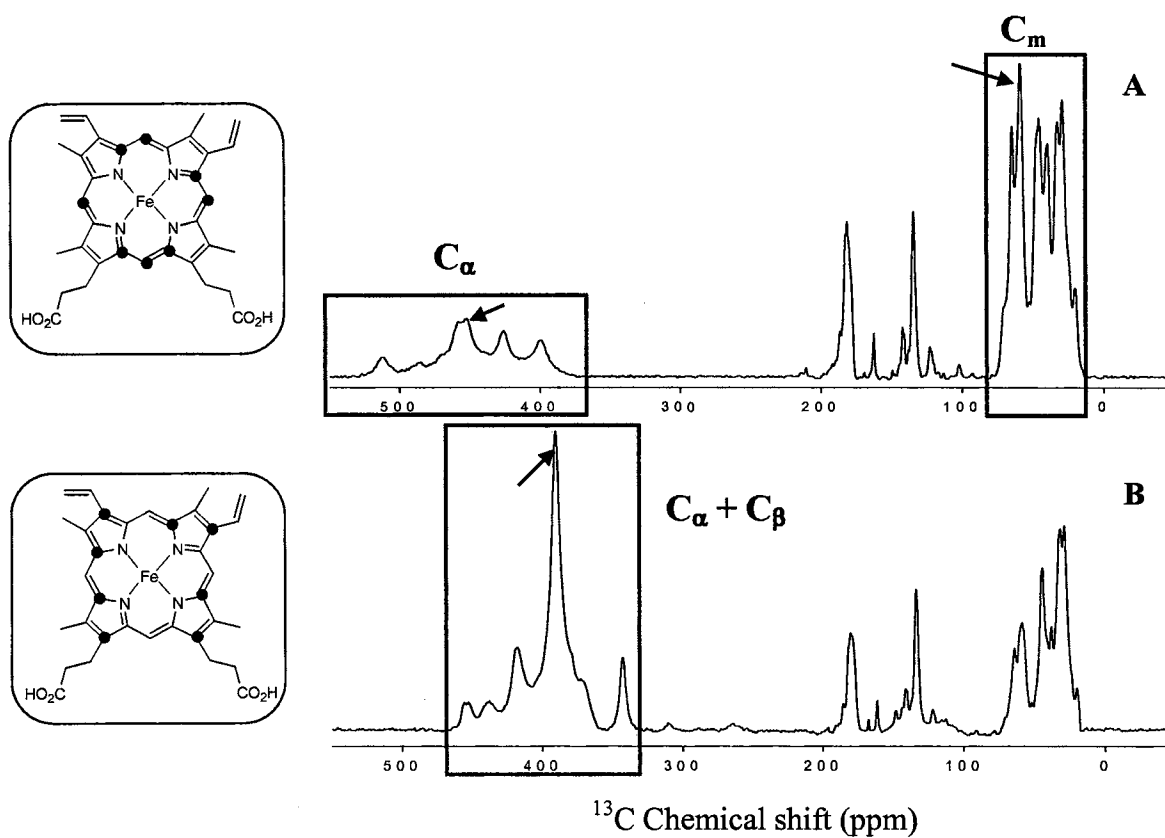


Figure 6. A portion of the ^{13}C NMR spectra obtained at $37\text{ }^\circ\text{C}$ from a solution of the Fe^{III} -OH complex of *pa*-HO (pH 10.3) reconstituted with heme labeled at C_α and C_m carbons (A) and at C_α and C_β carbons (B). The labeled carbons are highlighted by (•) in the structures shown to the left of each corresponding spectrum. The chemical shifts of the peaks highlighted by an arrow have been used to construct the temperature dependence plot of Figure 7.

from 10.3 to 6.3 the sets of highlighted resonances near 50 ppm and 450 ppm become less intense until at pH values below 7.0 they become unobservable (see Figure 5). Subsequent increase of the solution pH results in the appearance and growth of the set of resonances near 50 and 450 ppm and at pH 10.3 the spectrum shown in Figure 6-A is restored. This behavior is consistent with the reversible equilibrium between the $\text{Fe}^{\text{III}}\text{-H}_2\text{O}$ and $\text{Fe}^{\text{III}}\text{-OH}$ complexes of *pa*-HO shown in Figure 1. The electronic absorption and ^1H NMR spectra of the $\text{Fe}^{\text{III}}\text{-OH}$ complex suggest a low-spin electronic configuration for this species. However, the fact that resonances from core porphyrin carbons in Figure 6-A appear near 450 ppm strongly suggests that the electronic configuration of the $\text{Fe}^{\text{III}}\text{-OH}$ complex is not the common low-spin d_π . Indeed, model hemes and hemoproteins possessing a low-spin d_π electronic configuration give rise to ^{13}C NMR spectra displaying C_m resonances between 5 and 50 ppm, C_α resonances between -10 and 100 ppm, and C_β resonances between 150 and 250 ppm [18, 20, 23, 34] (see Figure 4-b). On the other hand, if the set of resonances at ca. 450 ppm can be attributed to meso carbons, it would then be possible to conclude that the electronic structure of the $\text{Fe}^{\text{III}}\text{-OH}$ complex of *pa*-HO is $S = 1/2$, $(d_{xy})^1$. However, it is important to note that when $[5\text{-}^{13}\text{C}]\text{-ALA}$ is used as a precursor for heme biosynthesis, the C_m and C_α carbons shown in Figure 6-A are labeled [20]. Consequently, in order to determine the electronic configuration of the $\text{Fe}^{\text{III}}\text{-OH}$ complex it is necessary to elucidate whether the set of resonances at 450 ppm in Figure 6-A originate from C_m or from C_α carbons. To this end, $[4\text{-}^{13}\text{C}]\text{-ALA}$ was used to label the C_α and C_β carbons shown in Figure 6-B, and the labeled heme was used to reconstitute the $\text{Fe}^{\text{III}}\text{-OH}$ complex of *pa*-HO. The corresponding ^{13}C NMR spectrum displays a set of resonances between 350 and 450 ppm, whereas the region near 50 ppm only shows peaks

originating from the polypeptide. These observations suggest that both the C_α and C_β carbons of the Fe^{III} -OH complex resonate between 350 and 500 ppm, therefore implying that the set of resonances near 450 ppm in Figure 6-A originate from C_α carbons, and that the set of accompanying resonances near 50 ppm arise from C_m carbons.

It is evident that the chemical shifts from the C_α , C_β and C_m carbons shown in Figure 6 are not consistent with a low-spin $(d_{xy})^1$ electronic configuration because ferrihemes with this electronic structure place significant unpaired electron density at the C_m carbons. This results in large downfield (~ 1000 ppm) C_m shifts, and by spin polarization, relatively large upfield (~ -300 ppm) C_α shifts (see Figure 4-b). On the other hand, the C_α and C_β chemical shifts depicted in Figure 6 are reminiscent of the recently reported $S = 1/2$, $S = 3/2$ spin state crossover that is characterized by C_α and C_β carbon shifts between 300 and 600 ppm and C_m chemical shifts near zero ppm [27, 35]. The C_α and C_β resonances shown in Figure 6 exhibit a pronounced temperature dependence that shifts the C_α carbons from ~ 260 ppm at $0^\circ C$ to ~ 460 ppm at $37^\circ C$, and the C_β carbons from ~ 250 ppm at $0^\circ C$ to ~ 400 ppm at $37^\circ C$ (Figure 6). It is therefore possible to rationalize the shifts in Figure 6 assuming that at $37^\circ C$ there is approximately $1/3 S = 3/2$, $(d_{xy})^2(d_{xz}, d_{yz})^2(d_z^2)^1$ and approximately $2/3 S = 1/2$, d_π contribution. As the temperature is lowered the contribution of $S = 1/2$, d_π increases and the core carbon chemical shifts approach the values expected for an $S = 1/2$, d_π Fe^{III} -porphyrinate. This behavior of the core carbon chemical shifts in response to changes in temperature is in agreement with that of Fe^{III} -porphyrinates known to exhibit the $S = 1/2$, $S = 3/2$ spin state crossover [31]. It is not yet clear why the chemical shifts of the C_m carbons exhibit a shallow temperature dependence. The alternative equilibrium between the $S = 1/2$, $(d_{xy})^1$

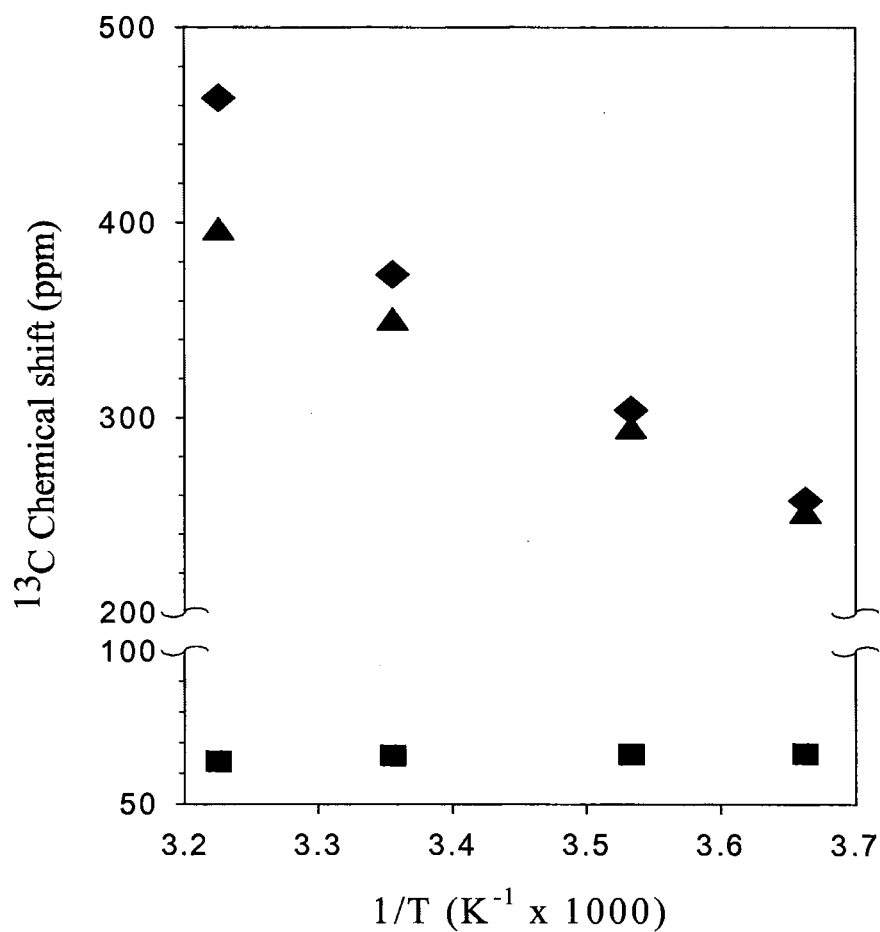


Figure 7. Temperature dependence of the C_α (◆), C_β (▲), and C_m (■) chemical shifts for the Fe^{III}-OH complex of *pa*-HO. The plot was constructed with chemical shifts corresponding to those peaks highlighted with an arrow in Figure 6-A and -B.

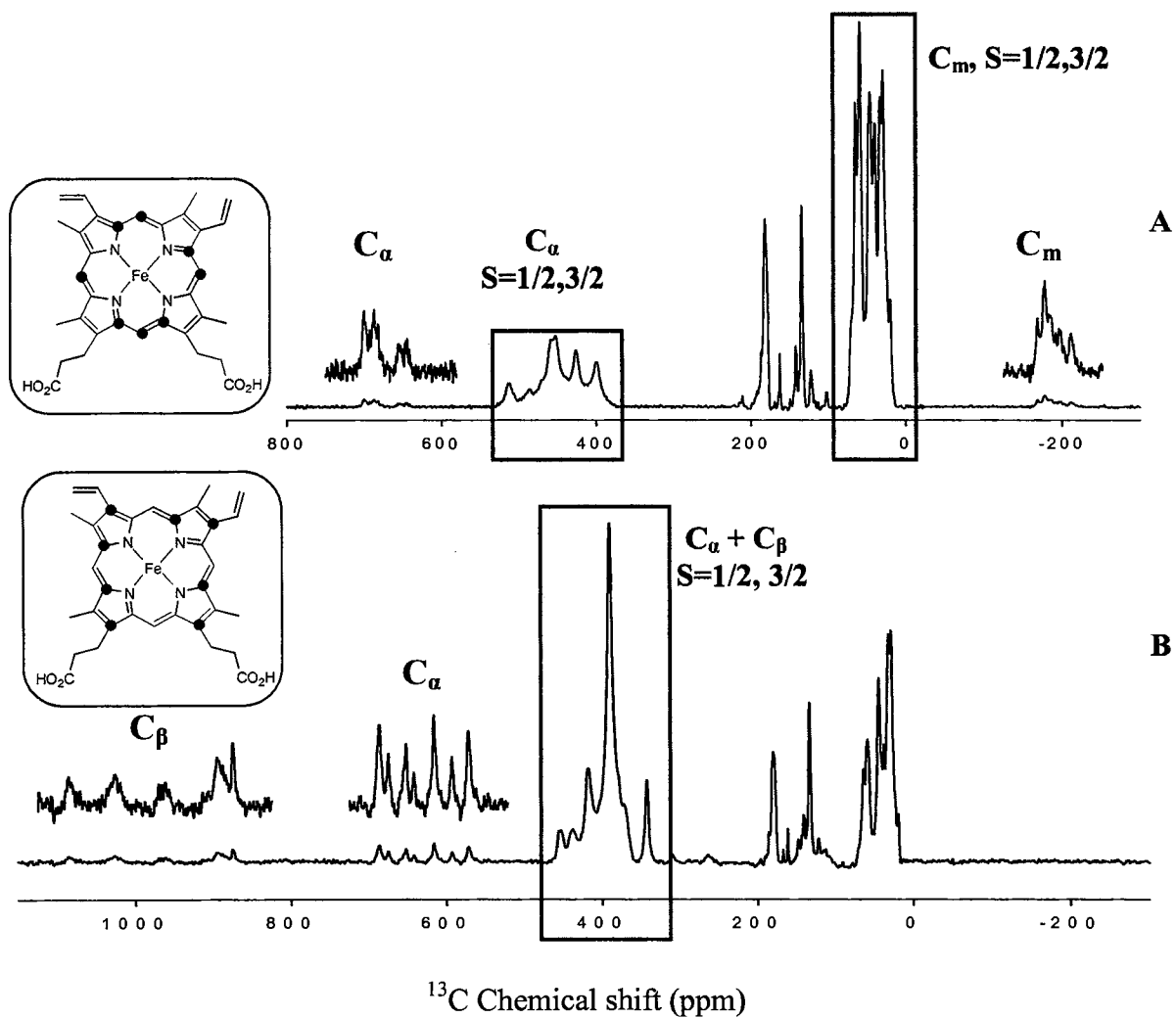


Figure 8. A portion of the ^{13}C NMR spectra obtained at 37 °C from a solution of the Fe^{III} -OH complex of *pa*-HO (pH 10.3) reconstituted with heme labeled at C_α and C_m (A) and C_α and C_β carbons (B). Peaks corresponding to the population with the $S = 1/2, S = 3/2$ spin state crossover are highlighted in a blue box (see Figure 6).

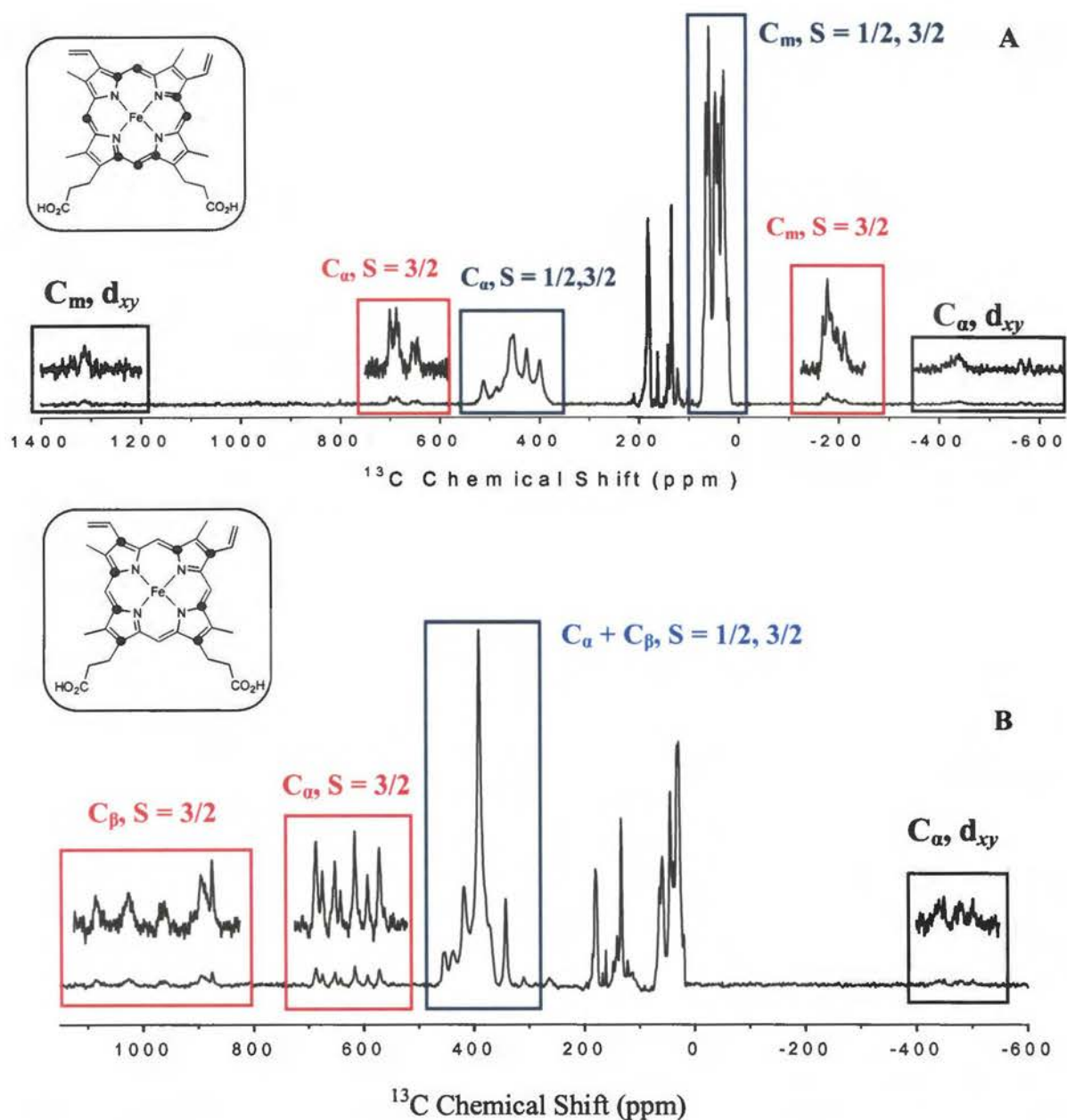


Figure 9. ^{13}C NMR spectra (37 °C) of the $\text{Fe}^{\text{III}}\text{-OH}$ complex of *pa*-HO (pH 10.3) reconstituted with heme labeled at the the C_α and C_m (A) and C_α and C_β carbons (B). Peaks corresponding to the population exhibiting the $S = 1/2, 3/2$ spin state crossover are highlighted by blue boxes, peaks corresponding to the population with the $S = 3/2$ spin state are highlighted by red boxes and peaks corresponding to the population with $S = 1/2, d_{xy}$ are highlighted by black boxes.

and $S = 3/2$, $(d_{xz}, d_{yz})^3(d_{xy})^1(d_z^2)^1$ can be ruled out on the basis of the temperature dependent changes of the core carbon chemical shifts because at the lower temperatures one would expect the main contribution to be from the $S = 1/2$, $(d_{xy})^1$ ground state. Thus, at the lower temperatures the C_m shifts should be large and positive (downfield) and the C_α shifts negative, with the C_β shifts near 50 ppm.

Figure 8-A depicts a larger spectral window of the ^{13}C NMR spectrum obtained from the $\text{Fe}^{\text{III}}\text{-OH}$ complex reconstituted with heme labeled at the C_α and C_m carbons. It is apparent that in addition to the peaks described above (blue box) there are additional resonances near 650 and -200 ppm. Although these resonances clearly originate from C_α and C_m carbons, it is not possible to assign them to their corresponding core carbons based solely on this spectrum. To circumvent this problem it is again useful to consider the spectrum obtained from the $\text{Fe}^{\text{III}}\text{-OH}$ complex reconstituted with heme labeled at the C_α and C_β carbons (Figure 8-B). Inspection of this spectrum clearly shows that the region near -200 ppm is devoid of peaks, thus implying that the resonances near -200 ppm in the spectrum obtained from enzyme reconstituted with heme labeled at the C_α and C_m carbons (Figure 8A) can be assigned to meso carbons. In the same vein, the peaks near 650 ppm in the spectra of Figure 8-A and 8-B must originate from C_α carbons, and the peaks centered near 1000 ppm in the spectrum of Figure 8-B must originate from C_β carbons. The large downfield shifts for α - and β -pyrrole carbons, accompanied by upfield shifted meso carbons is characteristic of an $S = 3/2$ spin state [27], where unpaired electron density in the d_{xz} and d_{yz} orbitals is delocalized into the α - and β -pyrrole carbons via the $3e(\pi)$ porphyrin orbital (see Figure 4). This orbital exhibits zero electron density

at the meso carbons, thus the large upfield C_m shifts have been ascribed to spin polarization from the neighboring C_α carbon atoms [24, 27].

Figure 9-A depicts the entire ^{13}C NMR spectrum of the $\text{Fe}^{\text{III}}\text{-OH}$ complex of *pa*-HO reconstituted with heme labeled at the C_α and C_m carbons. In this spectrum there are two new sets of peaks, one at ca. 1300 ppm and the other at ca. -500 ppm, in addition to the resonances corresponding to the $S = 1/2$, $S = 3/2$ spin crossover (blue box), and those corresponding to the population exhibiting the pure $S = 3/2$ spin state (red box). The significance of the resonances near 1300 ppm and -500 ppm is made clear once the ^{13}C spectrum of the $\text{Fe}^{\text{III}}\text{-OH}$ complex reconstituted with heme labeled at C_α and C_β carbons is considered. This spectrum (Figure 9-B) reveals the presence of a set of peaks ca. -500 ppm, which can be attributed to C_α carbons on the basis that the spectrum of $\text{Fe}^{\text{III}}\text{-OH}$ labeled at the C_α and C_m carbons (Figure 9-A) also displays peaks near -500 ppm.

Consequently, the peaks near 1300 ppm in the spectrum of Figure 9-A must originate from C_m carbons. Large downfield C_m shifts (500-1300 ppm) and large upfield C_α shifts (-400 to -600 ppm) are diagnostic of Fe^{III} porphyrinates exhibiting the low-spin $(d_{xy})^1$ electronic structure [12, 24]. These characteristically large downfield C_m shifts result from unpaired electron density delocalization from the iron d_{xy} orbital into the porphyrin $3a_{2u}(\pi)$ orbital [13] and the large upfield C_α shifts are a consequence of spin polarization from neighboring meso carbons [24]. Thus, the peaks at 1300 and -500 ppm in Figures 9-A and 9-B, respectively, indicate the presence of a population exhibiting the unusual $(d_{xy})^1$ electronic structure.

It is important to note that when CN^- is added to the $\text{Fe}^{\text{III}}\text{-OH}$ complex of *pa*-HO at pH 10.3, the ^{13}C NMR spectrum of the resultant $\text{Fe}^{\text{III}}\text{-CN}$ complex does not display the

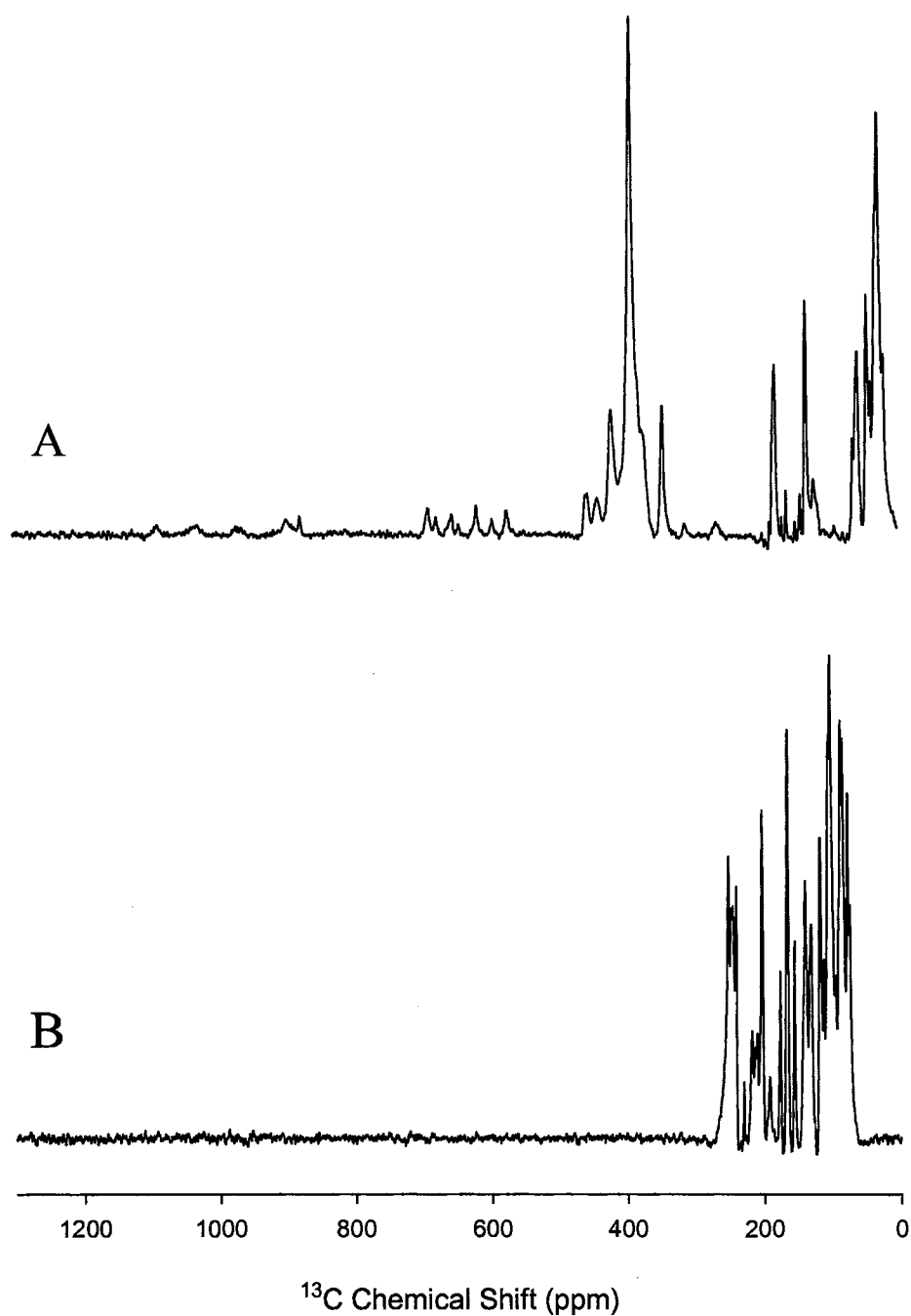


Figure 10: Carbon NMR spectra of *pa*-HO reconstituted with heme labeled with ^{13}C at the C_m and C_α positions. Spectrum A is that of the hydroxide complex of *pa*-HO at pH = 10.3 and 37 °C and B is the spectrum obtained after the addition of 4 equivalents of sodium cyanide under identical pH and temperature conditions.

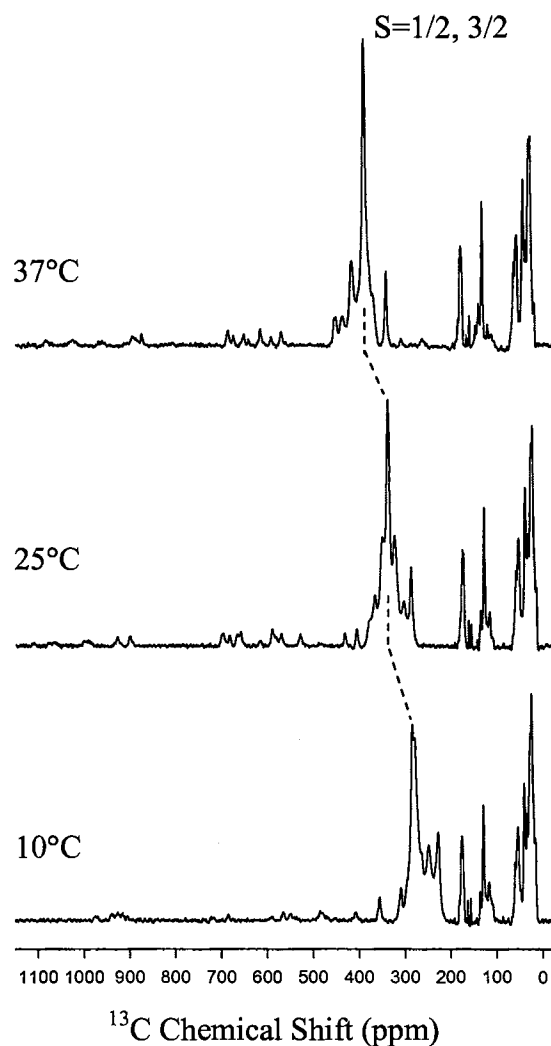


Figure 11. ^{13}C NMR spectra of the $\text{Fe}^{\text{III}}\text{-OH}$ complex of *pa*-HO obtained at different temperatures. The temperature dependence of the major population exhibiting the spin crossover between $S = 1/2$ and $S = 3/2$ spins states is highlighted by a dotted line. The downfield peaks corresponding to the minor population with the $S = 3/2$ spin state.

peaks originating from the major population with the $S = 1/2$, $S = 3/2$ spin state crossover or from the minor populations with the $S = 3/2$ and $S = 1/2$ (d_{xy})¹ spin states (see Figure 10). Instead, the spectrum is almost identical to that exhibited by the Fe^{III}-CN complex at pH 7.0, which has been shown to be $S = 1/2$, d_{π} . It is therefore apparent that the ¹³C resonance in Figures 6, 8 and 9, which have been attributed to the presence of different populations with unusual spin states, are only present when hydroxide is coordinated in the distal site of *pa*-HO. Therefore, it is reasonable to conclude that the Fe^{III}-OH complex of *pa*-HO exists as a mixture of multiple (at least three) conformers, each exhibiting a different spin state, and probably different degrees of nonplanar distortions. At 37 °C the major population exhibiting the $S = 1/2$, $S = 3/2$ spin state crossover accounts for approximately 88% of the total population, whereas those species exhibiting the $S = 3/2$ and the $S = 1/2$ (d_{xy})¹ electronic configurations account for ~ 10% and ~ 2% of the total population, respectively. Figure 11 illustrates the temperature dependence of the spectrum obtained from Fe^{III}-OH reconstituted with heme labeled at the C_α and C_β carbons. It has been pointed out (see above) that the resonances corresponding to the population exhibiting the $S = 1/2$, $S = 3/2$ spin state crossover exhibit a pronounced temperature dependence, with these resonances shifting upfield from ca. 400 ppm at 37 °C to ca. 250 ppm at 0 °C. The magnitude of the temperature dependent shifts and the fact that the chemical shifts move in the direction of those expected for the planar, low spin d_{π} complexes, suggest that low temperatures decrease the conformational flexibility of the heme pocket and shift the equilibrium toward the planar, $S = 1/2$, d_{π} electronic configuration. At this time it is not possible to ascertain whether the $S = 1/2$, d_{π} and $S = 3/2$ spin states are quantum mechanically admixed or simply in fast exchange relative to

the NMR time scale. Assuming fast exchange relative to the NMR time scale it is possible to estimate that the rate of exchange should be faster than $2.7 \times 10^5 \text{ s}^{-1}$. This value was estimated at 37 °C from the difference in shifts between the C_β carbons in the pure $S = 3/2$ spin state (~ 1000 ppm) and the C_β carbons in the pure $S = 1/2, d_\pi$ spin state (~ 200 ppm). The resonances corresponding to the population with the pure $S = 3/2$ spin state, C_α carbons at ca. 650 ppm and C_β carbons at ca. 1000 ppm, exhibit a significantly less pronounced shift as the temperature is lowered. However, it is interesting to note that these resonances become less intense as the temperature is lowered and are undetectable below 10 °C. This behavior suggests that the populations with the highly nonplanar $S = 1/2, (d_{xy})^1$ and $S = 3/2$ electronic configurations are in slow exchange with the major population exhibiting the $S = 1/2, S = 3/2$ crossover. For chemical exchange to be slow relative to the NMR time scale the exchange has to be much slower than $2.7 \times 10^5 \text{ s}^{-1}$. Thus, as the temperature is lowered, and the conformational flexibility of the heme binding site is decreased, these populations with highly nonplanar porphyrins decrease as the equilibrium shifts toward the planar $S = 1/2, d_\pi$ electronic configuration.

Shelnutt has pointed out that multiple conformers can occur for biological porphyrins because several potential energy minima can result from the protein environment [36]. The observations described above, therefore, are in agreement with this prediction, and imply that in the confines of the protein the relative energy of the porphyrin conformers, as well as the barriers of interconversion, can be modulated by the protein and by the spin state of the macrocycle.

Relevance to the mechanism of heme hydroxylation carried out by HO.

Axial ligand-metalloporphyrin interactions, among other things, are known to induce nonplanar distortions of the porphyrin ring [30, 37, 38]. For instance, it is well documented that the coordination of ligands that are poor σ -donors and good π -acceptors induce significant porphyrin ruffling and stabilization of the $(d_{xy})^1$ electronic configuration [13, 15, 25, 39]. Furthermore, crystal field theory indicates that decreasing axial ligand field strength leads to a transition from a low-spin to a high spin state. The $S = 3/2$ spin state is stabilized when the d_z^2 orbital is singly occupied and relatively close in energy to the d_{xy} , d_{xz} , and d_{yz} orbitals, and the $d_{x^2-y^2}$ orbital is vacant and at significantly higher energy [30, 40, 41]. The $d_{x^2-y^2}$ orbital can be destabilized further by increasing the field strength of the equatorial ligand (porphyrin), a strategy that has been utilized by Simonato and coworkers to stabilize the $S = 3/2$ spin state of model ferrihemes [30]. Moreover, as the axial ligand field strength is decreased, a compensating increase in equatorial field strength occurs; the increase in equatorial field strength, in turn, typically results in shorter Fe-N_p bond lengths and induces nonplanar distortions of the macrocycle. Therefore, axial ligands with the appropriate field strength are capable of stabilizing the unusual $S = 1/2$, $(d_{xy})^1$ and $S = 3/2$ spin states, which are typically associated with large nonplanar distortions of the porphyrin ring.

It is evident from the ^{13}C NMR spectra discussed above that the hydroxide ligand in the Fe^{III}-OH complex of *pa*-HO encourages the stabilization of the d_z^2 and the destabilization of the $d_{x^2-y^2}$ orbital, hence giving rise to two minor populations exhibiting a pure $S = 1/2$, $(d_{xy})^1$ and a pure $S = 3/2$ electronic configuration and a major population exhibiting a spin crossover between $S = 1/2$ and $S = 3/2$. It is noteworthy that these

observations are in striking contrast to those made with the hydroxide complex of globins, in that the complexation of a hydroxide ligand results in the formation of $S = 1/2$, d_x globin complexes [22]. A plausible explanation for the unusual behavior of the hydroxide complex of HO stems from at least two unique chemical properties shared by all known HO enzymes: (1) the presence of a well organized hydrogen bonding network in the distal site, and (2) the conformational flexibility of the heme binding domain. The relevance of these properties is discussed below.

(1) In addition to heme pocket flexibility (discussed below) the chemical nature of the distal pocket is likely to contribute significantly to the properties exhibited by the Fe^{III} -OH complex. In this context, the distal pocket in heme oxygenase enzymes supports an extensive and well-defined network of hydrogen bonded water molecules [8, 10, 42]. It is possible that one of these water molecules, by virtue of donating a hydrogen bond to the coordinated OH⁻ ligand, decrease its σ -donating ability and thereby lower its field strength. As has been discussed above, lowering the axial ligand field strength leads to the stabilization of the d_z^2 orbital and is also accompanied by a strengthening of the equatorial field. The latter induces nonplanar heme distortions and further destabilization of the $d_{x^2-y^2}$ orbital. It is thus conceivable that the ligand field strength of the coordinated hydroxide, which in HO is modulated by accepting a H-bond from the distal network of water molecules, induces the stabilization of these unusual electronic configurations and nonplanar porphyrin conformations. (2) The different populations with their different electronic configurations and likely different types of nonplanar distortions appear to be in slow exchange with one another relative to the NMR time scale. The relatively slow rate of interconversion between populations with different types of nonplanar distortions

is likely a consequence of obligatory accompanying conformational changes in the heme pocket. Thus, the flexibility of the pocket in HO facilitates the relatively large nonplanar heme distortions induced by the binding of hydroxide. At the same time, heme-polypeptide interactions slow down the rate of interconversion between the different types of distortions (populations) relative to the interconversion of Fe^{III}-porphyrinates not bound to a protein, such that it becomes possible to observe the different populations of HO complexes in slow exchange. By comparison, the more rigid heme binding site of the globins does not facilitate relatively large nonplanar distortions of the heme, therefore the binding of hydroxide results in the formation of a homogeneous population of nearly planar low-spin d_{π} complexes.

It is apparent that the above-described properties of HO must act in synergism so that the distal network of water molecules serves to lower the ligand field strength of the coordinated peroxide, thus providing the necessary impetus for the heme to deform from planarity. This impetus is reinforced by the flexibility of the distal pocket in HO, which facilitates the conformational changes “dictated” by the field strength of the coordinated hydroxide.

These findings suggest that if the field strength of the hydroperoxide ligand in the Fe^{III}-OOH intermediate could also be modulated by the distal network of hydrogen bonds, significant nonplanar deformations and large spin density at the meso carbons can indeed be expected for this complex. Thus, the efficient meso carbon hydroxylation reaction carried out by HO enzymes is likely a consequence of the chemical non-innocence of the macrocycle. Indeed, if this concept is operative in HO catalysis, it would expand the role currently attributed to the highly organized hydrogen bond

network in the distal pocket of HO to include modulation of the HOO⁻ ligand field strength. ENDOR spectroscopic studies have demonstrated that this hydrogen bond network efficiently delivers a proton to the terminal oxygen of Fe^{III}-OO⁻ in order to form the activated Fe^{III}-OOH intermediate [6]. The same study reported a second well defined ¹H signal (denoted H2), which only appears in the ENDOR spectrum upon annealing of the Fe^{III}-OOH intermediate to 200 K, and suggested that proton H2 is part of the activation that leads to meso hydroxylation [6]. We propose that proton H2, by virtue of forming a hydrogen bond with the coordinated oxygen in Fe^{III}-OOH can modulate the field strength of the hydroperoxo (hydroxo in the present studies) ligand and consequently induce the unusual spin states and nonplanar distortions that can make the heme macrocycle an active participant in its own hydroxylation.

Acknowledgements: The expression and purification of *pa*-HO was done in collaboration with Rahul Deshmuk and Dr. Angela Wilks at the School of Pharmacy, University of Maryland. The ¹³C labeled ALAs were obtained in collaboration with Dr. Richard Bunce from Oklahoma State University.

References

1. Tenhunen, R., Marver, H., S., and Schmid, R.; *J. Biol. Chem.*, (1969). **244**: 6388-6394.
2. Yoshida, T., Noguchi, M., and Kikuchi, G.; *J. Biol. Chem.*, (1980). **255**: 4418-4420.
3. Wilks, A., Torpey, J., and Ortiz de Montellano, P.R.; *J. Biol. Chem.*, (1994). **269**: 29553-29556.
4. Ortiz de Montellano, P.R. and Wilks, A.; *Adv. Inorg. Chem.*, (2000). **51**: 359-407.
5. Davydov, R., Macdonald, I.D.G., Makris, T.M., Sligar, S.G., and Hoffman, B.M.; *J. Am. Chem. Soc.*, (1999). **121**: 10654-10655.
6. Davydov, R., Kofman, V., Fujii, H., Yoshida, T., Ikeda-Saito, M., and Hoffman, B.M.; *J. Am. Chem. Soc.*, (2002). **124**: 1798-1808.
7. Schuller, D.J., Wilks, A., Ortiz de Montellano, P.R., and Poulos, T.L.; *Nature Struct. Biol.*, (1999). **6**: 860-867.
8. Schuller, D.J., Zhu, W., Stojiljkovic, I., Wilks, A., and Poulos, T.L.; *Biochemistry*, (2001). **40**: 11552-11558.
9. Sugishima, M., Omata, Y., Kakuta, Y., Sakamoto, H., Noguchi, M., and Fukuyama, K.; *FEBS Lett.*, (2000). **471**: 61-66.
10. Syvitski, R.T., Li, Y., Auclair, K., Ortiz de Montellano, P.R., and La Mar, G.N.; *J. Am. Chem. Soc.*, (2002). **124**: 14296-14297.
11. Fujii, H., Zhang, X., Tomita, T., Ikeda-Saito, M., and Yoshida, T.; *J. Am. Chem. Soc.*, (2001). **123**: 6475-6484.

12. Rivera, M., Caignan, G.A., Astashkin, A.V., Raitsimring, A.M., Shokhireva, T.K., and Walker, F.A.; *J. Am. Chem. Soc.*, (2002). **124**: 6077-6089.
13. Safo, M.K., Walker, F.A., Raitsimring, A.M., Walters, W.P., Dolata, D.P., Debrunner, P., G., and Scheidt, W.R.; *J. Am. Chem. Soc.*, (1994). **116**: 7760-7770.
14. Walker, F.A., Nasri, H., Torowska-Tyrk, I., Mohanrao, K., Watson, C.T., Shkhirev, N.V., Debrunner, P.G., and Scheidt, W.R.; *J. Am. Chem. Soc.*, (1996). **118**: 12109-12118.
15. Walker, F.A.; *Coord. Chem. Rev.*, (1999). **185-186**: 471-534.
16. Simonneaux, G., Schünemann, V., Morice, C., Carel, L., Toupet, L., Winkler, H., Trautwein, A.X., and Walker, F.A.; *J. Am. Chem. Soc.*, (2000). **122**: 4366-4377.
17. Ratliff, M., Zhu, W., Deshmukh, R., Wilks, A., and Stojilkovic, I.; *J. Bacteriol.*, (2001). **183**: 6394-6403.
18. Caignan, G.A., Deshmukh, R., Wilks, A., Zeng, Y., Huang, H., Moënne-Loccoz, P., Bunce, R.A., Eastman, M.A., and Rivera, M.; *J. Am. Chem. Soc.*, (2002). **124**: 14879-14892.
19. Rivera, M. and Walker, F.A.; *Anal. Biochem.*, (1995). **230**: 295-302.
20. Rivera, M., Qiu, F., Bunce, R.A., and Stark, R.E.; *JBIC*, (1999). **4**: 87-98.
21. Bunce, R.A., Shilling III, C.L., and Rivera, M.; *J. Labelled Compd. and Radiopharm.*, (1997). **39**: 669-675.
22. La Mar, G.N., Satterlee, J.D., and De Ropp, J.S., eds., ed. R. Guillard. Vol. 5. 2000, Academic Press. 185-297.
23. Mispelter, J., Momenteau, M., and Lhoste, J.M., in *Biological Magnetic Resonance*, J. Reuben, Editor. 1993, Plenum Press: New York. p. 299-355.

24. Ikeue, T., Ohgo, Y., Takashi, S., Nakamura, M., Fujii, H., and Yokoyama, M.; *J. Am. Chem. Soc.*, (2000). **122**: 4068-4076.
25. Ikewue, T., Ohgo, Y., Saitoh, T., Yamaguchi, T., and Nakamura, M.; *Inorg. Chem.*, (2001). **40**: 3423-3434.
26. Ikezaki, A. and Nakamura, M.; *Inorg. Chem.*, (2002). **41**: 6225-6236.
27. Ikewe, T., Ohgo, Y., Yamaguchi, M., Takahashi, M., Takeda, M., and Nakamura, M.; *Angew. Chem. Int. Ed.*, (2001). **40**: 2617-2620.
28. Walker, F.A., in *The Porphyrin Handbook*, R. Guilard, Editor. 2000, Academic Press. p. 81-183.
29. Ikeue, T., Saitoh, T., Yamaguchi, T., Ohgo, Y., Nakamura, M., Takahashi, M., and Takeda, M.; *Chem. Comm.*, (2000). 1989-1990.
30. Simonato, J.P., Pécaut, J., Le Pape, L., Oddou, J.L., Jeandey, C., Shang, M., Scheidt, R., Wojaczynski, J., Wolowiec, S., Latos-Grazynky, L., and Marchon, J.C.; *Inorg. Chem.*, (2000). **39**: 3978-3987.
31. Ikeue, T., Ohgo, Y., Yamaguchi, M., Takahashi, M., Takeda, M., and Nakamura, M.; *Angew. Chem. Int. Ed.*, (2001). **40**: 2617-2620.
32. Summers, M.F., Marzilli, L.G., and Bax, A.; *J. Am. Chem. Soc.*, (1986). **108**: 4285-4294.
33. Qiu, F., Rivera, M., and Stark, R.E.; *J. Magn. Reson.*, (1998). **130**: 76-81.
34. Goff, H.M.; *J. Am. Chem. Soc.*, (1981). **103**: 3714-3722.
35. Ohgo, Y., Ikewe, T., and Nakamura, M.; *Inorg. Chem.*, (2002). **41**: 1698-1700.
36. Shelmutt, J.A.; *J. Porphyrins Phthalocyanines*, (2000). **4**: 386-389.

37. Shellnutt, J.A., Song, X.Z., Ma, J.G., Jia, S.L., Jentzen, W., and Medforth, C.J.; *Chem. Soc. Rev.*, (1998). **27**: 31-41.
38. Roberts, S.A., Weichsel, A., Qiu, Y., Shelnutt, J.A., Walker, F.A., and Montfort, W.R.; *Biochemistry*, (2001). **40**: 11327-11337.
39. Guillmot, M. and Simonneaux, G.; *J. Chem. Soc., Chem. Commun.*, (1995). 2093-2094.
40. Reed, C.A., Mashiko, T., Bentley, S.P., Kastner, M.E., Scheidt, W.R., Spartalian, K., and Lang, G.; *J. Am. Chem. Soc.*, (1979). **101**: 2948-2958.
41. Cheng, R.-J., Chen, P.-Y., Gau, P.-R., Chen, C.-C., and Peng, S.-M.; *J. Am. Chem. Soc.*, (1997). **119**: 2563-2569.
42. Li, Y., Syvitski, R.T., Auclair, K., Wilks, A., Ortiz de Montellano, P.R., and La Mar, G.N.; *J. Biol. Chem.*, (2002). **277**: 33018-33031.

Chapter V

A NOVEL ELECTRONIC STRUCTURE IN THE AZIDE COMPLEX OF *PSEUDOMONAS AERUGINOSA* HEME OXYGENASE: MECHANISTIC IMPLICATIONS FOR HEME DEGRADATION.

Introduction

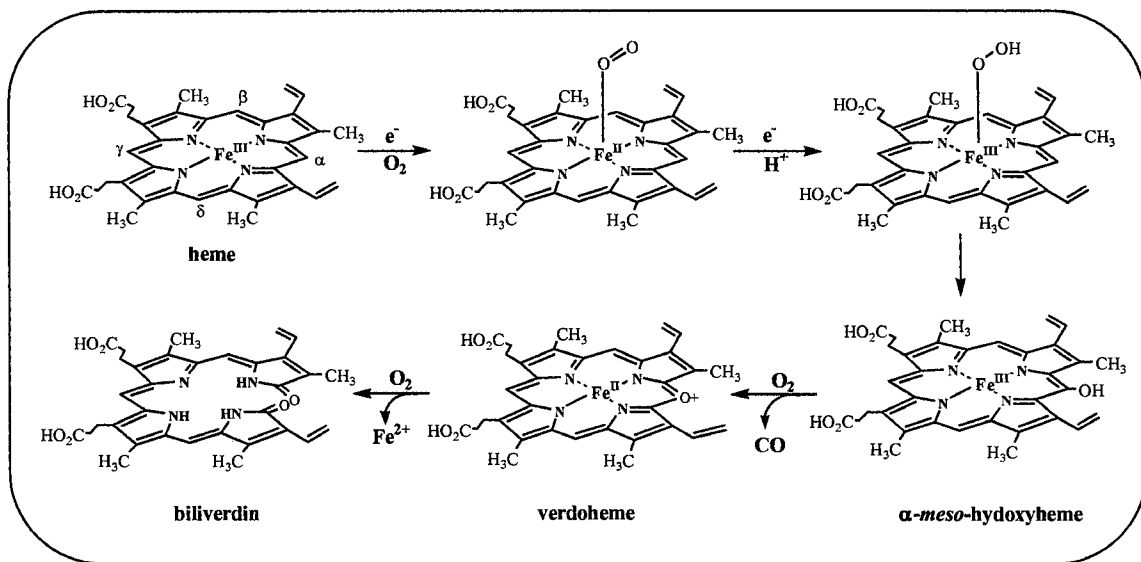
Heme oxygenase (HO) catalyzes the degradation of heme in a molecular oxygen and electron dependent fashion to produce biliverdin, free iron, carbon monoxide (CO) and biliverdin. In heme oxygenation, the first step in the catalytic cycle involves reduction of heme by NADPH cytochrome P450 reductase to its ferrous form. This is followed by the coordination of molecular oxygen to yield a metastable oxyferrous complex which is converted into ferric hydroperoxide after accepting a second electron from the reductase. The ferric hydroperoxide species is known to hydroxylate the heme at the α -meso carbon producing α -mesohydroxyheme [1]. The latter is then converted into verdoheme and CO in an oxygen dependent reaction. Finally a molecule of oxygen and additional electron equivalents will convert verdoheme into biliverdin which is the the end product of the HO catalytic cycle (see Scheme 1) [2].

Heme oxygenase is responsible for the the physiological catabolism of heme, which is known to be a strong oxidant in its free form. HO also plays an important role in iron homeostasis in mammals and the three heme oxygenation products have been tied to a variety of physiological functions. Plant and bacterial heme oxygenases have also been indentified and seem to function in a manner indentical to that of their mammalian

counterparts while playing a significant role in the synthesis of the tetrapyrrole-containing chromophores of photosynthetic organisms [3].

While the nature of the products of heme oxygenase activity has been known for some time it is only recently that the first step in the catabolic pathway of heme has been proven to go through a ferric hydroperoxide intermediate [1]. Evidence for the presence of this key intermediate was obtained by forming the oxygen complex of heme oxygenase followed by reduction at cryogenic temperatures (77 K). An EPR signal corresponding to the ferric hydroperoxide intermediate appears almost immediately while annealing to 214 K results in the appearance of α -meso-hydroxyheme [1, 4]. Interestingly, the catalytic cycles of peroxidases and monooxygenases also proceeds via the formation of an obligatory ferric hydroperoxy intermediate. In the latter case, however, the $\text{Fe}^{\text{III}}\text{-OOH}$ species decays into an iron(IV) ferryl species, which is responsible for the oxidative chemistry performed by this class of enzymes. The reason behind the distinct reactivity exhibited by the $\text{Fe}^{\text{III}}\text{-OOH}$, which leads to the hydroxylation of the heme macrocycle in the case of heme oxygenase and the formation of an Fe(IV)=O species in the case of monooxygenases and peroxidases is not yet completely understood. Recent studies conducted with a *tert*-butyl peroxide complex of tetraphenyl porphyrin [5] and with the hydroxide complex of the heme oxygenase from *Pseudomonas. aeruginosa* (*pa*-HO) [6] suggest that the critical $\text{Fe}^{\text{III}}\text{-OOH}$ intermediate adopts non-planar porphyrin conformations and unusual heme electronic configurations that are thought to impart the heme macrocycle with reactive character, thereby activating it to priming it to actively participate in its own hydroxylation [5, 6].

The study conducted with the alkyl peroxide complex of tetraphenylporphyrin revealed the presence of an equilibrium between a planar ferriheme possessing the common $S = 1/2$, $(d_{xy})^2 (d_{xz}, d_{yz})^3 (d_{\pi} \text{ hereafter})$ electronic configuration and a ruffled ferriheme with the less common $S = 1/2$, $(d_{xz}, d_{yz})^4 (d_{xy})^1 ((d_{xy})^1 \text{ hereafter})$ electronic configuration [5]; Ferrihemes with the $(d_{xy})^1$ electronic configuration are known to delocalize relatively large amounts of spin density at the meso carbons of the porphyrin ring [7, 8]. It was found that at physiological temperatures the observed equilibrium favors the non-planar $(d_{xy})^1$ electronic configuration [5]. This could justify the observed reactivity and regioselectivity of heme oxygenation as unpaired electron density at the meso positions would constitute an undeniable driving force for hydroxylation while the ruffled geometry of the macrocycle would place two meso carbons closer to the terminal oxygen of the iron-bound hydroperoxide. On the other hand, ^{13}C NMR analysis of the hydroxide complex of *pa*-HO, which was used as a less reactive model of the ferric hydroperoxide complex, revealed the existence of a mixture of unusual heme electronic configurations at ambient temperatures. Three populations with unique electronic configurations were observed: 1) a $S = 3/2$, $1/2$ spin-state crossover, 2) a pure $S = 3/2$ and 3) a pure $S = 1/2$, $(d_{xz}, d_{yz})^4 (d_{xy})^1$ [6]. Work conducted with model ferrihemes has demonstrated that the $S = 1/2$, $S = 3/2$ spin-state cross-over, the $S = 3/2$ and the $S = 1/2$, $(d_{xy})^1$ electronic configurations are associated with significant distortions of the porphyrin ring from planarity [9-12]. The $S = 3/2$ iron electronic configuration is interesting in that the large amounts of positive spin density at the α positions of the macrocycle create negative spin density at the adjacent meso positions by polarization when the porphyrin $3e(\pi)$ orbital is used for delocalization. Thus, three electronic configurations



Scheme 1: Heme oxygenase catalytic cycle

observed in the hydroxide complex of the *pa*-HO enzyme are associated with the presence of large amounts of spin density at the meso positions and significant distortions of the porphyrin ring from planarity. These observations led the authors to suggest that within the confines of the heme oxygenase pocket, the flexible nature of the latter in conjunction with the presence of an extended network of water molecules capable of hydrogen bonding to an axially bound hydroxide, or hydroperoxide, can alter the ligand field strength of the distal ligand, and stabilize unusual heme electronic configurations.

This prompted us to investigate the possibility that the unusual nature of the heme binding site in HO would promote the distortion of the heme macrocycle and the stabilization of unusual electronic structures upon binding of azide. This ligand was chosen because it is capable of accepting a hydrogen bond by the coordinated N atom but has a field strength that, while higher than that of hydroxide, is not too far removed [13]. As will be shown below, azide binding was found to induce the formation of a novel heme-iron electronic configuration whose properties are distinct from the typical planar d_{π} configurations usually observed for the low spin complexes of globins and are reminiscent of the likely non-planar distortions present in the hydroxide complex of *pa*-HO.

Experimental Section

a) Protein preparation and reconstitution with ^{13}C -labeled heme.

Heme oxygenase from *Pseudomonas aeruginosa* (*pa*-HO) was expressed and purified as described previously [14, 15]. ^{13}C -Labeled δ -aminolevulinic acids (ALA) were used as biosynthetic precursors for the preparation of protoheme IX (heme)

according to previously described methodology [16, 17]. [5-¹³C]- δ -Aminolevulinic acid ([5-¹³C]-ALA), [4-¹³C]-ALA and [1,2-¹³C]-ALA were synthesized according to methodology described previously [18]. [1,2-¹³C]-ALA was employed for the preparation of heme labeled at the methyl, β -vinyl and β -propionate carbons shown in Figure 4. [5-¹³C]-ALA was used to prepare heme labeled at the meso (C_m) and α -pyrrole (C_α) carbons shown in Figure 7-A, and [4-¹³C]-ALA was utilized to prepare heme labeled at the C_α and β -pyrrole (C_β) carbons shown in Figure 7-B. Isotopically labeled heme was initially purified in its complex with rat liver outer membrane (OM) cytochrome b_5 [16, 17]. ¹³C-labeled heme is then extracted from OM cytochrome b_5 as follows: While maintaining the temperature at 4 °C, 15 mL of pyridine was added to 2.5 mL of rat OM cytochrome b_5 (1 mM) dissolved in phosphate buffer ($\mu = 0.1$, pH = 7.0). Slow addition of chloroform (10-15 mL) typically resulted in the precipitation of the polypeptide, while maintaining the pyridine hemochrome in the supernatant. The latter was separated from the precipitate by centrifugation, allowed to equilibrate at room temperature, and then dried over anhydrous MgSO₄. The desiccant was separated by filtration and the solution evaporated to dryness with the aid of a rotary evaporator. The solid was redissolved in 1-2 mL of dimethyl sulfoxide and the resultant solution was immediately used to reconstitute HO. To this end, a solution (40 mL) containing approximately 2 μ mol of *pa*-HO was titrated with the solution containing ¹³C-labeled heme until the ratio A_{280}/A_{Soret} no longer changed. The resulting solution was incubated at 4 °C overnight and subsequently purified using a Sephadex G-50 column (3 cm x 100 cm), previously equilibrated with phosphate buffer, $\mu = 0.10$ and pH = 7.0.

b) Spectroscopic studies.

^1H and ^{13}C NMR spectra were acquired on a Varian Unity Inova spectrometer operating at frequencies of 598.611 and 150.532 MHz, respectively. ^1H spectra were referenced to the residual water peak at 4.8 ppm, and ^{13}C spectra were referenced to an external solution of dioxane (60% v/v in D_2O) at 66.66 ppm. Spectra from low spin HO were acquired with presaturation of the residual water peak, with an acquisition time of 250 ms, and a 25 ms relaxation delay, over a spectral width of 30 kHz. ^{13}C NMR spectra were typically collected from solutions containing approximately 3 mM HO in phosphate buffer with an ionic strength of 0.1 at pH 7.4; the pH readings have not been corrected for the deuterium isotope effect. The samples were concentrated to 250 μL in centrifugal concentrators equipped with 10,000 molecular weight cut-off membranes (Centricon-Millipore Co, Bedford, MA) and then transferred to Shigemi NMR tubes (5 mm) with susceptibilities matched to D_2O (Shigemi, Inc., Allison Park, PA). ^{13}C spectra were acquired over 48 K data points, with a spectral width of 60 kHz, an acquisition time of 80 ms, no relaxation delay and 250,000 scans. HMQC spectra were typically acquired with with spectrall widths of 30 kHz for ^1H and 60 kHz for ^{13}C and a 25 ms relaxation delay [19]. HMQC spectra obtained from samples containing HO reconstituted with heme labeled using $[1,2\text{-}^{13}\text{C}]\text{-ALA}$ as a heme precursor (see Figure 5) were acquired with refocusing delays based on $^1J_{\text{CH}} = 140$ Hz. Data were collected as an array of 2k x 256 points with 256 scans per t_1 increment and processed by zero-filling twice in both dimensions. This was apodized with a 90° -shifted squared sine bell and Fourier transformed. NOESY spectra were acquired with 30 kHz in both dimensions, 2k data points in t_2 , 256 increments in t_1 , 256 scans, a 25 ms relaxation delay and a mixing time

of 30 ms. The data were processed by zero-filling in both dimensions, apodized with a 90°-shifted squared sine bell and Fourier transformed.

The conversion of ferric *pa*-HO in water at pH 7.4 to low spin ($\text{Fe}^{\text{III}}\text{-N}_3$) *pa*-HO was effected by the addition of five molar equivalents of sodium azide from a 1 M solution prepared from the commercially available salt. The transformation of the aquo complex into its azido counterpart was monitored by electronic absorption spectroscopy, with the aid of a UV-Vis S2000 spectrophotometer (Ocean Optics, Dunedin, FL). To this end, a solution of (Fe^{III}) *pa*-HO in water (pH 7.4) was placed in a quartz cuvette (1-cm path length) where it was stirred continuously with the aid of a magnetic bar and a sodium azide solution was titrated in until a constant UV-Vis signature was obtained.

Results

*a) Electronic Absorption and ^1H NMR Spectroscopic characterization of the azide complex of *pa*-HO.*

Electronic absorption spectroscopy was used to characterize the azide complex of *pa*-HO. Figure 1 shows the electronic absorption spectra of *pa*-HO at pH 7.4 (Figure 1-A) and in complex with cyanide and azide (Figure 1-B and -C respectively). The spectrum of *pa*-HO-CN is illustrative of a ferric low spin species with a Soret band at 419 nm and α and β bands at wavelengths of 534 and 568 nm respectively. The spectrum of *pa*-HO at pH=7.4 however has a maximum absorption at 406 nm and a series of bands at 504, 540, 574 and 630 nm. The 504 and 630 nm absorption features are characteristic of high-spin ferric heme proteins while those at 530 and 570 correspond to the presence of a low-spin species [20]. The presence of these bands in the visible part of the spectrum is in

agreement with the presence of high-spin aquo ($\text{Fe}^{\text{III}}\text{-H}_2\text{O}$) and low-spin hydroxo ($\text{Fe}^{\text{III}}\text{-OH}$) species in equilibrium[6], because the aquo to hydroxo transition in *pa*-HO is characterized by $\text{pK}_a = 8.3$. Addition of azide to the solution of Figure 1-A results in the formation of the azide complex of *pa*-HO, a phenomenon immediately apparent from the resultant electronic absorption spectrum (Figure 1-B) which is typical of low spin iron (III) hemoproteins; Soret band at 418 in addition to α and β bands at 582 and 541 nm respectively. Excess azide (50 equivalents) is needed to stabilize the ^1H NMR analysis of the formation and properties of *pa*-HO- N_3 complex was also carried out. At pH 7.4, the high frequency portion of the ^1H NMR spectrum of (Fe^{III}) *pa*-HO (Figure 2-a) displays a set of resonances between 80 and 40 ppm and another ranging from 25 to 10 ppm. The hyperfine shifted peaks observed above 40 ppm correspond to the high spin ($\text{Fe}^{\text{III}}\text{-H}_2\text{O}$) complex of *pa*-HO while those in the 25-10 ppm region belong to the low spin ($\text{Fe}^{\text{III}}\text{-OH}$) complex. The pK_a of the $\text{Fe}^{\text{III}}\text{-H}_2\text{O}$ to $\text{Fe}^{\text{III}}\text{-OH}$ transition is 8.3, thus the presence of resonances characteristic of the high spin $\text{Fe}^{\text{III}}\text{-H}_2\text{O}$ and low spin $\text{Fe}^{\text{III}}\text{-OH}$ complexes in the spectrum at pH 7.4 is consistent with the previously established slow exchange between these complexes relative to the NMR time scale [6]. Upon addition of 0.5 equivalents of sodium azide to the solution of *pa*-HO at pH 7.4, the resonances corresponding to the $\text{Fe}^{\text{III}}\text{-H}_2\text{O}$ and $\text{Fe}^{\text{III}}\text{-OH}$ complexes decrease in intensity, with the concomitant appearance of a new set of peaks between 18 and 13 ppm(See Figure 2-b). Addition of 1.0 and 1.5 equivalents of sodium azide, results in further decrease of the concentration of the $\text{Fe}^{\text{III}}\text{-H}_2\text{O}$ and $\text{Fe}^{\text{III}}\text{-OH}$ species: in fact, when 1.5 equivalents have been added the conversion to $\text{Fe}^{\text{III}}\text{-N}_3$ is quantitative.

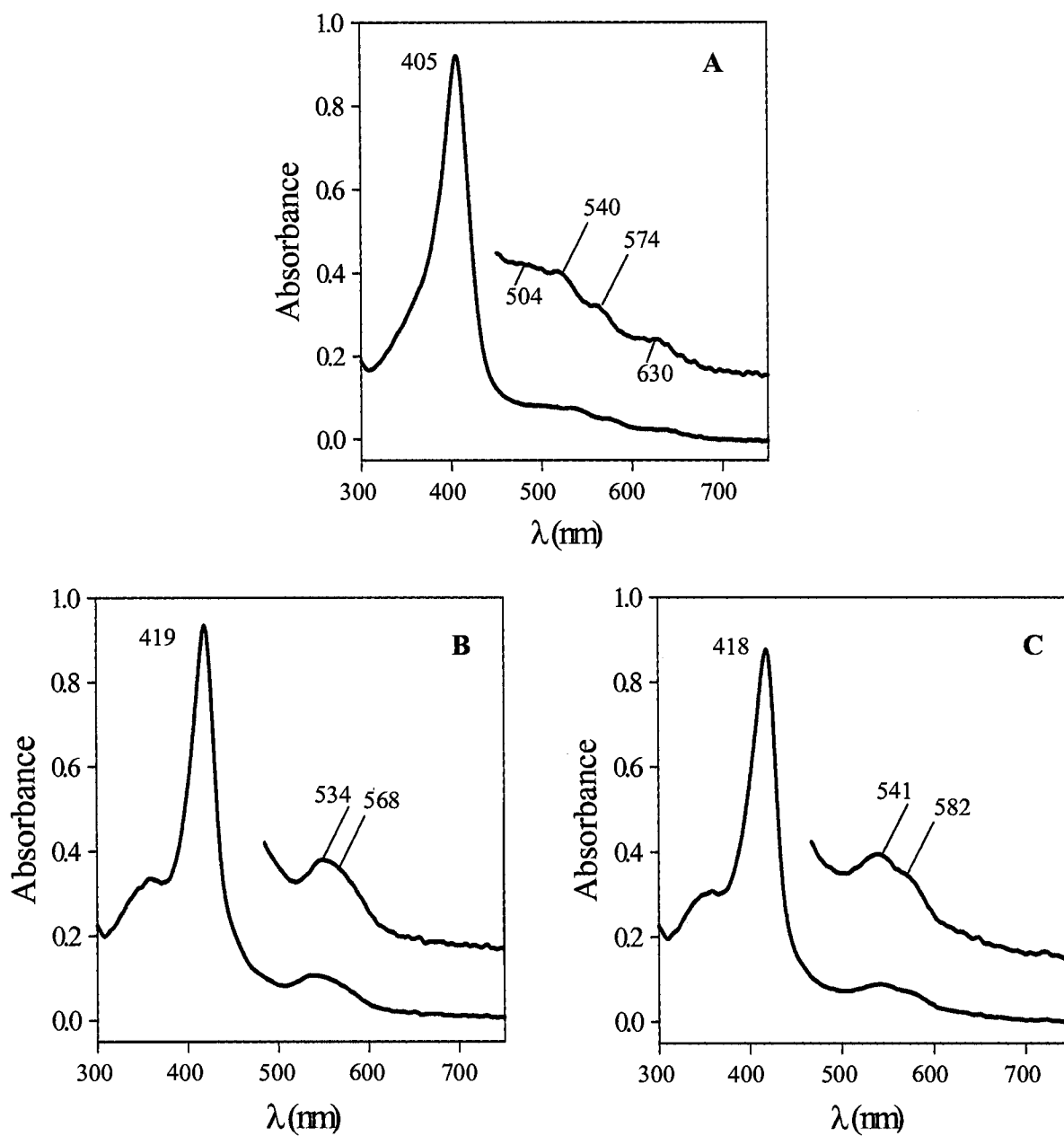


Figure 1. Electronic absorption spectra of *Pseudomonas aeruginosa* heme oxygenase at pH=7.4 (A) and in complex with azide (B) and cyanide (C). Spectra were recorded at room temperature.

It is evident that the chemical shifts observed for $\text{Fe}^{\text{III}}\text{-N}_3$ *pa*-HO (Figure 3-c) do not correspond to a high spin electronic configuration of the heme iron, as the five unpaired electrons in such cases produce much larger hyperfine shifts, typically ranging from 40 ppm to as much as 120 ppm [21]. The hyperfine shifted peaks present between 10 and 18 ppm more typical of the low-spin $S = 1/2$ electronic configuration, such as that exhibited by myoglobin or hemoglobin in complex with a cyanide ligand [21] or the bis-histidine coordinated cytochromes b [7]. It is noteworthy that the quantitative formation of the *pa*-HO- N_3 complex can be unambiguously determined from the complete disappearance of resonances corresponding to the high-spin $\text{Fe}^{\text{III}}\text{-H}_2\text{O}$ and low-spin $\text{Fe}^{\text{III}}\text{-OH}$ complexes. By comparison, the addition of azide to metmyoglobin from sperm whale and hemoglobin from *Chironomus thummi thummi* results in the formation of a low spin azide complex in fast exchange with the high-spin ($\text{Fe}^{\text{III}}\text{-H}_2\text{O}$) met-aquo form of the globins. Fast exchange is manifested in the relatively large chemical shifts of the heme methyl ($\delta > 35$ ppm) groups as a consequence of the weighted average between the high-spin and low-spin states [20, 22].

The ^1H NMR spectrum of *pa*-HO in complex with cyanide at pH 7.4 is shown in Figure 3 (a). This spectrum is representative of an $S = 1/2$ low spin iron in the $(d_{xy})^2 (d_{xz}, d_{yz})^3$ electronic configuration. Three resonances corresponding to the porphyrin methyl groups and two corresponding to vinyl β protons are hyperfine shifted out of the diamagnetic protein envelope to high and low frequency, respectively. The high and low portions of the ^1H NMR spectrum of the azide complex of *pa*-HO are shown in Figure 3 (c). This spectrum is different from that obtained for the *pa*-HO-CN complex in that the heme-methyl peaks are found at lower frequencies and the vinyl β resonances at higher

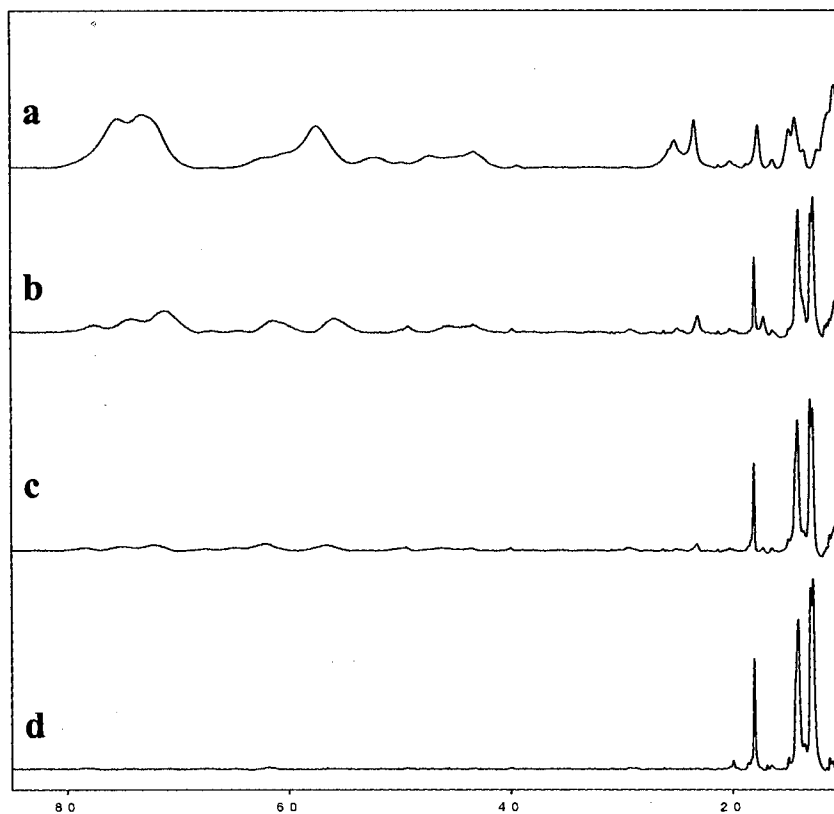


Figure 2. High frequency portion of the ^1H NMR spectra of *pa*-HO obtained at 25 °C and pH 7.4. Spectra after the addition of 0 (a), 0.5 (b), 1 (c) and 1.5 (c) equivalents of sodium azide.

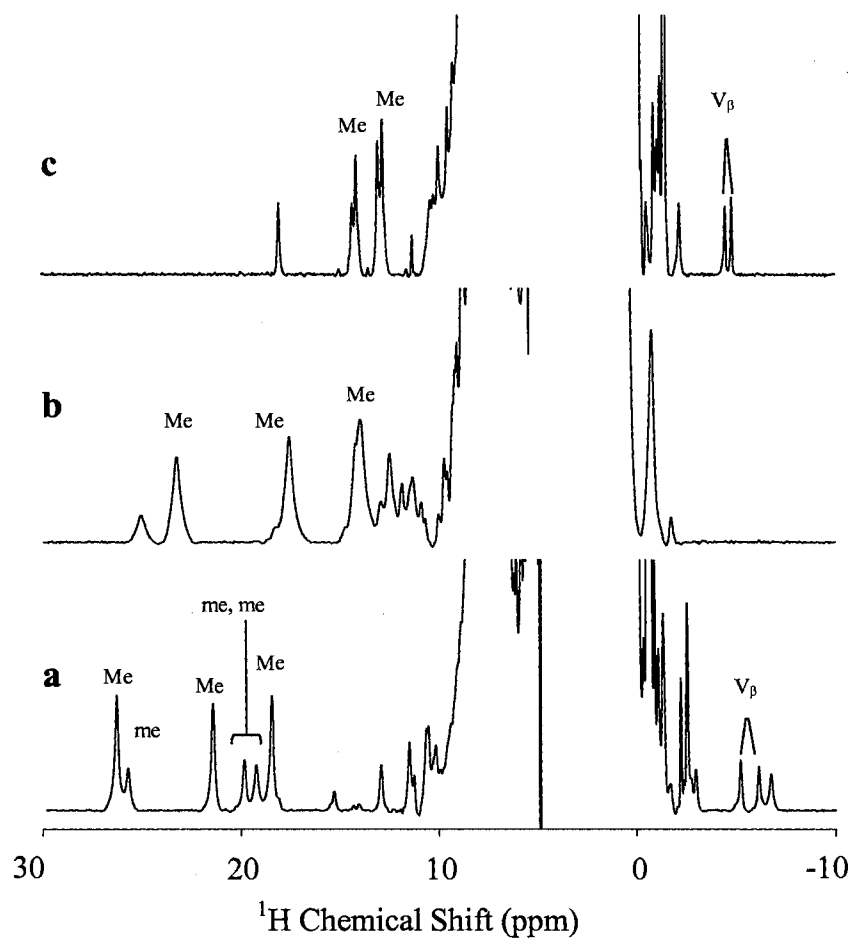


Figure 3. ¹H NMR spectra of (a) (Fe^{III}-N₃) *pa*-HO at pH 7.4, (b) (Fe^{III}-OH) *pa*-HO at pH 10.3 and (c) (Fe^{III}-CN) *pa*-HO at pH 7.4. All spectra were acquired at 25 °C.

frequencies. The azide complex of *pa*-HO exhibits reduced hyperfine shifts just as the hydroxide complex of the same enzyme did at pH 10.3. It is important to note however that in the case of *pa*-HO-N₃ the methyl shifts have been reduced to a much greater extent, in comparison to those of *pa*-HO-CN, than what was observed for the hydroxide complex. Indeed, the reduction in observed hyperfine shifts for the heme methyl substituents is such that instead of the three methyl resonances being resolved from the protein envelope of diamagnetic resonances, in the case of both *pa*-HO-CN and *pa*-HO-OH we see only two.

b) ¹H and ¹³C NMR Resonance assignments for *pa*-HO in complex with azide.

In an effort to further characterize the *pa*-HO-N₃ complex, partial assignment of the ¹H and ¹³C NMR resonances of the heme prosthetic group was carried out with the aid of 1- and 2-dimensional, homo- and hetero-nuclear experiments. Resonance assignments in paramagnetic heme proteins are typically met with multiple challenges. Short nuclear relaxation times induced by the presence of unpaired electrons result in low cross peak intensities and the compromised effectiveness of pulse sequences with multiple delays [21]. The asymmetric distribution of electron density on the porphyrin macrocycle will produce large hyperfine shifts for certain resonances and small shifts for others [23, 24]. In addition to the difficulties mentioned above, heme isomerism results in the doubling of resonances originating from the macrocycle [25, 26]. To attenuate these difficulties, heme labeled with ¹³C at different positions was used to reconstitute samples of *pa*-HO. Using a sample of *pa*-HO-N₃ reconstituted with heme labeled as in Figure 4, a non-decoupled carbon and HMQC experiments were obtained at 25 °C. The

high and low frequency portions of the HMQC spectrum thus obtained are shown in Figure 4. The portion of the ^1H -coupled ^{13}C NMR spectrum appended to the HMQC in Figure 4-A clearly shows that the heme methyl carbons (quartets) resonate between 5 and -20 ppm and that the corresponding ^1H chemical shifts are found at 14.92, 13.84, 7.20 and 6.8 ppm (Table 1). A similar appraisal of the high frequency portion of the carbon spectrum in Figure 4-B allows the relatively straightforward identification of the vinyl and propionate β carbons. The vinyl β resonances appear as triplets, with $^1J_{\text{CH}} \sim 140$ Hz, due to the two scalarly coupled methylene protons attached to the labeled carbon. The β propionate carbons also show signs of scalar coupling, with a triplet ($^1J_{\text{CH}} \sim 140$ Hz) of doublets ($^1J_{\text{CC}} \sim 40$ Hz) resulting from the two attached protons and the neighbouring ^{13}C labeled carbonyl carbon (Figure 4-inset). The heteronuclear correlations are well resolved and unambiguous allowing the proton chemical shifts corresponding to both the vinyl and propionate β groups to be obtained. The ^1H and ^{13}C chemical shifts for all four heme methyls as well as the two vinyl β and propionate β groups are summarized in Table 1.

Similarly, a sample of *pa*-HO was reconstituted with the labeled heme shown in Figure 9-A to study the meso proton and carbon resonances. While this sample was used to determine the ^{13}C chemical shifts of the meso carbons (C_m) as explained later on, the meso carbon to meso proton heteronuclear correlations could not be identified from the corresponding HMQC. With the aid of the previously determined ^1H shifts of the four heme methyls as well as the two vinyl β and two propionate β protons, the dipolar correlations represented schematically by red lines were identified in the NOESY spectrum of *pa*-HO- N_3 , acquired at 25 °C (See Figure 5). The methyl groups found at

Table 1: ^1H and ^{13}C chemical shifts for heme substituents of *pa*-HO-N₃

Group	^1H δ (ppm)	^{13}C δ (ppm)
Methyl	14.92	-16.72
	13.84	-14.71
	7.20	-0.99
	6.8	-1.6
Vinyl β	-4.37, -4.85	187.68
	0.41, -0.16	152.49
Propionate β	0.28, -0.38	110.37
	-0.99, -2.01	101.03

14.92 and 7.2 ppm in the HMQC of *pa*-HO-N₃ reconstituted with heme labeled using [1,2-¹³C]-ALA as a precursor, are dipolarly coupled to vinyl β proton resonances. This implies that these two methyl resonances correspond to heme methyl groups 1 and 3 in Figure 4, as they are the heme methyl substituents closest to the vinyl groups. The remaining two methyl resonances must correspond to heme methyl groups at positions 5 and 8. The correlation observed between the methyl resonance at 13.48 ppm in the NOESY spectrum of Figure 5 and the resonances identified as a set of propionate β methylene protons confirms the latter conclusion, as methyls 5 and 8 are in close proximity to the 6 and 7 propionates, respectively. In the absence of identified meso proton resonances, the assignment of heme substituent resonances could not be taken any further.

c) Heme methyl ¹H chemical shifts suggest that the heme electronic structure of *pa*-HO-N₃ is not the common $S = 1/2, d_{\pi}$

The effect of heme axial ligand orientation on the observed spread and intensity of heme methyl paramagnetic shifts in both heme proteins and porphyrin complexes is well known. It has been shown that the proton hyperfine shifts of heme methyl groups of Fe(III) heme complexes as well as those of ferric heme proteins are related to the angle ϕ , the axial histidine makes with the metal-pyrrole II nitrogen axis in histidine-cyanide low spin systems with d_{π} electronic configurations and planar hemes [27-30]. This is due to the interaction of the histidine-imidazole π orbitals with the iron centered π orbitals that individually interact with the porphyrin $3e(\pi)$ molecular orbitals. As the histidine rotates, the interaction of its π orbitals with the iron d_{xz} and d_{yz} orbitals will change. This

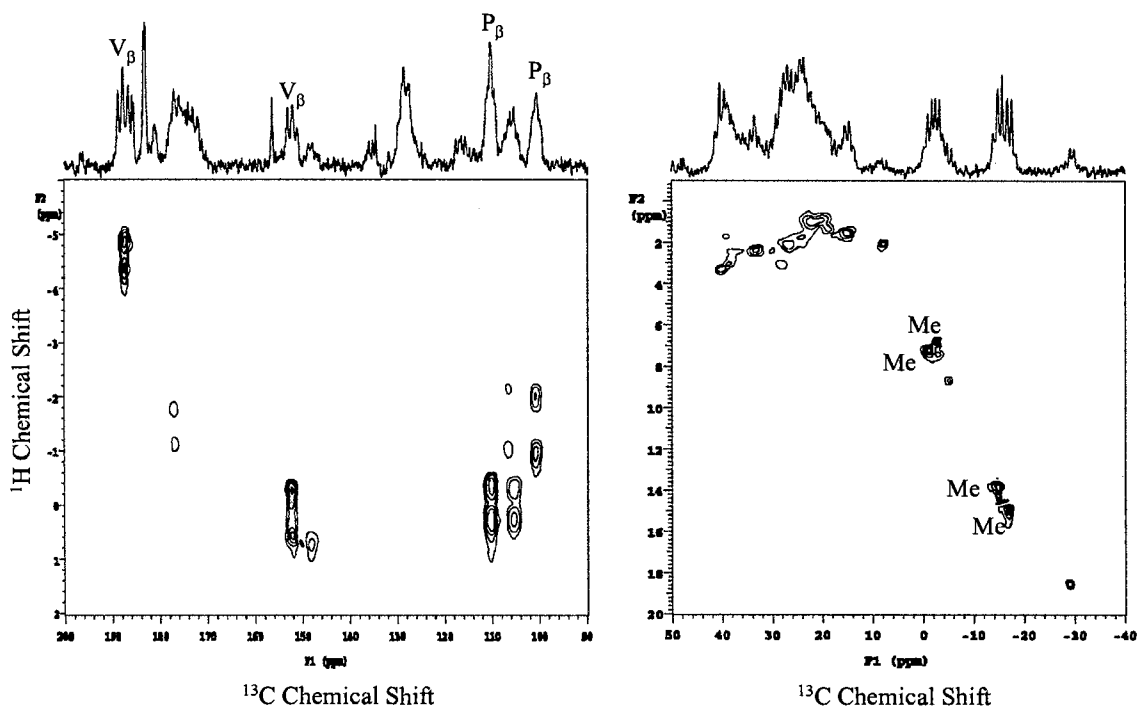
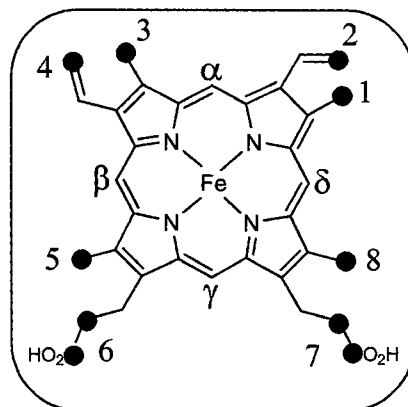


Figure 4. High (A) and low (B) frequency portions of the HMQC spectrum of *pa*-HO-N₃ reconstituted with ¹³C-labeled heme prepared from [1,2-¹³C]-ALA shown above (Labeled carbons are represented by ●). The methyl (Me), vinyl β (V_β) and propionate β (P_β) resonances corresponding to the major heme rotational isomer are labeled.

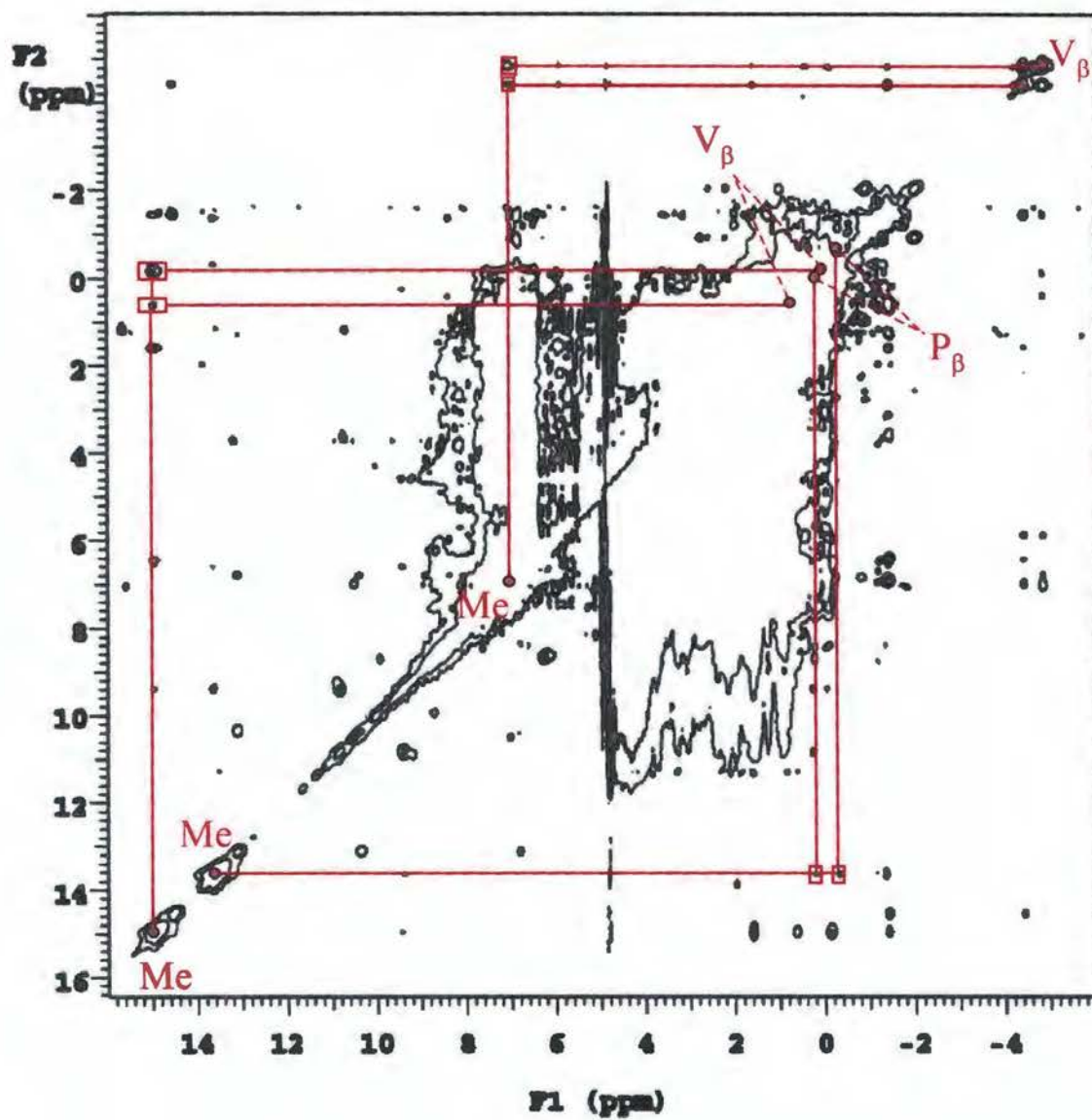


Figure 5. NOESY spectrum of *pa*-HO-N₃ at 25 °C. Heme methyl (Me) dipolar correlations to vinyl β (V_{β}) and propionate β (P_{β}) protons are represented by red lines.

varying interaction will be passed on to the porphyrin $3e(\pi)$ molecular orbitals, lift the degeneracy of the porphine orbitals by altering their energies thereby dictating the relative population of the same orbitals. The resulting differential in population of the $3e(\pi)$ porphine orbitals is largely responsible for the asymmetric distribution of spin density on the macrocycle.

Bertini *et al.* developed the following equation for heme proteins ligated by an endogenous histidine and an exogenous cyanide:

$$\delta_i = a \sin^2(\theta_i - \phi) + b \cos^2(\theta_i + \phi) + c \quad (1)$$

where δ_i is the chemical shift of methyl i , θ_i is the angle methyl i makes with the metal-pyrrole II nitrogen axis, ϕ is the angle that the histidine imidazole plane makes with the metal-pyrrole II nitrogen axis and the coefficients a , b and c have values of 18.4 ± 2.4 , -0.8 ± 2.0 and 6.1 ± 1.9 ppm, respectively (See Figure 6-Top) [31]. Using this equation, the ϕ values available from known crystal structures and the proton chemical shift assignments for the heme methyl groups of various proteins, the authors were able to construct a plot of the methyl chemical shifts calculated from their equation versus the chemical shifts observed in solution by ^1H NMR. The plot thus constructed showed very good agreement between the observed and calculated values of the methyl shifts, confirming the nearly quantitative relationship between axial ligand geometry and ^1H methyl shifts. A similar plot is shown in Figure 6-A for the cyanide complexes of myoglobin [32], *pa*-HO and *Corynebacterium diphtheriae* HO (*cd*-HO) that were used as examples to illustrate the correlation between experimental and calculated chemical shifts

that is typical of heme proteins possessing the low spin $S = 1/2$, d_{π} electronic configuration [14].

In this context it is interesting to consider the azide complex of sperm-whale metmyoglobin that is known to exist in solution as a mixture of high and low spin states in fast exchange relative to the NMR time scale [20, 33]. When the ^1H methyl shifts calculated for this species according to equation (1), are plotted against the values obtained from ^1H NMR solution measurements, the entries represented by yellow circles are obtained (See Figure 8-B). It is apparent that all of the heme methyl chemical shifts observed for the azide complex of myoglobin are larger than those calculated by equation (1). This is a manifestation of the fact that the observed chemical shifts are a weighted average of the very large chemical shifts of high-spin ($\sim 15\%$ character) and smaller chemical shifts ($\sim 85\%$) characteristic of low-spin ferrihemes. Consequently, all entries corresponding to the azide complex of myoglobin lie considerably below the diagonal correlating the experimental and calculated chemical shifts in pure low-spin, d_{π} ferrihemes. The entries corresponding to the myoglobin azide complex result in a behaviour that does not conform to that observed for pure low spin d_{π} complexes.

The heme methyl resonances of the azide complex of *pa*-HO although only partially assigned can still be used in the context of the plot presented above and the graph shown in Figure 6. Assuming that the orientation of the axial histidine in *pa*-HO- N_3 is the same as the one adopted by the histidine in *pa*-HO-CN, we can calculate the ^1H chemical shifts expected for each of the four heme methyls in the azide complex from equation (1). Assuming that the orientation of the axial histidine does not change upon binding of azide is reasonable because the crystal structures of rat HO in its resting state, and in complex

with azide show no changes in proximal histidine orientation [34]. As indicated previously we can group the heme methyl resonances into pairs. One pair (14.92, 7.20 ppm) corresponds to 1Me and 3Me while the other corresponds to 5Me and 8Me. For each pair of methyl groups we have two sets of possible assignments. It is therefore possible to plot the observed chemical shift for one of the methyl groups against two values of calculated chemical shift. For instance, the chemical shift at 14.92 ppm can be ascribed to 1Me or 3Me, thus the 14.92 ppm value can be plotted against two calculated chemical shifts, 3.97 and 20.43 (filled circle and triangle in Figure 8). It is apparent that none of the corresponding entries fall within the expected correlation typical of a $S = 1/2$, d_{π} electronic structure. Along the same vein, the second chemical shift in this pair (7.20 ppm) is plotted against the calculated chemical shift for 1Me and 3Me (open circle and triangle in Figure 8). In a similar manner, the observed chemical shifts for each methyl group in the pair that exhibit NOE crosspeaks with the heme propionates (6.80 ppm and 13.84 ppm) were plotted against calculated values for the 5Me and 8Me groups. It is evident that these entries exhibit significant differences from the correlation that is typical of $S = 1/2$, d_{π} complexes, an observation that strongly indicates that the electronic configuration of the heme in *pa*-HO-N₃ is not the $S=1/2$, d_{π} .

d) ¹³C NMR Spectroscopy of the porphyrin methyl carbons suggests a change in the electronic structure of the heme.

In an effort to gain a better understanding of the unusual ¹H chemical shifts observed for the heme methyl groups in *pa*-HO-N₃, a sample of the enzyme was prepared with heme labeled at the methyl carbons (See Figure 4). Resonances

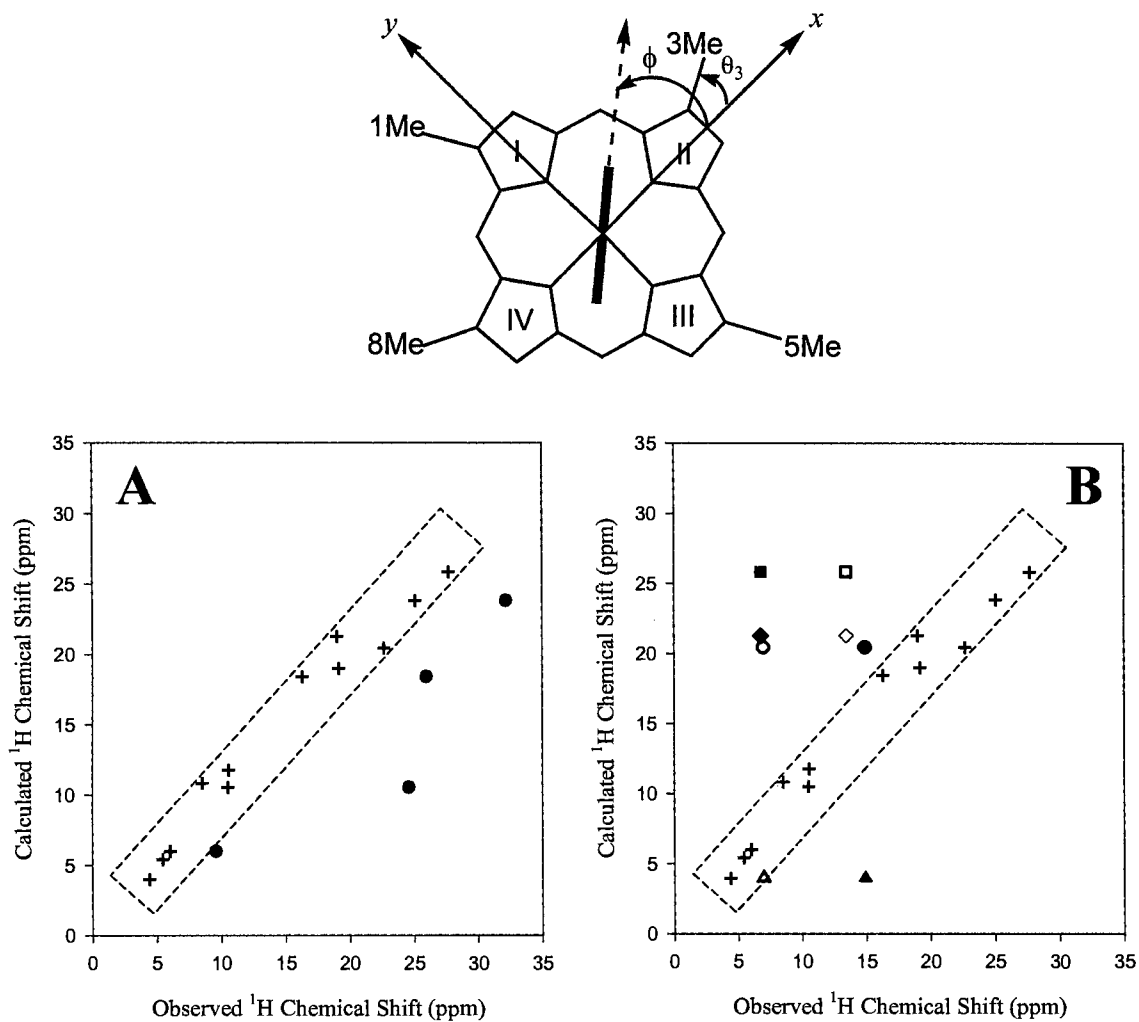


Figure 6. Plot of calculated versus observed shifts of heme methyl protons. Panel A: (+) Typical S=1/2, d_π cyanide complexes of heme oxygenase from *Pseudomonas aeruginosa*, *Corynebacterium diphtheriae* and sperm whale myoglobin; (•) azide complex of sperm whale myoglobin. Panel B: 1Me (• or ○), 3Me (▲ or Δ), 5Me (■ or □) and 8Me (◆ or ◇).

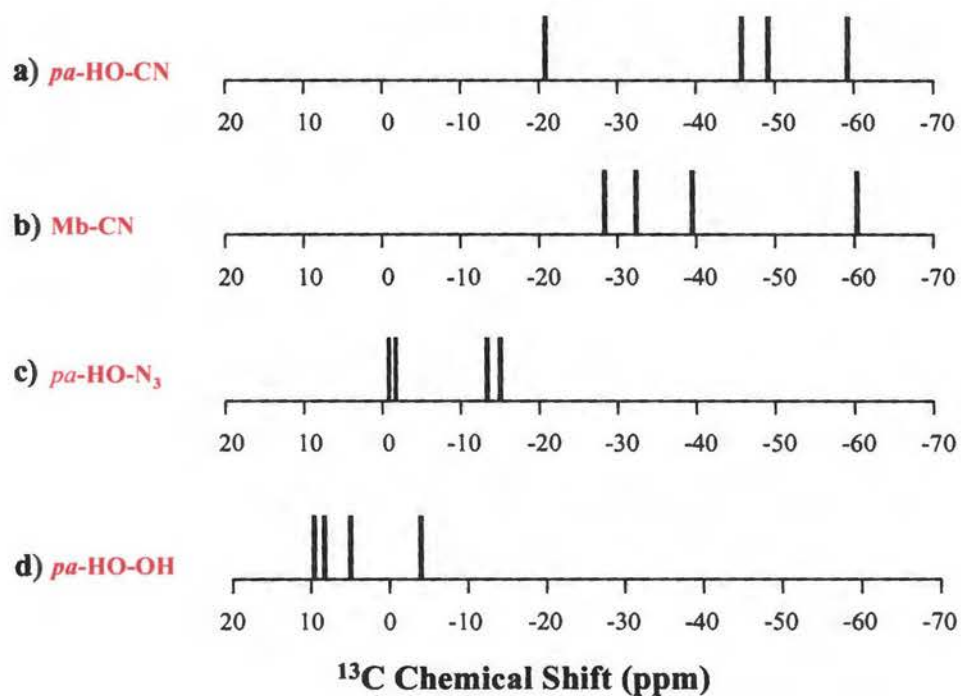


Figure 7. Schematic representation of the ¹³C NMR spectra of a) *pa*-HO-CN [14] , b) met-myoglobin cyanide [32] , c) *pa*-HO-N₃ and d) *pa*-HO-OH [32]. All the spectra were obtained at 25 °C with the exception of the one corresponding to *pa*-HO-CN which was taken at 10 °C.

originating from the carbons are readily identified as $J_{\text{CH}}^1 \sim 140$ Hz quartets. As has been illustrated in Figure 4-B, the methyl carbon chemical shifts obtained for *pa*-HO-N₃ are schematically summarized in a schematic fashion in Figure 7-c. Inspection of this figure reveals that the methyl carbon resonances occur at significantly higher frequencies than those observed for typical $S = 1/2$, d_{π} heme centers, such as met-myoglobin or *pa*-HO (Figures 7-a and 7-b). The latter complexes exhibit carbon chemical shifts that are centered around -40 ppm whereas those of azido *pa*-HO are clustered around -8 ppm

In the case of ferrihemes with the $S = 1/2$, d_{π} electron configuration the d_{xz} and d_{yz} orbitals interact with the $3e(\pi)$ porphyrin molecular orbital shown in Figure 8 [7, 35]. The latter molecular orbital has large wave function coefficients at the β pyrrole carbons (C_{β}). Thus, delocalization of the unpaired electron of the iron onto the porphyrin ring results in a large amount of positive π spin density at the C_{β} positions which is manifested in relatively large and positive C_{β} chemical shifts (~ 200 ppm) [16]. The attached methyl carbons will experience spin polarization, which is responsible for the large and negative carbon chemical shifts in the ^{13}C NMR spectra of low spin ($S = 1/2$, d_{π}) ferric heme proteins (See Figures 7-a and 7-b) [35].

As previously noted, the average ^{13}C chemical shift of the methyl resonances in the *pa*-HO-N₃ complex is approximately 40 ppm higher than the average chemical shift typical of $S = 1/2$, d_{π} ferric heme centers such as those of *pa*-HO-CN or myoglobin-cyanide. In the context of the spin density delocalization mechanism described above it is apparent that the amount of unpaired π electron density present at the C_{β} positions in *pa*-HO-N₃ is substantially smaller resulting in significantly smaller shifts for all the methyl carbon resonances in the spectrum of *pa*-HO-N₃. A similar situation is observed

in the ^{13}C -NMR spectrum of *pa*-HO-OH (Figure 7-d) which was previously found to exist as mixture of three electronic configurations [6]; A major population exhibits a spin cross over between $S = 1/2$ and $S = 3/2$, and two minor populations, one exhibiting a $S = 3/2$ electronic configuration and the other with the unusual $S = 1/2$, $(d_{xy})^1$ electronic structure. These findings strongly suggest the electronic structure of *pa*-HO-N₃ is not the common $S = 1/2$, d_π .

e) ^{13}C NMR Spectroscopy of porphyrin core carbons: An electronic configuration diagnostic tool.

^{13}C NMR spectroscopy has been shown to be powerful approach to the characterization of heme electronic configurations. A number of studies conducted with ferriheme model complexes have illustrated the diagnostic prowess of studying the chemical shifts originating from the porphyrin core carbons, C_m , C_α and C_β , to elucidate the electronic structure of ferric hemes [6, 36, 37]. This approach was recently employed to study the hydroxide complex of heme oxygenase from *Pseudomonas aeruginosa* reconstituted with heme containing ^{13}C labels at various core carbon positions [6]. Through a judicious choice of labeling schemes it was possible to identify core carbon resonances corresponding to three distinct electronic configurations of the heme iron. It was therefore decided to conduct a similar study with the azide complex of *pa*-HO in an attempt to gain a clearer understanding of the electronic structure of the heme in this complex.

Figure 8 summarizes in a schematic fashion the relationship between ^{13}C chemical shifts and the electronic configurations that are relevant to this study. In short,

ferrihemes with the common $S = 1/2$, d_π electronic structure, which are typically planar, and ferrihemes with the less common $S = 3/2$, $(d_{xy})^2 (d_{xz}, d_{yz})^2 (d_z)^1$ spin state, which usually show marked distortions from planarity and nominal D_{4h} symmetry make use of the $3e(\pi)$ porphyrin molecular orbital for spin delocalization [9, 38]. From the relative sizes of the circles in the schematic representation of the $3e\pi$ orbital it can be seen that the C_β carbons possess relatively large electron density, the C_α carbons relatively small electron density and the C_m carbons no electron density. Therefore in both the $S = 1/2$, d_π and $S = 3/2$ spin states the C_β carbons will exhibit large and positive (downfield) chemical shifts, and the C_α carbons will display smaller chemical shifts relative to those exhibited by the C_β carbons. The overall magnitude of the observed C_α and C_β shifts is greater in the $S = 3/2$ spin state because there are two unpaired electrons in the d_{xz} and d_{yz} orbitals, compared with only one unpaired electron in the $S = 1/2$, d_π spin state. An interesting consequence of the large spin density present on the C_α carbons of ferrihemes with the $S = 3/2$ spin state is that spin polarization will result in significant negative π spin density at the C_m carbons, which is manifested in relatively large and negative C_m resonances [39]. In the case of ferrihemes with the less common $S = 1/2$, $(d_{xy})^1$ electronic configuration, which typically adopt a ruffled geometry, spin delocalization onto the porphyrin ring involves the $a_{2u}(\pi)$ orbital shown in Figure 8 [7]. This results in large spin density at the C_m carbons and relatively small spin density at the C_α and C_β carbons. As a result the C_m carbons exhibit very large and positive shifts, whereas the

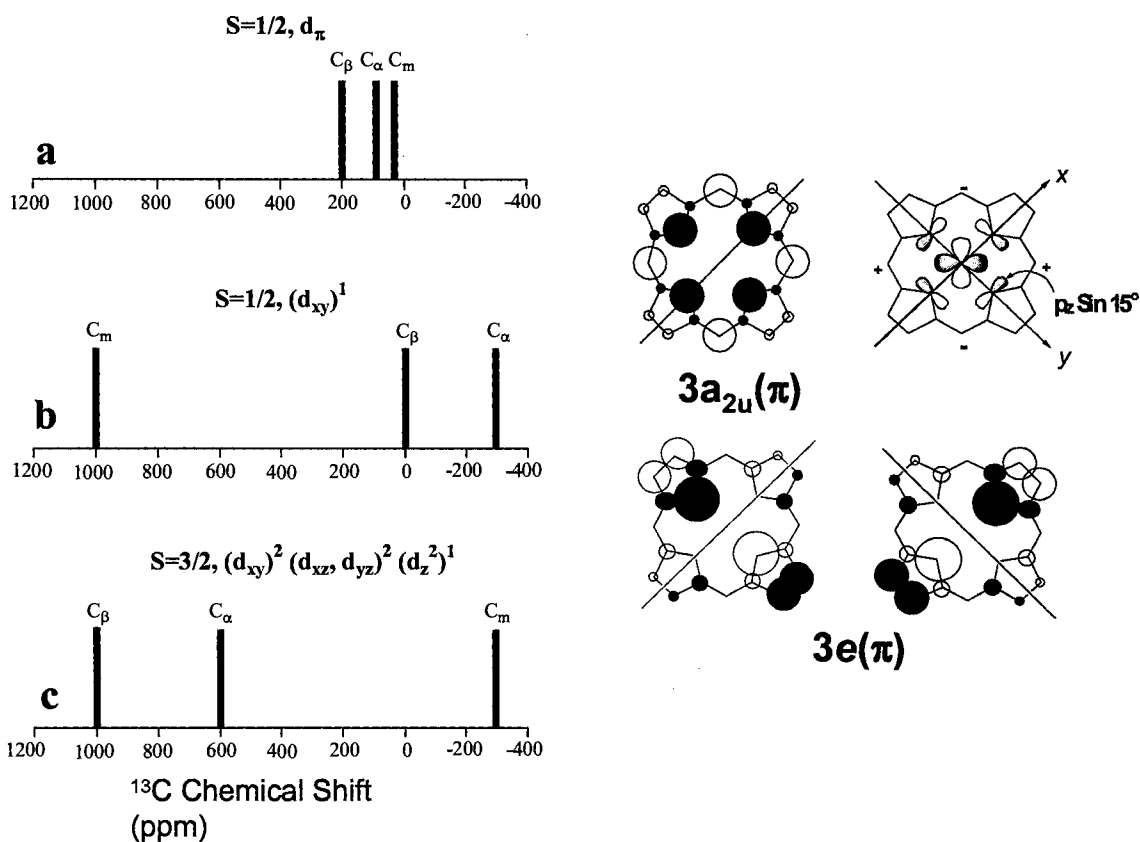


Figure 8. Left: Typical porphyrin core carbon chemical shifts for (a) Fe^{III}-porphyrinates with the $S = 1/2$, d_{π} electronic configuration, (b) Fe^{III}-porphyrinates with the $S = 1/2$, $(d_{xy})^1$ electronic configuration, and (c) Fe^{III}-porphyrinates with the $S = 3/2$, $(d_{xy})^2 (d_{xz}, d_{yz})^2 (d_z^2)^1$ electronic configuration. Right: Schematic representation (adapted from ref. 40 of the $3a_{2u}(\pi)$ and $3e(\pi)$ porphyrin orbitals. The relative size of the circles at each atom are proportional to the calculated electron density. The possible interactions between the d_{xy} orbital and the porphyrin nitrogens of a ruffled porphyrin which allow spin delocalization into the $3a_{2u}(\pi)$ orbital are shown schematically next to this orbital.

C_{β} carbons experience negligible shifts. Polarization from the C_m carbons results in relatively large and negative shifts for the C_{α} carbons position.

The ^{13}C NMR spectrum of a sample of *pa*-HO- N_3 reconstituted with heme labeled at the C_m and C_{α} carbons is depicted in Figure 9. Two sets of peaks are easily recognized: the first set consists of relatively narrow signals between 0 and 50 ppm while the second set is comprised of broader peaks in the 150-275 ppm region. Although the electronic absorption and ^1H NMR spectra are in agreement with an $S = 1/2$ low spin electronic configuration of the heme iron, the characteristics of the carbon spectrum shown in Figure 11-A are not: Low spin ferriheme complexes with an iron in the d_{π} electronic configuration typically result in C_m resonances between 0 and 50 ppm and C_{α} resonances below 100 ppm as depicted schematically in Figure 6-a. The presence of peaks corresponding to either C_m or C_{α} carbons above 150 ppm is unusual and strongly suggests a change in electronic structure of the heme iron.

The use of [5- ^{13}C -ALA] as a precursor for labeling introduces ^{13}C labels at both the alpha and meso positions of the heme. In order to elucidate the observed hyperfine shifts in terms of electronic structure we must be able to distinguish C_m from C_{α} resonances. To this end, [4- ^{13}C -ALA] was used to label the C_{α} and C_{β} carbons as shown in the inset of Figure 9-B and the labeled heme reconstituted into a sample of *pa*-HO which was subsequently converted into its azide complex. The ^{13}C NMR spectrum resulting from *pa*-HO- N_3 containing heme with ^{13}C labels at α and β positions is shown in Figure 9-B. While this new spectrum still shows a set of signals in the 150-275 ppm region, it has lost the resonances that were present below 50 ppm and acquired a new

group above 275 ppm. We can therefore assign this latter group of resonances to the C_β carbons and by deduction the signals of lower frequency in the same spectrum must belong to the C_α carbons. This further implies that the signals in the 50-0 ppm region of the spectrum in part A of Figure 9 must correspond to the C_m carbons.

At 35 °C, the azide complex of *pa*-HO has core carbon resonances which appear in the following order of increasing chemical shifts: C_m , C_α and C_β . This order corresponds to that which would be expected in case of an $S = 1/2$, d_π electronic configuration. However as shown in Figure 9-a, the relative intensity of the observed chemical shifts for the heme α and β pyrrole core carbons of *pa*-HO- N_3 , does not agree with model values. Although the C_m resonances show chemical shifts compatible with an Fe(III) $S = 1/2 - d_\pi$, spin state - electronic configuration of the heme iron, the C_α and C_β carbon resonances are found approximately 100 ppm downfield of their corresponding low spin d_π chemical shifts. This latter observation could be explained by invoking an $S = 3/2$ intermediate spin state with a $(d_{xy})^2 (d_{xz}, d_{yz})^2 (d_z^2)^1$ electronic configuration. Unpaired spin density would still be delocalized onto the porphyrin ring via the $3e(\pi)$ molecular orbital giving the same overall core carbon chemical shift order observed for the low spin d_π case while the additional unpaired electron density on the heme would shift the C_α and C_β carbon resonances to higher frequency. A 'pure' intermediate spin state is expected to shift C_α and C_β carbons to approximately 600 and 1000 ppm respectively while the negative spin density created by polarization at the meso position should shift the C_m carbons upfield to about -300 ppm [9, 10]. This is clearly not the case for *pa*-HO- N_3 . However, the observed chemical shifts for the C_α and C_β resonances are reminiscent of the rescently reported hydroxide complex of *pa*-HO whose major population was

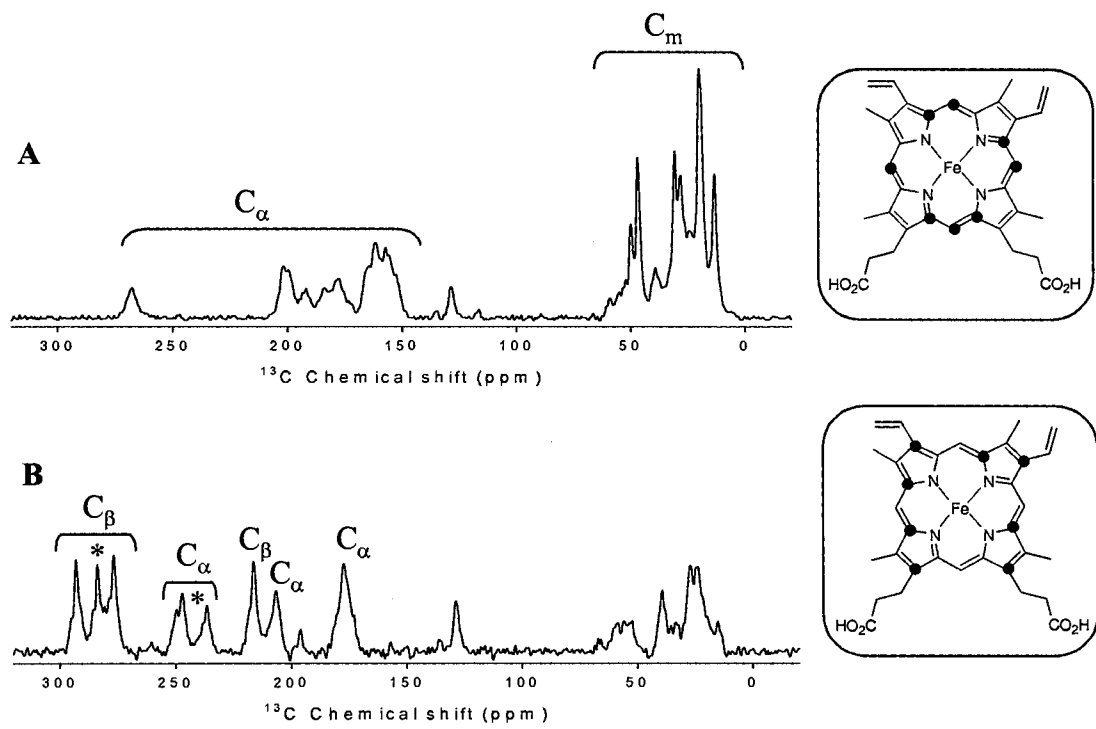


Figure 9. ^{13}C NMR spectra obtained at 35 °C from a solution of ferric azido- *pa*-HO reconstituted with labeled at the C_α and C_m carbons (A) and C_α and C_β carbons (B). The labeled carbons are highlighted by (●) in the structures shown to the right of the corresponding spectrum. The chemical shifts labeled with asterisks were used to construct the temperature dependent plot of Figure 10.

found to exist in a $S = 3/2, 1/2$ spin state crossover. The study conducted on the latter complex of *pa*-HO revealed that at 10 °C, the α and β carbons of the porphyrin could be found between 200 and 300 ppm which is similar to the 150-300 ppm range observed for the azide complex at 35 °C. Moreover, when the temperature dependent behaviour of the C_α and C_β resonances of the azide complex of *pa*-HO are compared to those of their hydroxo counterpart, almost identical slopes are found as shown in Figure 10. In addition to this it is interesting to notice that putting the two temperature dependent plots obtained for *pa*-HO-N₃ and *pa*-HO-OH side by side it is possible to transition from the azide plot to that of the hydroxide relatively smoothly. This observation leads us to believe that the azide complex of heme oxygenase from *Pseudomonas aeruginosa*, just like the hydroxide complex of the same enzyme, shows evidence of an $S = 3/2, 1/2$ spin crossover, albeit with a much smaller intermediate spin state character at the temperatures used in this study.

f) Deformations of the porphyrin ring from planarity allow a previously unobserved spin density delocalization mechanism.

It is interesting to once again note the apparent continuity between the two Curie plots corresponding to *pa*-HO-N₃ and *pa*-HO-OH shown in Figure 10. Not only does it strongly suggest that the Fe(III)-N₃ complex of *pa*-HO behaves like the $S = 3/2, 1/2$ spin crossover component of the hydroxide complex of the same enzyme but it illustrates a key change that occurs with increasing $S = 3/2$ character: the chemical shift values of the C_α carbon resonances become higher than those of the C_β carbon resonances. This is

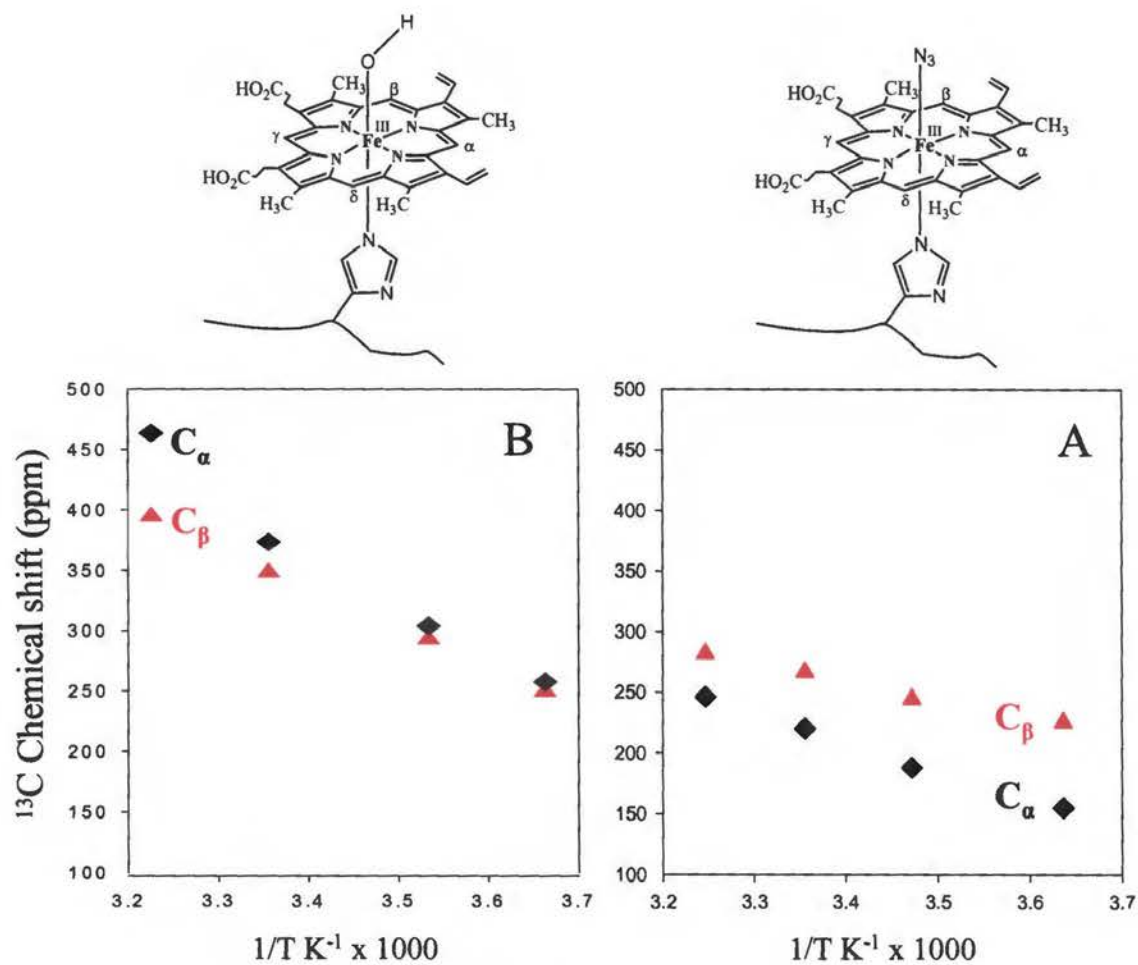
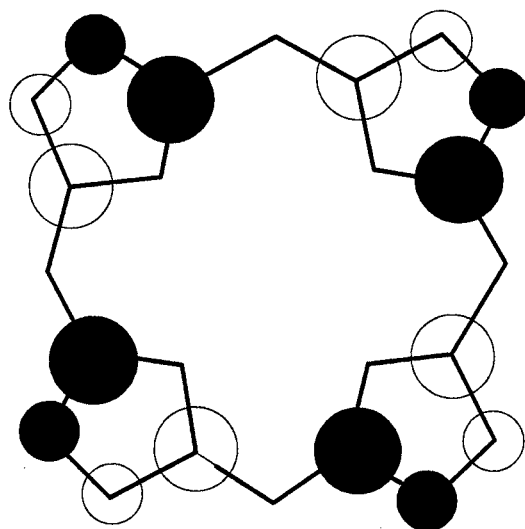


Figure 10. Temperature dependence of the C_α (◆) and C_β (▲) chemical shifts for the Fe^{III}-N₃ (A) and Fe^{III}-OH (B) complexes of *pa*-HO. The plot in panel A was constructed from the chemical shifts corresponding to the peaks highlighted by asterisks in Figure 9-B.

particularly noteworthy as to this date, the delocalization of electron density onto the porphyrin ring of model complexes and the recent $\text{Fe}^{\text{III}}\text{-OH}$ complex of *pa*-HO which exhibit intermediate spin character has been interpreted in terms of the $3e(\pi)$ molecular orbital [6, 9]. This orbital, schematically depicted in Figure 8, has larger wave function coefficients at the C_β positions than at the C_α positions. The amount of electron density delocalized through the use of that orbital being proportional to the aforementioned wavefunction coefficients, the β pyrrole carbons of the porphyrin should receive more spin density than their neighbouring α carbons and consequently exhibit higher chemical shifts. That is not what is observed for the $S = 3/2, 1/2$ spin crossover population present in both the azide and hydroxide complexes of heme oxygenase from *Pseudomonas aeruginosa*. In *pa*-HO-OH the major spin crossover population already has enough intermediate spin character at 10 °C to have α carbon chemical shifts above those of the β carbons. In the case of *pa*-HO- N_3 , the temperature dependent plot of Figure 10-A predicts that above 45 °C the complex would also see the order of the C_α and C_β resonances permuted. This change indicates an alteration in the relative amounts of unpaired electron density delocalized to the α and β carbons of the porphyrin which is in agreement with the unusually high chemical shifts observed for the heme methyl carbons of both the azido and hydroxo complexes of *pa*-HO that are presented in Figure 7. A smaller quantity of positive π spin density at the C_β carbon, relative to the C_α carbon, would, by polarization, create less negative π spin density on the adjacent methyl carbon reducing the intensity of the upfield chemical shift while simultaneously inverting the order of the actual C_β and C_α resonances in the ^{13}C NMR spectrum. In this context it becomes interesting to consider a recent article by Ru-Jen Chen and co-workers where it

is noted that non-planar deformations of the porphyrin alter the symmetry representations of the molecular orbitals of the metalloporphyrin thereby creating novel symmetry allowed interactions with certain heme iron orbitals [41]. Particularly noteworthy is the example given of a heme with a D_{2d} symmetry representation showing a symmetry allowed interaction of the metal d_{xy} and porphyrin $a_{1u}(\pi)$ orbitals. The a_{1u} porphyrin molecular orbital, depicted in Figure 11 would place relatively large amounts of spin density at the C_α carbons, relatively small amounts at the C_β carbons and no unpaired electron density at the C_m carbons. This is precisely the pattern of spin density distribution on the heme macrocycle that would generate the relative order of chemical shifts observed for the core carbons resonances of the $S = 3/2, 1/2$ spin crossover component of *pa*-HO-OH. Although the relative order of the core carbon resonances in the case of the almost pure $S = 3/2$ spin states reported for the $[\text{Fe}(\text{OEtPP})(\text{L})_2]^+$ complexes, where L is 4-cyanopyridine or tetrahydrofuran, was left unaddressed, they match those observed for the spin crossover component in our study of the hydroxide complex of *pa*-HO as well as those predicted by the Curie plot of Figure 12-A for *pa*-HO- N_3 at higher temperatures [9].

Model complex studies have well established the association of the $S = 1/2, (d_{xy})^1$ [8] electronic structure as well as that of the $S = 3/2$ and $S = 3/2, 1/2$ electronic configurations of ferric heme iron with significant distortions of the porphyrin ring from planarity [42, 43]. As the porphyrin macrocycle deforms from planarity its symmetry is lowered from the nominal D_{4h} symmetry to D_{2d} , in the case of ruffling. As a consequence both the metal d_{xy} and porphyrin a_{2u} orbitals will be of b_2 representation and can therefore interact [41]. This symmetry allowed interaction is born out by recent



a_{1u}

Figure 11. Schematic representation of the a_{1u} porphyrin π frontier molecular orbital. The relative size of the circles are proportional to the amount of spin density at the respective positions on the porphyrin ring.

evidence obtained from the study of certain six-coordinate ruffle-shaped metalloporphyrins in the low spin state that are found in the less common $(d_{xy})^1$ electronic configuration [11, 12]. In the same vein, the decrease in symmetry that accompanies the geometrical distortions of the saddled type seen in model complexes with $S = 3/2$ character could alter the symmetry representations of the iron orbitals containing unpaired electrons allowing these to interact with the a_{1u} porphyrin frontier orbital.

Mechanistic Implications for Heme Degradation and Concluding Remarks

The importance of heme distortions from planarity in heme protein function has been pointed out by Shelnutz [44, 45] and model complex studies have also underscored key aspects of reactivity resulting from changes in electronic structure brought about by non-planar hemes [5]. While model studies have established the propensity for good π -acceptor ligands and poor sigma donor axial ligands to induce the ruffling of metalloporphyrins, it has been noted that biological porphyrins may be found in multiple conformations as several potential energy minima can result from the protein environment [11, 45]. The observations made in this study are well in agreement with the above-mentioned comments and have significant implications in the context of heme oxygenation.

The mammalian and bacterial heme oxygenase enzymes catalyze the oxidative degradation of heme via a key ferric hydroperoxide intermediate responsible for the first step in the catalytic cycle [1, 4]. This crucial species has been shown by ENDOR spectroscopy to appear after cryoreduction of the heme oxygenase oxygen complex and protonation of the terminal oxygen atom belonging to the ferric peroxide adduct formed.

The proton delivered to the axially coordinated peroxide has been denoted H1 by the authors. While cryoreduction almost immediately results in the $\text{Fe}^{\text{III}}\text{-OOH}$ complex at 77 K annealing to temperatures above 200 K is necessary to produce α -hydroxyheme, the first product of heme oxygenation. Annealing below 200 K allows the detection of a new proton signal associated with the hydroperoxide moiety called H2. The delivery of H1 to the terminal oxygen atom of the peroxide takes place almost instantaneously at 77 K and implies a well defined and efficient protonation mechanism [4]. Recent crystal structures as well as solution state studies of heme oxygenases have revealed the presence of a very well defined network of hydrogen bonded water molecules in the distal pocket of the enzymes [34, 46, 47]. It has been proposed that the water molecule, denoted Wat1, which is closest to the active site is responsible for the protonation of the coordinated peroxide [47]. While this is indeed in agreement with the ENDOR studies described above as well as the presence of the network of hydrogen bonded water molecules characteristic of heme oxygenases the driving force behind the regioselective attack of the porphyrin remains unclear.

The results presented herein strongly suggest that binding of azide to the ferric resting state of heme oxygenase from *Pseudomonas aeruginosa* produces a novel electronic configuration corresponding to a $S = 3/2, 1/2$ spin crossover with a small amount of intermediate spin character at ambient temperatures. The relevance of this study to heme oxygenation lies in the capacity of azide to produce an unusual electronic structure associated with strong distortions of the porphyrin ring from planarity. We believe that while azide binding usually produces a low spin state of the ferric iron, the hydrogen network of water molecules present in heme oxygenases can by virtue of

donating a hydrogen bond to the coordinated azide nitrogen weaken this ligand's field strength. This weaker field strength being possibly accompanied by a compensating increase in the equatorial ligand field strength could produce porphyrin deformations from planarity which could find additional stability within the confines of the flexible HO pocket. These deformations of the heme placed in context of the symmetry allowed interactions emphasized by Chen and co-workers and the observed pattern of core carbon chemical shifts seen in the ^{13}C NMR spectra of *pa*-HO-N₃ at various temperatures, has led us to propose the novel use of the a_{1u} porphyrin frontier orbital for delocalization of electron density from the heme iron in a $S = 3/2, 1/2$ spin crossover. Moreover, the presence of an electronic structure known to be associated with significant deformations of the porphyrin reinforces the notion put forth that the flexible nature of the HO distal pocket in conjunction with its well defined network of water molecules can modulate the ligand field strength of a distally bound ligand producing novel electronic configurations [6]. If the physiologically relevant hydroperoxide is subjected to similar interactions it is likely the heme iron will adopt a non-planar conformation as well as a novel electronic configuration not corresponding to the common $S = 1/2, d_{\pi}$. We propose that the significance of the network of water molecules present in heme oxygenases lies in its capacity to create a hydrogen bond to the coordinated peroxide oxygen via the H2 proton mentioned by Davidov *et al.* [4]. The altered ligand field strength of the peroxide could therefore result in novel non-planar heme electronic structures where the $S = 1/2, (d_{xy})^1$ and $S = 3/2$ would be of particular interest as both would result in the presence of significant amounts of spin density at the meso positions priming the heme to participate in its own hydroxylation.

Acknowledgements: The expression and purification of *pa*-HO were done in collaboration with Rahul Deshmuk and Dr. Angela Wilks at the School of Pharmacy, University of Maryland. The ¹³C labeled ALAs were obtained in collaboration with Dr. Richard Bunce from Oklahoma State University.

References

1. Davydov, R.M., Yoshida, T., Ikeda-Saito, M., and Hoffman, B.; *J. Am. Chem. Soc.*, (1999). **121**: 10656-10657.
2. Ortiz de Montellano, P.R. and Wilks, A., in *Advances in Inorganic Chemistry*. 2000. p. 359-407.
3. Ortiz de Montellano, P.R. and Auclair, K., in *The Porphyrin Handbook*, R. Guilard, Editor. 2003, Elsevier Science (USA).
4. Davydov, R., Kofman, V., Fuji, H., Yoshida, T., Ikeda-Saito, M., and Hoffman, B.; *J. Am. Chem. Soc.*, (2002). **124**: 1798-1808.
5. Rivera, M., Caignan, G.A., Astashkin, A.V., Raitsimring, A.M., Shokireva, T.K., and Walker, F.A.; *J. Am. Chem. Soc.*, (2002). **124**: 6077-6089.
6. Caignan, G.A., Deshmuk, R., Zeng, Y., Wilks, A., Bunce, R.A., and Rivera, M.; *J. Am. Chem. Soc.*, (2003). **125**: 11842-11852.
7. Walker, F.A., in *The Porphyrin Handbook*, R. Guilard, Editor. 2000.
8. Ikeue, T., Ohgo, Y., Nakamura, M., Fujii, H., and Yokoyama, M.; *J. Am. Chem. Soc.*, (2000). **122**: 4068-4076.
9. Ikeue, T., Ohgo, Y., Yamaguchi, T., Takahashi, M., Takeda, M., and Nakamura, M.; *Angew. Chem. Int. Ed.*, (2001). **40**: 2617-2620.
10. Ikeue, T., Ohgo, Y., Takahashi, M., Takeda, M., Neya, S., Funasaki, N., and Nakamura, M.; *Inorg. Chem.*, (2001). **40**: 3650-3652.
11. Ikeue, T., Ohgo, Y., Saitoh, T., Yamaguchi, T., and Nakamura, M.; *Inorg. Chem.*, (2001). **40**: 3423-3434.

12. Safo, M.K., Gupta, G.P., Watson, C.T., Simonis, U., Walker, F.A., and Scheidt, W.R.; *J. Am. Chem. Soc.*, (1992). **114**: 7066-7075.
13. Evans, D.R. and Reed, C.A.; *J. Am. Chem. Soc.*, (2000). **122**: 4660-4667.
14. Caignan, G.A., Deshmuk, R.R., Wilks, A., Zeng, Y., Huong, H., Moenne-Locoz, P., Bunce, R.A., and Rivera, M.; *J. Am. Chem. Soc.*, (2002). **124**: 14789-14892.
15. Ratliff, M., Zhu, W., Deshmukh, R., Wilks, A., and Stojilovic, I.; *J. Bacteriol.*, (2001). **183**: 6394-6403.
16. Rivera, M., Qiu, F., Bunce, R.A., and Stark, R.E.; *J. Biol. Inorg. Chem.*, (1999). **4**: 87-98.
17. Rivera, M. and Walker, F.A.; *Anal. Biochem.*, (1995). **230**: 295-302.
18. Bunce, R.A., Shilling, C.L., and Rivera, M.; *J. Labelled Compd. Radiopharm.*, (1997). **39**: 669-675.
19. Summers, M.F., Marzilli, L.G., and Bax, A.; *J. Am. Chem. Soc.*, (1986). **108**: 4285-4294.
20. Iizuka, T. and Morilshima, I.; *Biochim. Biophys. Acta*, (1974). **371**: 1-13.
21. La Mar, G.N., Satterlee, J.D., and De Ropp, J.S., in *The Porphyrin Handbook*, R. Guilard, Editor. 2000, Academic Press. p. 185-297.
22. La Mar, G.N., Krishnamoorthi, R., Smith, K.M., Gersonde, K., and Sick, H.; *Biochemistry*, (1983). **22**: 6239-6246.
23. Banci, L., in *Biological Magnetic Resonance*, J. Reuben, Editor. 1993, Plenum: New York. p. 79-112.

24. Satterlee, J.D., Alam, S., Yi, Q., Erman, J.E., Constantinidis, I., Russel, D.J., and Moench, S.J., in *Biological Magnetic Resonance*, J. Reuben, Editor. 1993, Plenum: New York. p. 275-297.
25. Keller, R.M. and Wuthrich, K.; *Biochim. Biophys. Acta*, (1980). **621**: 204-217.
26. La Mar, G.N.; *Proc. Natl. Acad. Sci. U.S.A.*, (1978). **75**: 5755-5759.
27. Shokhirev, N.V. and Walker, F.A.; *JBIC*, (1998). **3**: 581-594.
28. Shokhirev, N.V. and Walker, F.A.; *J. Am. Chem. Soc.*, (1998). **120**: 981-990.
29. Walker, F.A.; *J. Am. Chem. Soc.*, (1980). **102**: 3254-3256.
30. Walker, F.A., Buehler, J., West, J.T., and Hinds, J.; *J. Am. Chem. Soc.*, (1983). **105**: 6923-6929.
31. Bertini, I., Luchinat, C., Parigi, G., and Walker, F.A.; *JBIC*, (1999). **4**: 515-519.
32. Yamamoto, Y.; *FEBS Letters*, (1987). **1**: 115-119.
33. Neya, S., Hada, S., Funasaki, N., Umemura, J., and Takenaka, T.; *Biochim. Biophys Acta*, (1985). **827**: 157-163.
34. Sugishima, M., Sakamoto, H., Higashimoto, Y., Omata, Y., Hayashi, S., Noguchi, M., and Fukuyama, K.; *J. Biol. Chem.*, (2002). **277**: 45086-45090.
35. Walker, F.A.; *Inorg. Chem.*, (2003). **42**: 4526-4544.
36. Mispelter, J., Momenteau, M., and Lhoste, J.M., in *Biological Magnetic Resonance*, J. Reuben, Editor. 1993, Plenum Press: New York. p. 299-355.
37. Nakamura, M., Hoshino, A., Ikezaki, A., and Ikeue, T.; *Chem. Comm.*, (2003). 1862-1863.
38. Ikezaki, A. and Nakamura, M.; *Inorg. Chem.*, (2002). **41**: 6225-6236.
39. Ikezaki, A. and Nakamura, M.; *Chem. Lett.*, (2000). 994-995.

40. Walker, F.A.; *Coord. Chem. Rev.*, (1999). **185-186**: 471-534.
41. Chen, R.-J., Chen, P.-Y., Lovell, T., Liu, T., Noodleman, L., and Case, D.A.; *J. Am. Chem. Soc.*, (2003). **125**: 6774-6783.
42. Simonato, J.P., Pecaut, J., Le Pape, L., Oddou, J.L., Jeandey, C., Shang, M., Scheidt, W.R., Wojaczynski, J., Wolowiec, S., Latos-Grazynski, L., and Marchon, J.C.; *Inorg. Chem.*, (2000). **39**: 3978-3987.
43. Ikeue, T., Saitoh, T., Yamaguchi, T., Ohgo, Y., Nakamura, M., Takahashi, M., and Takeda, M.; *Chem. Commun.*, (2000). 1989-1990.
44. Shelnut, J.A., Song, X.-Z., Ma, J.-G., Jia, S.-L., Jentzen, W., and Medforth, C.J.; *Chem. Soc. Rev.*, (1998). **27**: 31-41.
45. Shelnut, J.A.; *J. Porphyrins Pthalocyanines*, (2000). **4**: 386-389.
46. Friedman, J., Lad, L., Deshmukh, R., Li, H., Wilks, A., and Poulos, T.; *J. Biol. Chem.*, (2003). **278**: 34654-34659.
47. Lad, L., Wang, J., Li, H., Friedman, J., Bhaskar, B., Ortiz de Montellano, P.R., and Poulos, T.; *J. Mol. Biol.*, (2003). **330**: 527-538.

Chapter VI

THE OXIDATION OF HEME TO β - AND δ -BILIVERDIN BY *PSEUDOMONAS AERUGINOSA* HEME OXYGENASE IS A CONSEQUENCE OF AN UNUSUAL SEATING OF THE HEME

Introduction

Heme oxygenase oxidatively cleaves heme to biliverdin with the release of iron and CO [1, 2]. The heme oxygenase reaction consumes three molecules of oxygen and a total of seven electron equivalents in the form of NADPH to convert one heme molecule to biliverdin [2-4]. The transfer of electrons from NADPH to the mammalian enzyme is mediated by cytochrome P450 reductase [5]. The bacterial HOs, like their mammalian counterparts, are NADPH dependent enzymes that catalyze the oxidation of heme to biliverdin by a mechanism similar to that described for the mammalian enzymes [6-8]. Whereas HO in mammals functions to maintain heme homeostasis, the role of bacterial heme oxygenases appears to revolve around the breakdown of heme with the purpose of providing the bacterium with the ability to use heme as a source of iron [9-11]. Although the nature of several of the intermediates in the heme oxygenation reaction has been determined, the relationship between protein structure and factors such as ligand discrimination, oxygen activation, and regiospecificity are not yet well understood. The recent crystal structures of *N. meningitidis* HO [12] (*nm*-HO) and h-HO-1 [13] demonstrated that unlike the globins or the peroxidases, HOs do not have a distal histidine or a distal polar residue that may help stabilize an O₂ or ⁻OOH ligand. However, the crystal structures suggest that the carbonyl and NH groups of conserved

glycine residues (139 and 143 in h-HO-1) may carry out this role. Moreover, the flexibility imparted by these residues to the distal helix appears to be important for heme oxygenase catalytic activity. In agreement with this hypothesis, replacement of Gly-139 or Gly-143 with bulkier amino acids suppresses heme oxygenase activity, and in some cases the mutants acquire peroxidase activity [3, 14].

Insights gained from the crystal structures of the bacterial [12] and mammalian HOs [13, 15] suggest that the regioselectivity of the reaction is likely to be controlled by steric interactions between the distal helix and the heme, which restrict attack of the Fe^{III} -OOH oxidizing species to the β -, γ -, and δ -*meso* carbons. Electronic factors have also been implicated in the control of regiospecificity on the basis that electron donating and electron withdrawing substituents located on a *meso*-carbon exert a different influence on the regioselectivity of heme cleavage performed by HO [16, 17]. More recently, magnetic resonance studies conducted with models of the low-spin Fe^{III} -OOH intermediate of HO suggest that this key intermediate exists as an equilibrium mixture consisting of a planar heme with a $(d_{xy})^2(d_{xz}, d_{yz})^3$ electron configuration and a ruffled heme with a $(d_{xz}, d_{yz})^4(d_{xy})^1$ electron configuration [18]. At ambient temperatures the equilibrium favors the $(d_{xy})^1$ electron configuration and the ruffled porphyrinate ring is expected to aid the attack of the terminal oxygen of the Fe^{III} -OOH intermediate on the *meso*-carbon. In addition, the large spin density at the *meso*-carbons of a low-spin ferric heme possessing a $(d_{xy})^1$ electron configuration suggests the possibility of a radical mechanism for HO [18]. It is therefore conceivable that the regioselectivity of oxidative heme degradation is controlled by a combination of steric and electronic factors, where the ruffled $(d_{xy})^1$ heme places a pair of *meso*-carbons (α and γ , or β and δ) closer to the

terminal OH of Fe^{III}-OOH at any given moment. Steric interactions between the distal pocket and the heme are likely to determine which pair of *meso*-carbons is positioned closer to the coordinated peroxide and steric interactions are also likely to determine which *meso*-carbon from a pair (*e.g.* α or γ) is attacked [18].

Recent characterization of heme oxygenases from *Corynebacterium diphtheriae* (*cd*-HO) [6] and *Neisseriae meningitidis* (*nm*-HO) [7] revealed that these enzymes hydroxylate heme exclusively at the α -*meso* position, like the previously characterized mammalian proteins. In contrast, the *Pseudomonas aeruginosa* heme oxygenase (*pa*-HO) [8], which is 37% identical in amino acid sequence to *nm*-HO, hydroxylates heme predominantly at the δ -*meso* position. The study of *pa*-HO, therefore, is likely to provide additional insights into the factors that control the regioselectivity of oxidative cleavage during the process of heme catabolism.

As an initial step towards this goal, amino acid sequence alignments carried out in the context of the available X-ray crystal structures revealed that Lys-16 and Tyr-112 in *nm*-HO (Lys-16 and Tyr-134 in *h*-HO-1 and *r*-HO-1), which form hydrogen bonding and ionic interactions with the heme propionates, have been replaced by Asn-19 and Phe-117 in *pa*-HO. These observations led us to hypothesize that if the fold in *pa*-HO is similar to that of the other bacterial and mammalian HOs, δ -hydroxylation may be a consequence of alternative interactions experienced by the heme propionates that result in a heme seating different from that observed in the mammalian and *nm*-HOs. As will be shown below, NMR spectroscopic evidence strongly suggests that the heme seating in *pa*-HO is rotated $\sim 110^\circ$ from the heme seating common to the other known bacterial and mammalian heme oxygenases. It will also be shown that upon replacing Asn-19 and Phe-117 for Lys

and Tyr, respectively, the heme in the double mutant enzyme experiences a dynamic equilibrium between two heme seatings, one identical to that of wild type *pa*-HO, and the other typical of the previously characterized α -selective heme oxygenases. In addition the double mutant exhibits altered regioselectivity, in which both α and δ -biliverdin products are observed, reflecting the dynamic equilibrium of the two heme seatings in the double mutant.

Experimental

a) General methods.

Deionized, doubly distilled water was used for all experiments. Plasmid purification, subcloning and bacterial transformations were carried out as previously described [19]. Oligonucleotides were obtained from Sigma-Genosys and used without further purification. All absorption spectra of the heme-HO complexes were recorded on a Cary Varian 1E UV Spectrophotometer.

b) Bacterial strains.

E. coli strain DH 5 α [F', *ara* D(*lac-proAB*) *rpsL* ϕ 80*dlacZDM15 hsd* R17] was used for DNA manipulation and *E. coli* strain BL21 (DE3) pLysS [F⁻ *ompT hsdSB* (τ B⁻ mB⁻) *gal dcm* (DE3)] was used for expression of both the wild type and mutant heme oxygenase constructs.

c) Mutagenesis of pEHmuO.

Mutagenesis was carried out by polymerase chain reaction using the Quickchange

Mutagenesis Kit from Stratagene (La Jolla, CA). Oligonucleotides were designed to have melting temperatures (T_m) between 65-75 °C. All mutations were verified by DNA sequencing, which was carried out at the Biopolymer Laboratory, School of Medicine, University of Maryland, Baltimore.

d) Expression and purification of wild type and mutant *pa*-HOs.

The wild type heme oxygenase proteins and their corresponding mutants were purified as previously described [8]. A single colony of freshly transformed *E. Coli* BL21 (DE3) plysS cells was cultured overnight in 5 mL of LB-medium containing 100 µg/mL of ampicillin. The cells were subsequently sub-cultured into fresh LB-Ampicillin medium (100 mL) and grown at 37 °C to mid-log phase. The cells were then sub-cultured (10 mL) into LB-ampicillin media (1 L) and, on reaching mid-log phase, expression was induced by addition of isopropyl-1-thiol-(D)-galactopyranoside (IPTG) to a final concentration of 1 mM. The cells were grown further for 4-5 hours at 30 °C and harvested by centrifugation (10,000 x g for 20 min). Cells were lysed by sonication in 50 mM Tris-HCl (pH 7.8) containing 1mM EDTA and 1mM phenylmethanesulfonyl fluoride (PMSF). The cell suspension was then centrifuged at 27,000 x g for 40 min. The soluble fraction was applied to a Sepharose-Q Fast Flow column (1.5 x 10 cm) previously equilibrated with 20 mM Tris-HCl (pH 7.5). The column was washed with 3 volumes of 20 mM Tris-HCl (pH 7.5) containing 50 mM NaCl. The protein was then eluted with the same buffer with a linear gradient of NaCl from 50 mM-500 mM. The protein eluted at a concentration of 150 mM NaCl and the peak fractions were pooled and dialyzed against 10 mM potassium phosphate (pH 7.4) (2 x 4 L) at 4 °C. The *pa*-HO protein was then stored at -80 °C or reconstituted with heme as described below.

e) Reconstitution of the wild type and pa-HO mutants.

The heme-HO complexes were prepared as described previously [20]. Hemin was added to the purified HO proteins at a final 2:1 heme:protein ratio. The sample was then applied to a Q-sepharose column (1.5 x 6.0 cm) pre-equilibrated with 20 mM Tris-HCl (pH 7.8). The column was washed with equilibration buffer (5 volumes), followed by the same buffer containing 50 mM NaCl. The protein was then eluted with 20 mM Tris (pH 7.8) containing 250 mM NaCl. The protein fractions were pooled and dialyzed (2 x 4 L) against 20 mM Tris-HCl (pH 7.8) at 4 °C. The protein was concentrated by an Amicon filtration unit and stored at -80 °C. Samples for NMR and Resonance Raman analysis were passed down a Sephacryl S-100 HR column (3.0 x 100 cm) following concentration on an Amicon Filtration unit.

f) Electronic absorption spectroscopy of the wild type and mutant pa-HOs.

The UV-visible spectra of the wild type HOs and their respective mutants were recorded in 20 mM Tris (pH 7.5). The Fe(II)-CO spectra were obtained by saturating the solution with CO followed by the addition of a few grains of sodium dithionite. The Fe(II)-O₂ complexes were obtained by passage of the Fe(II)-CO complexes through a Sephadex G-25 column (1.0 x 3.0 cm).

g) Determination of the extinction coefficient for the heme:pa-HO complexes.

The mM extinction coefficient (ϵ_{405}) for the heme:HO complexes was determined as previously described [21]. The absorbance of a purified heme-HO sample at 405 nm was measured. An excess of dithionite was added and the spectrum of the reduced ferrous pyridine hemochrome was then recorded. The concentration was calculated from

the absorbance maxima at 418.5, 526, and 555 nm using mM extinction coefficient values of 170, 17.5 and 34.4, respectively.

h) Reaction of the heme:pa-HO complexes with NADPH cytochrome P450 reductase or ascorbate.

The reaction of the heme-HO complexes in the presence of NADPH reductase was carried out as previously described [6]. Purified human cytochrome P450 reductase was added to the heme-HO complex (10 μ M) at a molar ratio of reductase:HO equal to 3:1 in a final volume of 1 mL of 20 mM Tris-HCl (pH 7.5). The reaction was initiated by the addition of NADPH in 10 μ M increments to a final concentration of 100 μ M. The spectral changes between 300-750 nm were monitored over a 30 min time period at 1 min intervals. Following completion of the reaction, the product was extracted for HPLC analysis as described below. The ascorbic acid dependent conversion of heme to biliverdin was also monitored. Ascorbic acid at a final concentration of 5 mM was added directly to the heme-HO complex (10 μ M) in 20 mM Tris-HCl buffer (pH 7.5). The spectral changes between 300 and 750 nm were recorded over a 20 min time period. The products of the reaction were extracted and subjected to HPLC analysis as described below.

i) HPLC analysis of heme:pa-HO reaction products.

Following the reaction of the heme-HO complexes with NADPH cytochrome P450 reductase or with ascorbate, glacial acetic acid (20 μ L) and 3 M HCl (20 μ L) were added to the reaction (1 mL) before extracting into chloroform. The organic layer was

washed with distilled water (3 x 1 mL) and the chloroform layer removed under a stream of argon. The resultant residue was dissolved in 1 mL of 4% sulfuric acid in methanol and esterified for 12 h at room temperature. The esters were diluted (4-fold) with distilled water and extracted into chloroform. The organic layer was washed further with distilled water, dried over sodium sulfate, and the chloroform was again removed under a stream of argon. The residue was dissolved in 85:15 (v/v) methanol:water prior to HPLC analysis. The samples were analyzed by reverse phase HPLC on a ODS-AQ C18 (S-5) (YMC, Inc., Wilmington, NC) column (3.0 x 250 mm) eluted with 85:15 (v/v) methanol:water at a flow rate of 0.4 mL/min. The elutant was monitored at 380 nm and the biliverdin standards eluted in the order α (11.9 min), β (13.9 min), δ (14.8 min), and γ (18.5 min) [22]. The ratio of isomers was calculated by integration of the peaks within each experiment and averaged for five separate experiments.

j) Preparation of HOs reconstituted with ^{13}C -labeled heme.

^{13}C -labeled δ -aminolevulinic acids (ALA) were used as biosynthetic precursors for the preparation of protoheme IX (heme). [$3\text{-}^{13}\text{C}$]- δ -aminolevulinic acid ([$3\text{-}^{13}\text{C}$]-ALA), [$5\text{-}^{13}\text{C}$]-ALA, and [$1,2\text{-}^{13}\text{C}$]-ALA were synthesized utilizing methods described previously [23]. Heme labeled with ^{13}C was obtained utilizing previously reported methodology,[24] which was developed to take advantage of the fact that the first committed precursor in heme biosynthesis is δ -aminolevulinic acid (ALA) [25, 26]. Thus, ^{13}C -labeled heme, which is biosynthesized in *E. coli* upon addition of suitably labeled ALA, is trapped by simultaneously expressing rat liver outer mitochondrial membrane cytochrome b_5 (OM cyt b_5) [24]. The details of the biosynthetic protocol, which entail the expression and purification of OM cyt b_5 harboring ^{13}C -labeled heme

have been presented previously [27]. Reconstitution of HO with ^{13}C -labeled heme entails the removal of the isotopically labeled macrocycle from OM cyt b_5 , followed by the formation of the heme-HO complex. A typical protocol used to extract ^{13}C -labeled heme from OM cyt b_5 follows: Pyridine (15 mL) was added to 2.5 mL of 1 mM OM cyt b_5 in phosphate buffer ($\mu = 0.10$, pH = 7.0), while maintaining the temperature at 4 °C. Slow addition of chloroform, typically 10-15 mL, resulted in the precipitation of the polypeptide, while maintaining the pyridine hemochrome in the supernatant. The latter was subsequently separated from the denatured polypeptide by centrifugation, allowed to equilibrate at room temperature, and then dried over anhydrous MgSO_4 . The desiccant was removed by filtration and the filtered pyridine-chloroform solution transferred to a round-bottomed flask, where it was concentrated to dryness on a rotary evaporator. Finally, the resultant solid was redissolved in 3-4 mL of 0.1 M NaOH in the presence of a 10-fold excess of NaCN, and the pH adjusted to 9.5 (adjusting the pH to 9.5 in the absence of CN^- often results in heme aggregation and precipitation). HO was reconstituted with a freshly prepared solution of ^{13}C -labeled heme by titrating it into a 20 mL solution of 20 mM Tris containing $\sim 2 \mu\text{mol}$ of HO until the ratio A_{280}/A_{Soret} no longer changed. The resultant solution containing the cyanide-inhibited enzyme was then incubated at 4 °C overnight, dialyzed against 2.0 L of 10 mM phosphate (pH 7.5) over a period of 24 h and then purified by chromatography. HO from *C. diphtheriae* was loaded onto a hydroxyapatite column (2 cm x 12 cm) equilibrated at 4 °C with 10 mM phosphate buffer, pH 7.5, and eluted with a linear phosphate gradient (10-150 mM). Those fractions containing pure protein were concentrated in Amicon centrifugal concentrators to approximately 1 mL and then transferred to smaller Centricon concentrators in order to exchange the protein into deuterated phosphate buffer, pH 7.5, not corrected for the

deuterium effect. Purification of freshly reconstituted *pa*-HO was accomplished by loading it onto a Q-sepharose column (3 x 5 cm) and eluting it with a linear salt gradient (10-500 mM).

k) Resonance Raman spectroscopy.

Resonance Raman spectra were obtained on a McPherson 2061/207 spectrograph (0.67 m with variable gratings) equipped with a Princeton Instrument liquid N₂-cooled (LN-1100PB) CCD detector. Kaiser Optical supernotch filters were used to attenuate Rayleigh scattering. Excitation sources consisted of an Innova 302 krypton laser (413 nm), and a Liconix 4240NB He/Cd laser (442 nm). Spectra were recorded in a 90°-scattering geometry on samples at room temperature. Frequencies were calibrated relative to indene and CCl₄ standards and are accurate to ±1 cm⁻¹. CCl₄ was also used to check the polarization conditions. Electronic absorption spectra of the samples used for Raman spectroscopy were obtained on a Cary 50 Varian spectrophotometer, in order to monitor the samples both before and after laser illumination.

l) NMR Spectroscopy.

¹H and ¹³C spectra were acquired on a Varian Unity Inova spectrometer operating at frequencies of 598.611 and 150.532 MHz, respectively. ¹H spectra were referenced to the residual water peak at 4.8 ppm and ¹³C spectra were referenced to an external solution of dioxane (60% v/v in D₂O) at 66.66 ppm. Proton spectra were acquired with pre-saturation of the residual water peak over 15 k data points, a spectral width of 30 kHz, a 250 ms acquisition time, a 200 ms relaxation delay and 1024 scans. ¹³C spectra were collected over 24 k data points, a spectral width of 59 kHz, a 200 ms acquisition time, a

25 ms relaxation delay and 400,000 scans. HMQC spectra [28] were typically acquired with spectral widths of 30 kHz for ^1H and 50 kHz for ^{13}C , respectively, and a 200 ms relaxation delay. HMQC spectra obtained from samples containing HO reconstituted with heme labeled using 1,2- ^{13}C ALA as a heme precursor (see Figure 3) were acquired with refocusing delays based on $^1J_{\text{CH}} = 140$ Hz, while data obtained from HO reconstituted with heme labeled using 5- ^{13}C ALA as the heme precursor were acquired with $^1J_{\text{CH}} = 180$ Hz. Data were collected as an array of 2 k x 128 points with 512 scans per t_1 increment and processed by zero filling once in t_2 and twice in t_1 to obtain an 8 k x 8 k matrix. This was apodized with a 90° shifted squared sine bell function and Fourier transformed. WEFT NOESY [29, 30] spectra were acquired with 29 kHz in both dimensions, 2 k data points in t_2 , 256 increments in t_1 , 512 scans per t_1 increment, and (typically) a 40 ms mixing time. The data were processed by zero filling in both dimensions to obtain an 8k x 8k matrix, apodized with 90° shifted squared sine bell and Fourier transformed. EXSY [31] data were acquired in a similar manner except that the mixing time was set to 5 ms.

Results

a) Expression, purification and spectral characterization of the wild type and mutant pa-HOs.

The wild type and mutant *pa*-HOs were expressed and purified as previously described [8]. Each of the proteins was estimated to be > 95% pure by SDS-PAGE (data not shown). The Soret maxima of the ferric (Fe^{III}) state of the wild type and mutant proteins were essentially identical (Table 1). Upon reduction to the ferrous (Fe^{II}) state the Fe^{II} -CO

and $\text{Fe}^{\text{II}}\text{-O}_2$ complexes were in the range, 420-421 nm and 407-413 nm, respectively (Table 1). Characteristic visible bands for the Fe^{III} charge transfer bands and the $\text{Fe}^{\text{II}}\text{-CO}$ or $\text{Fe}^{\text{II}}\text{-O}_2$ α/β bands in all the mutant proteins remained relatively unchanged from those of the wild type protein (Table 1). These data suggest that the heme coordination in the mutant proteins was similar to that of the wild type protein, and were not grossly altered by the amino acid substitutions.

b) Resonance Raman characterization.

The high frequency region of RR spectra of hemoproteins obtained with Soret excitation is dominated by porphyrin skeletal modes, which are indicative of the oxidation state, spin state, and coordination state of the heme iron [32]. In the ferric heme-*nm*-HO complex the ν_3 and ν_2 modes at 1482 and 1560 cm^{-1} , respectively, are characteristic of a six-coordinated high-spin (6cHS) configuration. A minor six-coordinated low-spin (6cLS) population is also evidenced by a red-shifted ν_{10} at 1632 cm^{-1} (Figure 1-A). The ferric heme complexes of the wild type and the Asn-19Lys/Phe-117 Tyr double mutant of *pa*-HO exhibit nearly identical RR spectra, consistent with a mixture of 6cHS and 6cLS species (Figures 1-B and C). The combined ν_4 modes of the 6cHS and 6cLS species are observed at 1373 cm^{-1} in *pa*-HO rather than at 1370 cm^{-1} in *nm*-HO, and distinct 6cLS ν_3 and ν_2 in *pa*-HO spectra at 1502 cm^{-1} and 1580 cm^{-1} , respectively, are readily attributed to a greater content of 6cLS species in *pa*-HO than in *nm*-HO. Such mixtures of 6cHS / 6cLS configurations are observed in the ferric HO-1 and *cd*-HO proteins and are attributed to the ligation of an ionizable water ligand in the distal pocket, trans to the proximal histidine ligand [33, 34]. Upon reduction to the ferrous state, all three heme protein complexes display RR spectra characteristic of pentacoordinated high-spin

Table 1. Characteristic features of the UV-visible spectra of wild type and mutant *pa*-HO complexes

Enzyme	Soret Maxima (nm)			Visible bands (nm)			Soret Extinction coefficient (mM ⁻¹ cm ⁻¹)
	Fe ^{III}	Fe ^{II} -O ₂	Fe ^{II} -CO	Fe ^{III}	Fe ^{II} -O ₂	Fe ^{II} -CO	
Wild type	406	410	421	630	577/541	570/540	130
Asn-19 Lys	407	413	420	630	577/541	570/538	127
Phe-117 Tyr	406	412	420	629	577/541	570/537	112
Asn-19Lys/ Phe-117 Tyr	406	412	420	631	577/541	570/539	138

(5cHS) species (Figure 2). The dissociation of the sixth ligand present in the ferric heme upon reduction to the ferrous state further identifies this labile ligand as a water molecule. Most importantly, using a 442-nm laser excitation known to favor the resonance enhancement of iron-histidine stretching vibration in ferrous HS species, both *nm*-HO and *pa*-HO complexes show a strong RR band at 222 cm^{-1} (inset Figure 2). This vibration is also observed with similar bandwidth and intensity in the double mutant of *pa*-HO although its frequency is shifted by -2 cm^{-1} to 220 cm^{-1} . The $\nu(\text{Fe-His})$ mode is influenced by the microenvironment of the $\text{N}_\delta\text{His}$ and ranges from $\sim 200\text{ cm}^{-1}$ in the absence of hydrogen bonding interactions to $\sim 250\text{ cm}^{-1}$ when the imidazole is deprotonated [35]. The orientation of the imidazole ring relative to the Fe-N(pyrrole) axes is another factor that influences the $\nu(\text{Fe-His})$ stretch [36-38]. When the histidine ring is colinear with an axis along two heme *meso* carbons the $\nu(\text{Fe-His})$ is observed $\sim 20\text{ cm}^{-1}$ lower than when the histidine ring is oriented along a N-Fe-N (pyrrole) axis. Thus, the identical $\nu(\text{Fe-His})$ observed in *nm*-HO and *pa*-HO demonstrate that in both proteins the heme iron is bound to a proximal histidine with similar electronegativity and orientation with respect to the Fe-N(pyrrole) axes. The recent X-ray structure of *nm*-HO showed that, as in HO-1, the proximal histidine is engaged in a hydrogen bonding interaction with a carboxylate side chain and that the imidazole ring is oriented along the heme β - δ -*meso* axis [12]. In *pa*-HO, the proximal histidine is likely to adopt a similar orientation and to be hydrogen bonded to Glu-30, in a manner analogous to Glu-29 in h-HO-1. No significant perturbation of these structural parameters appears to take place in the Asn-19 Tyr/Phe-117 Tyr double mutant of *pa*-HO, since the $\nu(\text{Fe-His})$ is only 2 cm^{-1} lower than in the wild type protein. In contrast to the conserved $\nu(\text{Fe-His})$ observed in all three heme protein complexes, significant variations are observed in the 350 to 450 cm^{-1}

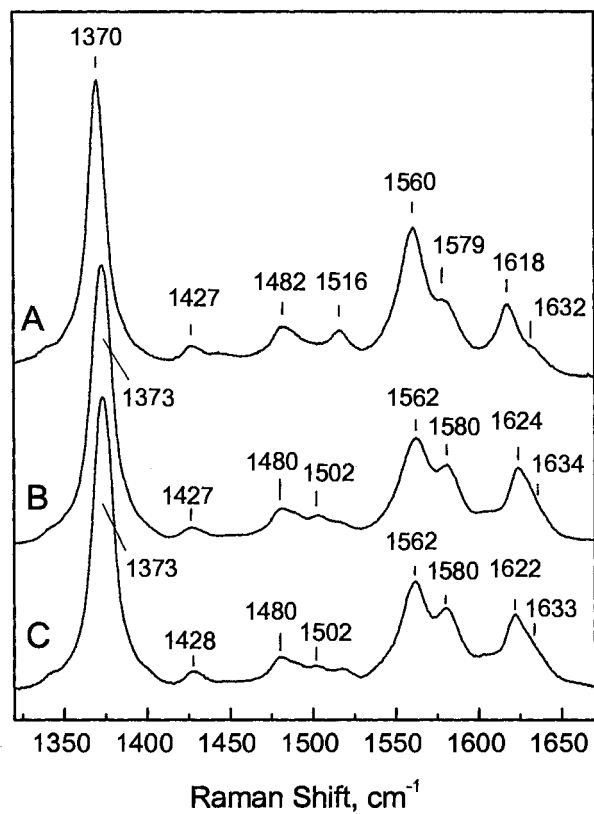


Figure 1. High-frequency region of the RR spectra of ferric heme — protein complexes in wt *nm*-HO (A), wt *pa*-HO (B), and N19K/F117Y *pa*-HO (C).

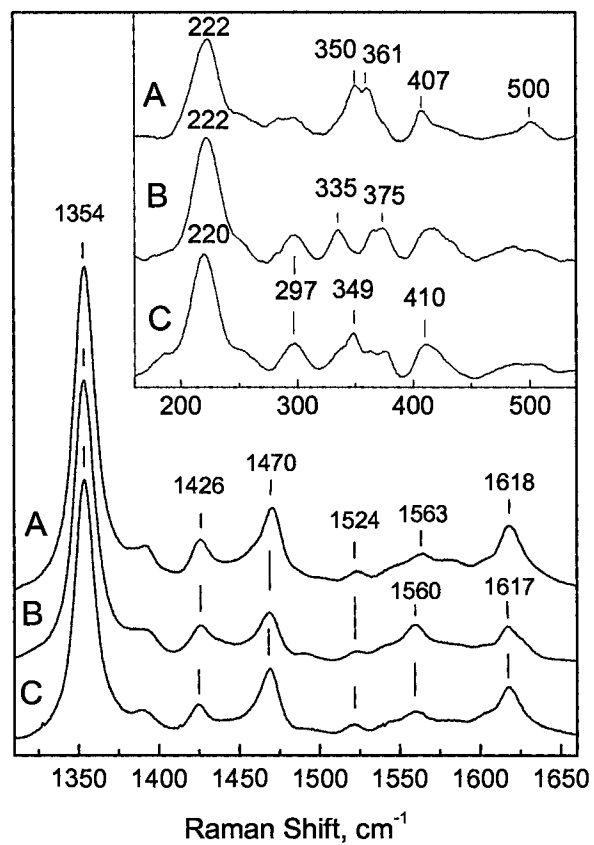


Figure 2. High-frequency region of the RR spectra of ferrous heme-protein complexes in *nm*-HO (A), wt *pa*-HO (B), and N19K/F117Y *pa*-HO (C). The inset shows the low-frequency region obtained with 442-nm excitation.

region, where bending modes of the peripheral propionate and vinyl groups occur [39]. These changes reveal differences in the configurations of the heme peripheral groups that are particularly worth pointing out when comparing the wild type and double mutant *pa*-HO because the Asn-19 Lys/Phe-117 Tyr mutations are aimed at changing the interactions experienced by the heme propionate groups.

c) Catalytic turnover of the *pa*HO mutants.

As previously reported for the wild type *pa*-HO the NADPH cytochrome P450 reductase catalyzed reaction yields ferric Fe^{III}-biliverdin as the product of the reaction (data not shown) [8]. Extraction of biliverdin from the reaction mixture, followed by esterification of the propionate groups and separation of the different isomers by HPLC, indicates the formation of δ -biliverdin (70 %) and β -biliverdin (30 %) (Table 2). As will be detailed below the β -biliverdin isomer is formed from oxidation of the minor (m) heme orientational isomer, related to the major isomer (M) by 180° rotation of the heme along the α - γ meso-axis, which places the β -meso-carbon of m in the site normally occupied by the δ -meso-carbon of M. Catalytic turnover of the single mutants Asn-19 to Lys and Phe-117 to Tyr, in the presence of NADPH cytochrome P450 reductase, shows no change in regioselectivity (Table 2). In contrast, analysis of the products obtained from the reaction catalyzed by the *pa*-HO double mutant (Asn-19 Lys/Phe-117 Tyr) indicates a significant change in the regioselectivity of the reaction, as is evident from the formation of α -biliverdin (55 %), δ -biliverdin (35%) and β -biliverdin (10%). The NMR studies outlined below demonstrate that the formation of α -biliverdin is a consequence of a dynamic equilibrium of two heme seatings in the double mutant.

Table 2. Regioselectivity of heme oxygenation

pa-HO	Biliverdin isomer ratio (%)*			
	α	β	δ	γ
WT	0	30	70	0
Asn-19 Lys	0	30	70	0
Phe-117 Tyr	0	30	70	0
Asn-19 Lys/Phe-117 Tyr	55	10	35	0

*The % of each isomer was obtained by integration of the peaks within each chromatogram. The reported values are an average obtained from five separate experiments. The standard deviation is $\pm 5\%$

d) Resonance assignments for cyanide-inhibited wild type pa-HO and cd-HO

In addition to the difficulties inherent in obtaining NMR spectra of short-lived, paramagnetically affected signals, the assignment of resonances corresponding to the heme active site of ferric hemoproteins is typically met with challenges imposed by heme isomerism which results in the virtual doubling of resonances originating from the macrocycle [40, 41]. Further complication arises from the asymmetric distribution of unpaired electron density on the heme macrocycle, which is manifested in large isotropic shifts for some nuclei and negligible for others [42-44]. To circumvent these problems we have devised a biosynthetic method for the isotopic labeling of protoheme IX (heme), which can be used to introduce ^{13}C to virtually any position in the macrocycle [24]. The availability of hemoproteins reconstituted with ^{13}C -labeled heme facilitates the resonance assignment process, as has been demonstrated by the complete assignment of ^1H and ^{13}C resonances in both heme orientational isomers of mitochondrial cytochrome b_5 [27]. As will be shown below, unambiguous ^1H and ^{13}C assignments of resonances originating from the heme active site of wild type and mutant heme oxygenases have been obtained utilizing enzymes reconstituted with ^{13}C -labeled heme. The assignment of heme resonances can be largely facilitated by judiciously labeling the heme macrocycle; this can be accomplished by carefully positioning the ^{13}C label in the heme precursors utilized in the biosynthesis of labeled heme. We used [1,2- ^{13}C]- δ -aminolevulinic acid ([1,2- ^{13}C]-ALA) as a heme precursor for the preparation of heme labeled at the four methyl, two vinyl- β , and carbonyl carbons [24, 27] (Figure 3-A), and [5- ^{13}C]-ALA was used to prepare heme labeled at the *meso*-carbons (Figure 3-B). The low-frequency portion of the 1-D ^{13}C NMR spectrum (^1H -coupled) obtained from wild type *pa*-HO reconstituted with heme labeled from [1,2- ^{13}C]-

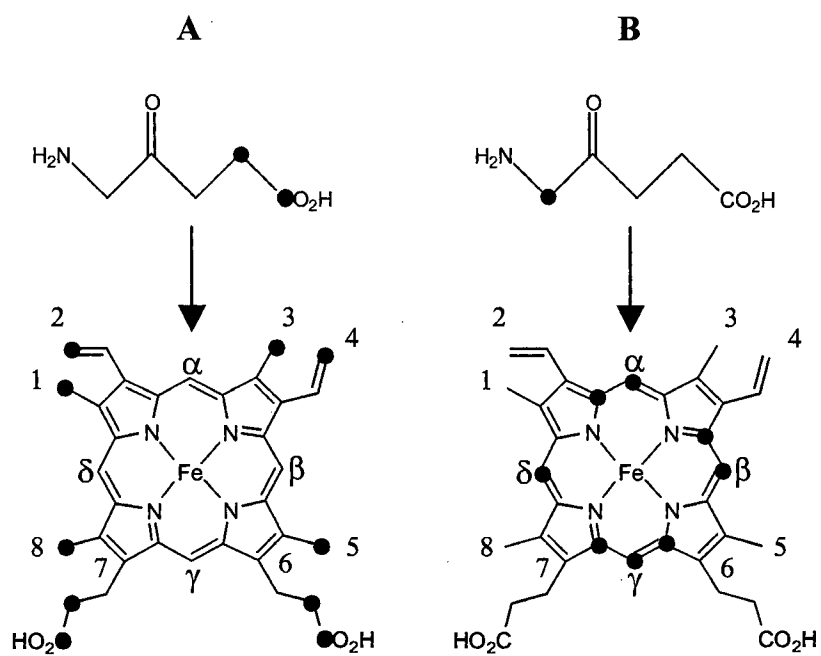


Figure 3. (A) ¹³C labeling pattern obtained when protoporphyrin IX is biosynthesized from [1,2-¹³C]-ALA, (B) ¹³C labeling pattern obtained from [5-¹³C]-ALA. (●) Positions labeled with ¹³C. For details see references [24,27].

ALA clearly shows that the heme methyl groups (quartets) resonate between -10 and -70 ppm (Figure 4-A). More than four methyl signals are observed in the spectrum because wild type *pa*-HO exists in solution as a mixture of two heme orientational isomers, coexisting in a 70:30 ratio of major to minor isomer, M:m = 70:30. In fact, the HMQC spectrum reveals the presence of 8 heterocorrelations in this region, which permit the identification of ^1H resonances originating from heme methyl groups in the major and minor heme orientational isomers. The assignments described below will only be concerned with resonances originating from the major isomer. The high-frequency portion of the ^{13}C -spectrum in Figure 4-B shows that the vinyl- β carbons (triplets) and carbonyl carbons (doublets) resonate between 190 and 140 ppm, and the heterocorrelations seen in the HMQC spectrum identify the corresponding vinyl- β protons. The doublets ($^1J_{\text{CC}} \sim 55$ Hz) originating from each of the propionate carbonyl carbons are a consequence of the fact that the ^{13}C -labeled carbonyl carbons are attached to a ^{13}C -labeled β -propionate (see Figure 3-A). In fact, this feature of the labeling pattern also permits the unambiguous identification of the β -propionate carbons because the corresponding resonances are triplets ($^1J_{\text{CH}} \sim 140$ Hz) of doublets ($^1J_{\text{CC}} \sim 55$ Hz) (data not shown); the corresponding β -propionate proton resonances are thus readily identified via heteronuclear HMQC correlations. It is therefore evident that the use of *pa*-HO reconstituted with heme labeled as shown in Figure 3-A permits the relatively straightforward identification of ^1H and ^{13}C resonances originating from all heme methyl, vinyl- β , and propionate- β groups. It is also readily apparent that the utilization of ^{13}C -labeled heme is especially useful in the unambiguous identification of ^1H resonances that are buried under the intense envelope of diamagnetic resonances. The next step in the assignment strategy entails correlating these resonances with the aid of a WEFT-NOESY

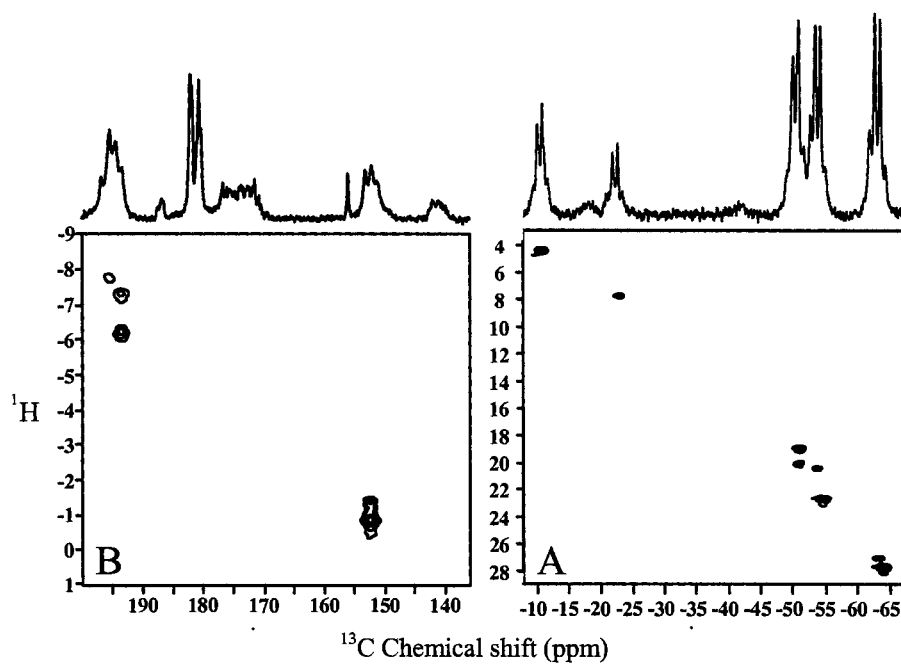


Figure 4. Low (A) and high (B) frequency (^{13}C) portions of the HMQC spectrum of wild type *pa*-HO-CN reconstituted with heme derived from $[1,2-^{13}\text{C}]$ -ALA (see Figure 3-A) showing both contour plot and 1-D ^{13}C spectrum.

spectrum after a suitable entry point has been identified. In this context, the labeling pattern of Figure 3-B is not only useful to identify the ^1H and ^{13}C resonances corresponding to the heme *meso* positions, but it also provides a suitable entry point for the interpretation of NOESY cross correlations. Figure 5 depicts the 1-D ^{13}C NMR spectrum obtained from *pa*-HO reconstituted with heme labeled as in Figure 3-B. This spectrum exhibits intense resonances at 84.8, 74.5 and -15.2 ppm devoid of HMQC correlations, which clearly indicates that these resonances must originate from the quaternary pyrrole- α carbons in the major isomer. In addition, the HMQC spectrum of Figure 5 reveals that four intense ^{13}C resonances (42.46, 28.24, 6.47, -0.92 ppm) exhibit heterocorrelations; these resonances must therefore originate from *meso*-carbons in the major isomer. Close inspection of the 1-D ^{13}C -NMR spectrum of Figure 5 reveals that three of the *meso*-carbon resonances (28.24, 6.47 and -0.92 ppm) are affected by $^1J_{\text{CC}}$ coupling, whereas the fourth (42.46 ppm) is not. This observation indicates that the resonance at 42.46 ppm arises from *meso*-carbon δ because this is the only *meso*-carbon that is not attached to a labeled pyrrole- α carbon (see Figure 3-B). The uniqueness of *meso*-carbon δ , which is conferred by the labeling pattern, makes this position an ideal entry point to interpret the NOESY cross correlations. Furthermore, NOESY cross correlations identifying heme resonances buried under the large envelope of diamagnetic resonances can be readily validated if they match the ^1H chemical shifts obtained from HMQC data.

As indicated above, the carbon resonance corresponding to *meso*- C_δ facilitates the identification of *meso*- H_δ , and provides a unique entry point for the interpretation of NOESY spectra. Thus, a WEFT-NOESY spectrum (Figure 6) reveals a correlation

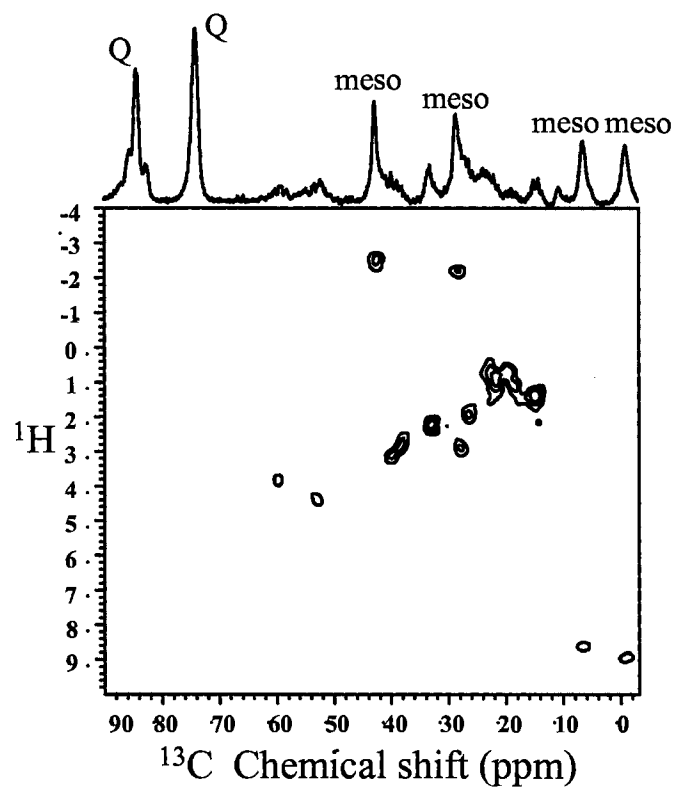


Figure 5. Portion of the HMQC spectrum of wild type *pa*-HO-CN reconstituted with heme derived from [5- ^{13}C]-ALA (see Figure 3-B) showing both contour plot and 1-D ^{13}C spectrum. Peaks in the 1-D ^{13}C spectrum labeled Q originate from porphyrin quaternary carbons.

between *meso*-H_δ (-2.51 ppm) and heme methyl 1 (1Me) at 22.69 ppm, which in turn is correlated to vinyl-β proton 2 (2V_β) at -0.80 ppm. Both 2V_β protons (-0.80 and -1.35 ppm) are correlated to the 2V_α proton at 10.74 ppm; the latter is correlated to the *meso*-H_α proton at 8.63 ppm and this *meso*-hydrogen is correlated to the 3Me proton at 4.41 ppm, which in turn, is correlated to 4V_β protons at -7.02 and -7.97 ppm. One of the 4V_β protons (-7.97 ppm) is correlated to the 4V_α proton (12.06 ppm) and this is correlated to the *meso*-H_β proton (-2.20 ppm), which can be correlated to the 5Me protons at 27.71 ppm. The assignments obtained for *pa*-HO are summarized in Table 3. The assignments for *cd*-HO (Table 3), were carried out in a similar manner to that described above for *pa*-HO. In brief, a 1-D proton coupled ¹³C NMR spectrum obtained with *cd*-HO reconstituted with heme labeled as in Figure 3-A allowed us to identify the ¹³C resonance frequencies corresponding to heme methyl, β-propionates and β-vinyl groups; the corresponding ¹H resonances were obtained from the HMQC spectrum in Figure 7. Enzyme reconstituted with heme labeled as in Figure 3-B was used to identify the resonances arising from *meso*-carbons and *meso*-hydrogens with the aid of the HMQC map of Figure 8, and the WEFT-NOESY map of Figure 9 permitted the assignment of these resonances to the corresponding heme groups, as described above for *pa*-HO.

e) Interpretive model for the NMR spectroscopic studies.

The influence of the geometry and nature of axial ligands on the properties of low-spin ferric porphyrins and hemoproteins is well known. For instance, it has been known for quite some time that the orientation of planar axial ligands exerts a large influence on the spread of the methyl resonances originating from low-spin ferric heme in hemoproteins,

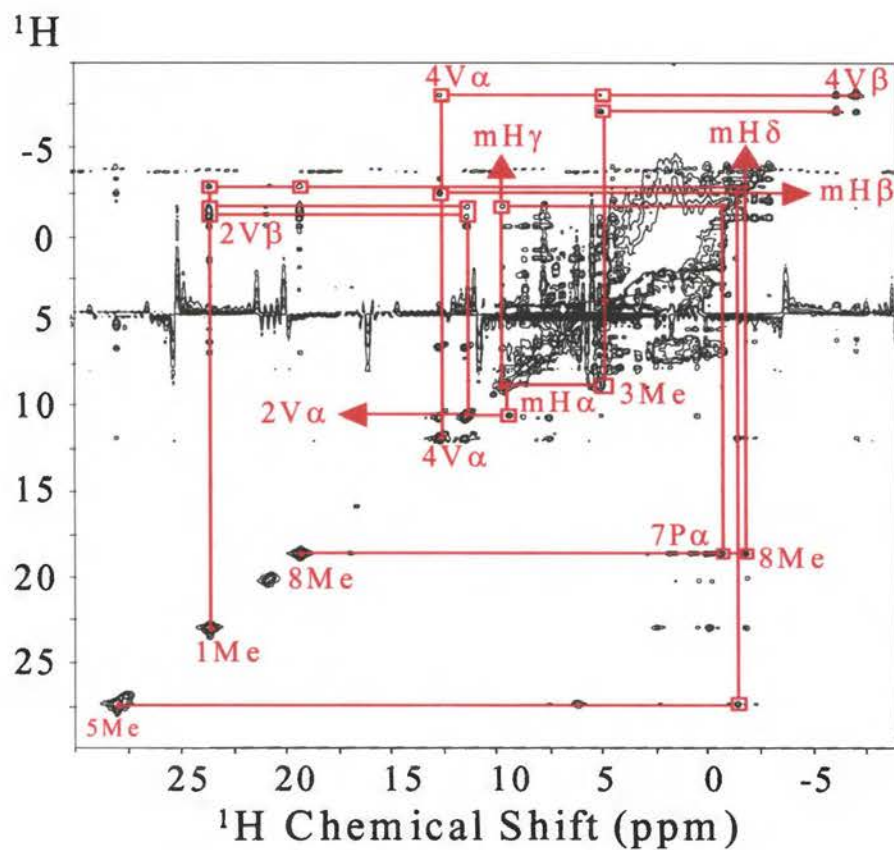


Figure 6. WEFT-NOESY of *pa*-HO reconstituted with heme derived from [5- ^{13}C]-ALA.

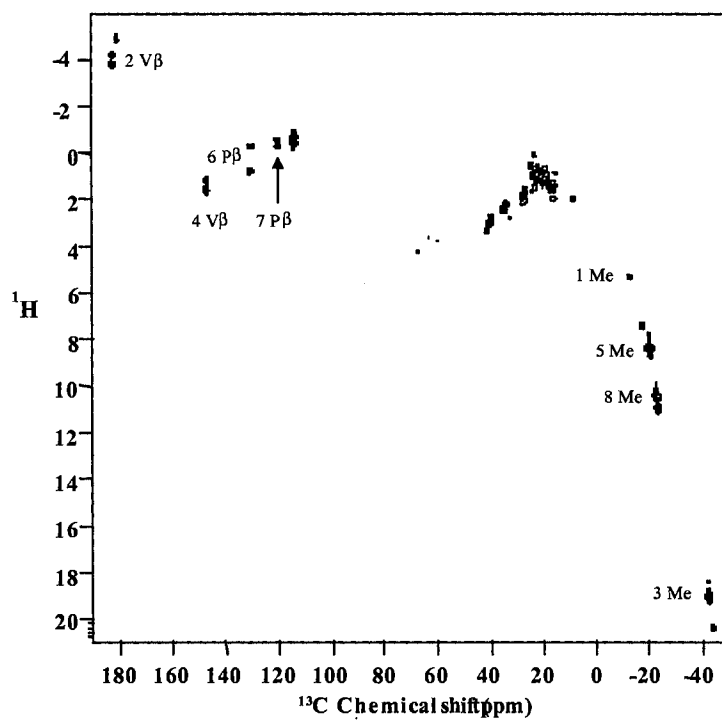


Figure 7. HMQC spectrum of *cd*-HO-CN reconstituted with heme derived from [1,2- ^{13}C]-ALA

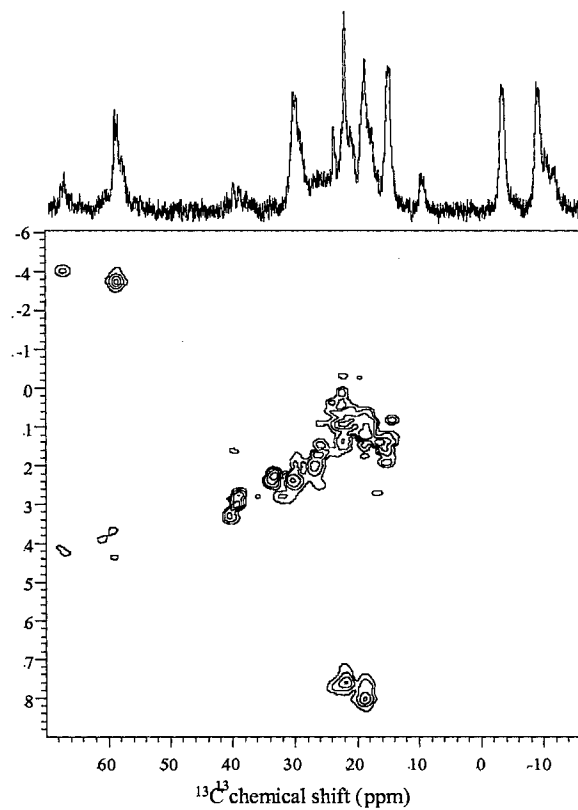


Figure 8. Portion of the HMQC spectrum of *cd*-HO-CN reconstituted with heme derived from [5-¹³C-ALA].

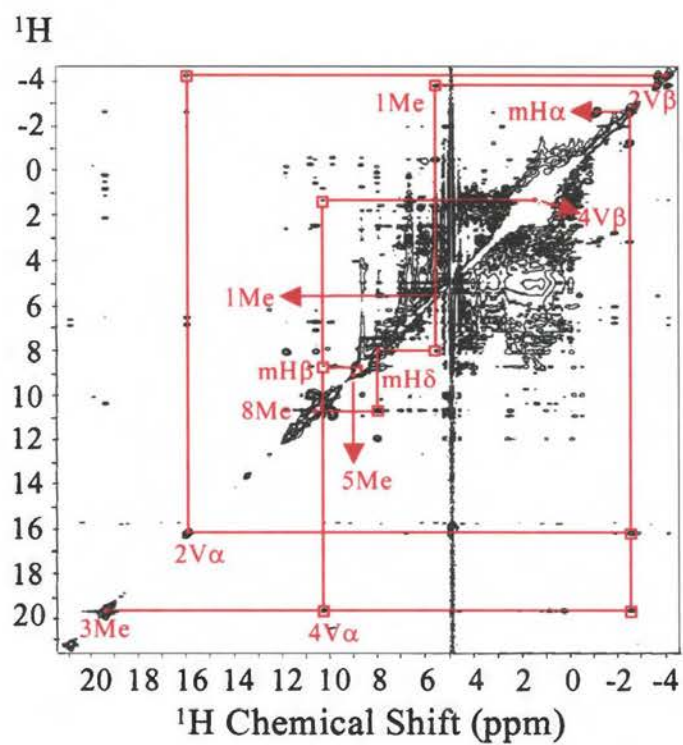


Figure 9. WEFT NOESY of *cd*-HO-CN reconstituted with heme derived from [5- ^{13}C]-ALA

Table 3. ^1H and ^{13}C NMR chemical shifts for the cyanide complexes of *pa*-HO and *cd*-HO

Position	<i>pa</i> -HO (10 °C)		<i>cd</i> -HO (35 °C)	
	^1H (ppm)	^{13}C (ppm)	^1H (ppm)	^{13}C (ppm)
1 Me	22.69	-55.32	5.44	-13.14
3 Me	4.41	-11.10	19.18	-42.52
5 Me	27.71	-64.44	8.52	-20.06
8 Me	19.01	-51.45	10.59	-22.88
2 V α	10.74	76.23	15.73	
2 V β	-0.80, -1.35	152.38	-3.69, -4.09	182.67
4 V α	12.06	31.11	10.10	
4 V β	-7.02, -7.97	193.59	1.70, 1.28	147.08
meso- α	8.63	6.47	-2.58	58.58
meso- β	-2.20	28.24	8.19	18.75
meso- γ	8.95	-0.92	2.42	33.27
meso- δ	-2.51	42.46	7.78	21.73
6 P- α	6.33	-14.5		
6 P- β			0.91, -0.15	130.42
7 P- α	-1.20	-1.64		
7 P- β			-0.28, -0.58	113.93

as well as in low-spin Fe^{III} porphyrinates [45-47]. The fundamental property that allows this mechanism to operate is the interaction of the proximal histidine with the iron-centered *e*-symmetry *d* orbitals, which in turn individually interact with porphyrin 3*e*(π) orbitals to reduce their degeneracy. The end result is the destabilization of one member of the porphyrin 3*e*(π) orbitals and the stabilization of another, hence leading to an uneven distribution of electron spin density among the four pyrrole rings in the porphyrin [45, 48]. More recently, the concept of counter-rotation of the *g* or χ tensor with rotation of axial ligand planes away from one of the N-Fe-N axes in the heme has been used to predict the orientation of the in-plane magnetic axis utilizing ¹³C-NMR [49-53] and ¹H NMR [54, 55] spectroscopic data. Shokhirev and Walker carried out Hückel calculations of the effect of axial ligand nodal plane orientation, assuming counter-rotation of the *g*-tensor, to produce heme methyl shifts that provide consistent predictions of the order and magnitude of observed methyl shifts for a large number of hemoproteins [55].

Figure 10 depicts schematically the orientation of the proximal histidine-imidazole plane projected onto the heme ring, where the imidazole plane forms an angle ϕ of 135° with the molecular *x*-axis, which is aligned along the nitrogen atoms of heme pyrrole rings II and IV [55]. Consequently, the molecular *z*-axis is aligned along the heme normal, and the molecular *y*-axis is aligned along the nitrogen atoms of pyrrole rings I and III. The plot shown in Figure 10, which is adapted from a plot summarizing the Hückel calculations performed by Shokhirev and Walker [55], shows the isotropic shift patterns predicted for heme methyl groups 1,3,5, and 8 as a function of the angle ϕ formed between the axial ligand plane and the molecular *x* axis. From the plot in Figure 10 it is possible to predict that for a histidine-imidazole plane angle of 178°, which

corresponds to the orientation of the proximal histidine-imidazole plane in the X-ray crystal structure of sperm-whale myoglobin [56], the heme-methyl isotropic shifts obtained experimentally for the cyano complex of sperm whale myoglobin [57] are: 5Me > 1Me > 8Me > 3Me (27.0, 18.6, 12.9, 4.8 ppm). It is evident that the order of methyl resonances is correctly predicted and that the predicted shifts are acceptable. In a similar manner, Shokhirev and Walker utilized the predictive power of the plot in Figure 10 to correctly suggest an angle ϕ of 125° for the proximal imidazole plane of h-HO-1, on the basis of NMR assignments reported by La Mar and coworkers [58, 59]. These assignments demonstrated that the order of chemical shifts in cyanide-inhibited h-HO-1 is 3Me > 8Me > 5Me > 1Me (19.6, 10.5, 9.0, 4.9), which in the context of the plot shown in Figure 10, suggest an angle ϕ of 130°, a value that was corroborated by the X-ray crystal structure of h-HO-1 [13] and r-HO-1 [15]. Similar types of comparisons carried out with many heme containing proteins clearly demonstrated the importance of axial ligand plane orientation on the observed proton shifts [55]. Consequently, the calculations of Shokhirev and Walker provide a predictive framework to study hemoproteins for which a structure has not yet been obtained. In this work we have made use of the predictive power of these calculations to estimate the angle of the histidine-imidazole plane in *cd*-HO, *pa*-HO and site directed mutants of *pa*-HO.

f) The orientation of the histidine plane in pa-HO is different from that of other known mammalian and bacterial heme oxygenases.

The high frequency portion of the ¹H NMR spectrum of *cd*-HO (Figure 11-a) is almost identical to that reported for r-HO-1 [58] and h-HO-1 [59], in that there is only one methyl resonance resolved from the diamagnetic envelope. The ¹H resonance

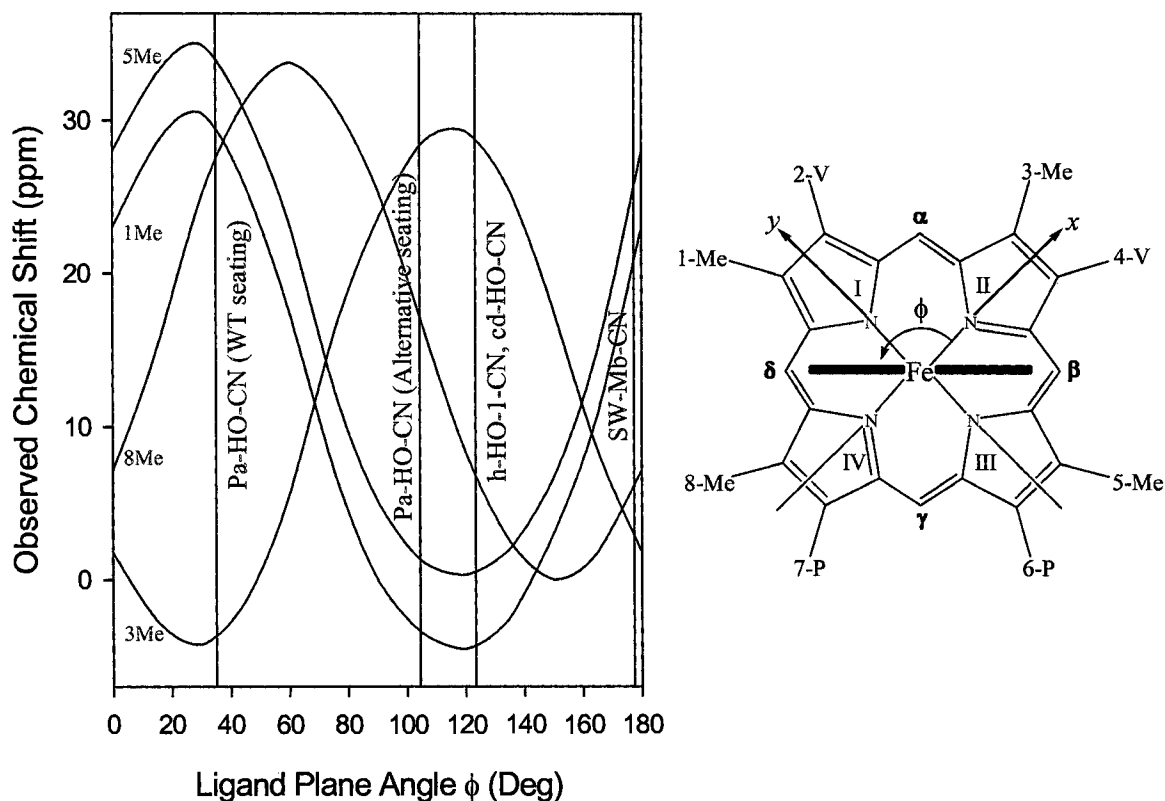


Figure 10. Right: Right-handed coordinate system and nomenclature used for describing the projection of the His-imidazole plane onto the porphyrin ring. The x axis is aligned along the nitrogen atoms of pyrrole rings II and IV of the heme, the y axis is along the nitrogen atoms of pyrrole rings I and III, and the z axis is normal to the heme. Left: Dependence of observed heme-methyl shifts on the angle ϕ formed between the molecular x axis and the projection of the imidazole plane. Adapted from Figure 5 in reference [55].

assignments summarized in Table 3 indicate that the order of heme methyl resonances is $3\text{Me} > 8\text{Me} > 5\text{Me} > 1\text{Me}$ (19.05, 10.45, 8.39, 5.30 ppm), which in the context of the calculations summarized in Figure 10 strongly suggests that the proximal histidine-imidazole plane in *cd*-HO forms an angle of approximately 130° with the molecular x axis and is nearly parallel to the heme β - δ -*meso*-axis. In comparison, the resolved portion of the ^1H NMR spectrum of *pa*-HO (Figure 11-b), displays three resolved methyl resonances originating from the major isomer, and is clearly distinct from those corresponding to *cd*-HO, *r*-HO-1 and *h*-HO-1. This feature of the ^1H spectrum strongly suggests that the histidine-imidazole plane in *pa*-HO is oriented at an angle ϕ that is different from the 130° typically observed in all other heme oxygenases for which this information is available. In fact, the ^1H resonance assignments of Table 3 indicate that the order of heme methyl resonances obtained from *pa*-HO is $5\text{Me} > 1\text{Me} > 8\text{Me} > 3\text{Me}$ (27.71, 22.69, 19.01, 4.41 ppm), consequently, the plot of Figure 10 predicts that the proximal histidine-imidazole plane forms an angle ϕ of $\sim 35^\circ$ with the molecular x axis and is aligned almost parallel to the heme α - γ -*meso* axis. It is interesting to note that in *pa*-HO, which forms β - and δ -biliverdin, the histidine-imidazole plane is oriented along the α - γ -*meso* axis, whereas in *r*-HO-1, *h*-HO-1 and *cd*-HO, which form α -biliverdin, the histidine-imidazole plane is oriented along the β - δ -*meso* axis. The orientations of the heme imidazole planes in wild type *pa*-HO and *cd*-HO are consistent with the fact that both proteins display identical $\nu(\text{Fe-His})$ at 222 cm^{-1} since this stretching vibration is insensitive to the *meso* axis (α - γ or β - δ) that is collinear with the imidazole plane.

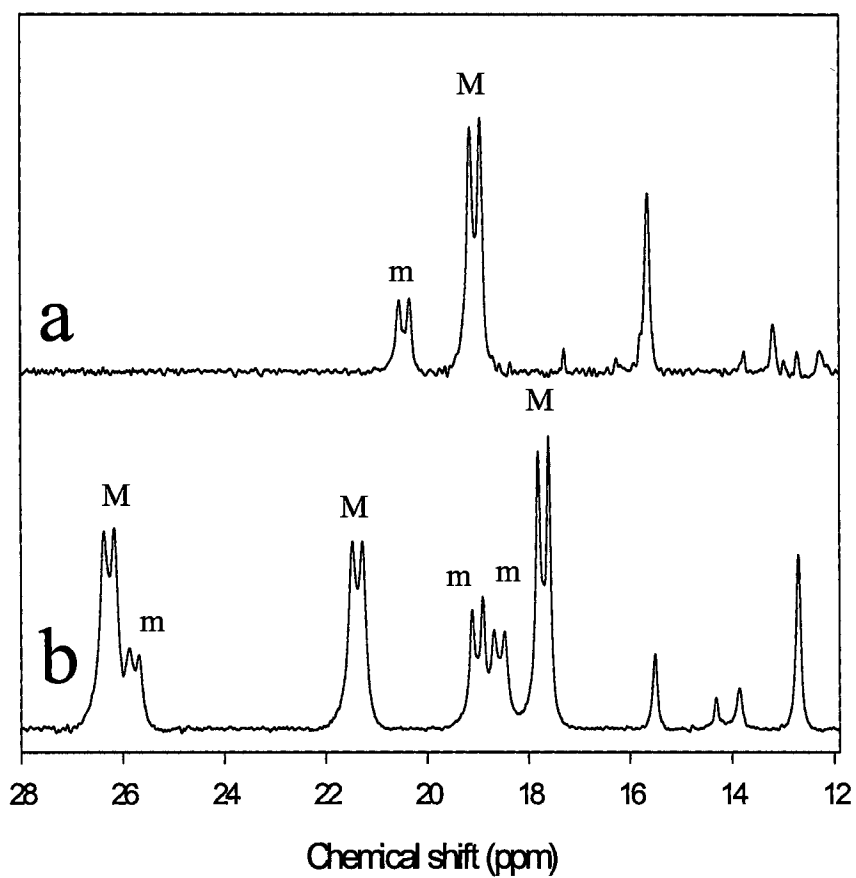


Figure 11. High frequency portion of the ^1H NMR spectra of (a) *cd*-HO-CN and (b) *pa*-HO-CN reconstituted with heme derived from $[1,2-^{13}\text{C}]$ -ALA. The $^1J_{\text{CH}}$ doublets originate from methyl groups in the major (M) and minor (m) heme orientational isomers.

g) A dynamic exchange between two heme seatings in Asn-19 Lys/Phe-117 Tyr pa-HO is responsible for the altered regioselectivity of the double mutant.

The crystal structures of *N. meningitidis* heme oxygenase (*nm*-HO) [12] and h-HO-1 [13] revealed that conserved residues Lys-16 and Tyr-112 in *nm*-HO interact with the heme propionates. By comparison, the amino acid sequence of *pa*-HO, in the context of the three-dimensional structure of *nm*-HO, indicates that these residues in *pa*-HO are Asn-19 and Phe-117, respectively. This observation suggested to us that the unique value of the angle ϕ formed between the histidine-imidazole plane and the molecular *x* axis, as well as the unique regioselectivity exhibited by *pa*-HO (β - and δ -biliverdin), might be related to different interactions between the heme propionates and the polypeptide, which presumably promote an alternative heme seating that is conducive to β - and δ -*meso* hydroxylation. This hypothesis was tested with the Asn-19 Lys/Phe-117 Tyr mutant, which was constructed with the aim of restoring the hydrogen bonding and ionic interactions observed between the heme propionates and these residues in h-HO-1, r-HO-1 and *nm*-HO. The double mutant was found to hydroxylate the heme at the δ - (35%), β - (10%), and α - (55%) meso positions. It will be shown below that this unusual pattern of regioselectivity is indeed a consequence of perturbing the microenvironment of the heme propionates, which results in the stabilization of two heme seatings related to one another by a 110° in-plane rotation of the heme.

The resolved portion of the ^1H NMR spectrum of Asn-19 Lys/Phe-117 Tyr *pa*-HO at 35 °C (Figure 12-a) displays broad and almost featureless peaks, however, as the temperature is lowered the peaks become gradually sharper and new peaks emerge. Below 15 °C the shapes of the spectra no longer change, except for the expected temperature-dependent shifts that are typical of paramagnetically affected

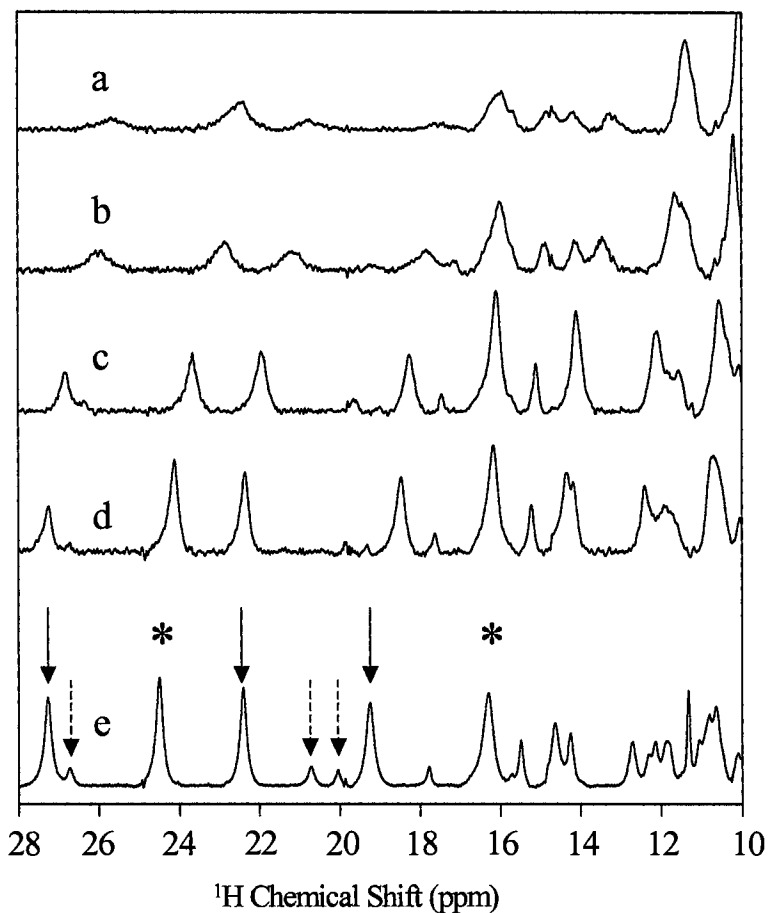


Figure 12. Variable temperature ^1H NMR spectra of the Asn-19 Lys/Phe-117 Tyr double mutant of *pa*-HO-CN. Spectra were acquired at (a) 35, (b) 30, (c) 20, (d) 15 and (e) 10 °C. The solid arrows in plot (e) correspond to methyl resonances originating from the major orientational isomer exhibiting the wild type seating, while dashed arrows highlight the corresponding minor isomer. Asterisks highlight two methyl resonances originating from the major orientational isomer displaying the alternative heme seating.

resonances [47]. A striking characteristic of the ^1H NMR spectrum of the double mutant at 10 °C (Figure 12-e) is the large number of resonances resolved from the diamagnetic envelope. The relative intensity of these resonances suggests that at least 5 of them are likely to originate from heme methyl groups. The large number of resonances originating from heme methyl groups suggests two possibilities: (a) the presence of two heme orientational isomers coexisting with almost identical concentrations or (b) two heme seatings exchanging with one another at a frequency which at 10 °C is slow relative to the NMR time scale but similar to it at 35 °C. Close inspection of the ^1H NMR spectrum of the Asn-19 Lys/Phe-117 Tyr double mutant at 10 °C (Figure 12-e) allowed us to rule out the first possibility. In this spectrum black arrows highlight those methyl resonances that are also observed in the ^1H NMR spectrum corresponding to the major isomer of WT *pa*-HO, and dashed arrows highlight the methyl resonances of the corresponding minor isomer. These observations, together with the temperature-induced changes in the NMR spectra, strongly suggest that the Asn-19 Lys/Phe-117 Tyr double mutant exists as a mixture of molecules harboring the heme in two distinct seatings. The two seatings, one of which is identical to the seating of the wild type enzyme, are related to one another by chemical exchange. Furthermore, the spectrum obtained at 10 °C also demonstrates that each of the heme seatings exists as a mixture of two heme orientational isomers.

In order to probe the hypothesis suggesting that the resonances highlighted by arrows and asterisks in Figure 12-e originate from heme methyl groups in two distinct heme seatings, the Asn-19 Lys/Phe-117 Tyr double mutant of *pa*-HO was reconstituted with heme labeled as in Figure 3-A. The resolved portion of the ^1H NMR spectrum of the double mutant reconstituted with labeled heme (Figure 13) demonstrates that, as

expected, those resonances with chemical shifts identical to the peaks originating from heme methyl groups in the major (solid arrows) and minor (dashed arrows) isomer of wild type *pa*-HO, exhibit ~ 140 Hz $^1J_{CH}$ splitting. It is also apparent that the peaks labeled with an asterisk in Figure 12-e and 13 are also split by ~ 140 Hz coupling constant, thus demonstrating that these peaks originate from heme methyl groups in the alternative heme seating. Furthermore, the 1H NMR spectrum of Figure 13 also facilitates the identification of two heme resonances that originate from the minor heme orientational isomer in the alternative heme seating, as is evident from the $^1J_{CH} \sim 140$ Hz doublets highlighted by an open circle. Additional evidence in support of the hypothesis that the resonances highlighted with arrows and asterisks in Figure 12-e correspond to heme methyl groups was obtained from 1-D ^{13}C (1H -coupled) and HMQC spectra, because the ^{13}C NMR spectrum (Figure 13) permits the identification of $^1J_{CH} \sim 140$ Hz quartets, which can be correlated to the corresponding heme-methyl 1H resonances by HMQC. In fact, the latter spectrum displays at least 15 resolved resonances originating from heme methyl groups, thus providing ample confirmatory evidence that the Asn-19 Lys/Phe-117 Tyr double mutant of *pa*-HO exists as a mixture of four different molecules; two different heme seatings create a set of two and heme isomerism creates a subset of two from each heme seating isoform.

The nature of the several isoforms of Asn-19 Lys/Phe-117 Tyr coexisting in solution having been established, we turned our attention to assign the heme methyl resonances originating from the heme in the alternative heme seating (major isomer). Since the two heme seatings are in slow exchange at 10 °C we used Exchange Spectroscopy (EXSY) [31] to map out those resonances that are correlated by exchange;

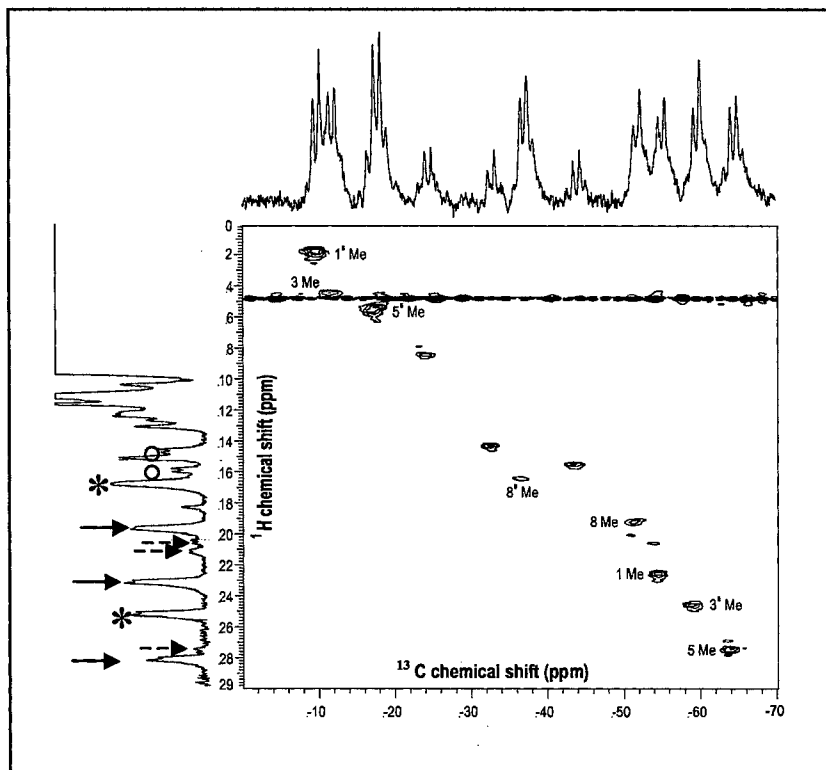


Figure 13. HMQC spectrum of the cyanide inhibited Asn-19 Lys/Phe-117 Tyr *pa*-HO reconstituted with heme derived from [1,2- ^{13}C]-ALA. Only the low frequency (^{13}C) region of the spectrum, which displays the heme methyl resonances, is shown. The 1-D ^1H and non-decoupled ^{13}C spectra are shown to illustrate the J_{CH} splitting. Arrows and dashed arrows, respectively, represent the major and minor orientational isomers exhibiting the wild type heme seating. Asterisks and open circles, respectively, represent the major and minor isomers exhibiting the alternative heme seating.

the data is summarized by the EXSY spectrum of Figure 14. In this spectrum the exchange cross peaks can be identified readily because they are significantly more intense than the NOE cross peaks. Thus, the exchange correlations of Figure 14 (summarized below) allowed us to assign the resonances originating from methyl groups in the alternative heme seating.

<i>Wild Type seating</i>		<i>Alternative Seating</i>
5 Me (27.71 ppm)	⇌	5' Me (5.38 ppm)
1 Me (22.69 ppm)	⇌	1' Me (1.74 ppm)
8 Me (19.01 ppm)	⇌	8' Me (16.33 ppm)
3 Me (4.41 ppm)	⇌	3' Me (24.55 ppm)

The assignments corresponding to heme methyl groups in the alternative heme seating reveal that the order of methyl shifts is 3'Me > 8'Me > 5'Me > 1'Me, therefore indicating that the proximal-histidine imidazole plane in the alternative heme seating of the Asn-19 Lys/Phe-117 Tyr mutant forms an angle ϕ of approximately 100° with the molecular x-axis (See Figure 10).

The orientation of the proximal histidine plane in the alternative heme seating, which is aligned along the nitrogen atoms of heme pyrrole rings II and IV, should result in a different $\nu(\text{Fe-His})$ in the double mutant, relative to the wild type protein. In the

absence of other determinant factors, the alternative seating is expected to display a $\nu(\text{Fe-His})$ above 222 cm^{-1} , possibly as high as 230 cm^{-1} [36, 37]. However, the $\nu(\text{Fe-His})$ observed in the double mutant protein is practically unchanged, at 220 cm^{-1} . Moreover, the relative intensity and bandwidth of the $\nu(\text{Fe-His})$ are unaffected, thus giving no indication of multiple heme seatings within the substrate pocket of the double mutant. Good agreement between NMR and RR spectroscopic studies of this kind has been observed with globins and peroxidases, despite the fact that one technique (NMR) characterizes the 6cLS ferric cyano complex and the other the 5cHS ferrous heme. However, these systems were not in equilibrium between two seatings, as is the case of the *pa*-HO double mutant. It is therefore tempting to speculate that while the ferrous state favors a single heme seating, the ferric hydroperoxide ($\text{Fe}^{\text{III}}\text{-OOH}$) intermediate, which defines the regioselectivity, adopts both heme seatings observed by NMR spectroscopy.

In what follows, the dynamic equilibrium between the two heme seatings in the mutant enzyme will be analyzed in the context of the fold of *nm*-HO, which is typical of the fold exhibited by heme oxygenases, and in the context of Scheme I, assuming that the heme rotates in-plane, while the proximal histidine-imidazole plane remains in place. It is felt that an in-plane rotation of the heme is more likely than a rotation of the proximal histidine-imidazole plane because the mutations that trigger the dynamic equilibrium described above are aimed at introducing hydrogen bonding and ionic interactions with the heme propionates, thus it is likely that the in-plane heme rotation is a result of the heme propionates sampling two environments that stabilize these groups to approximately the same extent.

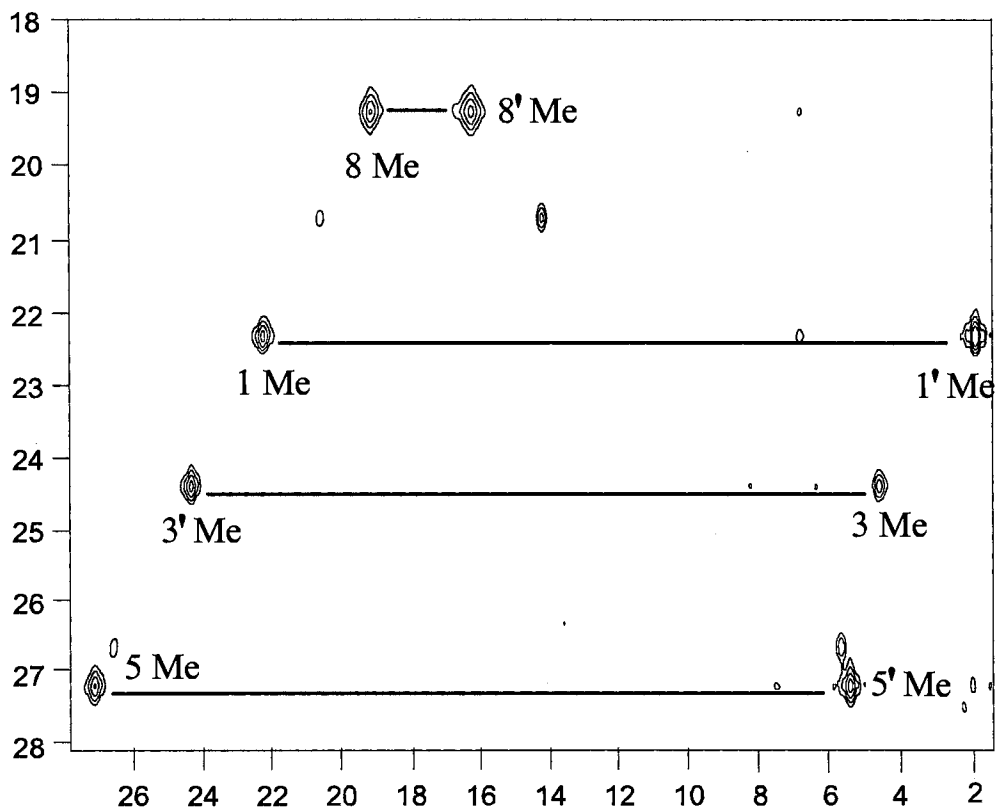


Figure 14. EXSY spectrum of the double mutant of *pa*-HO-CN. The heme methyl resonances arising from the wild type and alternative heme seatings are labeled as 1, 3, 5, 8 and 1', 3', 5', 8', respectively.

Until the recent discovery of *pa*-HO [8], a trademark of heme oxygenases from a variety of different sources (h-HO-1, r-HO-1, *cd*-HO, and *nm*-HO) has been their ability to degrade heme with exquisite α -regioselectivity. Consequently, *pa*-HO is unusual among heme oxygenases in that it is the only known heme oxygenase that degrades heme to δ -biliverdin. The structures of h-HO-1 [13] and r-HO-1 [15] share a homologous, largely α -helical fold with the structure of the bacterial heme oxygenases (*nm*-HO [12] and *cd*-HO), despite the low sequence identity [12]. It is therefore not unreasonable to expect that the overall fold of *pa*-HO is likely to be similar to that of the heme oxygenases for which a structure is known, given the relatively high degree of sequence identity (37%) between *nm*-HO and *pa*-HO. In fact, assuming that the fold of *pa*-HO is typical of other heme oxygenases allowed us to conclude that Lys-16 and Tyr-112 in *nm*-HO (Lys-16 and Tyr-134 in h-HO-1), which form important hydrogen bonding and electrostatic interactions with the heme propionates, are replaced by Asn-19 and Phe-117 in *pa*-HO. Also, by assuming that the overall fold of *pa*-HO is typical of other heme oxygenases, the amino acid alignments allowed us to hypothesize that in the absence of nearby residues capable of compensating for the lack of interactions between the heme propionates and Asn-19 and Phe-117 in *pa*-HO, replacing these residues for Lys and Tyr, respectively, would likely introduce the ionic and hydrogen bonding interactions typically experienced by the heme propionates of other heme oxygenases. Consistent with this hypothesis, the heme in the *pa*-HO double mutant experiences a dynamic equilibrium between two heme seatings, which at 10 °C coexist with approximately equimolar concentrations. The fold of *nm*-HO (Figure 15) makes it evident that the heme seating of the enzyme orients the heme propionates such that they can interact with Lys-16 and Tyr-112; moreover, the heme seating results in the placement of the α -*meso* carbon at the

bottom of the heme pocket, where it is susceptible to hydroxylation and the placement of the δ -*meso* carbon at the exposed heme edge. It is also noteworthy, that the 1.5 Å-resolution structure of *nm*-HO indicates that the predominant heme orientational isomer places pyrrole ring II and the β -*meso* carbon at the deep end of the heme pocket [12], an observation that is in agreement with our preliminary NMR spectroscopic investigations of *nm*-HO, which also indicate that one of the heme orientational isomers in this enzyme is largely predominant, M:m = 95:5 (data not shown).

The phenomenon in which two heme seatings are related to one another by an in-plane rotation of the heme in the Asn-19 Lys/Phe-117 Tyr *pa*-HO can be summarized by the equilibria in Scheme 1. The scheme was constructed by placing the site of attack as is seen in the fold of *nm*-HO (see Figure 15) and by assuming that the major orientational isomer is the same as that favored by *nm*-HO. Results obtained from the NMR spectroscopic studies conducted with the Asn-19 Lys/Phe-117 Tyr *pa*-HO indicate that in the major heme orientational isomer exhibiting the wild type heme seating the molecular *x* axis forms an angle ϕ of 35° with the imidazole-plane. This is illustrated by **1** in scheme I; consequently, the minor isomer exhibiting the wild type seating **2** is obtained by rotating **1** 180° about the α - γ -*meso* axis. Note that rotation of the heme about the α - γ -*meso* axis only affects the macrocycle, leaving the axial ligand unperturbed so that in the minor isomer exhibiting the wild type seating **2** the molecular *x* axis makes an angle ϕ of 55° with the histidine-imidazole plane. The different value of ϕ in the major and minor isomers is consistent with the different patterns of resolved methyl resonances observed for the heme orientational isomers. The alternative heme seating corresponding to the major isomer can be obtained by considering that the NMR spectroscopic studies led us

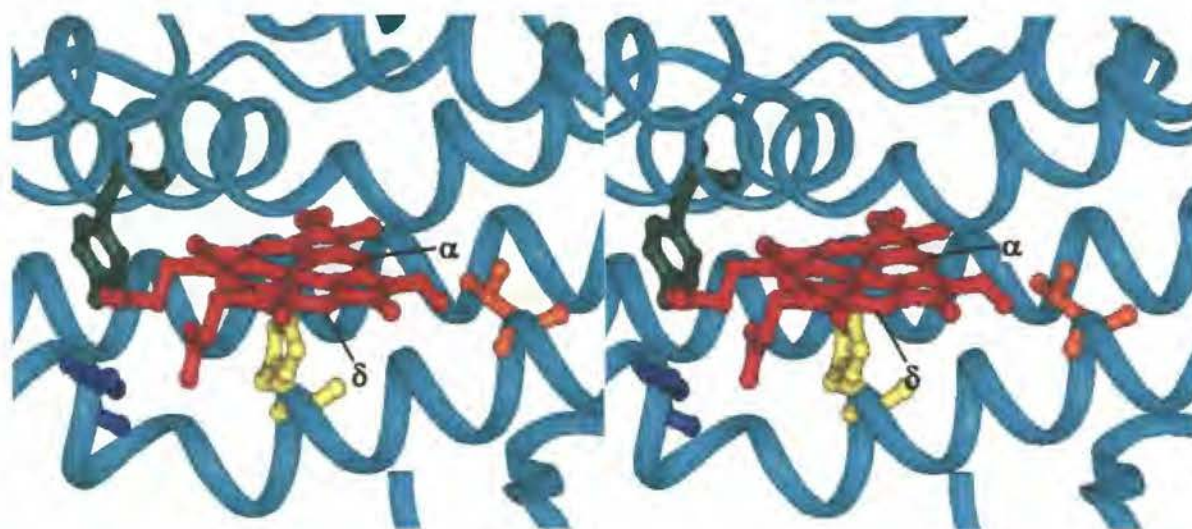


Figure15. Stereoview of the heme binding environment in *nm*-HO. The heme is red, the proximal His-23 is yellow, Tyr-112 is green, Lys-16 is blue and Val 30 is orange. The α -*meso* carbon, which is susceptible to attack in all α -hydroxylating heme oxygenases of known structure, is highlighted. PDB access code 1J77.

to conclude that the angle ϕ in the alternative heme seating is 100° . Thus, starting from the major isomer exhibiting the wild type heme seating **1**, it is possible to rotate the heme (hence, the x - y plane) 115° clockwise or 65° counterclockwise, in order to obtain **3** and **4**, respectively. The heme seating represented by **3** places the α -*meso* carbon where it can be hydroxylated by the enzyme, hence it is consistent with the regioselectivity of heme oxygenation exhibited by the Asn-19 Lys/Phe-116 Tyr double mutant of *pa*-HO, which we found produces α - (55%), δ - (35%), and β - (10%) biliverdin. On the other hand, the heme seating represented by **4** places the γ -*meso* carbon where it is susceptible to be hydroxylated in order to form γ -biliverdin. The fact that the double mutant enzyme does not oxidize heme to γ -biliverdin clearly indicates that the alternative heme seating displayed by the major isomer in the double mutant *pa*-HO is best represented by **3**. A similar analysis of the minor isomer is not possible because the relatively low intensity of the corresponding resonances precluded their unambiguous assignment. However, if we assume that the minor isomer rotates in-plane in a manner that is similar to that described for the major isomer, it is possible to estimate the angle ϕ by rotating the major isomer displaying the alternative heme seating by 180° about the α - γ -*meso* axis. In this manner, **5** and **6** are obtained by rotating **3** and **4**, respectively. It is apparent that **6** can be ruled out because it places the γ -*meso* axis where it is susceptible for attack, while on the other hand, **5** is conducive to the formation of α -biliverdin. Consequently, it is possible to conclude that **1** and **2**, respectively, represent the major and minor heme orientational isomers in the wild type seating, whereas **3** and **5**, respectively, represent the major and minor heme orientational isomers in the alternative heme seating.

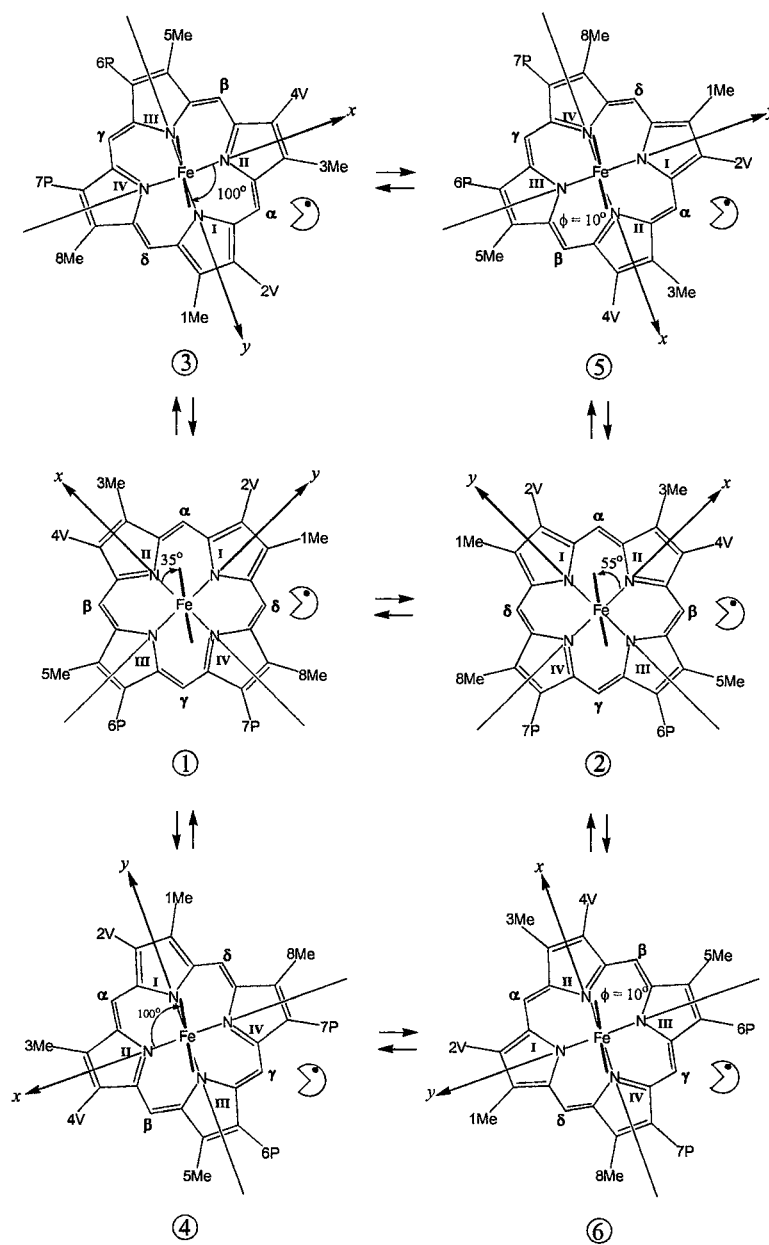
Careful integration of ^1H NMR signals attributed to heme methyl groups in the

major and minor isomers of molecules displaying the wild type heme seating **1** and **2** accounts for 45% of the total concentration, whereas the remaining 55% corresponds to major and minor isomers in the alternative heme seating **3** and **5**. The ^1H NMR spectrum also reveals that the ratio of heme orientational isomers **1:2** displaying the wild type heme seating is 87:13. This implies that 39% of the molecules harbor heme where the angle ϕ is 35° , which is conducive to attack at the δ -*meso* carbon, therefore explaining the formation of approximately 35% δ -biliverdin.

The 87:13 ratio of major to minor orientational isomers displaying the wild type heme seating also implies that approximately 6% of the molecules harbor a macrocycle that is rotated 180° about the α - γ -*meso* axis **2**. This rotation places the β -*meso* carbon in a position that is susceptible for attack, therefore explaining the formation of approximately 10% β -biliverdin (Table 2). α -Biliverdin, on the other hand, is derived from the alternative heme seating depicted by **3**, which places the α -*meso* carbon in a position where it is susceptible for attack. The ^1H NMR spectrum of the mutant reveals that the alternative heme seating, which accounts for 55% of the total concentration, is also heterogeneous in that two heme orientational isomers (**3:4** = 80:20) coexist. However, since 180° rotation of **3** about the α - γ -*meso* axis results in **5** but does not exchange the position of *meso*-carbon α , it is apparent that only the α -*meso* position is susceptible for attack, a prediction that is consistent with the experimental observations.

If **1** is incorporated into the fold of *nm*-HO, where Lys-16 and Tyr-112 have been replaced for Asn and Phe, respectively, a visual representation of the seating proposed for wild type *pa*-HO is obtained (Figure 16-A). This heme seating places the δ -*meso* carbon in a position where it can be hydroxylated by the enzyme, and rotation of the heme about

Scheme I



the α - γ -*meso* axis places the β -*meso* carbon where it is susceptible to hydroxylation, thus the proposed heme seating for wild type *pa*-HO is consistent with the characteristic δ - (70%) and β - (30%) regioselectivity displayed by the wild type enzyme. Note that in the model displayed in Figure 16-A the imidazole plane is aligned nearly parallel with the α - γ -*meso* axis and forms an angle ϕ of 35° with the molecular x -axis; the latter is aligned along the nitrogen atoms of pyrrole rings II (harboring 3Me) and IV (harboring 8Me).

The heme propionates point in the direction of the exposed heme edge, hence steric encumbrances between the relatively large (and charged) heme propionates and polypeptide residues is not anticipated. In a similar manner, a visual representation of the alternative heme seating in the Asn-19 Lys/Phe-117 Tyr double mutant of *pa*-HO can be modeled by inserting **3** into the fold of *nm*-HO (Figure 16-B). It can be seen that the heme propionates interact with Lys-16 (Lys-19 in the double mutant) and Tyr 112 (Tyr-117 in the double mutant), and that the α -*meso* carbon is placed at the bottom of the heme pocket, where it is observed in the structure of *nm*-HO. Also note that the imidazole plane is aligned nearly collinear with the N-Fe-N axis of pyrroles I and III and forms an angle ϕ of 110° with the molecular x axis, which lies along the nitrogens of pyrrole ring II (harboring 3'Me) and IV (harboring 8'Me). As discussed above, the NMR spectroscopic studies carried out with the double mutant led us to suggest that in the double mutant the heme seatings of Figure 16-A and B are related by a dynamic 110° in-plane rotation of the heme. In fact, a NOESY spectrum of the Asn-19 Lys/Phe-117 Tyr double mutant reveals an NOE between a signal at -0.75 ppm and the resonances corresponding to 1Me in the wild type seating (Figure 13-A) and 3'Me in the alternative seating (Figure 16-B). The signal at -0.75 ppm is tentatively attributed to one of the γ -methyl groups in Val-33 (Val

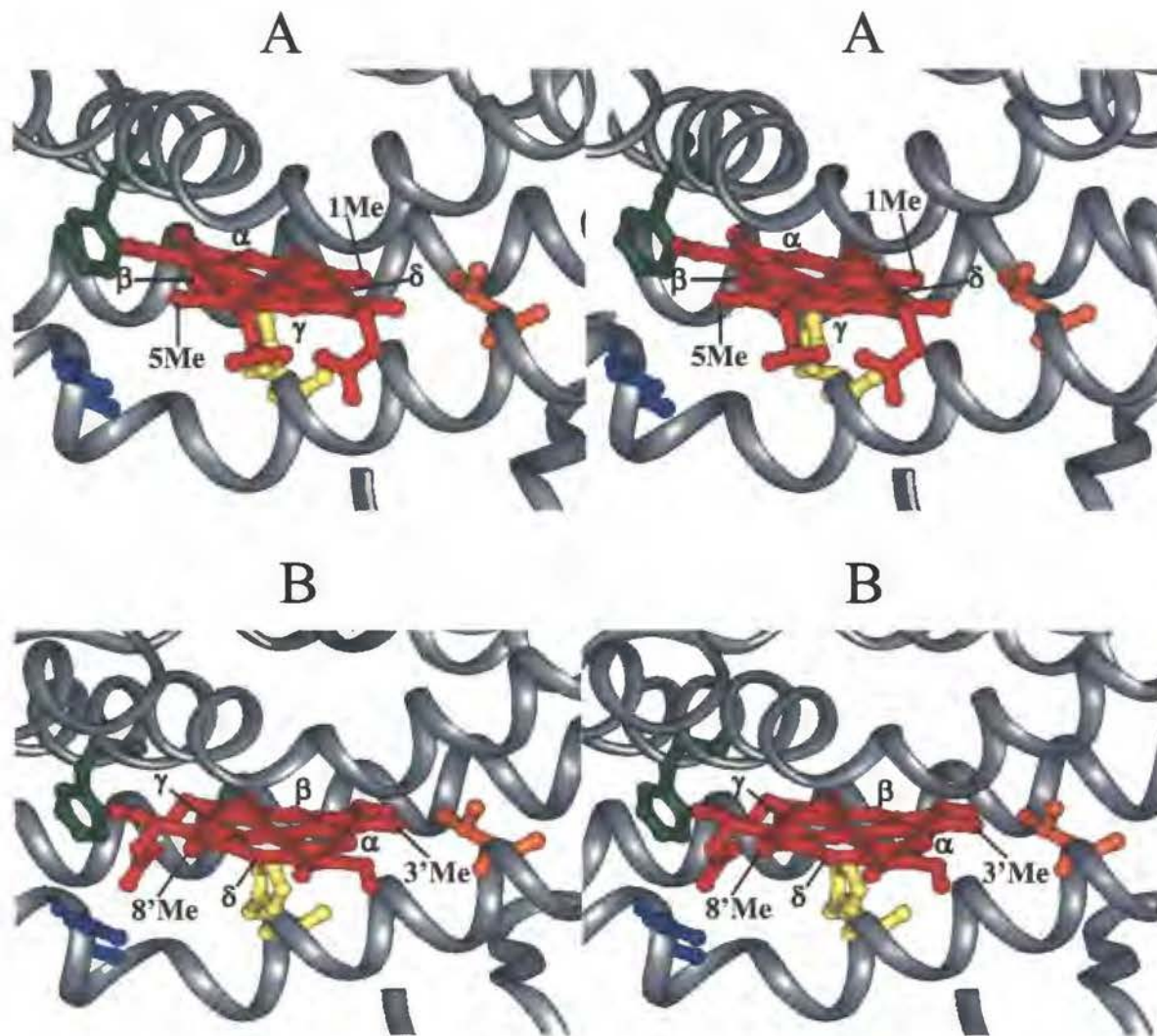


Figure 16. Stereoview of the predicted wild type (A) and alternative (B) heme seatings in mutant *pa*-HO-CN, modeled into the fold of *nm*-HO, where the heme is shown in red, Lys-16 and Tyr-112 in *nm*-HO have been replaced by Asn-19 (blue) and Phe-117 (green). Val 30 in *nm*-HO (orange) is Val-33 in *pa*-HO. The wild type seating of *pa*-HO (A) places the δ -*meso* carbon where it is susceptible to hydroxylation, whereas 110° in-plane rotation of the heme results in the alternative seating (B), thus positioning the α -*meso* carbon where it can be hydroxylated.

30 in *nm*-HO), hence the NOE between this side chain resonance and the 1Me and 3'Me groups is consistent with the presence of two heme seatings, related by a 110° in-plane rotation of the heme.

Relevance to the Mechanism of Action of HO and Concluding Remarks.

The discussion above suggests a strong contribution from steric interactions in the distal helix in dictating the regioselectivity of oxidative degradation, however, it is important to point out that electronic contributions are probably equally important, but cannot be discerned from the data at hand. In this context, it is interesting to consider the results obtained from the oxidation of *meso*-methyl hemes [16] and *meso*-formyl hemes [17] by heme oxygenase. The γ -*meso*-methylheme was oxidized exclusively at the γ -*meso* position, δ -*meso*-methylheme was oxidized at the δ - and α -*meso* positions, and the β -derivative was found to be a poor substrate [16]. On the other hand, all four isomers of *meso*-formylheme are never oxidized at the *meso* carbon bearing the electron withdrawing formyl group [17]. These observations, which are not compatible with a simple steric steering of the iron bound peroxide, suggest that the regioselectivity of heme oxygenation is also affected by the electronic structure of heme in heme oxygenase. Moreover, recent experiments carried out with heme models of the ferric hydroperoxide ($\text{Fe}^{\text{III}}\text{-OOH}$) complex of HO [18] suggest that the electronic structure of this key intermediate is crucial to the *meso*-hydroxylation of the heme in HO. These studies suggested that at ambient temperatures the electronic structure of this important ferric hydroperoxide intermediate is low-spin with the unpaired electron residing in a d_{xy} orbital. Work carried out with low-spin (d_{xy})¹ complexes has clearly demonstrated that in order to delocalize spin density from the d_{xy} orbital into the porphyrin π system, the

macrocycle has to ruffle significantly, so that the nodal planes of the p_z orbitals of the macrocycle are no longer in the xy plane and the components (projections) of these p_z orbitals in the xy plane have the proper symmetry to interact with the d_{xy} orbital [60]. The porphyrin orbital with the right symmetry to interact with the ruffled macrocycle $3a_{2u}(\pi)$ possesses large electron density at the *meso*-carbons,[18, 61, 62]; therefore, it has been proposed that the large spin density at the *meso*-carbons directs the attack of the Fe^{III} -OOH intermediate on a heme *meso*-carbon [18]. If the porphyrin ring of the Fe^{III} -OOH intermediate is ruffled by virtue of its $(d_{xy})^1$ electronic structure, it is expected to place pairs of *meso*-carbons *i.e.* α/γ and β/δ approximately 0.6 Å above and below the heme plane,[60-62] where one will be susceptible to attack by the coordinated peroxide. Consequently, exclusive attack of the α -*meso* carbon can only be explained if the γ -*meso* carbon is shielded from attack by steric protection, strongly suggesting that the outcome of heme oxygenation is governed by an interplay between electronic and steric contributions.

Finally, it is also interesting to point out that the plane of the proximal histidine in *pa*-HO, which hydroxylates the β -*meso* carbon, is aligned along the α - γ -*meso* axis, whereas the proximal histidine-imidazole plane in all other heme oxygenases (α -*meso* hydroxylation) is aligned along the β - δ -*meso* axis. The data in Table 3 reveals that the *meso* protons that lie on an axis that is perpendicular to the axis of the proximal ligand plane exhibit large isotropic shifts. For instance, *meso*- H_β and *meso*- H_δ in *pa*-HO exhibit chemical shifts of -2.2 and -2.5 ppm, whereas *meso*- H_α and *meso*- H_γ in *cd*-HO, *r*-HO-1 [59] and *h*-HO-1 [58] exhibit similar shifts. Thus, a relatively large amount of unpaired electron density appears to reside at the *meso*-hydrogens located along an axis that is perpendicular to that of the proximal ligand plane and might suggest a potential link

between the regioselectivity of oxidative cleavage and the orientation of the proximal histidine-imidazole plane. This potential correlation between regioselectivity and orientation of the proximal ligand, however, is not observed in the Asn-19 Lys/Phe-117 Tyr mutant of *pa*-HO-CN, where the alternative heme seating, which leads to the formation of 55% α -biliverdin, is likely to display a proximal histidine-imidazole plane that is oriented nearly parallel to the axis along the nitrogen atoms of pyrrole rings I and III (Figure 16-B). It is also important to point out that the cyanide complex of HO may not be the best system to study the effects of electronic structure on the reactivity and regioselectivity of the heme oxygenation reaction because the cyanide complexes of HO exhibit a $(d_{xy})^2(d_{xz},d_{yz})^3$ electronic configuration, with the unpaired electron residing in one of the d_{π} orbitals, d_{xz} or d_{yz} . Iron(III) porphyrinates exhibiting an unpaired electron in one of the d_{π} orbitals have been shown to possess small to negligible unpaired electron density at the *meso*-carbons [61, 62]. On the other hand, magnetic resonance studies conducted with models of the Fe^{III} -OOH complex of HO, which is believed to be the oxidizing species that attacks a *meso* carbon in the heme, have suggested that this intermediate possesses a $(d_{xz},d_{yz})^4(d_{xy})^1$ electronic structure [18]. As has been pointed out above, Fe^{III} porphyrinates exhibiting an unpaired electron in the d_{xy} orbital place large unpaired electron density at the *meso* positions [60-62]. Since this property of Fe^{III} porphyrinates helps to explain the attack on by the porphyrin *meso*-carbons by the coordinated peroxide in the Fe^{III} -OOH complex of HO, it is important that future efforts aimed at explaining the regioselectivity of the reaction also address the nature of the electronic structure of the highly reactive Fe^{III} -OOH intermediate.

Acknowledgement: The mutagenesis and expression of both wild type and mutant enzymes was carried out in collaboration with Rahul Deshmuk and Dr. Angela Wilks at the School of pharmacy of the University of Maryland. The Raman spectroscopy was carried out in collaboration with Hong-wei Huang and Dr. Pierre Moënne-Loccoz at the OGI School of Science and Engineering, Oregon. The ^{13}C Labeled ALAs were obtained in collaboration with Dr. Richard Bunce from Oklahoma State University.

References

1. Tenhunen, R., Marver, H., S., and Schmid, R.; *J. Biol. Chem.*, (1969). **244**: 6388-6394.
2. Ortiz de Montellano, P.R. and Wilks, A.; *Adv. Inorg. Chem.*, (2000). **51**: 359-407.
3. Liu, Y., Lightning, L.K., Huang, H., Moënne-Loccoz, P., Schuller, D.J., Poulos, T.L., Loehr, T.M., and Ortiz de Montellano, P.R.; *J. Biol. Chem.*, (2000). **275**: 34501-34507.
4. Ortiz de Montellano, P.R.; *Curr. Opin. Chem. Biol.*, (2000). **4**: 221-227.
5. Yoshida, T., Noguchi, M., and Kikuchi, G.; *J. Biol. Chem.*, (1980). **255**: 4418-4420.
6. Wilks, A. and Schmitt, M.P.; *J. Biol. Chem.*, (1998). **273**: 837-841.
7. Chu, G.C., Tomita, T., Sönnichsen, F.D., Yoshida, T., and Ikeda-Saito, M.; *J. Biol. Chem.*, (1999). **274**: 24490-24496.
8. Ratliff, M., Zhu, W., Deshmukh, R., Wilks, A., and Stojilkovic, I.; *J. Bacteriol.*, (2001). **183**: 6394-6403.
9. Stojilkovic, I. and Hantke, K.; *EMBO J.*, (1992). **11**: 4359-4367.
10. Stojilkovic, I. and Hantke, K.; *Mol. Microbiol.*, (1994). **13**: 719-732.
11. Zhu, W., Hunt, D.J., Richardson, A.R., and Stojilkovic, I.; *J. Bacteriol.*, (2000). **182**: 439-447.
12. Schuller, D.J., Zhu, W., Stojilkovic, I., Wilks, A., and Poulos, T.L.; *Biochemistry*, (2001). **40**: 11552-11558.
13. Schuller, D.J., Wilks, A., Ortiz de Montellano, P.R., and Poulos, T.L.; *Nature Struct. Biol.*, (1999). **6**: 860-867.
14. Koenigs Lightning, L., Huang, H., 3 Moënne-Loccoz, P., Loehr, T.M., Schuller,

- D.J., Poulos, T.L., and Ortiz de Montellano, P.R.; *J. Biol. Chem.*, (2001). **276**: 10612-10619.
15. Sugishima, M., Omata, Y., Kakuta, Y., Sakamoto, H., Noguchi, M., and Fukuyama, K.; *FEBS Lett.*, (2000). **471**: 61-66.
 16. Torpey, J., Lee, D.A., Smith, K.M., and Ortiz de Montellano, P.R.; *J. Am. Chem. Soc.*, (1996). **1118**: 9172-9173.
 17. Torpey, J. and Ortiz de Montellano, P.R.; *J. Biol. Chem.*, (1997). **272**: 22008-22014.
 18. Rivera, M., Caignan, G.A., Astashkin, A.V., Raitsimring, A.M., Shokhireva, T.K., and Walker, F.A.; *J. Am. Chem. Soc.*, (2002). **124**: 6077-6089.
 19. Sambrook, J., Fritsch, E.F., and Maniatis, T., *Molecular Cloning: A Laboratory Manual*. 2nd ed. 1989, Cold Spring Harbor, NY: Cold Spring Harbor Press.
 20. Wilks, A. and Ortiz de Montellano, P.R.; *J. Biol. Chem.*, (1993). **268**: 22357-22362.
 21. Fuhrop, J.H. and Smith, K.M., in *Porphyryns and Metalloporphyryns*, K.M. Smith, Editor. 1975, Elsevier: Amsterdam. p. 804-807.
 22. Sakamoto, H., Omata, Y., Adachi, Y., Palmer, G., and Noguchi, M.; *J. Inorg. Biochem.*, (2000). **82**: 113-121.
 23. Bunce, R.A., Shilling III, C.L., and Rivera, M.; *J. Labelled Compd. and Radiopharm.*, (1997). **39**: 669-675.
 24. Rivera, M. and Walker, F.A.; *Anal. Biochem.*, (1995). **230**: 295-302.
 25. Warren, M.J. and Scott, A.I.; *Trends Biochem. Sci.*, (1990). **15**: 426-431.
 26. Scott, A.I.; *Angewandte Chemie*, (1993). **32**: 1223-1376.
 27. Rivera, M., Qiu, F., Bunce, R.A., and Stark, R.E.; *JBIC*, (1999). **4**: 87-98.

28. Summers, M.F., Luigi, G.M., and Bax, A.; *J. Am. Chem. Soc.*, (1986). **108**: 4285-4294.
29. Patt, S.L. and Sykes, B.D.; *J. Chem. Phys.*, (1972). **56**: 3182-3184.
30. Lankhorst, P.P., Wille, G., van Boom, J.H., Altona, C., and Haasnoot, C.A.G.; *Nucl. Acids Res.*, (1983). **11**: 2839-2856.
31. Jeneer, J., Meier, B.H., Bachmann, P., and Ernst, R.R.; *J. Chem. Phys.*, (1979). **71**: 4546-4553.
32. Spiro, T.G., T.G. Spiro, Editor. 1988, John Wiley & Sons: New York. p. 1-37.
33. Sun, J., Wilks, A., Ortiz de Montellano, P.R., and Loehr, T.M.; *Biochemistry*, (1993). **32**: 14151-14157.
34. Wilks, A. and Moënne-Loccoz, P.; *J. Biol. chem.*, (2000). **275**: 11686-11692.
35. Kitagawa, T., T.G. Spiro, Editor. 1988, John Wiley & Sons: New York. p. 97-131.
36. Bangcharoenpaurpong, O., Schomacker, K.T., and Champion, P.M.; *J. Am. Chem. Soc.*, (1984). **106**: 5688-5698.
37. Smulevich, G., Feis, A., Focardi, C., Tams, J., and Welinder, K.G.; *Biochemistry*, (1994). **33**: 15425-15432.
38. Othman, S., Richaud, P., Verméglio, A., and Debois, A.; *Biochemistry*, (1996). **35**: 9224-9234.
39. Hu, S., Smith, K.M., and Spiro, T.G.; *J. Am. Chem. Soc.*, (1996). **118**: 12638-12646.
40. Keller, R.M. and Wüthrich, K.; *Biochim. Biophys. Acta*, (1980). **621**: 204-217.
41. La Mar, G.N.; *Proc. Natl. Acad. Sci. U.S.A.*, (1978). **75**: 5755-5759.
42. La Mar, G.N. and S., d.R.J., in *Biological Magnetic Resonance*, J. Reuben, Editor. 1993, Plenum: New York. p. 1-78.

43. Banci, L., in *Biological Magnetic Resonance*, J. Reuben, Editor. 1993, Plenum: New York. p. 79-112.
44. Satterlee, J.D., Alam, S., Yi, Q., Erman, J.E., Constantinidis, I., Russell, D.J., and Moench, S.J., in *Biological Magnetic Resonance*, J. Reuben, Editor. 1993, Plenum: New York. p. 275-297.
45. Walker, F.A.; *J. Am. Chem. Soc.*, (1980). **102**: 3254-3256.
46. Goff, H.; *J. Am. Chem. Soc.*, (1980). **102**: 3252-3254.
47. Satterlee, J.D.; *Annu. Rep. Nucl. Magn. Reson. Spectrosc.*, (1986). **17**: 79-178.
48. Walker, F.A., Buehler, J., West, J.T., and Hinds, J.L.; *J. Am. Chem. Soc.*, (1983). **105**: 6923-6929.
49. Turner, D.L., Salgueiro, C.A., Schenkels, P., LeGall, J., and Xavier, A.V.; *Biochim. Biophys. Acta*, (1995). **1246**: 24-28.
50. Turner, D.L.; *Eur. J. Biochem.*, (1993). **211**: 563-568.
51. Banci, L., Pierattelli, R., and Turner, D.L.; *Eur. J. Biochem.*, (1995). **232**: 522-527.
52. Pierattelli, R. and Turner, D.L.; *Eur. Biophys. J.*, (1996). **24**: 342-347.
53. Louro, R.O., Correia, I.J., Brennan, L., Coutinho, I.B., Xavier, A.V., and Turner, D.L.; *J. Am. Chem. Soc.*, (1998). **120**: 13240-13247.
54. Shokhirev, N.V. and Walker, F.A.; *J. Am. Chem. Soc.*, (1998). **120**: 981-990.
55. Shokhirev, N.V. and Walker, F.A.; *JBIC*, (1998). 581-594.
56. Quillin, M.L., Tiansheng, L., Olson, J.S., Phillips, G.N., Dou, Y., Ikeda-Saito, M., Regan, R., Carlson, M., Gibson, Q.H., Li, H., and Elber, R.; *J. Mol. Biol.*, (1995). **245**: 416-436.
57. Emerson, S.D. and La Mar, G.N.; *Biochemistry*, (1990). **29**: 1545-1556.

58. Hernandez, G., Wilks, A., Paolesse, R., Smith, K.M., Ortiz de Montellano, P.R., and La Mar, G.N.; *Biochemistry*, (1994). **33**: 6631-6641.
59. Gorst, C.M., Wilks, A., Yeh, D.C., Ortiz de Montellano, P.R., and La Mar, G.N.; *J. Am. Chem. Soc.*, (1998). **120**: 8875-8884.
60. Safo, M.K., Walker, F.A., Raitsimring, A.M., Walters, W.P., Dolata, D.P., Debrunner, P., G., and Scheidt, W.R.; *J. Am. Chem. Soc.*, (1994). **116**: 7760-7770.
61. Walker, F.A.; *Coord. Chem. Rev.*, (1999). **185-186**: 471-534.
62. Walker, F.A., in *The Porphyrin Handbook*, R. Guilard, Editor. 2000, Academic Press. p. 81-183.

Vita



GREGORI A. A. CAIGNAN

Candidate for the Degree of

Doctor of Philosophy

Thesis: THE NATURE OF THE FERRIC HYDROPEROXIDE INTERMEDIATE IN
HEME OXYGENASE: A MAGNETIC RESONANCE INVESTIGATION

Major Field: Chemistry

Biographical:

Education: Bachelor of Science in chemistry with honors from Université des Sciences et Technologies de Lille, Villeneuve d'Ascq, France in 1998. Master of Science in chemistry from Oklahoma State University, Stillwater, Oklahoma in December 2000. Completed the requirements for the Degree of Doctor of Philosophy with a major in chemistry at Oklahoma State University, Stillwater, Oklahoma in December 2003.

Professional Experience: Graduate teaching assistant, Department of Chemistry, Oklahoma State University, 1998-2000. Research assistant, Department of Chemistry, Oklahoma State University, 2000-2003.